Current & Future Challenges in Energy Issues

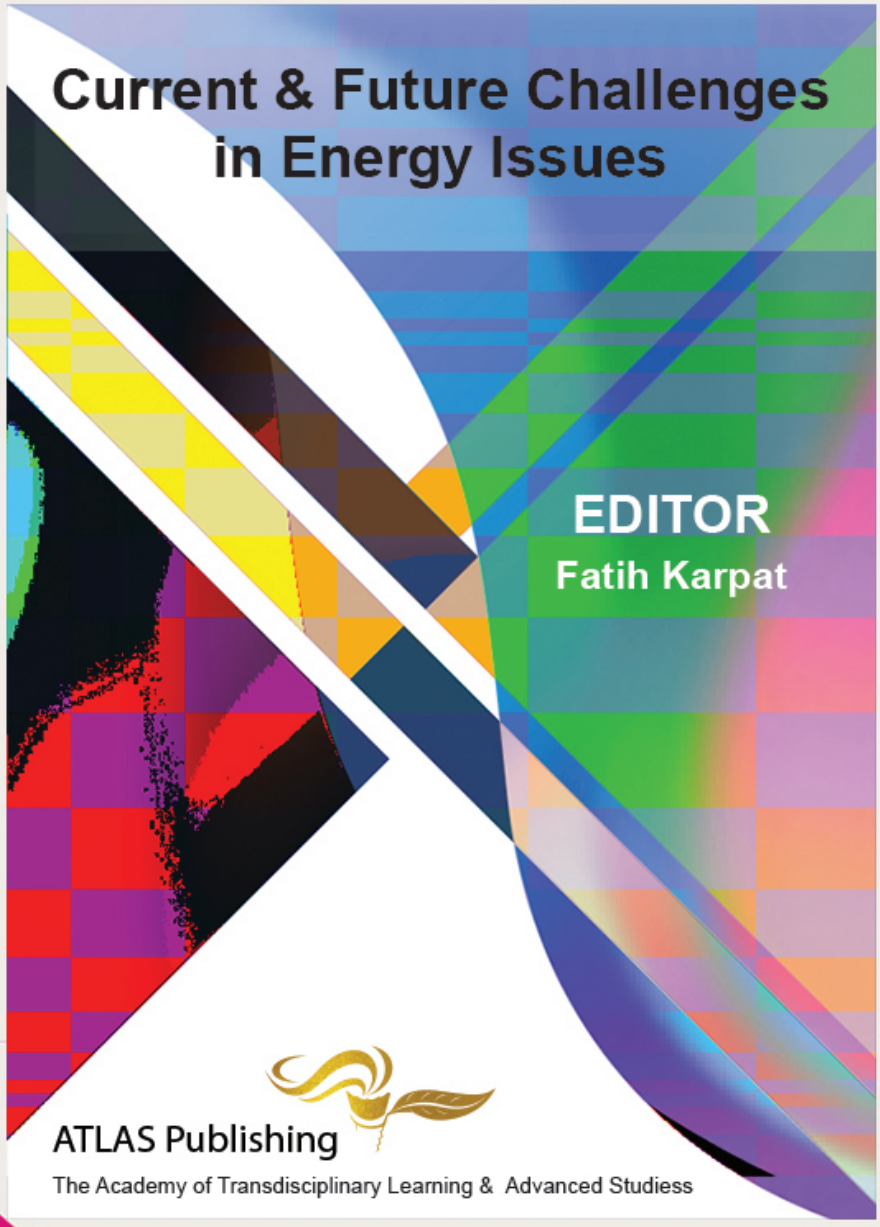

EDITOR

Fatih Karpat

ATLAS Publishing

The Academy of Transdisciplinary Learning & Advanced Studiess

Current & Future Challenges in Energy Issues

Editor
Fatih Karpat

Editor
Fatih Karpat
Bursa Uludağ Üniversitesi
Bursa, Turkey

ATLAS Publishing, March 2023

This is a reprint of articles from the Special Issue published online in the open access journal materials (ISSN: 1949-0569 online) (available at: https://www.atlas-tjes.org/index.php/tjes/issue/view/13).

For citation process, cite each article independently as indicated on the article page online and as indicated below:

LastName, A.A.; LastName, B.B. (**Year**). Article Title, *Journal Name*, Volume Number, Page range, doi number.

ISBN: 978-0-9998733-6-6 (PDF)

Preface

Providing reliable, safe, and affordable energy to support human activities is a significant challenge now and in the future. With the growing global population and increased industrialization in developing nations, the need for the energy of humanity has reached record levels. New technologies and innovation are the solutions to the energy transition. This book examines the role of new technologies in tackling current and future energy challenges, with a limited number of examples. The book consists of thirteen chapters illustrating a wide range of areas where energy is subject. These areas include physics, chemical engineering, mechanical engineering, biology, nanoscience, transportation, and control systems, system modeling, and simulation. Many interesting problems related to wind turbines, electric cars, solar energy systems, decarbonizing energy systems, diesel engines, dehumidification processes, unmanned aerial vehicles, bicycles, and machines have been included throughout the book, and its contents will be beneficial for students, and professionals in wide areas of interest.

Fatih Karpat
Editor

About the Editor

Dr. Fatih Karpat is a Professor in the Department of Mechanical Engineering at the Bursa Uludag University in Turkey. He received a Ph.D. degree in Mechanical Engineering from Uludag University, Turkey in 2005. He has served as the Vice-Chair of the Department of Mechanical Engineering at Uludag University since 2011, and was appointed as the Institutional Coordinator of the Mevlana Exchange Program in 2013, was appointed as the vice director of Uludag University Material Science Research Center in 2018, and also managed the Product Design & Development Laboratory in the department.

Prior to joining the faculty, he worked as a Post-Doctoral Research Associate in the Mechanical Engineering Department at Texas Tech University in 2006 and 2010. His research interests include, but not limited to, experiments and numerical simulation of power transmission systems (gears, clutch, etc.), lightweight designs, and advanced joining technology (laser welding, etc.), sustainability. His research has been supporting by the Ministry of Science, Industry, and Technology of Turkey, The Scientific and Technological Research Council of Turkey (TUBITAK), the Bursa Uludag University (BUU), the Turkish Aircraft Industries Corporation (TUSAS), and industry. He has published more than 100 peer-reviewed articles. He co-authored "Solved Problems on Design of Machine Elements" in Turkish. He is a member of the European Society of Biomechanics (ESB). He is also a member of the Bursa Uludag University Senate.

Table of Contents

CHAPTER 1

Influence of Operational Variables in Bicycle Driven Bamboo Slicing Phenomena by Methodology of Response Surface Approach

Siddharth K. Undirwad

Article citation information: (2022), *TJES*, Vol. SP-2, pp. 23-41, doi:10.22545/2022/00174

Since global energy consumption rises, there seems to be a pressing need to create innovative technologies for saving energy and power production, especially those with lower ecological effects. There is indeed a current must to discover an alternate for renewable sources of energy to be used at any time from any location as well as being accessible to the entire public. Human energy is indeed a kind of alternative energy which has been employed to varying degrees throughout history. In this regard, this research consists of the design and construction of a pedal-driven bamboo slivering (sliver making) machine powered by a human-powered flywheel motor (HPFM). This article evaluates the overall impacts of several process factors upon the outputs of the human-powered bamboo slivering (sliver cutting) phenomenon, such as torque -resistive, sliver numbers and processing time. The 108 sets of experiments were carried out based on which experimental based models were formulated by using designed experiments and the influence of several independent (input)factors on response (output factors) variables were investigated in cutting the slivers of bamboo using an approach of response surface methodology.

Keywords: Bamboo sliver, HPFM, response surface methodology, energy, dependant variable, independent variable.

1.1 Introduction

The power of human and its energy was disregarded during periods of increasing utilization of fossil fuels. However, because of extremely high costs of fossil fuels and the severe pollution of environment caused by them, human power has resurfaced as a sustainable source of energy. There are serious power shortfall issues as a result of increased industrialization, as well as

due to constraints on non-availability of electricity in the interior and further power generation challenges. In this sense, the energy sources are human-powered systems, which are classified as non-conventional sources of energy. Bamboo compares favorably to other materials of building such as timber, concrete and steel in terms of energy needs during construction, simplicity of usage and safety, stiffness per unit area of material and strength. Bamboo's adaptability is partly owing to its anatomical structure, which adds to its mechanical qualities. Bamboo is the best to use everywhere due to its simplicity in production [1]. Aside from numerous of conventional methods and kinds where bamboo is largely employed for residential construction of buildings and houses, a number of commercially made items and components are used in construction of building [2]. Slivers of Bamboo are continually used for bamboo mats weaving, which have a broad range of uses such as wall paneling, handicrafts, furniture, wall papers, and so on, demonstrating the vast usage of slivers of bamboo in the industries and business manufacturing [3]. There is a significant influence of human activities on workings of Earth system such as growth in population, development of economy, and rising demands of energy. This enhances the need of dependable and reliable supply of energy that is robust to internal and external challenges which can conform unforeseen shocks in future. It is vital to emphasize that energy transformation should viewed as a means for dealing with grand energy challenges rather than global challenge [4]. In the current scenario, there is immediate requirement to identify alternative forms of power generation. The technologies of renewable or alternative energy are already acknowledged to have the potential to considerably cover the power demand resulting in reduction of emissions. To contribute to the sustainable development and prevent global catastrophe, it requires a speedy and worldwide shift to technology of renewable or alternative energy sources [5]. According to the reports and study, the renewable or alternative sources of energy may increase its proportion of total primary supply of energy from fifteen percent (in 2015) to sixty-three percent (in 2050). This probable growth of renewables along with increased energy efficiency may generate ninety-four percent of the reduction in emissions. While actual numbers may differ, the current scenario assessments agree that energy efficiency and alternative energy are more important to achieve the climate goals [6].

Alternative or renewable energies having lower environmental impacts can be considered to be only the possible solution for sustainability challenge which is been fought since long back. The global adoption of renewable energy remains restricted despite of growing knowledge of its numerous benefits. For the long term period, the traditional methods of power generation with exhaustible fuels like gas, oil and coal is usually seen as unreliable due to growing knowledge of environmental impacts [7]. Papadis, E. and Tsatsaronis, G. [8] in their paper examine the historical evolution of worldwide decarbonization facts and evaluated that technology pertaining to every sector. They assess the technological solutions whether feasible and sustainable for future trends of energy field and presented the analysis of issues in the view of economical, technical, societal and ecological challenges. The current state of affairs in the energy sector's decarbonization is far away from adequacy. Recent advances in atmospheric changes and rising emissions of carbon dioxide globally demonstrate that there is an urgent need to boost the efforts greatly for decarbonization of the energy issues [8]. Keeping view towards the severe challenges of energy crisis and its generation, many researchers have worked and are working on these issues to find out the solution. Modak J. P. and his colleagues [9 to 12] have constructed human powered machinery capable of energizing the process units requiring 3-7 HP which can be operated intermittently. The HPFM driven machines were designed and developed for wood turning [10], chaff cutter [11] and electricity generation [12] etc. which motivated the author to design and fabricate the human powered bamboo slicing machine. Sakhale, C. N. et al [13] had designed and developed

Figure 1.1: *Human powered bamboo slivering machine.*

the comprehensive bamboo processing machine run by an electric motor which comprises of four operations namely, (a) Bamboo cross cutting, (b) Bamboo Splitting, (c) Sliver cutting operation and (iv) Stick making. This machine is operated by means of electric motor which is again pointing towards the limitations on availability of electric power.

Therefore, with respect to a context of human powered operated systems as few of the forms of non-traditional energy, the bamboo slivering machine run by HPFM was designed, constructed and experiments were performed by identifying various process parameters (e.g. independent and dependent parameters) applying the design of experiments and experimentation theory [14]. The whole world is experiencing power and energy shortages as a result of lack of power in the interior and rural region. This is also due to various limitations on generation of additional power and energy. Thus, since this is the human operated machine and doesn't require electricity to run, this human powered machine is the best option in such energy crisis situation because the human energy is easily and globally available in ample quantity in every corner of the world. Human energy is proven to be the form of energy which does not have any severe impacts on climate, environment and atmosphere etc. The unskilled, semiskilled operator can operate this machine easily; hence it is very useful for the people facing the problems of power shortages which add to the enhancement of bamboo technology for low profiled people from the point of view of human powered mechanization.

1.2 Experimental Machine Set Up

The experimental machine set up consists of three major units viz. HPFM unit is bicycle driven unit which is energy unit with a flywheel and gear pair for speed raising, Unit of transmitting mechanical power comprising of gear pair for amplification of torque and clutch, and processing unit (used to cut the bamboo sliver) which consists of sliver cutter, feeder, adjusting knobs and two pairs of spring loaded rollers etc. These three units assemble the experimental set up of human powered bamboo slivering machine as shown in Figure 1.1. The unit of HPFM, unit of transmitting mechanical power and processing unit (bamboo sliver cutting unit) are shown in Figures 1.2, 1.3 and 1.4 respectively.

Figure 1.2: *HPFM Unit.*

Figure 1.3: *Mechanical power transmission unit.*

Figure 1.4: *Different views of bamboo sliver cutting unit.*

1.2.1 Working Details of Experimental Set Up

When pedals of the bicycle driven unit are operated by operator, the energy is stored in the flywheel. Power of maximum cycling has an impact due to fatigue, rate of pedaling, composition of fiber and size of muscle. Rolling and aerodynamic friction restrict cycling speed, and any mismatch in applied vs necessary power leads to the variations in energy of the system[15]. When

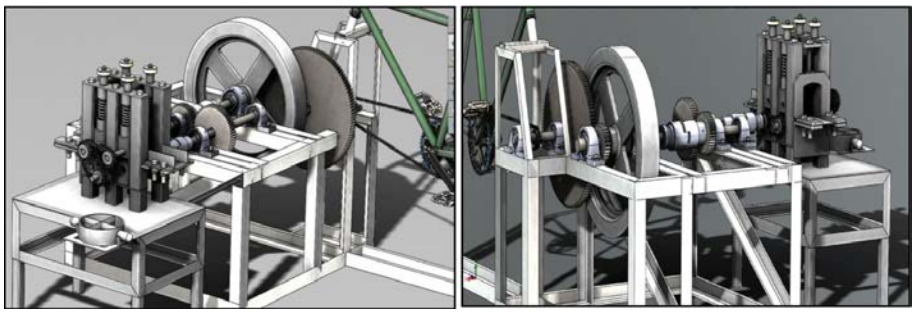

Figure 1.5: *CAD Model of Experimental set up (different views).*

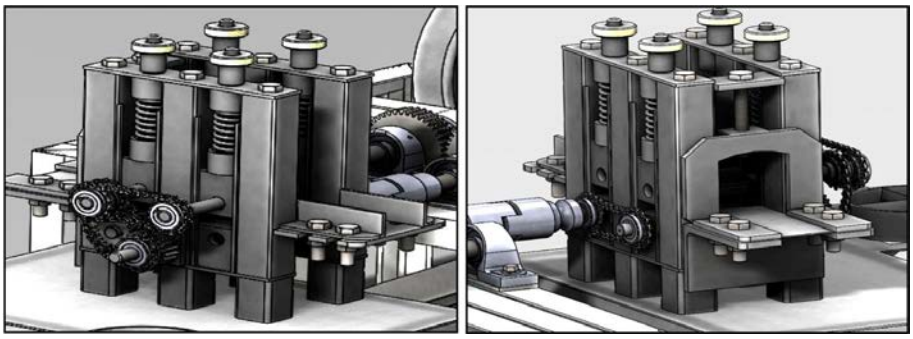

Figure 1.6: *CAD Model of Slivering Unit (different views).*

the flywheel stores sufficient required energy after pedaling, the flywheel energy is transmitted by engagement of clutch to the bamboo slivering unit via mechanical power transmission unit which commences the unit of bamboo sliver cutting to run. The feeder of slivering unit is fed with split bamboo which passes through the first pair of the push-in rollers and it further goes through the second pair of push-out rollers. Split bamboo strikes the cutter when it leaves push-out rollers which commence the cutting of sliver. The cutter is placed exactly in front of second pair of rollers. The sliver cutting action takes place instantly after the engagement of clutch and continues for the duration of about 5 to 20 seconds until flywheel stops rotating. The effect of increasing bicycle mass is insignificant with the most widely used gear ratios more than 1.5 [16]. The machine may be operated at various speeds by selecting the appropriate torque amplification gear ratio supplied on the slivering unit shaft. The CAD model of experimental machine set up is shown in Figure 1.5 and that of different views of slivering unit is shown in Figure 1.6.

The phenomena have been observed to be complicated owing to fluctuation in the dependent pi terms which fluctuates because of continual change in the angular or rotational speed of the bamboo slivering machine shaft. The variance in bamboo slivering machine shaft is decreasing rapidly. It is concerning with the resistance of operational process and inertial resistances, rely on linearly varying load torque due to fluctuations in human power or energy, bamboo material quality and non linear or varying cross sectional area of bamboo.

In the existing manual slivering machines, the manufacturers were capable of making the bamboo slivers of 1.0 to 1.5 feet long, but this HPFM driven machine can effectively manufacture the bamboo slices of 1.5 to 2.5 feet in length. The majority of the available manually operated

Table 1: Process parameters in sliver cutting phenomenon

Sr. No.	Parameters	Unit	Dimension	Type of Parameter
1	E_f = Stored Flywheel Energy	N-mm	ML^2T^{-2}	Independent
2	t_f = Speeding-up time of flywheel	Second	T	
3	Ω_f = Flywheel angular speed	Rad/s	T^{-1}	
4	L_b = Bamboo split length	mm	L	
5	g = Gravitational Acceleration	mm/s^2	LT^{-2}	
6	t_b = Bamboo split thickness	mm	L	
7	G = Gear Ratio	--	$M^0L^0T^0$	
8	W_b = Bamboo split width	mm	L	
9	E_c = Elastic Modulus of Cutter	N/mm^2	$ML^{-1}T^{-2}$	
10	C_H = Central (Horizontal) Distance between pairs of roller	mm	L	
11	Φ_c = Cutter's Cutting Angle	Degree	-	
12	L_{rc} = Cutter Tip to Roller Centre Distance	mm	L	
13	E_b = Elastic Modulus for Bamboo	N/mm^2	$ML^{-1}T^{-2}$	
14	C_V = Central (Vertical) Distance between pairs of rollers	mm	L	
15	n = Number of Slivers	--	$M^0L^0T^0$	Dependant
16	t_p = Processing Time	Second	T	
17	T_r = Torque (resistive)	N-mm	ML^2T^{-2}	

slivering machineries are hand operated, but the present HPFM driven machine is powered by bicycle where the leg muscles are used which are marked superior to the arm muscles keeping view towards the power and energy requirements, and approaching output in the less operating time. Previously in all HPFM driven machines, most of the researchers have worked upon only the average torque of their operation. In the present research, the models are constructed for resistive torque (average) as well as resistive torque (total) in the bamboo slivering phenomena so that the influence of input factor upon the responses can be compared for both.

1.3 Experimental Design and Methodology

The methodology of theory of experimentation [14] was applied in this work. By applying the method of dimensional analysis using the approach of design of experiments (DoE), mathematical models for various dependent and independent process parameters were formulated after the proper determination of variables in the phenomenon of bamboo sliver cutting. Experiment design includes benefits like increasing the result attained, reducing variability, and bringing the result closer to the aim, as well as shortening the time period and lowering the cost. Several independent and dependent factors in the phenomena of cutting the slivers were identified which are shown in Table 1, dimensional analysis was applied for the formation of pi-terms of all factors or parameters and independent (input) factors' pi-terms were reduced (refer Table 2) to lessen the intricacy and achieve simplicity in the nature of the phenomena of cutting the slivers. Test planning to determine the experimental plan, test envelope, test sequence and test points was also performed. And after experimental design, experiment conduction and filtering or purifying experimental records, the models were formulated, optimized and reliability was also determined.

1.3.1 Experimental Procedure

Classical experimentation plan [14] was utilized to perform the experiment. The experiment was designed and performed to accommodate the whole test envelope along with entire test points

Table 2: Process parameters' Pi terms

Parameters	Pi terms of parameters	Equations of Pi terms	Details of Equations of Pi terms
Independent / Input parameters	π_1	$\pi_1 = \frac{E_f}{L_h^3 E_b}$	Refers to the flywheel energy
	π_2	$\pi_2 = \omega_f \sqrt{\frac{L_b}{g}}$	Refers to the flywheel angular speed
	π_3	$\pi_3 = t_f \sqrt{\frac{g}{L_b}}$	Refers to the speeding-up time of flywheel
	π_4	$\pi_4 = G$	Refers to the gear ratio
	π_5	$\pi_5 = \left(\frac{W_b t_b C_H C_V L_{rc}}{L_b^5}\right)$	Refers to the machine's geometrical parameters
	π_6	$\pi_6 = \frac{E_c}{E_b}$	Refers to the elastic modulus of materials
	π_7	$\pi_7 = \varphi_c$	Refers to cutter's cutting angle
Dependent / Output Parameters	π_{D1}	$\pi_{D1} = t_p \sqrt{\frac{g}{L_b}}$	Refers to the time of processing or operational time
	π_{D2}	$\pi_{D2} = n$	Refers to the sliver numbers
	π_{D3}	$\pi_{D3} = \frac{T_r}{L_b^3 E_b}$	Refers to the torque (resistive)

contained in the vicinity of test envelope. All independent pi terms with the exception of one are kept fixed at their predetermined fixed level values in experimental classical plan, and the aforementioned independent pi terms within attention are changed throughout the largest feasible range as determined by the test envelope.

The experimental procedure comprises of the processing of split bamboo of different widths, of different lengths (2.5, 2.0 and 1.5 in feet) having variety of diameters (50 to 60, 40 to 50 and 30 to 40 in mm). The machining process of sliver making from bamboo was performed at four different speeds (600, 500, 400 and300 in rpm). The process was performed at different gear ratios as1/4, 1/3 and 1/2. As a result, numerous bamboo varieties are employed during experiment to assess the machine's real practicality and feasibility. With the help of specifically built electronic kit (proper instrumentation) as shown in Figure 1.7, flywheel speeding-up time, sliver numbers, torque (resistive) and processing time etc. are estimated and noted. In this experiment, one hundred and eight total sets of readings were performed. Table 3 gives the sample observation and experiment plan. For independent parameters related to slivering unit, the experimental observations are taken and some sample observations are presented in Table 4. The experimental observations for energy unit as well as for the response factors of slivering phenomena are also taken and noted which are depicted in Table 5.

1.3.2 Model Formulation

During experimentation the data of various dependent and independent variables are gathered. To formulate the mathematical model, the interrelation between dependent pi terms and independent pi terms in the sliver cutting phenomena is developed. Since the formulation of the model is performed pertaining to the data produced through the experiments, it is also termed as generalized

Figure 1.7: *Designed electronic instrumentation system and experimental reading generation.*

Table 3: Sample observations for pedal powered Slivering Operation and Plan of Experiment (where Gear Ratio = 0.33)

Sr. No.	Bamboo Diameter Range (D_b) mm	Gear Ratio (G)	Bamboo split length (L_b) ft	Bamboo split length (L_b) mm	Speed (N) rpm	Bamboo split width (W_b) mm	Bamboo split thickness (t_b) mm	Flywheel speeding-up time (ω_f) sec	Processing Time (t_p) sec	Sliver number (n)
1	40-50	0.33	1.5	457.5	300	31	4.1	31.4	60	4
2	40-50	0.33	1.5	457.5	400	31.5	4.5	41.87	55	4
3	40-50	0.33	1.5	457.5	500	31.2	4.7	52.33	70	5
4	40-50	0.33	1.5	457.5	600	31.4	4.22	62.8	80	6
5	40-50	0.33	2	610	300	35	9.1	31.4	65	4
6	40-50	0.33	2	610	400	35.1	9.6	41.87	70	5
7	40-50	0.33	2	610	500	35.5	9	52.33	85	6
8	40-50	0.33	2	610	600	35.3	9.4	62.8	95	6
9	40-50	0.33	2.5	762.5	300	25.4	15.1	31.4	45	3
10	40-50	0.33	2.5	762.5	400	24.8	15.7	41.87	60	4

Table 4: Sample Observation table showing independent factors of bamboo sliver cutting unit

	Processing unit related independent factors or input parameters														
Sr. No.	D_b (mm)	W_b (mm)	t_b (mm)	L_b (ft)	L_b (mm)	N (rpm)	ω_f (rad./s)	G	E_b (N/mm²)	E_c (N/mm²)	C_H (mm)	C_V (mm)	L_{rc} (mm)	φ_c (deg)	φ_c (rad.)
1	40-50	31	4.1	1.5	457.5	300	31.4	0.33	20000	206000	115	65	45	15	0.261667
2	40-50	31.5	4.5	1.5	457.5	400	41.86667	0.33	20000	206000	115	65	45	15	0.261667
3	40-50	31.2	4.7	1.5	457.5	500	52.33333	0.33	20000	206000	115	65	45	15	0.261667
4	40-50	31.4	4.22	1.5	457.5	600	62.8	0.33	20000	206000	115	65	45	15	0.261667
5	40-50	35	9.1	2	610	300	31.4	0.33	20000	206000	115	65	45	15	0.261667
6	40-50	35.1	9.6	2	610	400	41.86667	0.33	20000	206000	115	65	45	15	0.261667
7	40-50	35.5	9	2	610	500	52.33333	0.33	20000	206000	115	65	45	15	0.261667
8	40-50	35.3	9.4	2	610	600	62.8	0.33	20000	206000	115	65	45	15	0.261667
9	40-50	25.4	15.1	2.5	762.5	300	31.4	0.33	20000	206000	115	65	45	15	0.261667
10	40-50	24.8	15.7	2.5	762.5	400	41.86667	0.33	20000	206000	115	65	45	15	0.261667
11	40-50	25.1	15.4	2.5	762.5	500	52.33333	0.33	20000	206000	115	65	45	15	0.261667
12	40-50	25	15.6	2.5	762.5	600	62.8	0.33	20000	206000	115	65	45	15	0.261667

experimental model. The models formulated for the dependent variables like time of processing (t_p), sliver number (n), resistive torque-average (T_{ravg}) and resistive torque-total (T_{rtotal}) are given in equations 1, 2, 3 and 4 respectively.

Table 5: Observation (sample) table for dependent factors and energy unit

Sr. No.	Energy unit related independent factors					Dependent or Output Factors	
	I_f (kg.m²)	g (mm/s²)	E_f (N-m)	t_f (sec)	t_p (sec)	Res. Torque- Avg. T_r (N-mm)	n
1	3.44	9810	4710.698	50	70	21692.86	3
2	3.44	9810	6783.405	35	75	23760	3
3	3.44	9810	1695.851	30	35	20728.57	3
4	3.44	9810	3014.847	35	40	23387.5	3
5	3.44	9810	4710.698	45	55	23045.45	4
6	3.44	9810	6783.405	55	60	24208.33	4
7	3.44	9810	1695.851	25	45	21711.11	2
8	3.44	9810	3014.847	30	45	23336.36	3
9	3.44	9810	4710.698	30	65	23169.23	3

$$t_p = 5.15\,X10^{-10}\sqrt{\frac{L_b}{g}}\left\{\begin{matrix}\left(\frac{E_f}{L_b^3E_b}\right)^{0.2889}\left(\omega_f\sqrt{\frac{L_b}{g}}\right)^{0.1564}\left(t_f\sqrt{\frac{g}{L_b}}\right)^{-0.1769} \\ (G)^{-0.3499}\left(\frac{W_b t_b C_H C_V L_{rc}}{L_b^5}\right)^{0.0371}\left(\frac{E_c}{E_b}\right)^{-3.1676}(\varphi_c)^{-30.5644}\end{matrix}\right\} \quad (1)$$

$$n = 174.1406\left\{\begin{matrix}\left(\frac{E_f}{L_b^3E_b}\right)^{0.5082}\left(\omega_f\sqrt{\frac{L_b}{g}}\right)^{-0.3148}\left(t_f\sqrt{\frac{g}{L_b}}\right)^{-0.1208} \\ (G)^{-0.5089}\left(\frac{W_b t_b C_H C_V L_{rc}}{L_b^5}\right)^{-0.1823}\left(\frac{E_c}{E_b}\right)^{1.3087}(\varphi_c)^{-1.4871}\end{matrix}\right\} \quad (2)$$

$$T_{ravg.} = 1.08E + 10\left(L_b^3E_b\right)\left\{\begin{matrix}\left(\frac{E_f}{L_b^3E_b}\right)^{0.7824}\left(\omega_f\sqrt{\frac{L_b}{g}}\right)^{-1.0005}\left(t_f\sqrt{\frac{g}{L_b}}\right)^{-0.351} \\ (G)^{-1.4423}\left(\frac{W_b t_b C_H C_V L_{rc}}{L_b^5}\right)^{0.0889}\left(\frac{E_c}{E_b}\right)^{4.289}(\varphi_c)^{23.515}\end{matrix}\right\} \quad (3)$$

$$T_{rtotal} = 7.68\,X10^{10}\left(L_b^3E_b\right)\left\{\begin{matrix}\left(\frac{E_f}{L_b^3E_b}\right)^{0.7188}\left(\omega_f\sqrt{\frac{L_b}{g}}\right)^{-1.2769}\left(t_f\sqrt{\frac{g}{L_b}}\right)^{0.0101} \\ (G)^{-1.3708}\left(\frac{W_b t_b C_H C_V L_{rc}}{L_b^5}\right)^{0.0265}\left(\frac{E_c}{E_b}\right)^{-7.5718}(\varphi_c)^{6.7265}\end{matrix}\right\} \quad (4)$$

1.4 Response Surface Methodology (RSM) Approach

The response surface method's benefit as a strong analytical methodology is that, as compared to the conventional strategy, it provides a sharper visual depiction of focused connection [17]. RSM is a set of statistical as well as mathematical approaches which can be used to model and analyze issues wherein an interest response is influenced by numerous factors and the goal is to maximize this response. The RSM equation is given as:
Here response surface is the surface that is represented or notified by, $\eta = fx_1, x_2$

The type of connection between independent variables and the response is uncertain & un-

$$Y_R = f(x_1, x_2) + E \tag{5}$$

Here, E is the error having Y_R response

x_1 is Operational parameter 1

x_2 is Operational parameter 2

Let $E(Y_R)$ be the responses expected, then it is given by:

$$E(Y_R) = \eta = f(x_1, x_2) \tag{6}$$

known in the majority of RSM applications. Hence, the RSM's first step is to discover suitable and good approximate solution to the real functional relation between collection of independent variables and Y_R. In most cases, a polynomial of lower order in some area of independent or input parameters is often used. If response modeling is done well by functional linearity of input or independent parameter, the function of approximation results in the model of first order is:

$$Y_R = \beta_0 + \beta_1 x_1 + \beta_2 x_2 + \cdots\cdots\cdots + \beta_n x_n + E \tag{7}$$

The fitted surface is then utilized to perform the analysis of response surface. Analyzing the fitted surface is roughly comparable to analyze the actual data when the fitted surface is a good approximation of the underlying or real function of response.

If the system has a curve, the greater degree polynomials like the model of second order must be utilized by equation 8.

1.4.1 Design of the Response Surface

Design of experiment, construction of model of response surface, testing of adaptability of model, search for optimum combination strategy and other procedures are included in the design of response surface. The accompanying second model of response surface may be utilized to generate a response surface of three-dimensions and contour line of two-dimensions, which intends to rapidly determine the correct values of response for various elements [18]. A quadratic surface can be appropriately fitted with the help of the RSM approach and aids in optimizing process variables with small number of tests/experiments while also analyzing parameter interaction. RSM is a statistical strategy that employs quantifiable information from relevant experiment to develop a model of regression and optimize an output or response parameter that is impacted by numerous input or independent factors [19]. Response Surface Approach is a descriptive statistics of experiments wherein the output is assumed to be fixed by one or more controllable parameters. The basic purpose of response surface approach is to identify an optimal response by employing a succession of experiment designs. This notion drives the need to carry out tests properly by selecting the correct design and motivates the pursuit of operating circumstances with a variety of controllable elements that result in an optimal response [20].

$$Y_R = \beta_0 + \sum_{i=1}^{n} \beta_i x_i + \sum_{i=1}^{n} \beta_{ii} x_i^2 + \sum \sum_{i<1}^{n} \beta_{ij} x_i x_j + E \quad (8)$$

According to the approach of dimensional analysis adopted in this work, the total seven numbers of π terms were formed affecting the responses of the phenomena. Because these π terms are dimensionless, they may be simply divided in to three classes. To create the response surface, these three classes are transformed into 3-dimensions in space. Thus,

$$X = \pi_1 \times \pi_2 \times \pi_3, Y = \pi_4 \times \pi_5 \times \pi_6 \times \pi_7, Z = \pi_{D1} \quad (9)$$

The X, Y (input) and Z (output) ranges are more flexible and variant. As a result, the scaling of aforementioned factors X, Y (input) and Z (output) is depicted below by the use of principle of scaling:

$$x = \frac{X}{\max(X)}, \quad y = \frac{Y}{\max(Y)}, \quad z = \frac{Z}{\max(Z)} \quad (10)$$

1.5 Construction of Model by RSM

Models of RSM in conjunction with experiment design can be used as statistical and mathematical tools. This technique not only performs well in the optimizing facts, but it has also been validated for the approach of analysis and is useful for enrichment of product [21]. The numerical as well as experimental responses can be approximated by the use of response surface approach. There is requirement of two stages such as approximation function to be well defined and design & creation of the experimental plan. Therefore, it was decided to develop RSM model and compare its performance with the mathematical model developed in this investigation. The process variable values were established to evaluate their influence on the output variables in a total of 108 tests of readings in the experiment. Response surface approach was used to plan the design of experiments and carry out the studies of behavior of process variables. By the use of "MATLAB R2009a", the construction of response surface models and the selection of acceptable models were carried out. For the output parameters, total resistive torque, sliver number, process time and average resistive torque, regression equations of best fitting for the chosen model were produced [22]. For finding out the influence of various process variables on the characteristics of output responses, the equations of response surface are derived from the data of experiments and displayed in the Figures 1.8 to 1.11. Sample calculations for processing time of RSM models are given in Table 1.6, whereas Table 7 gives the concerned calculations for number of slivers. The response surface calculations are also performed for torque-average and torque-total and are presented in Tables 1.8 and 1.9 respectively.

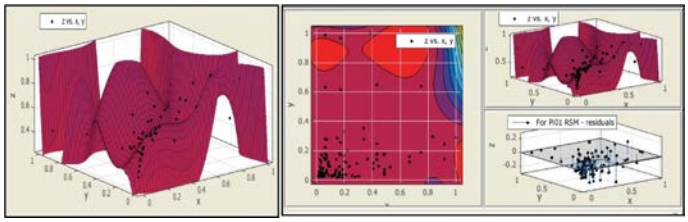

Figure 1.8: *RSM model and Contour, RSM and Residual plot for processing time.*

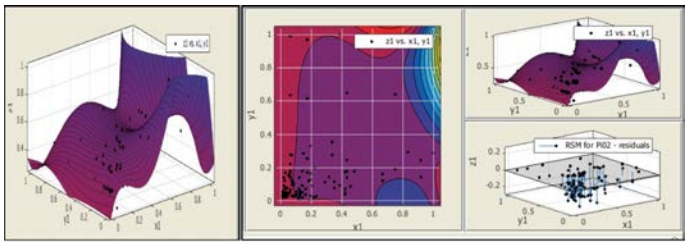

Figure 1.9: *RSM model and Contour, RSM and Residual plot for number of slivers.*

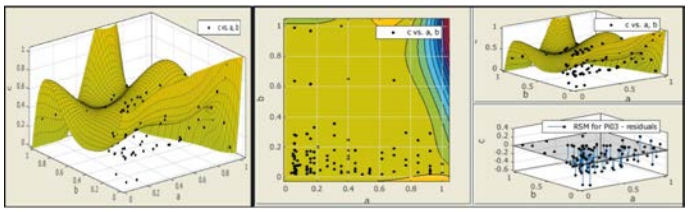

Figure 1.10: *RSM model and Contour, RSM and Residual plot for resistive torque (average).*

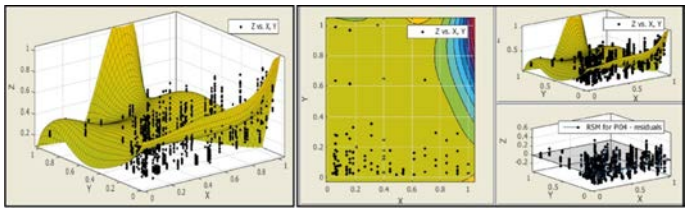

Figure 1.11: *RSM model and Contour, RSM and Residual plot for resistive torque (average).*

Table 6: Sample Calculation of RSM Model for processing time

Π_{D1}= tp(Model)	X=K'*Π1*Π2*Π3	Y=Π4*Π5*Π6*Π7	Π_{D1}= tp (Exp)	Π_{D1}= tp(RSM)	Xmax	Ymax	Zmax	X/Xmax =X'	Y/ymax= Y'	Z/Zmax =Z'	(Poly.Model)Z'
46.48245	1.80134E-07	3.31362E-06	40	66.92421	2.88 E-06	1.18 E-05	110	0.0625	0.280843	0.363636	0.6084
57.45825	4.26985E-07	3.3829E-06	50	68.22344	2.88 E-06	1.18 E-05	110	0.148148	0.286714	0.454545	0.62021
65.78584	9.72948E-07	3.27376E-06	50	69.84033	2.88 E-06	1.18 E-05	110	0.337577	0.277464	0.454545	0.63491
68.48212	2.88215E-06	3.4232E-06	65	64.12058	2.88 E-06	1.18 E-05	110	1	0.29013	0.590909	0.58291
41.74024	8.77505E-08	8.59642E-07	40	70.37635	2.88 E-06	1.18 E-05	110	0.030446	0.072858	0.363636	0.63978
51.47401	2.08001E-07	8.23248E-07	55	71.01566	2.88 E-06	1.18 E-05	110	0.072169	0.069774	0.5	0.6456
57.71298	5.4167E-07	8.56385E-07	60	72.05478	2.88 E-06	1.18 E-05	110	0.18794	0.072582	0.545455	0.65504
63.60235	1.17001E-06	9.23072E-07	60	72.3402	2.88 E-06	1.18 E-05	110	0.405949	0.078234	0.545455	0.65764
37.86127	5.86032E-08	4.3084E-07	45	71.1143	2.88 E-06	1.18 E-05	110	0.020333	0.036515	0.409091	0.64649
46.80633	1.38911E-07	4.41105E-07	60	71.47164	2.88 E-06	1.18 E-05	110	0.048197	0.037385	0.545455	0.64974

Table 7: Sample Calculation of RSM Model for number of slivers

Π_{D2}= n(Model)	X=Π1*Π2*Π3	Y=Π4*Π5*Π6*Π7	Π_{D2}= n(Expem)	Π_{D2}= n(RSM)	Xmax	Ymax	Zmax	X/Xmax =X'	Y/ymax =Y'	Z/Zmax =Z'	(Poly.Model)Z'
3.067968	8.34133E-07	3.31362E-06	3	3.088089	1.33 E-05	1.18 E-05	7	0.0625	0.280843	0.428571	0.44116
3.739983	1.9772E-06	3.3829E-06	4	3.978539	1.33 E-05	1.18 E-05	7	0.148148	0.286714	0.571429	0.56836
4.318878	4.50535E-06	3.27376E-06	5	4.61021	1.33 E-05	1.18 E-05	7	0.337577	0.277464	0.714286	0.6586
4.561559	1.33461E-05	3.4232E-06	5	4.844311	1.33 E-05	1.18 E-05	7	1	0.29013	0.714286	0.69204
2.460794	3.519E-07	8.59642E-07	2	2.675928	1.33 E-05	1.18 E-05	7	0.026367	0.072858	0.285714	0.38228
3.034989	8.34133E-07	8.23248E-07	3	3.256655	1.33 E-05	1.18 E-05	7	0.0625	0.069774	0.428571	0.46524
3.403551	2.17222E-06	8.56385E-07	4	3.946803	1.33 E-05	1.18 E-05	7	0.16276	0.072582	0.571429	0.56383
3.714002	4.692E-06	9.23072E-07	4	4.301708	1.33 E-05	1.18 E-05	7	0.351563	0.078234	0.571429	0.61453
1.907783	2.10202E-07	4.3084E-07	2	2.49514	1.33 E-05	1.18 E-05	7	0.01575	0.036515	0.285714	0.35645
2.324459	4.98256E-07	4.41105E-07	2	2.889732	1.33 E-05	1.18 E-05	7	0.037333	0.037385	0.285714	0.41282

Table 8: Sample Calculation of RSM Model for resistive torque-average

Π_{D3}= TrAvg(Model)	X=K'*Π1*Π2*Π3	Y=Π4*Π5*Π6*Π7	Π_{D3}= TrAvg (Expem)	Π_{D3}= TrAvg (RSM)	Xmax	Ymax	Zmax	X/Xmax =X'	Y/ymax =Y'	Z/Zmax =Z'	(Poly.Model)Z'
17182.67	1597491.83	3.31362E-06	21500	28399.7	27689858	1.18 E-05	72136.36	0.057692	0.280843	0.298047	0.39369
20248.48	3786647.302	3.3829E-06	20840	36055.76	27689858	1.18 E-05	72136.36	0.136752	0.286714	0.288897	0.49983
21692.74	8628428.096	3.27376E-06	23580	44429.01	27689858	1.18 E-05	72136.36	0.31161	0.277464	0.326881	0.6159
19978.21	25559869.29	3.4232E-06	24107.69	17368.3	27689858	1.18 E-05	72136.36	0.923077	0.29013	0.334196	0.24077
16748.77	1597491.83	8.59642E-07	24475	34518.48	27689858	1.18 E-05	72136.36	0.057692	0.072858	0.339288	0.47852
19625.27	3786647.302	8.23248E-07	20909.09	37511.39	27689858	1.18 E-05	72136.36	0.136752	0.069774	0.289855	0.52001
20191.66	9861060.681	8.56385E-07	22533.33	39424.74	27689858	1.18 E-05	72136.36	0.356125	0.072582	0.312371	0.54653
20832.13	21299891.07	9.23072E-07	25591.67	41114.09	27689858	1.18 E-05	72136.36	0.769231	0.078234	0.354768	0.56995
16054.83	1863740.469	4.3084E-07	2366.667	40160.12	27689858	1.18 E-05	72136.36	0.067308	0.036515	0.032808	0.55673
18924.21	4417755.185	4.41105E-07	2008.333	42915.66	27689858	1.18 E-05	72136.36	0.159544	0.037385	0.027841	0.59492

Table 9: Sample Calculation of RSM Model for resistive torque-total

Π_{D3}= Tr tot(Model)	X=K'*Π1*Π2*Π3	Y=Π4*Π5*Π6*Π7	Π_{D3}= Tr tot(Exp)	Π_{D3}= Tr tot(RSM)	Xmax	Ymax	Zmax	X/Xmax =X'	Y/ymax =Y'	Z/Zmax =Z'	(Poly.Model)Z'
19935.54	1597492	3.44 E-06	21700	33306.29	27689858	1.22 E-05	94600	0.057692	0.280843	0.229387	0.352075
19935.54	1597492	3.44 E-06	21900	33306.29	27689858	1.22 E-05	94600	0.057692	0.280843	0.231501	0.352075
19935.54	1597492	3.44 E-06	23500	33306.29	27689858	1.22 E-05	94600	0.057692	0.280843	0.248414	0.352075
19935.54	1597492	3.44 E-06	22700	33306.29	27689858	1.22 E-05	94600	0.057692	0.280843	0.239958	0.352075
19935.54	1597492	3.44 E-06	21000	33306.29	27689858	1.22 E-05	94600	0.057692	0.280843	0.221987	0.352075
19935.54	1597492	3.44 E-06	21400	33306.29	27689858	1.22 E-05	94600	0.057692	0.280843	0.226216	0.352075
19935.54	1597492	3.44 E-06	20100	33306.29	27689858	1.22 E-05	94600	0.057692	0.280843	0.212474	0.352075
19935.54	1597492	3.44 E-06	19700	33306.29	27689858	1.22 E-05	94600	0.057692	0.280843	0.208245	0.352075
20890.26	3786647	3.51 E-06	21700	41079.93	27689858	1.22 E-05	94600	0.136752	0.286714	0.229387	0.434249
20890.26	3786647	3.51 E-06	22200	41079.93	27689858	1.22 E-05	94600	0.136752	0.286714	0.234672	0.434249

1.5.1 Model Construction for Processing Time

Equation of response surface or equation of polynomial of the response surface model of fifth order is evaluated and developed for output variable, processing time and is given below:

$$t_P\sqrt{\frac{g}{L_b}} = 0.6522 + 0.1308x - 0.232y - 0.2394x^2 + 0.2493xy - 0.003853y^2 + 0.01659x^3 - 0.03742x^2y - 0.03488xy^2 + 0.547y^3 + 0.1101x^4 - 0.3119x^3y + 0.02459x^2y^2 + 0.02152xy^3 - 0.316y^4 - 0.03037x^5 + 0.0904x^4y + 0.03629x^3y^2 - 0.01943x^2y^3 - 0.006172xy^4 + 0.04596y^5$$

Goodness of fit: summed Square of residuals or SSE: 1.123,
R square (R^2): 0.5872,
R-square (adjusted): 0.4923,
RMSE- Root Mean Square Error: 0.1136

1.5.2 Model Construction for Number of Slivers

Equation of response surface or equation of polynomial of the response surface model of fifth order is evaluated and developed for output variable, sliver numbers and is given below:

$$n = 0.3129 + 3.279x - 0.1789y - 19.41x^2 + 7.776xy - 0.7621y^2 + 43.66x^3 + 19.83x^2y - 38.92xy^2 + 4.978y^3 - 32.36x^4 - 85.82x^3y + 39.02x^2y^2 + 44.54xy^3 - 6.561y^4 + 5.319x^5 + 56.09x^4y + 1.971x^3y^2 - 24.32x^2y^3 - 17.63xy^4 + 2.497y^5$$

Goodness of fit: summed Square of residuals or SSE: 1.188,
R square (R^2): 0.6012,
R-square (adjusted): 0.5095,
RMSE- Root Mean Square Error: 0.1169

1.5.3 Model Construction for Resistive Torque (Average)

Equation of response surface or equation of polynomial of the response surface model of fifth order is evaluated and developed for resistive torque-average and is given below:

$$Avg.\frac{T_r}{L_b^3E_b} = 0.6923 - 0.797x - 4.251y + 10.73x^2 + 5.562xy + 20.83y^2 - 35.71x^3 - 48.27x^2y + 33.36xy^2 - 55.86y^3 + 45.79x^4 + 85.2x^3y + 33.56x^2y^2 - 94.12xy^3 + 73.59y^4 - 19.5x^5 - 53.96x^4y - 20.04x^3y^2 - 5.127x^2y^3 + 56.55xy^4 - 34.83y^5$$

Goodness of fit: summed Square of residuals or SSE: 4.625,
R square (R^2): 0.2288,
R-square (adjusted): 0.05148,

RMSE- Root Mean Square Error: 0.2306

1.5.4 Model Construction for Resistive Torque (Total)

Equation of response surface or equation of polynomial of the response surface model of fifth order is evaluated and developed for resistive torque-total and is given below:

$$Tot.\frac{T_r}{L_b^3 E_b} = 0.4953 + 0.1362x - 2.104y - 0.1849x^2 + 6.717xy + 8.484y^2 + 1.592x^3 - 48.01x^2y + 22.54xy^2 - 22.86y^3 - 4.218x^4 + 83.75x^3y + 21.07x^2y^2 - 57.81xy^3 + 30.33y^4 + 3.145x^5 - 46.48x^4y - 28.69x^3y^2 + 11.58x^2y^3 + 29.08xy^4 - 14.14y^5$$

Goodness of fit: summed Square of residuals or SSE: 39.15,
R square (R^2): 0.1634,
R-square (adjusted): 0.1511,
RMSE- Root Mean Square Error: 0.1697

1.6 Optimization of RSM Models

According to the objective function of the response variables in this human powered bamboo slicing process, RSM models' optimum values are noted from the plot of response surface model. For the maximization objective function, highest part of the plot or graph is to be selected and accordingly the values for optimization are chosen. For the minimization objective function, the lowest part of the graph is to be selected and accordingly the values for optimization are chosen. The scaled values for process time, sliver numbers, resistive torque-average and total resistive torque are shown in Figures 1.8 to 1.11 respectively.

1.6.1 Analysis of the Models

It is of prime importance to study and note the behavior and impact of indices of the different pi terms of independent factors on all pi terms of output factors. This influence was studied and is depicted below. The indices and constants of pi terms of independent factors on output pi terms are given in Table 10.

The models for the dependent pi terms π_{D1}, π_{D2}, π_{D3} are given in equations 11, 12, 13 and 14 for process time, sliver numbers, resistive average torque and resistive total torque, respectively. The equations 13 & 14 represent the models of resistive torque (average) and resistive torque (total) i.e. $\pi_{D3\,Avg.}$ and $\pi_{D3\,Total}$ respectively. The primary conclusions of above models are described below which appear to be justified from the analysis.

(i) In case of π_{D1} and π_{D2}, the factors π_1 (refers to flywheel energy) and π_6 (refers to material elasticity) having highest indices viz.0.2889 and 1.3087 respectively, are the most influencing terms in these models. The positive values of these indices indicate that flywheel energy and material elasticity have strong impact on π_{D1} and π_{D2} respectively. Whereas

Table 10: Indices and Constant of Response variables

Pi terms	Processing Time (tp)	Number of slivers (n)	Resistive torque-average	Resistive torque-total
K	5.15×10^{-10}	174.1406	1.08×10^{10}	7.68×10^{10}
π_1	0.2889	0.5082	0.7824	0.7188
π_2	0.1564	-0.3148	-1.0005	-1.2769
π_3	-0.1769	-0.1208	-0.351	0.0101
π_4	-0.3499	-0.5089	-1.4423	-1.3708
π_5	0.0371	-0.1823	0.0889	0.0265
π_6	-3.1676	1.3087	4.289	-7.5718
π_7	-30.5644	-1.4871	23.515	6.7265

$$\pi_{D1} = t_P\sqrt{\frac{g}{L_b}} = 5.15\times10^{-10}(\pi_1)^{0.2889}(\pi_2)^{0.1564}(\pi_3)^{-0.1769}(\pi_4)^{-0.3499}(\pi_5)^{0.0371}(\pi_6)^{-3.1676}(\pi_7)^{-30.5644} \quad (11)$$

$$\pi_{D2} = n = 174.1406\,(\pi_1)^{0.5082}(\pi_2)^{-0.3148}(\pi_3)^{-0.1208}(\pi_4)^{-0.5089}(\pi_5)^{-0.1823}(\pi_6)^{1.3087}(\pi_7)^{-1.4871} \quad (12)$$

$$\pi_{D3} = \frac{T_r}{L_b^3E_b} = 1.08\times10^{10}(\pi_1)^{0.7824}(\pi_2)^{-1.0005}(\pi_3)^{-0.351}(\pi_4)^{-1.4423}(\pi_5)^{0.0889}(\pi_6)^{4.289}(\pi_7)^{23.515} \quad (13)$$

$$\pi_{D3} = \frac{T_r}{L_b^3E_b} = 7.68\times10^{10}(\pi_1)^{0.7188}(\pi_2)^{-1.2769}(\pi_3)^{0.0101}(\pi_4)^{-1.3708}(\pi_5)^{0.0265}(\pi_6)^{-7.5718}(\pi_7)^{6.7265} \quad (14)$$

for $\pi_{D3\,Avg.}$ and $\pi_{D3Total}$, the factor π_7 (refers to cutter's cutting angle) having highest indices viz.23.515 and 6.7265 respectively, are the most influencing terms in these models. The positive value of these indices indicates that there is a significant influence of cutter's cutting angle on $\pi_{D3\,Avg}$ as well as $\pi_{D3Total}$ respectively.

(ii) The factors π_5 (refers to machine's geometrical factors) having lowest indices viz. 0.0371 and 0.0889 for π_{D1} and $\pi_{D3Avg.}$ respectively is the least influencing term in these models, hence there is a need to improve machine's geometrical factors for these models of π_{D1} and $\pi_{D3\,Avg.}$ Whereas for π_{D2} and $\pi_{D3Total}$, the factors π_1 (refers to flywheel energy) and π_3 (refers to speeding-up time of flywheel) respectively are the terms which makes least influence in this model and the improvement is needed for the same.

(iii) When there are negative indices then it indicates that there is a need of improving that particular model. It shows that π_{D1} has inverse effects with π_3, π_4, π_6 and π_7, π_{D2} has inverse relationship with π_2, π_3, π_4, π_5 and π_7, $\pi_{D3\,Avg.}$ has also inverse effects with π_2, π_3 and π_4, and $\pi_{D3Total}$ has inverse impacts with π_2, π_4 and π_6.

(iv) In case of π_{D1}, the constant term is having the value less than one (i.e. 5.15×10^{-10}), and therefore it is not having effect of magnification in the calculated value from numerous term's product of this model; whereas for π_{D2}, $\pi_{D3\,Avg.}$ and $\pi_{D3Total}$, constant term had a value greater than one (i.e. 174.1406, 1.08×10^{10} and 7.68×10^{10} respectively), hence those constants have a greater effect of magnification in the calculated value from numerous term's product of their respective models.

The influence of independent or input factors in terms of sensitivity on output factors is given in Table 11. This table shows the sequence of influence in increasing order from left to right.

It is notified that cutter's cutting angle is the most influencing factor in case of output factors processing time (π_{D1}), sliver numbers (π_{D2}) and resistive torque-avg ($\pi_{D3\,avg}$). But for resistive torque-total ($\pi_{D3\,total}$), elastic modulus of materials is most impacting factor. Thus overall, the

Table 11: Sequencial influence of input pi-factors upon output pi-factors

Dependent Pi-factors	**Sequence of input pi-factors as per influence**						
Processing time: Π_{D1}	π_5 (Machine's geometrical parameters)	π_2 (Flywheel angular speed)	π_3 (Speeding -up time of flywheel)	π_1 (Flywheel energy)	π_4 (Gear ratio)	π_6 (Elastic modulus of materials)	π_7 (Cutter's cutting angle)
Sliver numbers: Π_{D2}	π_3 (Speeding-up time of flywheel)	π_5 (Machine's geometrical parameters)	π_2 (Flywheel angular speed)	π_1 (Flywheel energy)	π_4 (Gear ratio)	π_6 (Elastic modulus of materials)	π_7 (Cutter's cutting angle)
Torque resistive-(average) Π_{D3} Tr-avg	π_5 (Machine's geometrical parameters)	π_3 (Speeding-up time of flywheel)	π_1 (Flywheel energy)	π_2 (Flywheel angular speed)	π_4 (Gear ratio)	π_6 (Elastic modulus of materials)	π_7 (Cutter's cutting angle)
Torque resistive-(total) Π_{D3} Tr-total	π_3 (Speeding-up time of flywheel)	π_5 (Machine geometrical parameters)	π_1 (Flywheel energy)	π_2 (Flywheel angular speed)	π_4 (Gear ratio)	π_7 (Cutter's cutting angle)	π_6 (Elastic modulus of materials)

cutter's cutting angle and elastic modulus of materials are having more influence on all response factors. Furthermore, machine's geometrical parameter is the least influencing factor in case of processing time (π_{D1}) and resistive torque-avg ($\pi_{D3\,avg}$) whereas speeding-up time of flywheel is having less impact on output factors like sliver numbers (π_{D2}) and resistive torque-total (π_{D3} total). Thus in general, machine's geometrical parameter and speeding-up time of flywheel are having lesser impacts on the response or output factors. The remaining input factors such as flywheel energy, flywheel angular speed and gear ratio have moderate influence over the output variables.

1.7 Discussion and Conclusions

(i) The properties of machining such as torque (resistive) and time of processing for human powered or pedal powered bamboo slivering process are established through theory of experiments.

(ii) Because data is acquired through real testing and actual experiments, the finding and related concluding remarks of this work accurately indicate the level of engagement of many independent factors

(iii) The analysis of the models in this research work gives the exact behaviour of the independent variables with respect to the particular response variables in terms of level of influence, level of impact, level of improvement if any etc. in case of human powered bamboo slivering machine. It also gives an idea about the magnification effects of the constants in these models.

(iv) RSM models give the scaled values for resistive torque (total), resistive torque (average), process time, and sliver numbers that are involved in the bamboo slivering machine run by pedal power.

(v) The comparative analysis of R-square value of RSM model with the formulated mathematical model gives idea of accuracy of fitness of different factors involved in the human driven bamboo sliver making phenomena. The numerical as well as experimental responses can be approximated by using the response surface approach.

(vi) The developed response surface equations and the relatively plotted graphs gives the appropriate investigation about the impact of different operational factors on numerous characteristics responses like resistive average torque, process time, resistive total torque and sliver numbers which are responsive in human driven bamboo slivering phenomena.

Funding: The author wishes to express his gratitude to the All India Council of Technical Education (AICTE), New Delhi, Govt. of India, for granting research funds via RPS (Research Promotion Scheme) to perform this research. [Grant Letter No.20/AICTE/RIFD/ RPS(POLICY-III)134/2012-13, 6th March,2013].

Conflicts of Interest: The author declares no conflict of interest.

Acknowledgments: The author wishes to thank Dr. M. P. Singh and Dr. C.N. Sakhale for their useful guidance, advice and constant support during this research work.

References

1. Janssen Jules, J. A. (1985). The Mechanical Properties of Bamboo. INBAR Bamboo Report, International Bamboo Workshop (China), 6-14, (pp. 250-256).
2. Bamboo Brochure. Bamboo- A Material for Cost Effective and Disaster Resistant Housing. Building Materials and Technology Promotion Council (BMTPC), Ministry of Urban Development and Poverty Alleviation, Govt. of India, 1-24.
3. Cottage Industry Manual.Bamboo MAT Weaving Techniques and Applications. Work of Mr. Yunhua, Edited & Revised by Dr. Victor Brias, UNIDO Consultant and Dr. Jinhe Fu (INBAR) under supervision of UNIDO Project Manager, Mr. Juergen Hierold, 1-29.
4. Gribkova, D., Milshina, Y. (2022). Energy Transition as a Response to Energy Challenges in Post-Pandemic Reality. *Energies*, 15, 812, 1-26.
5. Kumar, J., Majid, M.A. (2020). Renewable energy for sustainable development in India: current status, future prospects, challenges, employment, and investment opportunities. *Energy Sustainability and Society,* 10, 2, 1-36.
6. Gielen, D., Boshell, F., Saygin, D., Morgan D., Bazilian, M. D., Wagner, N., &Gorini, R. (2019). The role of renewable energy in the global energy transformation. *Energy Strategy Reviews,* 24, 38–50.
7. Seetharaman, Moorthy, K., Patwa, N., Saravanan, Gupta, Y. (2019). Breaking barriers in deployment of renewable energy. *Heliyon,* 5, 1-23. e01166.

8. Papadis, E., Tsatsaronis, G. (2020). Challenges in the decarbonization of the energy sector. *Energy,* 205, 118025, 1-15.
9. Modak, J. P., (2007). Human powered flywheel motor concept, design, dynamics and applications. Keynote lecture at 12th *World Congress IFToMM 2007,* Besancon, France, 17-20 June, (www.iftomm.org/iftomm/proceedings/ proceedings/A983).
10. Modak, J. P., Bapat, A. R. (1993). Manually driven flywheel motor operates wood turning process. *Contemporary Ergonomics*, Proceedings of International Ergonomics Society Annual Convention, Edinburgh, Scotland,13-16 April, (pp 352-357).
11. Zakiuddin, K. S., & Modak, J. P. (2010). Design and Development of the Human Energized Chaff Cutter. *New York Science Journal,* Vol.3, No. (4), 104-108.
12. Deshpande, S. B. & Tarnekar, S. (2003). Confirming Functional Feasibility and Economic Viability of Adoption of Manually Energized Flywheel Motor for Electricity Generation. *Proceedings of International Conference on CAD/CAM Robotics Autonomous Factories*- at Indian Institute of Technology, New Delhi, Aug 11-14.
13. Sakhale, C. N., Modak, J. P., Singh, M. P. & Bapat, P. M. (2011). Formulation of Approximate Generalised Experimental Data Based Model for Machining Properties of Bamboo. *13th World Congress in Mechanism and Machine Science*, at Guanajuato, Mexico, 19-25 June, A23-467, (pp 1-11).
14. Hilbert Schenck J. (1968). *Theory of Engineering Experimentation*. New York, Mc Graw Hill.
15. Martin, James C., Davidson, Christopher J., & Pardyjak, Eric R. (2007). Understanding Sprint-Cycling Performance: The Integration of Muscle Power, Resistance, and Modelling. *International Journal of Sports Physiology and Performance,* Human Kinetics, Inc., 2, 5-21.
16. Stepniewski, Andrzej A. & Grudziński J. (2014). The influence of mass parameters and gear ratio on the speed and energy expenditure of a cyclist. *Acta of Bioengineering and Biomechancs,* Vol. 16, No. 2, DOI: 10.5277/abb140206.
17. Lin, Hsing-Er, Hsu, Dan K. ,Hong, Michelle C. & Yongchuan Shic. (2021). Validating the response surface method in entrepreneurship management research. *Elsevier B.V.,MethodsX.*; 8: 101534, 1-7.
18. Zheng Bin, Wang Xin, Zhang Jingdong. (2021). Structure Optimization Design for Brake Drum Based on Response Surface Methodology. *Manufacturing Technology,* Vol. 21, No. 3, 413-420.
19. Behera, S. K., Meena, Himanshu, Chakraborty, Sudipto & Meikap, B.C. (2018). Application of response surface methodology (RSM) for optimization of leaching parameters for ash reduction from low-grade coal. *International Journal of Mining Science and Technology,* Elsevier, 28, 621–629.
20. Joseph, Cheruiyot C., Anthony, Waititu & Anthony,Wanjoya. (2018). Response Surface Methodology in Application of Optimal Manufacturing Process of Axial-Flow Fans Adopted by Modern Industries. *American Journal of Theoretical and Applied Statistics*, 7(6), 235-241.
21. Riswanto, FDO, Rohman A, Pramono S, Martono S. (2019). Application of response surface methodology as mathematical and statistical tools in natural product research. *Journal of Applied Pharmaceutical Science,* 9(10), 125–133.
22. Sakhale, C.N., Waghmare, S.N., Undirwade, S.K., Sonde, V.M. & Singh, M.P. (2014). Formulation and Comparison of Experimental based Mathematical Model with Artificial Neural Network Simulation and RSM (Response Surface Methodology) Model for Optimal Performance of Sliver Cutting Operation of Bamboo. *3rd International Conference on Materials Processing and Characterisation (ICMPC 2014), Procedia Materials Science,* 6, 2211-8128 © Elsevier Ltd., (pp 877 – 891).

About the Author

Dr. Siddharth K. Undirwade is currently working as Professor of Mechanical & Dean IQAC at P. E. S. College of Engineering, Aurangabad, Maharashtra, India. He is B. E. in Mechanical Engineering, M. E. in Mechanical Design and Ph. D. in Mechanical Engineering. He is having 25 years of experience in Academics, Industry and Administration in the field of Technical Education. He has also worked as the Principal of the Engineering Colleges in his tenure of working. He has published over 34 research articles in National / International Conferences / Journals so far. He is the member of Professional Societies such as Institution of Engineers (India), Indian Society for Technical Education (ISTE), Association for Machines & Mechanisms (AMM) and the Fellow of Indian Society of Mechanical Engineering etc.

CHAPTER 2

Waste Heat Recovery From The Hot Water Boiling Plant Analysis using CFD

D. D. Palande, N.C.Ghuge, Chetan R. Dapase

Article citation information: (2022), *TJES*, Vol. SP-1, pp. 43-52, doi:10.22545/2022/00170

To fulfill the world's growing need for fossil fuel energy, renewable energy harvesting is required, and the rate of depletion of non-renewable energy sources must be slowed. Currently, many of these techniques are available, but with less effectiveness than before. These techniques result in a long payback period of investment. The goal of this research is to look at many elements of convective heat transfer enhancement using finned heat pipes, as well as the recovery of industrial waste heat. To validate these new energy-saving concepts, ANSYS 2020 R1 is used, including control strategies and simulation techniques. An integrated waste heat recovery system using finned heat pipes is having a significant effect on overall efficiency. The efficiency is increased by 10.5%–18.8% for various load conditions.

Keywords: Finned heat pipe, Nusselt Number, Euler Number and convection.

2.1 Introduction

The energy crisis, brought on by a lack of oil and the rapid depletion of fossil fuels, draws attention to energy issues and leads to research into new and renewable energy sources, as well as a list of activities that must be undertaken to save energy. The country's economic development depends on energy conservation. Furnaces and heat equipment available in India have an efficiency of not more than 50%. This implies that the exhaust dissipates more than half of the energy created. A large quantity of fuel may be saved if this lost heat can be correctly captured. Waste heat is energy that is produced through the combustion of fuels or chemical reactions and then "dumped" into the atmosphere, despite the fact that it may still be employed for something useful and economically beneficial. A significant amount of primary fuel could be saved if some of this waste heat could be recovered. It is impossible to recover all of the energy lost in squandering gases. As a human being, it is the responsibility of every single person to save natural resources for the benefit of the next generation. As an engineer, it is the responsibility of every engineer to save any possible waste energy available in the industry and help the cause of saving natural resources. Because

of the high cost of fuel, most Indian enterprises did not pay attention to the cost of fuel savings from recovered waste heat created in the sector two decades ago. In order to save fuel, it is important to retrieve heat from waste and reuse it in the process. With the goal of providing a user-friendly, efficient, and simple-to-operate system for extracting heat from waste, this project developed a highly efficient and static heat pipe based on a recovery system to convalesce any type of waste heat accessible in the industry and use it in the process to save fuel. Among the most effective waste heat recovery methods are heat exchangers built from heat pipes. A heat pipe has the advantage over all other methods. It can carry high volumes of heat over long distances with a compact design and no additional energy input.

Many researchers have worked on heat pipes and waste heat recovery. S.H. Noie-Baghban et al. [1] studied the design and heat transmission constraints of single heat pipes for three types of wick and three working fluids were explored in this study, which began with computer simulation. The minimum heat transfer rate for three working fluids (acetone, water, and methanol) was found to be significantly higher than the needed heat transfer rate. The heat exchanger's low efficiency (0.16) was attributed to the pipe's high pitch to diameter ratio and the lack of fins. Fabian Korn [2]examine the second key aspect: mass transport via porous medium due to vaporization and condensation. There are also capillary effects, pressure impacts, and heat conduction effects to consider, resulting in a complex heat transfer structure requiring a great deal of understanding. The study's goal was to design, build, and test a waste heat recovery system from a hot brass forging furnace using a heat pipe air-preheater. A mathematical model was built to forecast the heat transfer rate and was used to compute the heat pipe air-preheater. The heat pipe air-preheater can efficiently save energy by reducing the amount of gas used in the furnace. According to H. Hagens et al. [4], offered data and forecasting for a heat pipe exchanger with an R134a proportion of 19% and 59%. In relation to its diameter, the thermos-siphon is somewhat long. The rate of air fluctuated between 0.4 and 2.0 kg/s. The evaporator side of the heat pipe reached temperatures of 40 to 70 °C, while the condenser side reached temperatures of 20–50 °C. Timothy J. Rennie and colleagues [5] studied the laminar fluid flow and heat transfer characteristics of a double-pipe helical heat exchanger and were computationally modeled for different fluid flow rates and tube sizes. The heat transfer characteristics of a double-pipe helical heat exchanger for both parallel and counter flow were computationally studied using a computational fluid dynamics tool (PHOENICS 3.3). Validation runs were carried out with constant wall temperature and constant heat flux as boundary conditions. These simulations produced findings that were well within the range of those seen in the literature for helical coils. The goal of this research is to look at how geometric design affects the thermal performance of star-groove micro-heat pipes. Heat transport capacity improves as the cross-sectional area of the micro-heat pipe grows. The heat transfer capacity of the micro-heat pipe, on the other hand, decreases as the total length of the pipe increases. When the adiabatical section length is reduced but the overall length remains constant, the heat transport capacity increases. Ehsan Firouzfar et al. [7]This analysis of the use of heat pipe heat exchangers (HPHEs) in HVAC systems reveals that HPHEs are highly efficient heat transfer devices that may be simply deployed as thermal linkages and heat exchangers in air conditioning systems to save energy and protect the environment. T. Mallikharjuna Rao et al. [8] Thousands of condenser tubes are replaced by hundreds of "heat pipes" in this study. The material of the heat pipe, the length of the heat pipe, and the diameter of the heat pipe for condensation purposes are all detailed in detail.Zare Aliabadi et al. [9] studied the impact of several factors on the thermal performance of a gas-liquid HPHE. As Hussam Jouhara et al. [10] summarise, this research shows that increasing energy efficiency in industrial processes by utilizing waste heat recovery is possible using a variety of methodologies and state-of-the-art technologies. However, in order

to achieve the highest possible efficiency for a system through waste heat recovery, the type of process in question should always be evaluated and analysed before a waste heat recovery method for energy efficiency optimization is assigned. Yiyu Men et al [12] studied the concept of further waste heat recovery is examined, and existing technologies are compared, as well as the waste heat potential and assessment index.Robert Stefan vizitiu et al[13] studied the efficiency improvement of heat pipe heat exchangers by using phase change material. From the above literature review, it is clear that for waste heat recovery purposes, the heat pipe heat exchanger is the best solution for the problem of waste heat recovery from hot water generation plants.

The objective of this study is to develop, manufacture, and assess a heat recovery system from a hot water boiler process employing a heat pipe air-preheater.

2.2 Potential of Waste Heat Revival in Industries

2.2.1 Waste Heat

Waste heat is additional energy that is expelled at a high temperature above normal air pressure from a system in order to obtain additional utility from it. According to the temperature range, waste heat systems are divided into two groups. They are waste heat with a high temperature range of more than 650 °C and waste heat with a low temperature range of less than 230 °C.

2.2.2 Present Working System

Figure 2.1 shows the present working of the hot water boiling plant. In this system, waste heat recovery is done at the end of the economizer where the flue gas temperature is 150 to 160 °C. Waste heat can be recovered by adding the heat pipe air-preheater at the end of the economizer, where the exhaust temperature is reduced by up to 65–75 °C. This heat is used to heat the atmospheric air, and this preheated air is supplied to the generator. This will result in saving the fuel supply system. The experiment's findings revealed that as the temperature of the hot gas grew, so did the rate of heat transmission. The heat pipe air-preheater can lower the amount of gas used in the boiler, resulting in significant energy savings. Using a heat recovery system at the exhaust of the economizer and supplying the preheated air to the blower again will help to improve boiler efficiency and save the Liquefied Petroleum Gas (LPG) fuel supply effectively.

Figure 2.2 shows the proposed system for the waste heat recovery from a hot water boiler plant where the heat pipe heat exchanger system is fixed at the outlet of the economizer for the cooling purpose of the flue exhaust gas and to heat the atmospheric air by passing air around the tubes. This preheated air is supplied to the generator, which helps to improve the efficiency of the generator as well as help consume the fuel supply.

Only pure liquid and vapor pass through heat pipes that run on a closed two-phase cycle. Until the operational temperature reaches between the triple point and the critical point, the working fluid stays saturated. Heat is delivered to the liquid via the shell when heat is transferred to the heat pipe's evaporator. The liquid in the evaporator part vaporizes when it receives enough heat energy. The vapor transports thermal energy from the adiabatically to the cooling coil, in which it is cooled to liquid and the latent heat of evaporation is released. The condensate is knocked to the evaporator from the condenser by the liquid's driving force.

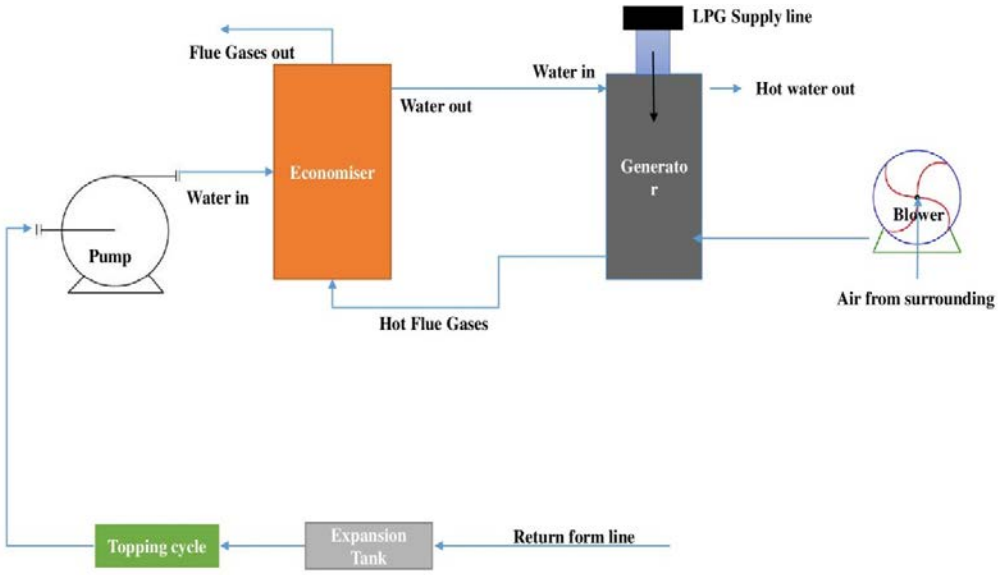

Figure 2.1: *Layout of system present condition.*

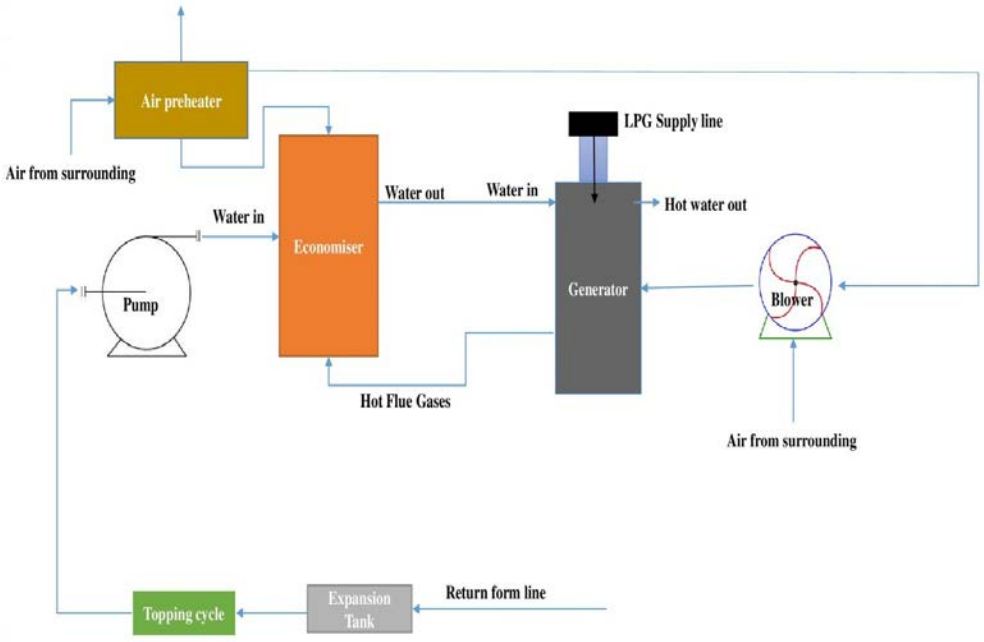

Figure 2.2: *Working system with heat pipe air-preheater.*

Table 1: Experiment Result

Sr. No.	Hot Exhaust air from (Flue gas)	Unit	Qty
1	Volume of the flue gas	m³/hr	1305
2	FLue gas Temperature (Exchanger inlet)	deg.c	140
3	Flue gas Temperature (Exchanger outlet)	deg.c	70
4	Temperature .difference	deg.c	70
5	Density of the flue gas at 140°C		0.963
6	Mass of the flue gas	kg/hr	1113.65
7	Possible energy recovery		18709.34
8	Type of system		air to air
9	Fuel used		LPG
10	Calorific value of the LPG	Kcal/kg	10000
11	Cost of the LPG	Rs	75
12	Working	hrs/day	20
13	Total working	Days	300

2.3 Description of Model

Figure 2.3(a) exhibits a model of the heat pipe generator [1], whereas Figure 3(b) depicts a real-life heat pipe heat exchanger. The parameters of an existing waste heat recovery system are shown in Table 1. The construction of the heat exchanger is the most expensive aspect of this work. It covers the costs of design, materials, and labor.

2.4 FEM analysis

In this work physical models of a heat exchanger with a single tube are used in this study. In the heat exchanger, a heat pipe is constructed, and a constant intake temperature for cold and hot fluid is selected. Inside the duct, a heat pipe is installed. Table 2 shows the size of heat exchangers. ANSYS was used to model the different heat pipe models. Figures 2.4 to 2.5 show the different aspects of the ANSYS FLUENT model of the heat exchangers.

2.4.1 Governing Equations

Steady, three dimensional turbulent, and incompressible flow is present in the tube. Turbulent models are selected based on the comparison of RNG $k-\varepsilon$ nd Realizable $k-\varepsilon$ models with Enhanced wall function. Since the accurate prediction of the adverse $k-\varepsilon$ (RKE) model is selected in the present work.

The basic governing equations (continuity, momentum, energy, turbulent kinetic energy (k), and dissipation of energy (ε) are

Continuity equation

$$\frac{\partial \rho}{\partial t}\ \frac{\partial \rho u}{\partial x}\ \frac{\partial \rho v}{\partial y}\ \frac{\partial \rho w}{\partial z} = 0 \tag{2.1}$$

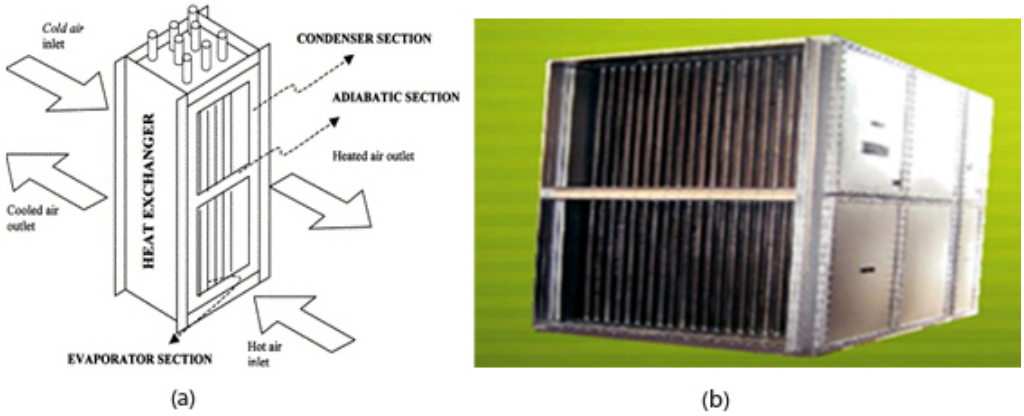

Figure 2.3: *(a) Representation of heat pipe heat exchanger [1], (b) Actual heat pipe heat exchanger.*

Table 2: Dimensions of Duct

Dimensions	Value
Duct height	1400
Duct Width	400

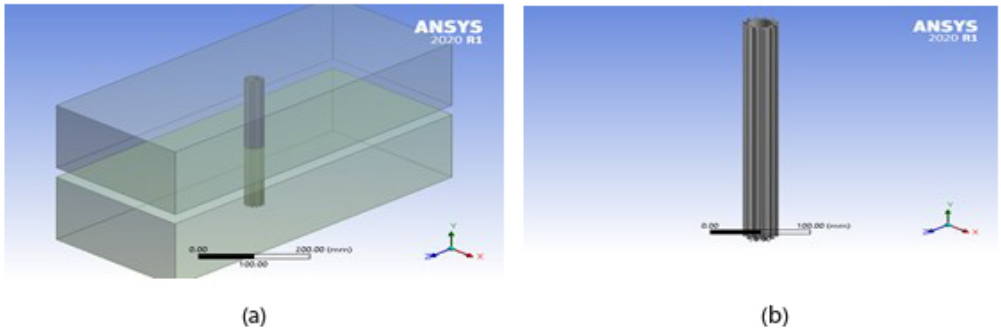

Figure 2.4: *(a) Heat exchanger model with single heat pipe, (b) Heat pipe model with finned surface.*

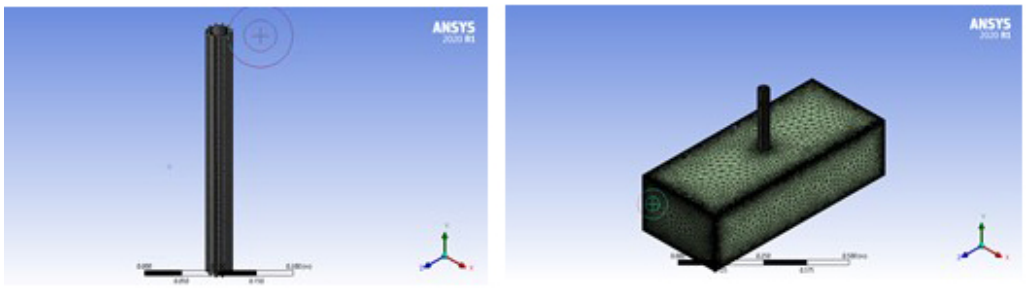

Figure 2.5: *(a) Heat pipe Model after grid independence study, (b) Heat pipe Model with Hot Fluid Domain with Fin meshing considering grid size after grid independence study.*

X-Momentum Equation

$$\rho\frac{Du}{Dt} = -\frac{\partial p}{\partial x} \frac{\partial}{\partial x}\left[2\mu\frac{\partial u}{\partial x} \lambda\, div\, u\right] \frac{\partial}{\partial y}\left[\mu\left(\frac{\partial u}{\partial y} \frac{\partial v}{\partial x}\right)\right] \frac{\partial}{\partial z}\left[\mu\left(\frac{\partial u}{\partial z} \frac{\partial w}{\partial x}\right)\right] Smx \quad (2.2)$$

Y-Momentum Equation

$$\rho\frac{Dv}{Dt} = -\frac{\partial p}{\partial y} \frac{\partial}{\partial x}\left[\mu\left(\frac{\partial u}{\partial y} \frac{\partial v}{\partial x}\right)\right] \frac{\partial}{\partial y}\left[2\mu\frac{\partial v}{\partial y} \lambda\, div\, u\right] \frac{\partial}{\partial z}\left[\mu\left(\frac{\partial v}{\partial z} \frac{\partial w}{\partial y}\right)\right] Smy \quad (2.3)$$

Z-Momentum Equation

$$\rho\frac{Dw}{Dt} = -\frac{\partial p}{\partial y} \frac{\partial}{\partial x}\left[\mu\left(\frac{\partial u}{\partial z} \frac{\partial w}{\partial x}\right)\right] \frac{\partial}{\partial y}\left[\mu\left(\frac{\partial v}{\partial z} \frac{\partial w}{\partial y}\right)\right] \frac{\partial}{\partial z}\left[2\mu\frac{\partial w}{\partial y} \lambda\, div\, u\right] Smz \quad (2.4)$$

Energy Equation

$$\frac{\partial}{\partial t}(\rho E) \frac{\partial}{\partial x_i}\left[u_i(\rho E\ p)\right] = \frac{\partial}{\partial x_j}\left[\left(k_{eff}\frac{\partial T}{\partial x_i} u_i(\tau_{ij})_{eff}\right)\right] S_h \quad (2.5)$$

Where E is the total energy, k_{eff} is the effective thermal conductivity, and $\tau_{ij\,eff}$ is the deviatoric stress tensor.

Transport Equation of Turbulence:

The transport equations for the Realizable $k-\varepsilon$ turbulence model in the tensor form is given by:

$$\frac{\partial}{\partial t}(pk) \frac{\partial}{\partial x_j}(pku_j) = \frac{\partial}{\partial x_j}\left[\left(\mu \frac{\mu_t}{\sigma_k}\right)\frac{\partial k}{\partial x_j}\right] G_k\ G_b - \rho\varepsilon - Y_M\ S_k \quad (2.6)$$

$$\frac{\partial}{\partial t}(p\varepsilon) \frac{\partial}{\partial x_j}(p\varepsilon u_j) = \frac{\partial}{\partial x_j}\left[\left(\mu \frac{\mu_t}{\sigma_\varepsilon}\right)\frac{\partial \varepsilon}{\partial x_j}\right] \rho C_1 S\varepsilon\ \rho C_2\frac{\varepsilon^2}{k\sqrt{\vartheta\varepsilon}}\ C_{1\varepsilon}\frac{\varepsilon}{k}C_{3\varepsilon}G_b\ S_\varepsilon \quad (2.7)$$

$$C_1 = \max\left[0.43, \frac{\eta}{\eta\ 5}\right], \eta = S\frac{k}{\varepsilon}, S = \sqrt{2S_{ij}S_{ij}} \tag{2.8}$$

In these equations, G_k represents the generation of turbulence kinetic energy due to the mean velocity gradients, calculated in modeling turbulent production in the $k-\varepsilon$ models. G_b is the generation of turbulence kinetic energy due to buoyancy in the effects of buoyancy on turbulence in the $k-\varepsilon$ models. Y_M represents the contribution of the fluctuating dilatation incompressible turbulence to the overall dissipation rate, in the effects of compressibility on turbulence in the $k-\varepsilon$ models. C_2 and $C_{1\varepsilon}$ are constants. σ_k and σ_ε are the turbulent Prandtl numbers for k and ε, respectively. S_k andS_ε are user-defined source terms.

$$\eta_t = \rho C_\mu \frac{\mu^2}{\varepsilon} \tag{2.9}$$

Is the turbulent viscosity and ε is the dissipation rate $\sigma_k, \sigma_\varepsilon, C_2, C_{1\varepsilon}$ and C_μ are the model constants with values of 1.0, 1.2, 1.9, 1.44 and 0.085, respectively.

In the present study, velocity inlet and pressure outlet boundary conditions are selected for the computational domain. The Uniform flow rate of cold air with a temperature of 298 K is assumed to be constant in the axial and radial direction and the uniform flow rate of hot flue gases with a temperature of 413 K is assumed to be constant in the axial and radial direction. A near-wall modeling approach can be done by employing the logarithmic law of the wall to estimate the kinetic energy and momentum at all rigid boundaries. FLUENT can combine the two-layer model with improved wall function. ANSYS FLUENT 2020 R1 is used to solve governing equations. A heat transfer between fluid and heat pipe is accepted even though it is negligible to understand the actual heat transfer phenomenon. The effect of gravity is considered. Thermo-physical properties of air and flue gases remain constant at the mean fluid temperature.

For Evaporation and condensation Equilibrium Model Equilibrium models are used to compute equilibrium ratios in Equation, The equilibrium models consider the case in which the species on the two phases are in dynamic equilibrium. The interphase mass transfer rate is determined from the relationship between the equilibrium species concentrations on the two phases. Typically at equilibrium the species concentrations on the two phases are not the same. However, there exists a well-defined equilibrium curve relating the two concentrations. For binary mixtures, the equilibrium curve depends on the temperature and pressure. For multi-component mixtures, it is also a function of the mixture composition. The equilibrium curve is usually monotonic and nonlinear, and is often expressed in terms of equilibrium mole fractions of species and on phases and

$$X^i_{q,e} = F\left(X^j_{p,e}\right) \tag{2.10}$$

The simplest curve or relationship is quasi-linear and assumes that at equilibrium the mole fractions of the species between the phases are in proportion:

$$X^i_{q,e} = K^X_{q^i p^j} X^j_{p,e} \tag{2.11}$$

2.4.2 Boundary Condition and Data Reduction

Required boundary conditions are assigned to the computational domain as the internal regions are assigned as fluid domains as they have common faces that are shared. The incompressible,

Newtonian, turbulent, and 3D model is to be analyzed therefore velocity inlet boundary conditions and pressure outlet boundary conditions are used for this model. Constant temperature wall boundary conditions at the tube wall and coupled heat transfer boundary conditions are used in this 3D model.

It is required to analyze the performance of the given system based on heat transfer parameters and hydraulic parameters. For forced convective heat transfer following non-dimensional parameters are selected as follows.

Reynolds number

$$R_e = \frac{\rho V D}{\mu} \tag{2.12}$$

Nusselt Number

$$N_{u_{local}} = \frac{h_{local} \times D}{K_f} \tag{2.13}$$

Where is the h_{local} local convective heat transfer coefficient, and K_f is the thermal conductivity of the fluid. The area-averaged Nusselt number (Nu) can be calculated as:

Average Nusselt Number

$$N_u = \frac{1}{A} \int N_{u_{local}} \times dA \tag{2.14}$$

Where A is the heat transfer surface area.

2.4.3 Numerical Analysis

Ansys ICEM CFD 2020 R1 is used for meshing and grid generation. The new polyhedral unstructured grid is used near walls to get refined wall treatment and to understand near-wall velocity gradient phenomenon. To simulate the flow field and heat transfer rate through a fine relevance center with maximum and minimum size equal to (2mm) and high smoothing mesh near the wall to give Y + $\leq$ 5. Polyhedral mesh is prepared in FLUENT itself, this type of cell is a new grid technique that gives quicker convergence with less interaction, lower values of residual, robust convergence, and the solution runtimes can be faster than other mesh types by supplying the same computational results. Ansys 2020 R1 is used for numerical analysis and for solving governing equations using finite volume method (FVM). The SIMPLE algorithm is given by Patankar S.V.[11] is selected to solve the flow field while second-order upwind scheme is used for discretization of the momentum, energy, and turbulent equations to transact with the problem of pressure gradient and velocity. The convergence of solution is monitored based on Outlet temperature and convergence criteria. The solution is considered converged when all flow equation becomes less than 10^{-6} and Energy equation becomes less than 10^{-7}. The outlet temperature does not show any fluctuations with respect to iteration at these conditions.

2.4.4 Grid Independence Study

Grid size selection is important in the numerical analysis as both computational time and the accuracy of the result are dependent on this parameter. Grid size can be varied by changing element size in meshing. Six different element sizes are chosen, which further gives six different

grid sizes. 0.003m, 0.00275m, 0.0025m, 0.002m, 0.001m are selected and the corresponding grid sizes are 354847, 407568, 565029, 854875, 1054871, and 2654874 for grid independence study as shown in table 3. The Nusselt number and outlet temperature are selected for monitoring the changes in these parameters against changes in mesh elements. Deviations are in the range of 0.00388% to 1.46% for Nu, and 0.001150% to 5.46% for Tout.

Table 3: Grid Independence Study

Case	Mesh Element	Nu	% error	$T_{out(K)}$	% error
Case1	354847	28.97	-	324.20	-
Case2	407568	29.687	1.464	324.55	0.1082
Case3	565029	29.887	0.402	325.32	0.2366
Case4	854875	29.895	0.0160	325.33	0.0015
Case5	1054871	29.894	0.0045	325.33	0.0001
Case6	2654874	29.893	0.0038	325.33	0.00007

2.5 Result and Discussion

The results of heat transfer (Nusselt Number), the outlet temperature of the cold fluid, and steam volume fraction are estimated. The following section explains different facts about all these output parameters.

2.5.1 Influence of the Inlet Temperature of Hot Fluid

In the heat, the Nusselt number increases due to the increase in hot fluid. Compared to a plane tube, a heat pipe-assisted heat exchanger increases the Nusselt number while increasing the Reynolds number and decreasing cold fluid inlet temperature. In a heat pipe, fluid in a core region remains less heated, while the fluid in the outer region gets heated. This causes flow circulation in the core region, which assists in the mixing of fluid to enhance heat transfer. This flow circulation depends on the heat transfer rate and temperature difference.

As the temperature difference decreases, heat transfer also decreases, and steam volume fraction also increases. In the present study, Nu and VOF are more in the core region where the strong vortex flow is produced, which interrupts the boundary layer development. This vortex flow causes mixed axial and tangential flow, resulting in more fluctuations in energy among fluid layers and, subsequently, more thermal energy being transmitted into layers of fluid. This also causes separate vortex flow regions in between the core and the near-wall region, as shown in Figure 2.6(a). This can be explained by the secondary phase caused in the middle region, which allows flow mixing of two separate vortex flows in two regions in Figure 2.6(b). Turbulent kinetic energy (TKE) contours show maximum TKE in the evaporation region.

It is also noted that the fluid flow caused by evaporation fluid transportation rate increases with a significant temperature difference. Also, the heat transfer rate is dependent on these criteria regarding fluid transportation. As shown in Figures 2.7(a) and 2.7(b), the velocity of the fluid in the cold region is higher, so the heat recovery process can be improvised significantly in this region. In spite of the vapor state of the fluid, the heat transfer rate is more due to this random motion of the fluid.

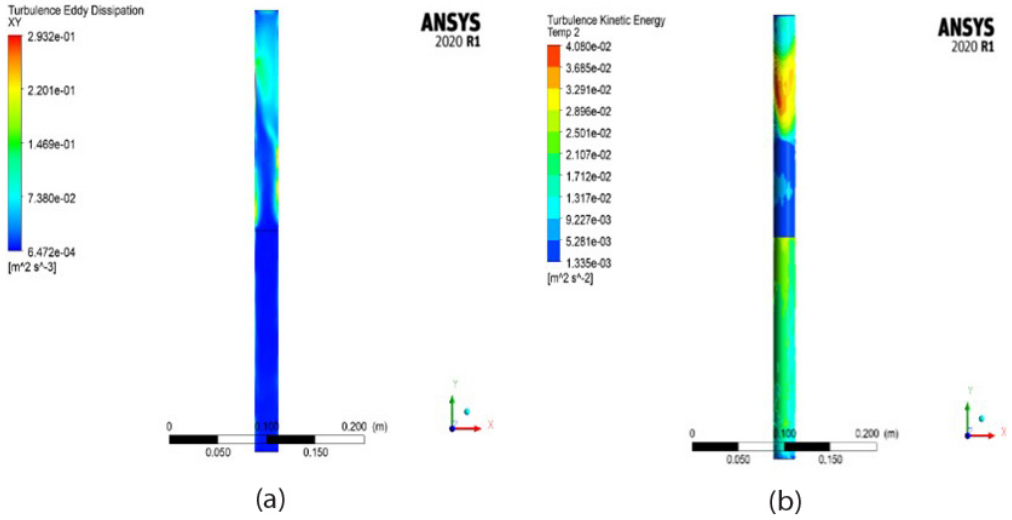

Figure 2.6: *(a) Turbulent eddy dissipation (TED) evaporation region, (b) Turbulent Kinetic Energy (TKE) evaporation region.*

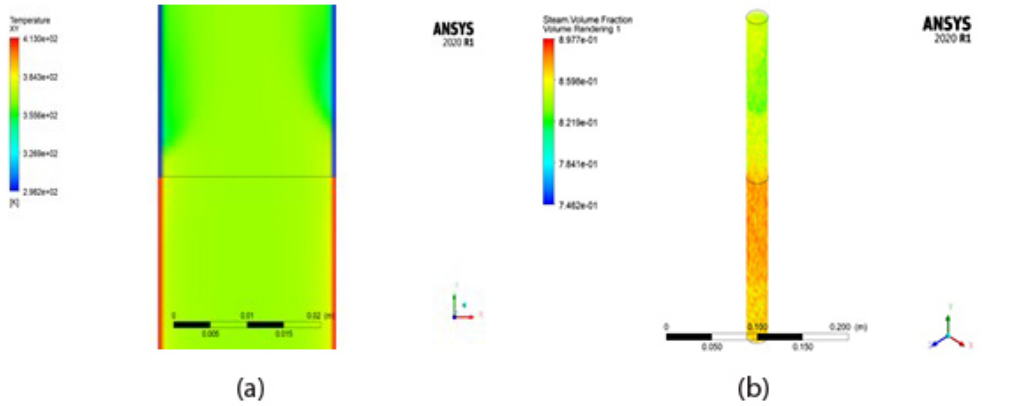

Figure 2.7: *(a) Near wall temperature of the hot region and cold fluid, (b) Steam Volume fraction in core region.*

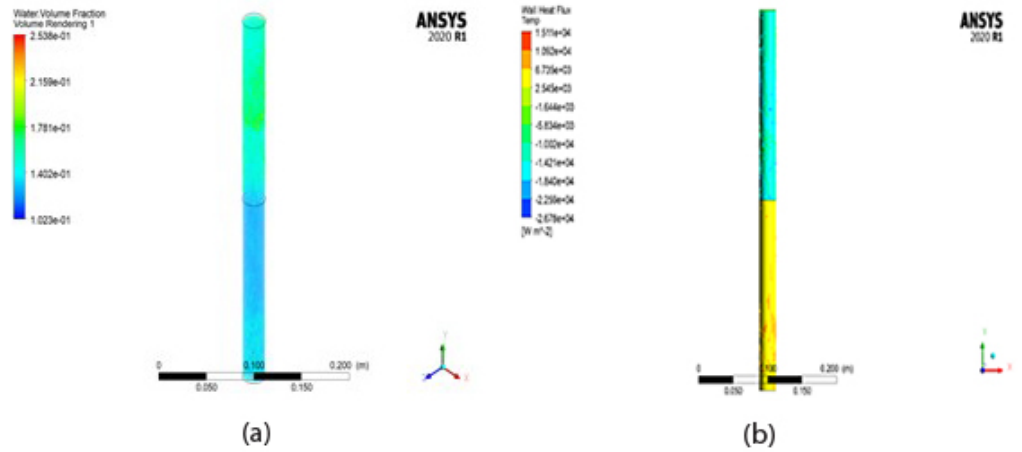

Figure 2.8: *(a) Water volume fraction in the core region, (b) Heat transfer rate from hot region and cold region.*

As revealed in Figures 2.8(a) and 2.8(b), the heat transfer rate is greater in the near wall region as compared to the far-wall region. As a result, the temperature difference is greater in this region, which causes a sudden rise in the heat content of the fluid in that region and will cause the formation of fluid vapours in this region. As shown in Figure 2.8(a), it is needed to consider the fact that the rate of evaporation is an important parameter in the case of heat transfer from a heated liquid to a cooled fluid.

2.5.2 Effect of Steam Volume Fraction on Heat Transfer Rate

As the fluid gets evaporated, the volume fraction of steam increases. This rise in volume fraction indicates the evaporation process, and this is an important part of this heat transfer process. As this heat transfer increases with continuous evaporation of fluid in the hot fluid region and condensation in the cold fluid region, there is the formation of a mixture of liquid and vapor in the core region.

The rate of condensation in the cold region is less as compared to the evaporation rate as the heat transfer rate in the cold region is greater as the vapor form of fluid causes dissipation of heat more quickly than the liquid fluid in the hot region of the heat pipe as shown in Figures 2.9(a) and 2.9(b). The temperature contour and air flow across the heat pipe are shown in Figure 2.10(a) and 2.10(b) The heat transfer rate in a hot region is 172.49 w/m^2 and in a cold region is 282.98 w/m^2.The heat transfer coefficient of fluid in a cold region is found to be 30.06 w/m^{2}K and that of hot fluid is 30.48 w/m^{2}K.

2.5.3 Impact of Heat Pipe on Heat Exchanger

The occurrence of a combined evaporation and condensation action of fluid in the heat pipe allows heat transfer from hot to the cold fluid. Hot fluid with a velocity of 5.13m/s is passing over the heat pipe and as the fluid is cold at high pressure, it takes continuous heat from the hot fluid and gets

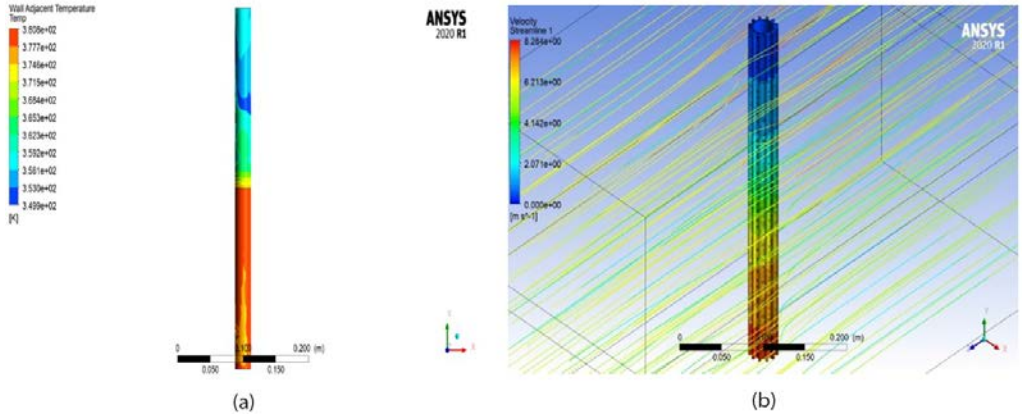

Figure 2.9: *(a) Temperature contour of heat pipe during heat transfer, (b) Air flow across finned heat pipe for heat transfer from hot fluid to cold fluid.*

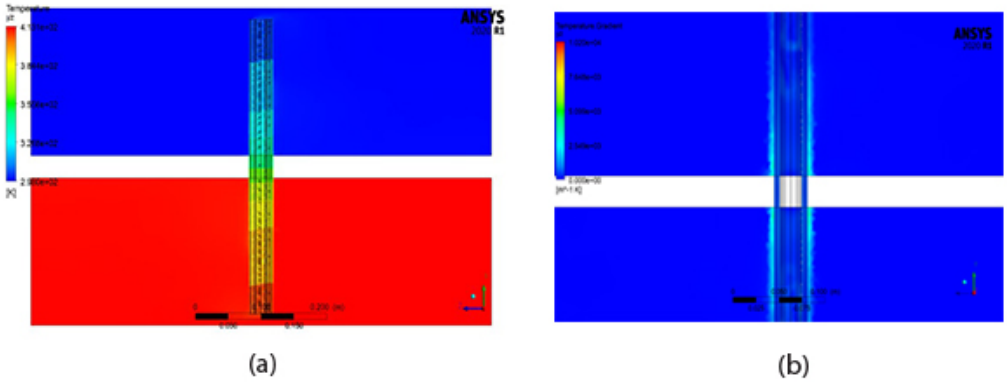

Figure 2.10: *(a) Performance of heat pipe in heat exchanger, (b) All adjacent temperature gradient.*

evaporated, and then it transfers its heat to the cold fluid which is passing over the upper portion of the heat pipe. As the cold fluid has a velocity of 6.13m/s, it gains heat from the evaporated vapors of fluid inside the heat pipe.

This heat loss from vapors causes condensation of the vapors and gets accumulated at near-wall locations of the heat pipe where film-wise or drop-wise condensation will occur. This condensate was then collected in the lower portion of the heat pipe for further evaporation and condensation. As depicted in Figures 2.10(a) and 2.10(b), cold and hot fluids move through the heat pipe, causing the fluid inside the heat exchanger to be heated and cooled simultaneously. Consider a graphic with varying wall temperatures nearby to demonstrate this. The concept of heat exchange from hot to cold fluid as the temperature differential can be used to figure out how well heat exchangers work, as shown in Figures 2.11(a) and 2.11(b). The heat transfer also depends on the fluid flow parameters like velocity and pressure of the fluid passing over the finned heat pipe.

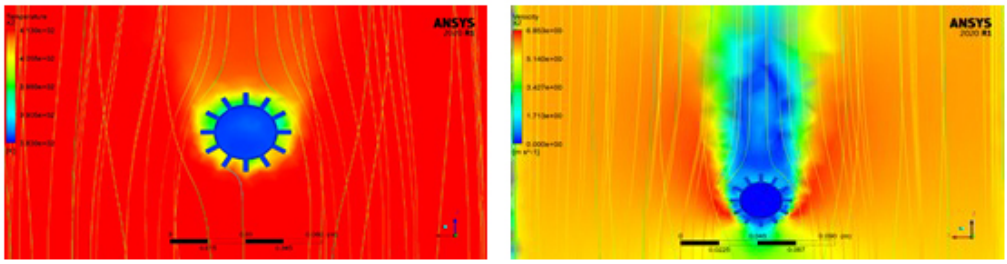

Figure 2.11: *(a) Temperature contours across finned heat pipe in hot fluid region, (b) Velocity contours across finned heat pipe in hot fluid region.*

2.6 Conclusion

The heat pipe provides a substantial increase in heat transfer while keeping pressure drop to a minimum. Although dimensionless parameters for heat transfer (Nu) and pressure drop (Δp) are very important for the scaling of the results of the heat exchanger with similar geometries, comparison of the performances of different heat transfer surfaces. Heat transfer and pressure drop compared with enhanced surfaces about 14% - 18%. Despite the pressure drop, fins had a considerable influence on the heat transfer increase in the overheated pipe. Heat transmission is increased by 10% to 15%. This increases by 10% when using a heat pipe. The basic results showed that Nusselt number and pressure drop were more effective than active heat transfer enhancement techniques. It is a cheap technique. It improves the heat transfer rate. While dimensionless heat transfer number (Nu) and pressure drop (p) characteristics are important for scaling heat exchanger findings with similar geometries, they don't provide a way to compare the performance of different heat transfer surfaces. Instead, comparing performance using such metrics will give the erroneous impression that non-enhanced (bare) surfaces are more efficient in terms of heat transfer and pressure drop. Heat transfer rate increases with increasing Reynolds number for all pin fin arrangements, but there is a significant difference between Reynolds number and flow rate due to flow reversal and continuous turbulence generation caused by the pin fin. The use of heat exchangers with heat pipes in an Integrated Waste Heat Recovery System has a substantial impact on the power plant's overall efficiency. This is due to the utilization of more space available in power plants, and this can enhance the effective heating of the water supplied to the economizer and any other utility.

Funding: This research received no external funding.

Conflicts of Interest: The authors declare no conflict of interest.

Authors Contributions: Co-authors contributed equally.

References

1. S.H. Noie-Baghban, G.R. Majideian, (2000). Waste heat recovery using heat pipe heat exchanger (HPHE) for surgery rooms in hospitals. *Applied Thermal Engineering*, (20) 1271-1282.
2. Fabian Korn,(2008). Heat pipes and its applications. 2008MVK160 *Heat and Mass Transport,* Sweden.
3. Lerchai Yodrak, Sampan Rittidech,(2010). Waste heat recovery by heat pipe Aar-preheater to energy thrift from the furnace in a hot boiling process. *American Journal of Applied Sciences*, 7 (5): 675-681.
4. H. Hagens, F.L.A. Ganzevles,(2007). Air heat exchangers with long heat pipes: Experiments and predictions. *Applied Thermal Engineering*, (27) 2426–2434.
5. Timothy J. Rennie, Vijaya G.S. Raghavan (2006). Numerical studies of a double-pipe helical heat exchanger. *Applied Thermal Engineering*, (26) 1266–1273.
6. Yew Mun Hung, Q'bert Seng(2011). Effects of geometric design on thermal performance of star-groove micro-heat pipes. *International Journal of Heat and Mass Transfer*, (54) 1198–1209.
7. Ehsan Firouzfar, Mohammad Soltanieh(2011). Application of heat pipe heat exchangers in heating, ventilation and air conditioning (HVAC) systems. *Scientific Research and Essays*, Vol. 6(9) 1900-1908.
8. T. Mallikharjuna Rao (2014). Heat pipes for steam condensation. *IOSR Journal of Mechanical and Civil Engineering*, (IOSR-JMCE) Vol.11(2) 16-19.
9. H. Zare Aliabadi, H. Ateshi (2009). An experimental and theoretical investigation on thermal performance of a gas-liquid thermosyphon heat pipe heat exchanger in a semi-industrial plant. *Iranian Journal of Chemical Engineering*, Vol. 6(3) 13-25.
10. Hussam Jouhara, Navid Khordehgah, Sulaiman Almahmoud, Bertrand Delpech, Amisha Chauhan, avvas A. Tassou(2018). Waste heat recovery technologies and applications. *Thermal Science and Engineering Progress*, (6) 268–289.
11. Patankar S.V (1980). *Numerical heat transfer and fluid flow*. Taylor and Francis.
12. Yiyu Men, Xiaohua Liu,Tao Zhang (2021). A review of boiler waste heat recovery technologies in the mediumlow temperature range. *Energy*, (237) 121560.
13. Robert Stefan vizitiu et al (2019). CFD analysis of an innovative heat recovery system. *Procedia Manufacturing*, (32) pp 488–495.

About the Authors

Dr.D.D.Palande is currently working as an Associate Professor in the Mechanical Engineering Department at Matoshri College of Engineering and Research center Nasik. He is B.E (Mechanical) M.E.(Thermal Power Engineering) and Ph.D. (Mechanical Engineering). He is having 21 years of experience in teaching and

administration. He is a member of Professional Societies such as the Institution of Engineers (India), and the Indian Society for Technical Education (ISTE). He has published many research papers in various national and international Journals.

Dr.Nilesh C. Ghuge is currently working as an Associate Professor in the Mechanical Engineering Department at Matoshri College of Engineering and Research center Nasik. He is B.E (Mechanical) M.E.(Mechanical Engineering) and Ph.D. (Mechanical Engineering). He is a member of Professional Societies such as the Institution of Engineers (India), the Indian Society for Technical Education (ISTE), He is having 22 years of experience in Industry and teaching and administration. He has published many research papers in various national and international Journals.

Mr. Chetan Dapase has completed M.E.(Heat Power Engineering). He is having 10 years of experience in the Industry. Currently he is working as director of Gayatri Enterprises at Nasik.(M.S.).

CHAPTER 3

Energy and Exergy Analyses for Flue Gas Assisted Organic Rankine Cycle

Mucahit T. Uysal, Burak Turkan, and Akin B. Etemoglu

Article citation information: (2022), *TJES*, Vol. SP-2, pp. 57-69, doi:10.22545/2022/00186

Effective use of industrial heat waste at low and medium temperatures is seen as one of the solutions that can be used to increase energy efficiency and reduce the problem of environmental pollution. Within the understanding of this framework, the organic Rankine cycle (ORC) maintains to gain attention and further development by researchers and/or manufacturers due to its technical and economical use and credibility. This study presents thermodynamic and economic analyses on flue gas assisted organic Rankine cycle (FGA-ORC) based on both concepts of energy and exergy. The heat source for the FGA-ORC system is the exhaust flue gas of the stenter machine, which is highly used in the textile finishing process. In this study, an optimization investigation has been carried out for a cycle architecture, which converts thermal energy into electrical and/or mechanical energy. The effect of the working parameters of the stenter frame on the performance indicators such as efficiency, performance ratio and economic profit was parametrically analyzed, and the net-work, exergy destruction and efficiency values were determined. The results of these analyses showed that the optimum working parameters of the FGA-ORC system were P_1=1311 kPa, P_{mid}=970 kPa, $T_{gas,in}$=140$^\circ C$, PC=35%, T_o=25$^\circ C$ for an exergetic efficiency of 68.86%.

Keywords: Waste-heat recovery, organic rankine cycle, exergy analyses, flue-gas, energy analyses.

3.1 Introduction

It is well known that because of the gradual increase in industrialization and as a result an increase in energy consumption, mankind is faced with economic and environmental issues. In order to counter these adverse effects, new energy policies, and environmental regulations have been put forth which pushed countries and businesses to use alternative forms of energy and investigate re-using techniques. To do so, detailed performance evaluations have become a must for energy conversion systems.

One of the toughest challenges engineers face in today's world is to design a system that is cost-effective with low initial capital investment and also has a low running cost while also meeting government requirements on environmental conservation. While energy demands are increasing, our natural resources are dwindling, and it is becoming increasingly crucial to use our recurse more efficiently day by day [1]. A great example of wasted energy would be most industrial heating processes. Generally, the waste energy generated from these processes cannot be recovered very efficiently and low-grade waste energy results in thermal pollution because it is thrown out completely. So, we can safely say that using these wasted low-grade energy sources would benefit the world both economically and environmentally.

It is known that using traditional steam power cycles with low-grade waste heat as an energy source is not feasible because of their low efficiency with low-grade heat sources and high cost. But the organic Rankine cycle is said to be a good way to utilize the wasted low-grade heat energy [2]. Studies were done to investigate the effects of different working fluids on the waste recovery organic Rankine cycle's performance by Wei et al [3], Liu et al. [4] and Hung [5]. The organic Rankine cycle converts waste heat into power by using organic materials, which have low boiling temperatures, as working fluids and because of its simple construction, ability to be easily implemented to different working conditions, its size and its power generating capability makes the organic Rankine cycle a great choice for producing heat and power using low-grade waste heat sources [6]. There is a great deal of research in the literature when it comes to the organic Rankine Cycle and yet this area is still very active due to its inclusion of better energy use. This is supported by the studies of Velez et al. [7], Tchanche et al. [8], Wang et al. [9], Chen et al. [10], Papadopoulos et al. [11], Desai and Bandyopadhyay [12] and Saleh et al. [13].

A number of review articles have been published to help navigate future endeavors on the subject of the organic Rankine cycle [14,15]. Yamamoto et al. examined the closed type organic Rankine cycles performance and characteristics by using HCFC-123 and water as working fluids [16]. From this study it can be seen that the organic Rankine cycle could be implemented with low-grade heat sources effectively and that HCFC-123 significantly increases the organic Rankine cycles performance. In a study by Hung et al., cryogens such as benzene, ammonia, R11, R12, R134a and R113 were used as working fluids for the organic Rankine cycle and the efficiencies were parametrically analysed and compared [17]. They concluded that the beast chois for recovering low-temperature heat was isentropic fluids. Etemoglu proved that the operation conditions and the working fluid could change the systems performance drastically [18]. Kermani et al. presented an optimization technique to obtain the optimum thermal architecture by changing the operating conditions and the working fluid [19]. A thermal analyses was done to investigate the effects of different fluid on the ORC and steam turbines using geothermal energy as the heat source by Akbay et al. [20]. Yuksel presented a thermal and performance evaluation of an integrated geothermal energy based multigeneration plant which includes hydrogen, electricity, hot water, drying, cooling and heating [21].

A heat recovery and working fluid testing system was constructed by Panesar et al. [22] to investigate a wide range of realistic gaseous sources such as the direct utilization of High Temperature (HT) exhaust gases.

To obtain a more optimum and cost-effective ORC system, the continuation of these researches is essential. This study presents thermodynamic and economic analyses on flue gas assisted organic Rankine cycle (FGA-ORC) based on both concepts of energy and exergy. The heat source for the FGA-ORC system is the exhaust flue gas of the stenter frame, which is highly used in the textile finishing process. In this study, an optimization investigation has been carried out to find the best cycle conditions for a system, which converts thermal energy into electrical and/or mechanical energy. This study shows a straightforward method to calculate the energy and exergy analyses of the FGA-ORC system and assess the economic contribution of the system and the exergy destruction of each component of the system using this method, which is based on the first and second law of thermodynamics, thus showing where the most effective improvements can be applied. ORC systems should provide a more efficient energy utilization for the needs of specific operating conditions of the industrial processes. Therefore, the new thermal architecture of the cycle is designed to improve the work-output of the ORC system (see Figure 1). In this new thermal architecture, the effects of the turbine-to-heater mass flow rate and the internal heat exchanger on the system performance parameters are investigated. In this study, an optimization technique is presented to get the optimal operating conditions for a new thermal architecture with a specific working fluid.

3.2 Material and Methods

3.2.1 Theoretical Analyses

The stenter-frame, which is a continuous dryer regularly used in the textile industry, is an apt choice as a new energy source for recovery because, at the end of the stenter-frames drying process, a considerable amount

of low-temperature flue-gas is released to the atmosphere.

The maximum possible amount of useful work that can be obtained from a system is the work potential of the energy contained in that very system at a specified state. The term that best describes this is exergy. Exergy is generated from a wide variety of flows (mass, heat, work, etc.) flowing through the system.) it quantitatively represents useful energy or the ability to do or receive work - work content [23,24]. Thus, making it a very useful tool for designing, analyzing and classifying thermal systems. The specific flow exergy of a fluid at any state, e, ignoring the changes in kinetic and potential energy, can be calculated with Eq. (1).

$$e = h - h_o - T_o s - s_o \tag{3.1}$$

where h is the specific enthalpy ($kJkg$), s is the specific entropy ($kJkgK$), T is the temperature (K) and o is the dead state conditions. The exergy rate, E, is calculated by multiplying the specific exergy, e, with the fluids mass flow rate, m.

$$E = me \tag{3.2}$$

The entropy generation rate can be calculated with Eq. (3).

$$\underbrace{S_{in} - S_{out}}_{\text{Net entropy transfer rate}} = \underbrace{S_{gen}}_{\text{Entropy generation rate}} \tag{3.3}$$

and for a steady-flow system, the entropy generation rate, s_{gen}, can be calculated from Eq. (4).

$$s_{gen} = m_{out} s_{out} - m_{in} s_{out} - \frac{Q}{T} \tag{3.4}$$

where q is the heat transfer rate. The exergy destruction rate (i.e., rate of irreversibility), I for the steady state can be expressed by the following equation based on the general exergy ratio equilibrium for the open system:

$$I = T_o S_{gen} \tag{3.5}$$

where T_o is the dead state temperature. The performance ratio of the ith component of the system, PR_i, is calculated by comparing the exergy destruction rate of that component to the total exergy destruction, I_{TOTAL}, which is calculated by adding up the exergy destruction rate of each device.

$$PR_i = \frac{I_i}{I_{TOTAL}} \tag{3.6}$$

The first law efficiency by itself is not enough to measure the performance of thermal devises. To compensate for this deficiency the second law efficiency is used. The second law efficiency, η_{II}, also known as the exergetic efficiency, is the ratio of the device's performance to that same device's performance under reversible conditions for the exact final state [23].

$$\eta_{II} = \frac{\eta}{\eta_{rev}} \tag{3.7}$$

whereη is the thermal efficiency of the FGA-ORG with the irreversibilities taken into account and η_{rev} is the highest possible thermal efficiency under the same conditions. The work-done and/or the heat transfer rate can be calculated based on the first law of thermodynamics for the turbine, pumps, evaporator, condenser, heat exchanger and the heater which are steady-flow engineering devices. For the i_{th} apparatus of the system,

$$Q_i - W_i = H_{i,outlet} - H_{i,inlet} \tag{3.8}$$

and

$$m_{i,inlet} = m_{i,outlet} \tag{3.9}$$

The economical profit of the FGA-ORC for one hour operation can be expressed as the total price of the net electricity generated in the system. The assumptions made for the FGA-ORC system's first and second law analyses are as follows [25]:

1. All systems are steady-state and steady flow with negligible effects of kinetic and potential energy with no chemical or nuclear reactions.
2. The positive directions for the heat and work transfers for the system are, to the system and from the system respectively.
3. The turbine operations adiabatic efficiency is 80%.
4. The circulation pumps adiabatic efficiencies are 85%.
5. Pressure drops are neglected.
6. The condenser's output temperature is $25^{\circ}C$ and the quality is 0.
7. The dead state temperature is $T_o = 20^{\circ}C$ and the dead state pressure is P_o=100 kPa.

The energy of the stenter-frame's flue gas, which is the waste heat source, is transferred to the cycle's working fluid at the evaporator. Thus, the required heat energy is provided to the system. At the turbine outlet, some of the working fluid is dispatched to the heater and some to the heat exchanger. This approach makes it possible to examine the effect of the amount of fluid separated from the turbine to the heater on efficiency. As a result, system efficiency is increased by a heat exchanger and a heater located on two separate channels at the turbine outlet. For this cycle architecture, the goal of the highest efficiency is achieved, depending on equipment layout and parameters (Figure 3.1).

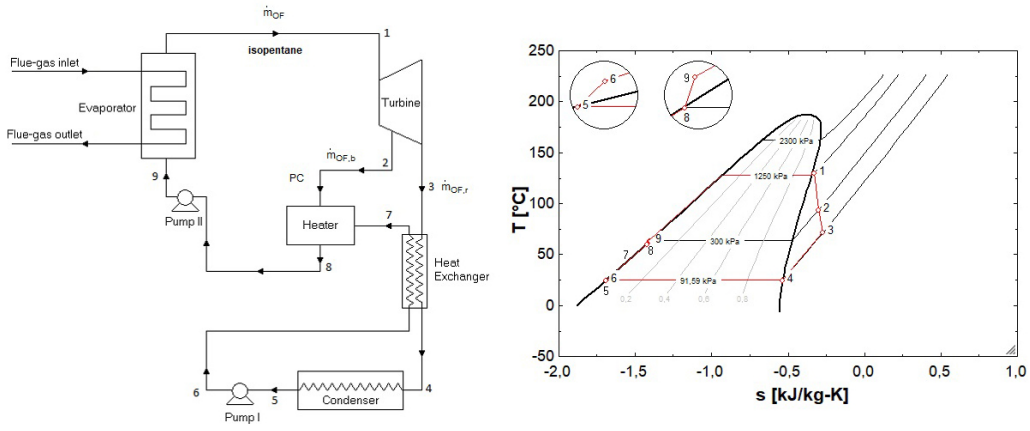

Figure 3.1: *Schematic illustration of the FGA-ORC system.*

3.3 Results and Discussion

The optimization for this thermal architecture is based on our codes on Engineering Equation Solver, EES. The present study can be used to predict the effects of many parameters such as temperature, pressure, mass flow rate, and dead state conditions on the performance of this FGA-ORC system. Since the irreversibility value of the heat exchanger is negative at 1312 kPa turbine inlet pressure under the conditions discussed, the thermodynamic limit is exceeded and the system cannot operate. In other words, the highest inlet pressure that can be reached is 1311 kPa. The evaporator capacity is constant so we can calculate the flow rate of the organic fluid used in the system for every different pressure value from the energy equilibrium of the

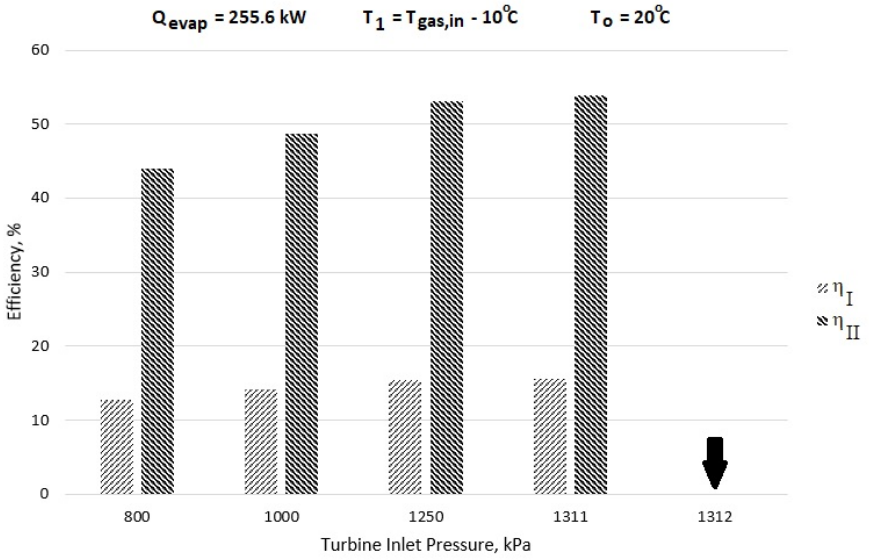

P, kPa	800	1000	1250	1311	1312
m_OF, kg/s	0.5671	0.577	0,5928	0.5975	-
Profit_E, $/h	3	3.318	3,617	3,677	-
I-Evaporator, kW	19.71	16.48	13,49	12.89	-
I-Turbine, kW	6.797	7,692	8,633	8.845	-
I-Heat Exchanger, kW	1.076	0.789	0,5265	0.4762	I < 0
I-Condenser, kW	2.131	2.168	2,228	2.245	-
I-Pump I, kW	0,01647	0.01676	0,01722	0.01736	-
I-Heater, kW	11.85	10,95	9,917	9.661	-
I-Pump II, kW	0.08404	0,1166	0,1595	0.1706	-
PR-Evaporator, %	47.3	43.12	38,57	37.58	-
PR-Turbine, %	16.31	20,13	24,69	25.78	-
PR-Heat Exchanger, %	2.583	2.065	1,506	1.388	-
PR-Condenser, %	5.115	5.675	6,371	6.545	-
PR-Pump I, %	0,03953	0.04386	0.04924	0.05059	-
PR-Heater, %	28.45	28.67	28,36	28.16	-
PR-Pump II, %	0.2017	0.305	0.4562	0.4972	-

Figure 3.2: *Effect of turbine inlet pressure on the FGA-ORC system.*

evaporator. Thus, allowing us to investigate each pressure condition for the constant evaporator capacity. In these analyses, the highest irreversibility calculated is at the evaporator (37,58%) for P=1311 kPa. The effect of the evaporator, heater and turbine, which are the three equipment with the highest irreversibility, on the total irreversibility was calculated as 91%. These equipment constitute the greatest irreversibility. As seen in these analyses, as the turbine inlet pressure increases from 800 kPa to 1311 kPa, the first law efficiency increases, and the profit from electricity generation increases by approximately 23%. At the same time, as the turbine inlet pressure increases from 800 kPa to 1311 kPa, as expected the second law efficiency of the system increases because of the decrease in the total irreversibility value of the system. The results are consistent with each other (see Figure 3.2).

This is the first of the graphs prepared for the effect of the cycle mid-pressure. When 300, 400, 500

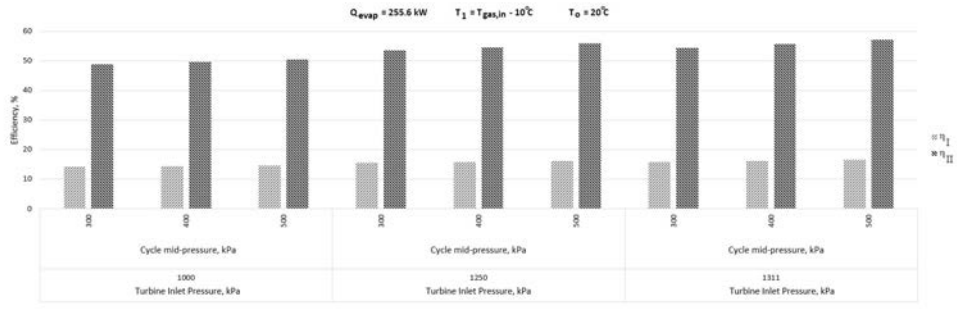

Turbine Inlet Pressure, kPa	1000			1250			1311		
Cycle mid-pressure, kPa	300	400	500	300	400	500	300	400	500
η_I	14.16	14.36	14.62	15.5	15.82	16.2	15.77	16.12	16.53
η_{II}	48,91	49,58	50.47	53.51	54.62	55.93	54.45	55.66	57,07
m_OF, kg/s	0.5991	0.6409	0.6812	0.6161	0.6605	0.7034	0.6212	0.6663	0.7101
Profit_E, $/h	3.334	3.38	3.441	3.648	3.723	3.813	3.712	3.794	3.89
I-TOTAL, kW	38.04	37.54	36.88	34.63	33.81	32.84	33.94	33.04	32

(a)

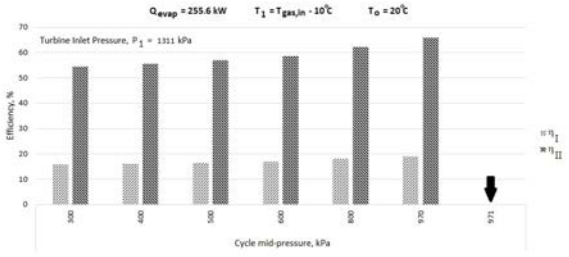

Turbine Inlet Pressure, kPa	1311						
Cycle mid-pressure, kPa	300	400	500	600	800	970	971
η_I	15.77	16.12	16.53	16.99	18.05	19.11	-
η_{II}	54.45	55.66	57.07	58.66	62.32	65.98	-
m_OF, kg/s	0.6212	0.6663	0.7101	0.7535	0.8424	0.9225	-
Profit_E, $/h	3.712	3.794	3.89	3.998	4.248	4.498	-
I-TOTAL, kW	33.94	33.04	32	30.83	28.11	25.4	-

(b)

Figure 3.3: *(a) Effect of the cycle mid pressure, (b) Effect of the cycle mid pressure on the FGA-ORC system.*

kPa are used as the mid pressure, the 1st law efficiency, the 2nd law efficiency, profit increases, and the total irreversibility decreases in all cases when the mid pressure increases from 300 to 500 (Figure 3.3a).

Figure 3.3b was prepared to find the best possible "cycle mid pressure" for a turbine inlet pressure of 1311 kPa. The mid pressure can be increased up to a maximum of 970 kPa. At 971 kPa, the Heater can operate under current thermodynamic conditions only if it receives extra energy from the outside. In other words, the system will not operate at 971 kPa mid pressure. Again, it is seen from the graph that for P_1=1311 kPa, as the cycle mid pressure increases, the efficiency of the first law of thermodynamics increases, and the profit that can be obtained increases accordingly. Similarly, as the cycle mid pressure increases, the total irreversibility decreases and accordingly the second law efficiency increases. These increases are limited by the thermodynamic operating condition of the heater.

PC represents the percentage of the working fluid sent from the turbine to the heater. When it is reduced from 50%, the efficiency increases up to 35%. The heater provides heat transfer to the outside (i.e., negative value) as it should be. However, at 34%, it becomes necessary to give additional heat from outside for the heater to work, which is against the working conditions of the cycle. Thus, PC reaches the limit value of 35% (Figure 3.4).

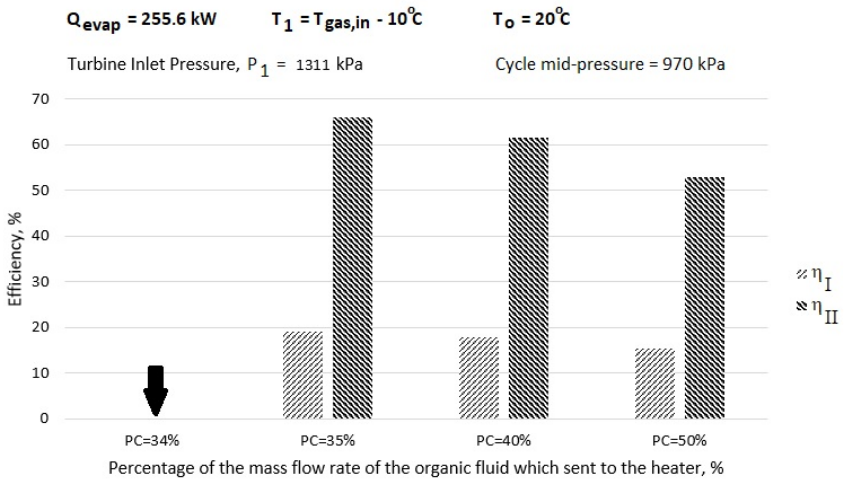

	PC=34%	PC=35%	PC=40%	PC=50%
η_I	-	19,11	17,85	15,34
η_{II}	-	65,98	61,64	52,95
m_OF, kg/s	0,9225			
Profit_E, $/h	-	4,498	4,202	3,61
Q-heater, kW	3,72	-0,08104	-19,2	-57,43
PR-heater, %	-	19,83	32,53	50,94

Figure 3.4: *Effect of PC on the FGA-ORC system.*

The maximum possible operation of a system in a given situation depends on the conditions of the dead state, as well as on the thermo-physical properties of the system. In other words, exergy is a property of the combination of the system and its environment. Thus, the results of the energy and exergy analyses of the calculated performance indicators of the FGA-ORC are sensitive to changes in the above-mentioned characteristics. The results obtained from the analyses with an increase in the dead state temperature show that the exergy efficiency increases (see Fig. 3.5). But thermodynamic limits should always be considered because FGA-ORC cannot be operated over the dead-state temperature of 26^{o}C due to I-Condenser$<$0. Figure 3.5 also shows the irreversibility values in some equipment of the cycle.

Figure 3.6 shows the PR values of the FGA-ORC equipment for the optimum condition. In the optimum case, the total irreversibility value of the system is 22.31 kW, and the calculations show that the turbine, evaporator, and heater have the highest PR ratios.

Under the optimum conditions, which are P_1=1311 kPa, P_{mid}=970 kPa, T_{gas},in=140°C, PC=35%, T_o=25°C, the cycles efficiencies are η_I=0.1911 and η_{II}=0.6888 and the exergy destruction rates (I) for each component under these optimum conditions are shown in Table 3.1.

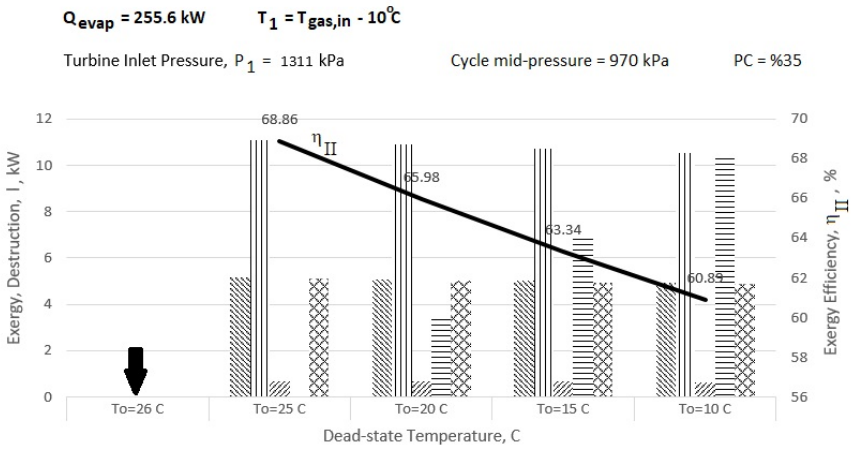

I-Evaporator, kW		5.181	5,094	5.008	4.921
I-Turbine, kW		11.08	10.9	10.71	10.53
I-Heat Exchanger, kW		0.6847	0.6732	0.6617	0.6503
I-Condenser, kW	< 0	0.00004	3.467	6.933	10.4
I-Heater, kW		5.121	5.036	4.952	4.867
η_{II}		68.86	65.98	63.34	60.89

Figure 3.5: *Effect of the dead state temperature (To) on the FGA-ORC system.*

3.4 Conclusions

ORCs are a promising feasible, and economical technology with minimizes the risk to human health and the environment. Energy and exergy-based thermodynamics analyses were carried out for FGA-ORC to provide better guidance for system improvement. In this study, a thermal architecture for FGA-ORC was investigated using isopentane as an organic fluid to provide high flexibility and efficiency for waste heat recovery from low to moderate heat sources.

Exergetic optimization is a valuable method for determining the optimal design of thermal systems under thermodynamic constraints. Optimum pressure, temperature, and mass flow rate values for FGA-ORC were obtained from the analysis results. From the results of the analyses for FGA-ORC, it is found that the maximum value of exergetic efficiency is 68.86% at P_1=1311 kPa, P_{mid}=970 kPa, T_{gas},in=140°C, PC=35%, T_o=25°C.

As mentioned before, exergy is the maximum useful work that could be obtained from the system at a given state in a specified environment. Exergy represents the upper limit of the amount of work a device can deliver without violating any thermodynamic laws. Exergy destruction is the wasted-work-potential during a process as a result of irreversibilities. The smaller the exergy destruction associated with a process, the greater the work that is produced [23]. As the amount of work produced by the turbine increases, so will electricity production and economic profit. As expected, the turbine work output and economic profit increase while the total exergy destruction decreases.

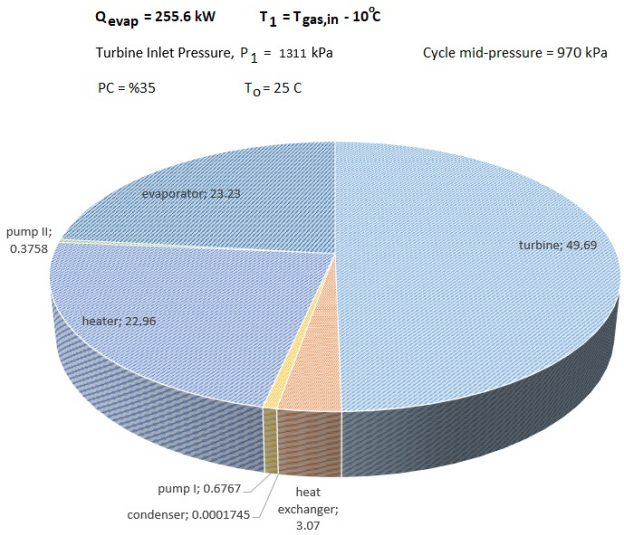

Figure 3.6: *Pie chart for the performance ratios (PR) of the equipment under optimum cycle conditions.*

Table 3.1: *Exergy destruction rates of each component under optimum cycle conditions*

Components	**Exergy destruction rate (I), kW**
Evaporator	5.181
Turbine	11.08
Heat Exchanger	0.6847
Condenser	0.00003893
Pump I	0.151
Heater	5.121
Pump II	0.08383
TOTAL	22.31

Abbreviations

The following abbreviations are used in this manuscript:

e specific exergy (kJ/kg)
E exergy rate (kW)
h specific enthalpy (kJ/kg)
H enthalpy (kJ)
I exergy destruction (kW)
m mass flow rate (kg/s)
P pressure (kPa)
PC percentage ratio (%)
PR performance ratio (%)
Q the heat transfer rate (kW)
s specific entropy (kJ/kgK)
T temperature (°C or K)
W work (kW)
η efficiency (%)

Subcripts

o	dead state conditions
II	second law
$evap$	evaporator
in	inlet
out	outlet
OF	organic fluid

Funding: This research received no external funding.

Conflicts of Interest: The authors declares no conflict of interest.

Authors Contributions: Authors contributed equally.

References

1. Pulat, E., Etemoglu, A.B., Can, M. (2009). Waste heat recovery potential in Turkish textile industry: case study for city of Bursa. *Renewable and Sustainable Energy Reviews,* 13 (3) 663-672.
2. Dai, Y, Wang, J., Gao, L. (2009). Parametric optimization and comparative study of organic Rankine cycle (ORC) for low grade waste heat recovery. *Energy Conversion and Management,* 50, 576–582.
3. Wei, D., Lu, X., Lu, Z., Gu, J.(2007). Performance analysis and optimization of organic Rankine cycle (ORC) for waste heat recovery. *Energy Conversion and Management,* 48, 1113-1119.
4. Liu, B., Chien, K., Wang, C. (2004). Effect of working fluids on organic Rankine cycle for waste heat recovery. *Energy,* 29, 1207–1217.
5. Hung, T. (2001). Waste heat recovery of organic Rankine cycle using dry fluids. *Energy Conversion and Management,* 42, 539–553.
6. Türkan, B., Etemoglu, A.B. (2020). Performance Evaluation For Thermal Architectures of Flue-Gas Assisted Organic Rankine Cycle Systems. *J. of Thermal Science and Technology,* 40(1), 65-76.
7. Vélez, F., Segovia, J.J., Martín, M.C., Antolín, G., Chejne, F., Quijano, A. (2012). A technical, economical and market review of organic Rankine cycles for the conversion of low-grade heat for power generation. *Renewable and Sustainable Energy Reviews,* 16, 4175–4189.
8. Tchanche, B.F., Lambrinos, G., Frangoudakis, A., Papadakis, G. (2011). Low-grade heat conversion into power using organic Rankine cycles — a review of various applications. *Renewable and Sustainable Energy Reviews,* 15, 3963–3979.
9. Wang, T., Zhang, Y., Peng, Z., Shu, G. (2011). A review of researches on thermal exhaust heat recovery with Rankine cycle. *Renewable and Sustainable Energy Reviews,* 15, 2862–2871.
10. Chen, H., Goswami, D.Y., Rahman, M.M., Stefanakos, E.K. (2011). Energetic and exergetic analysis of CO_2- and R32-based transcritical Rankine cycles for low-grade heat conversion. *Applied Energy,* 88 (8), 2802–2808.
11. Papadopoulos, A.I., Stijepovic, M., Linke, P. (2010). On the systematic design and selection of optimal working fluids for organic Rankine cycles. *Applied Thermal Engineering,* 30, 760–769.
12. Desai, N.B., Bandyopadhyay, S. (2009). Process integration of organic Rankine cycle. *Energy,* 34, 1674–1686.

13. Saleh, B., Koglbauer, K., Wendland, M., Fischer, J. (2007). Working fluids for low-temperature organic Rankine cycles. *Energy,* 32, 1210–1221.
14. Chen, H., Goswami, D.Y., Stefanakos, E.K. (2010). A review of thermodynamic cycles and working fluids for the conversion of low-grade heat. *Renewable and Sustainable Energy Reviews,* 14(9), 3059–3067.
15. Bao, J., Zhao, L. (2013). A Review of Working Fluid and Expander Selections for Organic Rankine Cycle. *Renewable and Sustainable Energy Reviews,* 24, 325–342.
16. Yamamoto, T., Furuhata, T., Arai, N., Mori, K. (2001). Design and testing of the organic Rankine cycle. *Energy,* 26, 239–251.
17. Hung, T.C., Shai, T.Y., Wang, S.K. (1997). A review of organic Rankine cycles (ORCs) for the recovery of low-grade waste heat, *Energy,* 22(7), 661–667.
18. Etemoglu, A.B. (2008). Thermodynamic evaluation of geothermal power generation systems in Turkey. *Energy Sources,* Part A, 30, 905–916.
19. Kermani, M., Wallerand, A.S., Kantor, I.D., Maréchal, F. (2018). Generic Superstructure Synthesis of Organic Rankine Cycles for Waste Heat Recovery in Industrial Processes. *Applied Energy,* 212, 1203–1225.
20. Akbay, O., Yılmaz, F. (2021).Thermodynamic Analyzes and Performance Comparison of Flash Binary Geothermal Power Generation Plant. *ECJSE,* 1, 445-461.
21. Yuksel, Y.E. (2020). Thermodynamic and performance evaluation of an integrated geothermal energy-based multigeneration plant. *ECJSE,* 3, 381-401.
22. Panesar, A., Morgan, R., Kennaird, D. (2017). Organic Rankine Cycle Thermal Architecture - From Concept to Demonstration. *Applied Thermal Engineering,* 126, 419–428.
23. Cengel, Y.A., Boles, M.A. (1989). *Thermodynamics: An Engineering Approach.* McGraw Hill Book Co., Singapore.
24. Bejan, A. (2002). Fundamentals of Exergy Analyzes, Entropy Generation Minimization, and the Generation of Flow Architecture. *International Journal of Energy Research,* 26, 545-565.
25. Safarian, S., Aramoun, F. (2015). Energy and Exergy Assessments of Modified Organic Rankine Cycles (ORCs). *Energy Reports,* 1, 1–7.

About the Authors

Mucahit Turker UYSAL graduated from the Mechanical Engineering Department of Sakarya University in 2019. In 2020 he was appointed to the Mechanical Engineering Department of Bursa Uludag University as a research assistant to work on his MSc and Ph.D. He is currently a MSc student and research assistant at Bursa Uludag University. His main research interests are CFD, impinging jets, heat and mass transfer, energy and exergy analysis and vortex tubes.He has been the Occupational Health and Safety Director of GONCA OSGB since the day it was founded.

Burak TURKAN graduated from the Mechanical Engineering Department of Bursa Uludag University in 2009. In 2011 he was appointed to the Mechanical Engineering Department of Bursa Uludag University as a research assistant to work on his MSc and Ph.D. He received MSc and Ph.D. degrees in energy area at the same department in 2014 and 2020 respectively. He is currently a lecturer Vocational School of Gemlik, Department of Mechanics at Bursa Uludag University. His main research interests are drying, heat and mass transfer, thermal insulation, optimization, energy and exergy analysis.

Akin Burak ETEMOGLU graduated from Mechanical Engineering Department at Uludag University in 1994. He received MSc and Ph.D. degrees in energy area at the same department in 1996 and 2003 respectively. He is currently a professor in the Mechanical Engineering Department at Bursa Uludag University. His research interests are simultaneous heat and mass transfer operations, waste-heat recovery, ORC systems, geothermal energy, and exergy.

CHAPTER 4

Fault Classification of Wind Turbine Gearbox Bearings Based on Convolutional Neural Network

Fatih Karpat, Onur Can Kalay, Ahmet Emir Dirik, and Esin Karpat

Article citation information: (2022), *TJES*, Vol. SP-2, pp. 71-83, doi:10.22545/2022/00190

Gearbox bearings are critical elements of wind power generation systems. Their stable operation supports the power generation, thus reducing the downtime and improving the economic efficiency of wind farms. With the wide availability of sensors, data-driven methods have started to be utilized instead of physical-based methods for condition monitoring of wind energy infrastructures. Deep learning provides significant advantages to achieving this end due to its ability to extract and select representative features without expert knowledge. The present study proposed an intelligent method based on one-dimensional convolutional neural networks (1D-CNN) to extract useful features from the vibration signals and classify different bearing faults. The performance of the proposed 1D-CNN model was evaluated employing the Case Western Reserve University dataset. As a result, the proposed method achieved an average prediction accuracy of 99.56%. The findings confirmed that the method has good stability and potentially be used to reduce operation and maintenance costs.

Keywords: Wind power, rolling bearing, fault diagnosis, deep learning.

4.1 Introduction

Energy is among the main pillars of human evolution. Due to global warming (i.e., climate change), the minimization of pollution besides operation and maintenance (O&M) costs during energy production is a matter of concern worldwide [1]. In this regard, energy collected from renewable sources and existing over a broad geographical region offers a great option to achieve this end. Due to its sustainable and clean characteristics, the wind energy sector has attracted continuous attention and has significantly grown during the past two decades [2]. For example, Global Wind Energy Council reported that the global wind energy sector had shown year-to-year growth of 19% in 2019 [3]. The wind turbine (WT) is utilized in order to transfer the wind energy first to mechanical and then the electrical energy [4, 5]. With the exponentially increased wind power capacity, the high O&M costs have become an issue that needs to be addressed extensively. WTs are subjected to harsh environmental conditions such as volatile (i.e., complex alternating) loads, extreme temperature differences, and frequent impact, and therefore, are prone to failure [6]. According to statistics, the annual O&M cost of a WT may reach approximately 3% of its original cost [3]. Currently, how to minimize the wind farm O&M costs with the early and accurate prediction of WT faults stands as an urgent problem to be solved for the wind energy community.

Reliability and safety are among the key terms of industrial operations [7]. Damage to critical components such as gearbox, blades, and generator may lead to considerably high O&M costs of WTs. For example, WT gearboxes are located at high altitudes, so their maintenance is challenging in case of failure. Evidence in the literature indicates that approximately 70% of WT gearbox failures are accounted for due to bearing failures [6]. Any faults in the bearings that support the weight of the WT besides rotating loads affect the efficiency, precision, and stability of the entire unit [8]. Failure to diagnose an incipient bearing fault then may threaten the reliability of WT; consequently, financial loss (i.e., high O&M costs) caused by downtime or even severe health risks (i.e., casualties) are inevitable. Condition monitoring (CM) aims to identify a deviation from the normal operation condition (i.e., fault indication) by monitoring a signal collected from a mechanical system. Many sensors are installed on WT equipment in order to collect WT data and perform CM tasks [9]. Deteriorating performance of a WT gearbox bearing manifests itself with abnormal variations of the temperature, vibration, motor current, and torque responses [10]. Among them, the vibration data are usually utilized to achieve bearing diagnostics and prognostics tasks owing to its advantages, for example, low cost and convenient implementation [8, 11]. An in-depth research work regarding the early fault diagnosis of WT bearings is significant for minimizing the O&M costs, increasing annual power generation, and maximizing the economic benefits [12]. Many scholars have proposed different techniques to diagnose bearing faults based on the traditional (signal processing + feature extraction + machine learning) methods.

To eliminate uncorrelated content, Mishra et al. [13] utilized the instantaneous angular position instead of time for signal processing and benefited from enveloping and order tracking. The researchers tested their four-stage sequential signal processing approach through the data collected from a bearing test setup. The pre-fabricated fault-defined bearings (e.g., rolling element fault) were mounted to the experimental test rig, and the vibration data were then collected under variable shaft speeds. Glowacz et al. [14] proposed an approach to perform a bearing fault diagnosis task. To this end, a feature vector was created employing a method, namely, "Method of Selection of Amplitudes of Frequency." Three traditional methods were utilized to classify bearing faults: 1) Gaussian Mixture Models, 2) Nearest Neighbor, and 3) Nearest Mean classifiers. Later, Zhao et al. [15] processed the vibration data utilizing stochastic subspace identification to extract fault features. The constructed feature vectors were inputted to the multi-kernel support vector machine (SVM) to classify WT-bearing faults. The study concluded that the proposed multi-kernel SVM technique outperformed the traditional pattern recognition methods evaluated within the scope of the research work.

Manual feature selection is a blind, labor-oriented, and subjective process that mainly depends on advanced expertise knowledge. In addition, the traditional fault diagnosis methods consist of shallow structures that are not suitable for learning complicated nonlinear relationships [16]. So, the conventional methods cannot meet the wind farms' actual implementation needs. To overcome these shortcomings, deep learning (DL), which can capture sensitive fault information without expert knowledge, has started to be utilized to diagnose rotary machinery faults over the last decade. As an emerging research field, DL could be a powerful tool to extract the representative features from sensor data and automatically learn discriminative features to classify WT-bearing faults.

In order to perform WT bearing fault diagnosis, Zhang et al. [6] combined the SVM classifier and a one-dimensional convolutional neural network (1D-CNN). The features extracted with the 1D-CNN were then inputted into an optimized SVM classifier. Their study evaluated ten bearing statuses through the vibration signals collected from the Case Western Reserve University (CWRU) dataset. Consequently, it was observed that the proposed method could classify different WT-bearing faults with a recognition accuracy of 98.2%. Hao et al. [16] proposed a new network structure based on a deep belief network (ResNet) to reduce losses and diagnose bearing faults. The researchers replaced the fully connected layer part of the ResNet with the general average pooling technology. The study benefited from the CWRU dataset to interpret the efficacy of the proposed network structure. As a result, it was indicated that the proposed model performed an average accuracy of 99.83% and shortened the training time. Karpat et al. [17] proposed a 1D-CNN model to classify healthy state, inner raceway (IR), and outer raceway (OR) faults under variable operating conditions (i.e., shaft speeds and load torques). The study employed the Paderborn University dataset, another prominent benchmark dataset, to validate their 1D-CNN model. A total of nine classes were identified within the scope of research work; consequently, an average classification accuracy of 93.97% was achieved. He et al.

[18] endeavored to diagnose different bearing faults (i.e., healthy state, IR, OR, and rolling element faults) and developed a new intelligent approach by adopting a novel weight strategy to improve robustness. By utilizing the CWRU dataset, a multi-class classification problem that contains ten classes was solved. The proposed method reached a testing accuracy of 99.71%. To solve the problem that small datasets cannot be trained on deep networks, Chen et al. [19] designed an improved model utilizing a deep transfer CNN. The researchers benefited from two experimental datasets (i.e., CWRU and centrifugal pump datasets) to evaluate their model's performance. The study concluded that the proposed deep transfer CNN architecture could reach a prediction accuracy of near 100%. Karpat et al. [20] performed an early fault diagnosis task utilizing simulated vibration data. To this end, the study developed a six-degrees-of-freedom dynamic model of a single-stage gearbox mechanism. In addition, a signal-to-noise ratio of 10 was considered to make the classification task more complicated. As a result, an average accuracy of 93.07% was achieved. Even if the above-discussed methods could accurately diagnose bearing faults in many cases, there is still room for further improvements in this research field.

The present study proposed a 1D-CNN model to extract useful features from original vibration signals and classify different WT-bearing faults. To this end, a multi-class classification problem was solved in the presence of IR, OR, and rolling element faults. The experimental data of the CWRU (i.e., a prominent benchmark dataset) was employed to evaluate the performance of the proposed 1D-CNN model. In order to interpret the stability of the proposed DL-based method, the experiments were repeated five times (number of trials), and the standard deviation value was calculated. As a result, the average prediction accuracy of 99.56% was achieved. The findings showed that the developed method was suitable (in terms of robustness and stability) for detecting outliers and diagnosing different WT gearbox bearing faults. It can potentially reduce O&M costs and improve the predictive maintenance strategies by early WT gearbox bearing fault diagnosis.

The remainder of the current paper is organized as follows. The "Methodology" section introduces the fault characteristics of WT-bearings, the CWRU experimental dataset, and the structure of the proposed 1D-CNN model. The "Results and Discussion" section comparatively interprets the experimental findings obtained. The "Conclusion" section summarizes the paper along with the future improvements.

4.2 Methodology

This section will detail the WT gearbox fault signature, the experimental procedure (i.e., the CWRU dataset), and the layers and main attributes of the proposed 1D-CNN model.

4.2.1 WT Gearbox Fault Signature

Rotary machinery plays an irreplaceable role and accounts for more than 80% of modern machinery [7]. In a WT gearbox, an unexpected failure inevitably influences the reliability of other linked mechanical equipment. Among all of the rotating machinery, the bearings are one of the key but also vulnerable components. Their health status directly affects the reliability and safety of the entire unit [12]. From this point of view, it is critical to detect and replace faulty WT-bearings in time to prevent catastrophic accidents [8]. The existing literature shows a high failure rate of WT bearings besides yaw-and-pitch systems has been observed [21]. So, an intelligent method that can automatically extract and select useful features to diagnose WT faults is valuable to guide engineering practice. Figure 4.1 depicts the general structure of a WT.

Bearing faults can generally be addressed under two main categories, considering the fault development stages: 1) single-point fault and 2) generalized roughness [22]. Single-point faults include IR, OR, rolling elements, and cage faults. As above-discussed, the deteriorating performance of a WT-bearing manifests itself with abnormal variations of the temperature, vibration, motor current, and torque responses [10]. When a localized WT-bearing fault develops, the collision among the IR, OR, and rolling elements will excite the mechanical system's vibration response. Meanwhile, it should be noted that the vibration response of a WT gearbox (and its components) has the characteristics of continuity and volatility. Figure 4.2 illustrates the configuration of a typical rolling-element bearing that contains IR, OR, rolling elements, and the cage.

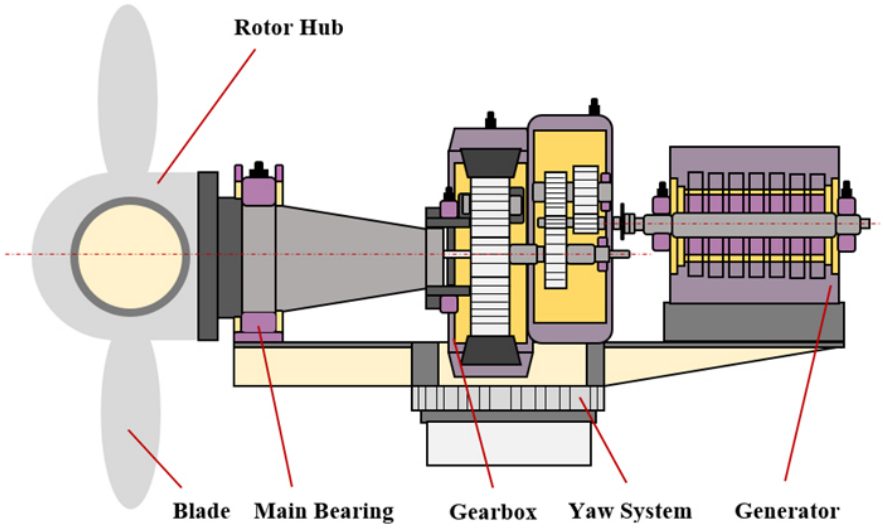

Figure 4.1: *General structure of a WT.*

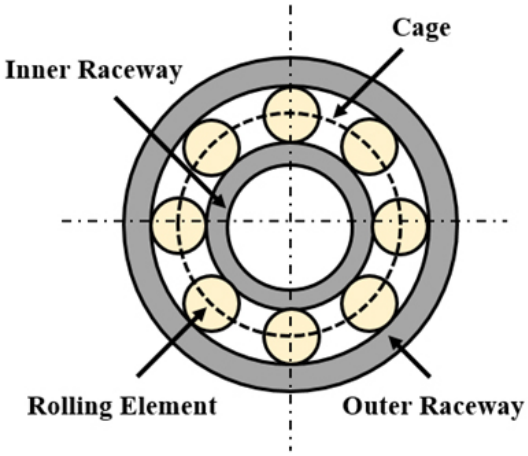

Figure 4.2: *Configuration of a typical rolling bearing.*

In addition, the bearing rotating frequency and geometry are other merits that influence the single-point fault characteristics [23]. The corresponding problem of WT gearbox bearing fault diagnosis is how to process the collected vibration signals through sensors to obtain useful diagnostic fault features [24]. To achieve this end, the present study proposes a DL-based approach to extract useful features from original vibration signals and classify bearing faults.

4.2.2 Experimental Description

The present study utilized the vibration signals collected from the CWRU [25] experimental test rig to evaluate the performance of the proposed DL-based method. The sub-section will address the details of the experimental setup and health conditions (i.e., classes) considered within the scope of research work.

The experimental setup of the CWRU consists of a 2 HP electric motor, a torque transducer/encoder, and a load (i.e., dynamometer). Single-point faults, ranging from approximately 0.18 mm to 1 mm (in diameter), were introduced to the 6205-2RS SKF test bearings with electro-discharge machining. The CWRU dataset includes the vibration signals of the healthy state and three faulty (i.e., IR, OR, and rolling element faults) conditions. Afterward, the bearings (healthy + faulty) supporting the motor shaft were remounted on the test motor, and the data were collected through the accelerometers attached to the housing. The schematic diagram of the CWRU bearing test rig is presented in Figure 4.3.

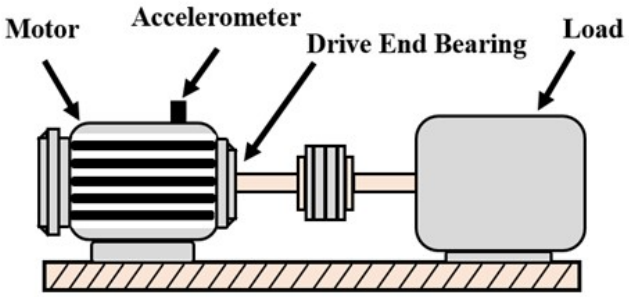

Figure 4.3: *The schematic diagram of the CWRU test rig.*

This study selected ten classes among the CWRU dataset for testing the proposed 1D-CNN model's performance. In order to interpret the model capabilities under variable conditions, four health statuses (i.e., healthy, IR, OR, and rolling element faults) were considered. In addition, the bearing faults, ranging from 0.18 mm to 0.54 mm (0.007 inches to 0.021 inches), were selected to evaluate the influence of fault diameter on the classification accuracy. The vibration data were collected at 0 HP and 1797 RPM conditions and the samples were collected with 12,000 and 48,000 samples/second sampling rates for drive-end bearing experiments. The description of the dataset considered within the scope of research work is shown in Table 1.

4.2.3 Model Structure

CNN is a feed-forward multi-stage neural network that mainly contains five layers, namely, (1) convolution layer, (2) activation layer, (3) pooling layer, (4) fully-connected layer, and (5) output layer (see Figure 4.4). The convolution layer is used to execute convolution operation and then extract local features through the activation layer. CNN structure benefits from the activation layer in order to carry out a nonlinear transformation on the input data (e.g., vibration signal of a WT gearbox bearing). Plus, the Rectified Linear Units (ReLu), Sigmoid, and Hyperbolic Tangent (tanh) are among the most commonly utilized activation functions [6]. On the other side, the pooling layer is mainly utilized to perform a down-sampling operation, prevent overfitting, and reduce the amount of calculation [26].

The present study used 70% of the data for training, 15% for testing, and 15% for validation. The window size was defined as 25000. Dropout is a common method to solve the overfitting problem in DL algorithms [16]. Some neurons are randomly dropped by Dropout to ensure that the neural network only propagates forward during the training iteration. In this regard, the Dropout ratio was set to 0.5 in the present research work. Epoch size was set to 5. The developed 1D-CNN model includes two convolutions and pooling layers (see Table 2).

Table 1: Description of the dataset.

Fault Location	Fault Diameter (mm)	Label
None (Healthy)	None	H_0
Inner Raceway	0.18	IR_1
Inner Raceway	0.36	IR_2
Inner Raceway	0.54	IR_3
Rolling Element	0.18	B_4
Rolling Element	0.36	B_5
Rolling Element	0.54	B_6
Outer Raceway (Centered @6:00)	0.18	OR_7
Outer Raceway (Centered @6:00)	0.36	OR_8
Outer Raceway (Centered @6:00)	0.54	OR_9

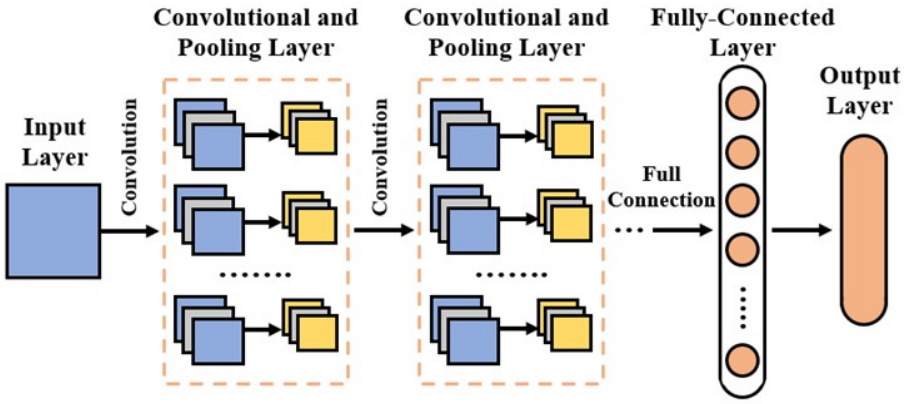

Figure 4.4: *Classical structure of CNN.*

Table 2: The layers and main attributes of 1D-CNN model.

Layer (Type)	Output Shape	Param #
conv1d (Conv1D)	(None, 25000, 4)	8
max_pooling1d (MaxPooling1D)	(None, 12500, 4)	0
conv1d_1 (Conv1D)	(None, 12500, 4)	20
max_pooling1d_1 (MaxPooling1D)	(None, 6250, 4)	0
dropout (Dropout)	(None, 6250, 4)	0
flatten (Flatten)	(None, 25000)	0
dense (Dense)	(None, 256)	6400256
dense_1 (Dense)	(None, 128)	32896
dense_2 (Dense)	(None, 64)	8256
dense_3 (Dense)	(None, 10)	650

The present research work used 4 feature maps with kernel size 1 and ReLu function as the activation function in the first layer. The feature map and the kernel size in the second convolution layer were also determined as 4 and 1. The tanh function was utilized as the activation function in the second layer. The Adam (Adaptive Moment Estimation) optimizer was adopted to optimize the network and improve the overfitting problem [16]. The categorical cross-entropy loss function, which has fast convergence speed and strong generalization ability, was used to learn a multi-class classification problem [26].

4.3 Results and Discussion

The present study developed a DL-based approach in order to classify different WT gearbox bearing faults and evaluated its prediction ability, considering multiple fault diameters (from 0.18 mm to 0.54 mm). The CWRU benchmark dataset was employed [25] to achieve this end. In order to evaluate the stability of the proposed DL-based method, the experiments were repeated five times (i.e., number of trials), and the standard deviation value was calculated.

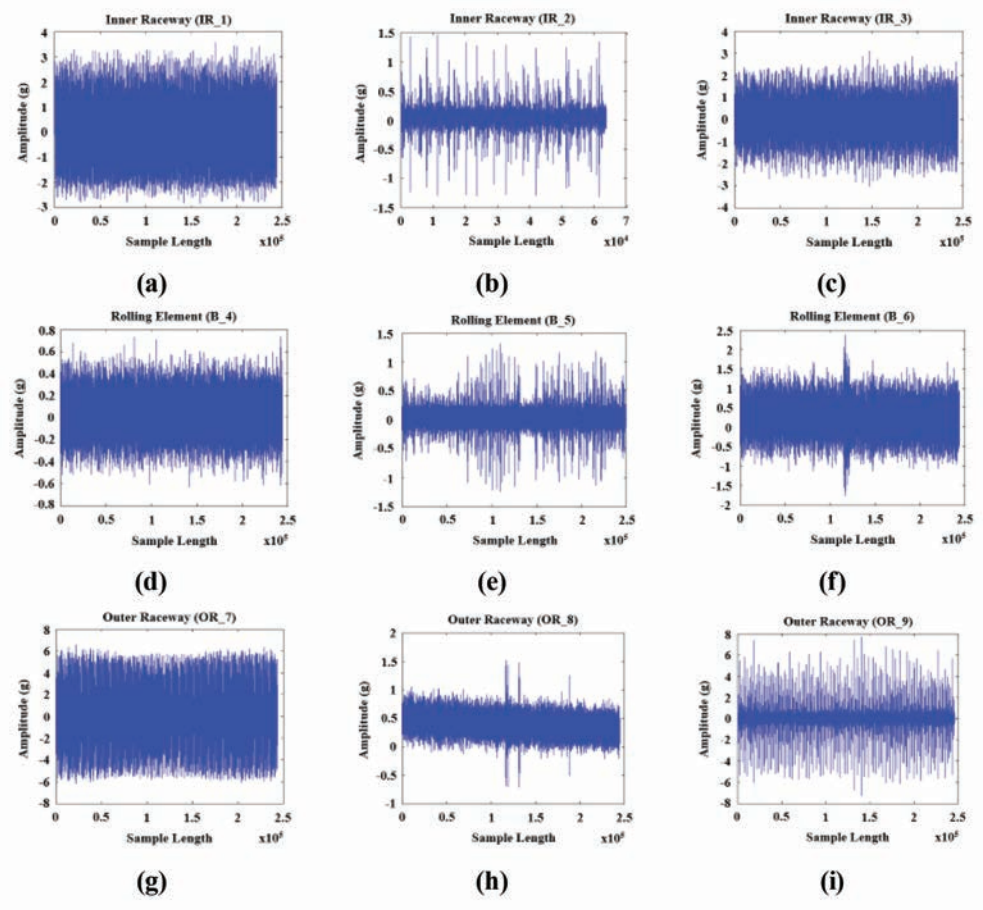

Figure 4.5: *Vibration signals of fault class IR_1 to OR_9, respectively.*

The vibration signals collected for the different bearing health conditions (see Table 1) through the CWRU

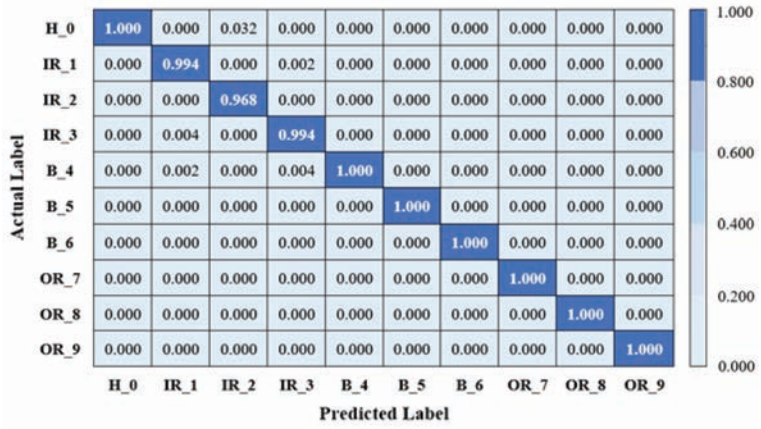

Figure 4.6: *Confusion matrix for the first trial.*

experimental setup are demonstrated in Figure 4.5. Figures 4.5(a) to (c) represent the signals collected for the bearings with IR fault (labels IR_1, IR_2, and IR_3). Figures 4.5(d) to (f) stand for rolling element fault data (B_4, B_5, and B_6). Figures 5(g) to (i) depict the signals obtained for bearings with OR fault (labels OR_7, OR_8, and OR_9).

The present study plotted a confusion matrix to interpret further the results obtained. In this regard, the confusion matrix of the first trial is presented in Figure 4.6. The experimental results showed that the proposed 1D-CNN model classified the healthy state (H_0), rolling element (B_4, B_5, and B_6), and OR faults (OR_7, OR_8, and OR_9) perfectly. With this in mind, Figure 4.6 also indicates that the model performed relatively poorly in classifying IR faults.

As above-mentioned, the experiments were repeated five times (i.e., number of trials) to evaluate the model stability. The classification accuracies (confusion among the classes) differed slightly between the five tests. Considering all five tests executed, it is worth mentioning that the method has also slightly confused classifying IR_1 and IR_3 and IR_3 and OR_1 classes among themselves. In all tests, the proposed 1D-CNN model showed a prediction accuracy of more than 99%. In this regard, the prediction accuracies obtained were 99.56%, 99.82% (maximum), 99.72%, 99.54%, and 99.16% (minimum), respectively. The standard deviation value was calculated as 0.25. As a result, the average classification accuracy was 99.56% after testing the model with the CWRU dataset.

After five epochs, the loss and accuracy curves obtained for the first trial are depicted in Figure 4.7. The model has started to converge after only two epochs, indicating a strong converge ability (see Figure 4.7). The results reported point out that the proposed 1D-CNN model showed good robustness and stability characteristics.

The CWRU dataset is considered a standard reference for model validation and is widely employed for bearing fault diagnostics tasks. For example, Sun et al. [7] proposed a novel diagnosis approach based on an interpretable anti-noise efficient multi-scale CNN. Their study benefited from the CWRU dataset and identified fifteen classes (i.e., healthy state, IR, OR, and rolling element faults) among the benchmark dataset. The proposed approach achieved an average accuracy of near 100% and outperformed the other methods considered within the scope of research work. Yang et al. [21] combined the 2D-CNN and the random forest (RF) classifier in order to diagnose different WT-bearing faults, considering noisy environments. After training the 2D-CNN, the feature vectors were inputted to the RF classifier to improve its generalization ability. The study concluded that the proposed 2D-CNN-RF model could reach an average prediction accuracy of 99.548% after testing its performance with the CWRU dataset. In order to diagnose bearing faults accurately and automatically, Shao et al. [26] proposed a novel technique, namely, ensemble deep auto-encoders. The study employed the vibration signals collected from the CWRU test rig and further identified twelve (i.e.,

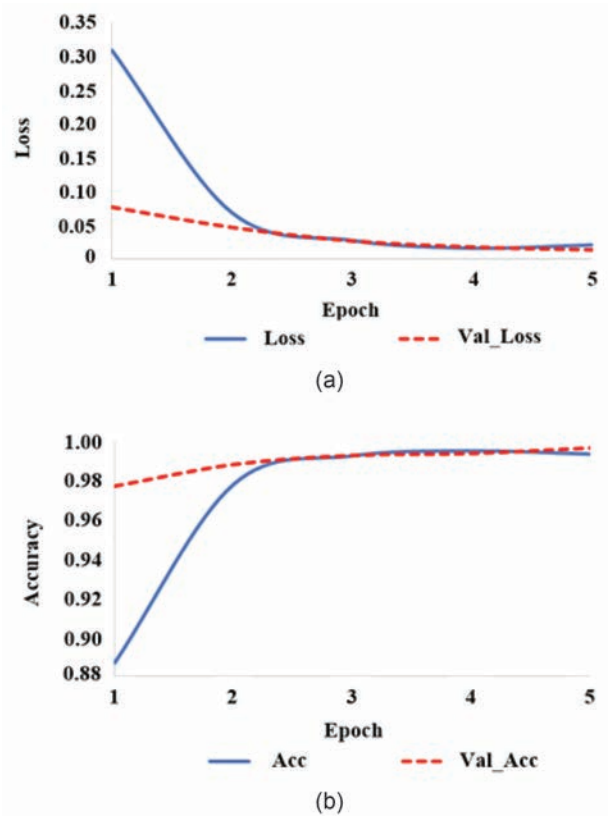

Figure 4.7: *The performance evaluation for the first trial: (a) loss and (b) accuracy curves.*

healthy state, IR, OR, and rolling element faults) health classes. The findings indicated that the proposed technique performed superior to the other intelligent methods evaluated within the scope of research work.

Even if the above-discussed methods could accurately diagnose bearing faults in many cases, there is still room for further improvements in this research field. The present study proposed a 1D-CNN model to extract useful features from original vibration signals and classify different WT-bearing faults. WTs are subjected to harsh environmental conditions such as complex alternating loads and extreme temperature differences and are prone to failure [6]. A lack of prompt and accurate diagnosis of bearing faults may lead to financial loss and severe health risks [27, 28]. To manage the potential failure of WT gearboxes, the automatic and timely monitoring of rolling-element bearing faults is essential. The proposed DL-based approach could reduce O&M costs and improve the predictive maintenance strategies by early WT gearbox bearing fault diagnosis.

4.4 Conclusions

Wind energy is one of the fastest-growing and promising ways to generate renewable energy. With the wide availability of sensor technologies and ever-increasing computation power, CM has attracted continuous attention for reducing downtime and, thus, O&M costs of WTs. The data-driven intelligent methods could be utilized to establish a relationship between the system's inputs and outputs and achieve CM tasks.

The present study proposed an intelligent WT-bearing fault diagnosis method based on 1D-CNN. The proposed architecture was utilized to extract useful features from original vibration signals and solve a

multi-class classification problem. The procedure was applied to the experimental vibration signals, and its performance was comparatively interpreted, considering multiple fault locations and diameters.

The experiments were repeated five times in order to evaluate the model's robustness and stability. As a result, the average classification accuracy of 99.56% was achieved. In addition, the standard deviation value was calculated as 0.25, indicating the stability of the proposed method. The results confirm that the proposed 1D-CNN method was suitable for identifying WT gearbox bearing faults and can optimize maintenance costs by early fault detection. Our method can be easily extended to other large industrial fields. The authors will continue to test their model under variable operating conditions to expand the scope of implementation.

Acknowledgments

The authors acknowledge the Council of Higher Education in Turkey 100/2000 Ph.D. Scholarship Program.

Funding: This research is partially supported by the Bursa Uludag University, Grant Number FGA-2021-496.

Conflicts of Interest: The authors declares no conflict of interest.

Authors Contributions: F.K. is the project leader of this research work. A.E.D and E.K. supported the projects through research design and idea generation. O.C.K. collected the data and performed analyses. O.C.K. and F.K. wrote the first draft manuscript, and all authors edited and agreed to the manuscript.

References

1. Encalada-Dávila, Á., Puruncajas, B., Tutivén, C., Vidal, Y. (2021). Wind turbine main bearing fault prognosis based solely on SCADA data. *Sensors (Basel)*, 21, 1-22. doi: 10.3390/s21062228
2. Ding, X., Xu, J., Wang, J., Zheng, J. (2022). Fault diagnosis of wind turbine generator bearings using fast spectral correlation. *Wind Engineering*, 46(3), 724-736. doi: 10.1177/0309524X211046381
3. Wu, Y., & Ma, X. (2022). A hybrid LSTM-KLD approach to condition monitoring of operational wind turbines. *Renewable Energy,* 181, 554-566. doi: 10.1016/j.renene.2021.09.067
4. Doğan, O., Kalay, O. C., Karpat, F. (2021). Influence of linear profile modifications on the dynamic loading of a spur gear. *Uludag University Journal of The Faculty of Engineering,* 26(2), 707-722. doi: 10.17482/uumfd.829930
5. Guo, J., Wang, X., Zhai, C., Niu, J., Lu, S. (2019). Fault diagnosis of wind turbine bearing using synchrosqueezing wavelet transform and order analysis. Paper presented at 2019 14th IEEE Conference on Industrial Electronics and Applications, Xi'an, China, 19-21 June (pp. 2384-2387). doi: 10.1109/ICIEA.2019.8833879
6. Zhang, X., Han, P., Xu, L., Zhang, F., Wang, Y., Gao, L. (2020). Research on bearing fault diagnosis of wind turbine gearbox based on 1DCNN-PSO-SVM. *IEEE Access,* 8, 192248-192258. doi: 10.1109/ACCESS.2020.3032719
7. Sun, H., Cao, X., Wang, C., Gao, S. (2022). An interpretable anti-noise network for rolling bearing fault diagnosis based on FSWT. *Measurement,* 190, 110698. doi: 10.1016/j.measurement.2022.110698

8. Wang, X., He, Y., Wang, H., Hu, A., Zhang, X. (2022). A novel hybrid approach for damage identification of wind turbine bearing under variable speed condition. *Mechanism and Machine Theory,* 169, 104629. doi: 10.1016/j.mechmachtheory.2021.104629
9. Xie, Y., Zhao, J., Qiang, B., Mi, L., Tang, C., Li, L. (2021). Attention mechanism-based CNN-LSTM model for wind turbine fault prediction using SSN ontology annotation. *Wireless Communications and Mobile Computing,* 2021, 1-12. doi: 10.1155/2021/6627588
10. Li, H., Deng, J., Yuan, S., Feng, P., Arachchige, D. D. K. (2021). Monitoring and identifying wind turbine generator bearing faults using deep belief network and EWMA control charts.*Frontiers in Energy Research,* 9, 1-10. doi: 10.3389/fenrg.2021.799039
11. Wang, X., Mao, D., Li, X. (2021). Bearing fault diagnosis based on vibro-acoustic data fusion 1D-CNN network. *Measurement,* 173, 108518. doi: 10.1016/j.measurement.2020.108518
12. Yüce, C., Gecgel, O., Doğan, O., Dabetwar, S., Yanik, Y., Kalay, O. C., Karpat, E., Karpat, F., Ekwaro-Osire, S. (2022). Prognostics and health management of wind energy infrastructure systems. *ASCE-ASME Journal of Risk and Uncertainty in Engineering Systems*, Part B: Mechanical Engineering, 8(2), 1-18. doi: 10.1115/1.4053422
13. Mishra, C., Samantaray, A. K., Chakraborty, G. (2016). Rolling element bearing defect diagnosis under variable speed operation through angle synchronous averaging of wavelet de-noised estimate. *Mechanical Systems and Signal Processing,* 72-73, 206-222. doi: 10.1016/j.ymssp.2015.10.019
14. Glowacz, A., Glowacz, W., Glowacz, Z., Kozik, J. (2018). Early fault diagnosis of bearing and stator faults of the single-phase induction motor using acoustic signals. *Measurement*, 113, 1-9. doi: 10.1016/j.measurement.2017.08.036
15. Zhao, H., Gao, Y., Liu, H., Li, L. (2019). Fault diagnosis of wind turbine bearing based on stochastic subspace identification and multi-kernel support vector machine. *Journal of Modern Power Systems and Clean Energy,* 7(2), 350-356. doi: 10.1007/s40565-018-0402-8
16. Hao, X., Zheng, Y., Lu, L., Pan, H. (2021). Research on intelligent fault diagnosis of rolling bearings based on improved deep residual network. *Applied Sciences,* 11, 1-14. doi: 10.3390/
17. Karpat, F., Kalay, O. C., Dirik, A. E., Doğan, O., Korcuklu, B., Yüce, C. (2021). Convolutional neural networks based rolling bearing fault classification under variable operating conditions. Paper presented at IEEE 2021 International Conference on Innovations in Intelligent Systems and Applications, Kocaeli, Turkey, 25-27 August (pp. 1-6). doi: 10.1109/INISTA52262.2021.9548378
18. He, J., Ouyang, M., Yong, C., Chen, D., Guo, J., Zhou, Y. (2020). A novel intelligent fault diagnosis method for rolling bearing based on integrated weight strategy features learning. *Sensors (Basel),* 20, 1-20. doi: 10.3390/s20061774
19. Chen, Z., Cen, J., Xiong, J. (2020). Rolling bearing fault diagnosis using time-frequency analysis and deep transfer convolutional neural network. *IEEE Access,* 8, 150248-150261. doi: 10.1109/ACCESS.2020.3016888
20. Karpat, F., Dirik, A. E., Kalay, O. C., Yüce, C., Doğan, O., Korcuklu, B. (2021). Fault diagnosis with deep learning for standard and asymmetric involute spur gears. Paper presented at 2021 ASME International Mechanical Engineering Congress and Exposition, Virtual, Online, 1-5 November (pp. 1-9).
21. Yang, S., Yang, P., Yu, H., Bai, J., Feng, W., Su, Y., Si, Y. (2022). A 2DCNN-RF model for offshore wind turbine high-speed bearing-fault diagnosis under noisy environment. *Energies,* 15, 3340. doi: 10.3390/en15093340
22. Stack, J. R., Habetler, T. G., Harley, R. G. (2004). Fault classification and fault signature production for rolling element bearings in electric machines.*IEEE Transactions on Industry Applications,* 40(3), 735-739. doi: 10.1109/TIA.2004.827454
23. Gong, X., & Qiao, W. (2013). Bearing fault diagnosis for direct-drive wind turbines via current-demodulated signals.*IEEE Transactions on Industrial Electronics,* 60(8), 3419-3428. doi: 10.1109/TIE.2013.2238871

24. Chen, J., Pan, J., Li, Z., Zi, Y., Chen, X. (2016). Generator bearing fault diagnosis for wind turbine via empirical wavelet transform using measured vibration signals.*Renewable Energy,* 89, 80-92. doi: 10.1016/j.renene.2015.12.010
25. https://csegroups.case.edu/bearingdatacenter (accessed 25 March, 2022).
26. Shao, H., Jiang, H., Lin, Y., Li, X. (2018). A novel method for intelligent fault diagnosis of rolling bearings using ensemble deep auto-encoders. *Mechanical Systems and Signal Processing,* 102, 278-297. doi: 10.1016/j.ymssp.2017.09.026
27. Maties, V., Vlaşin, I., Tamas, V. (2019). Transdisciplinarity, mechatronics and organizational learning. *Transdisciplinary Journal of Engineering & Science,* 10, 158-168. doi: 10.22545/2019/0126.
28. Mambo, W. (2022). Aligning software engineering and artificial intelligence with transdisciplinary. *Transdisciplinary Journal of Engineering & Science,* 13, 21-36. doi: 10.22545/2022/00177.

About the Authors

Dr. Fatih Karpat is a full professor in the Department of Mechanical Engineering at the Bursa Uludag University in Turkey. He earned B.Sc. and M.Sc. degrees in Mechanical Engineering from Uludag University, Turkey, in 1998 and 2001, respectively. He received a Ph.D. degree in Mechanical Engineering from Uludag University, Turkey, in 2005. Prior to joining the faculty, he worked as a Post- Doctoral Research Associate in the Mechanical Engineering Department at Texas Tech University in 2006 and 2010. His research interests include, but are not limited to, experiments and numerical simulation of power transmission systems (gears, clutch, etc.), lightweight designs, advanced joining technology (laser welding, etc.), sustainability, and biomechanics.

Onur Can Kalay is a Ph.D. Candidate in the Department of Mechanical Engineering at the Bursa Uludag University in Turkey. He received his B.Sc. degrees in Mechanical Engineering and Business Administration from Bursa Uludag University and Anadolu University, Turkey, in 2017, respectively. In 2020, he worked as a Visiting Scholar at the University of Central Oklahoma, Department of Engineering and Physics. He worked on research projects supported by the Scientific and Technological Research Council of Turkey, the Turkish Aerospace Industries, the Higher Education Council in Turkey, and the Bursa Uludag University. His research interests include, but are not limited to, experiments and numerical simulations of power transmission systems, biomechanics, and early fault diagnosis with artificial intelligence.

Ahmet Emir Dirik received a B.Sc. degree in Electronics Engineering from Uludag University in 1999. He received an M.Sc. degree in Electronics Engineering and M.B.A. degree in 2001 from Uludag University. He received Ph.D. in 2010 from the Polytechnic Institute of New York University. During his Ph.D. studies, he worked as a research fellow at the Polytechnic Institute of New York University. In 2007, 2008, and 2009 he worked at Pitney Bowes, Shelton, CT. and IBM, T.J. Watson Research Center, NY, on various multimedia related research projects. Currently, he works in the Computer Engineering Department at Bursa Uludag University as Professor. His research interests include but are not limited to multimedia forensics, multimedia processing, and pattern recognition.

Esin Karpat received her B.S., M.S., and Ph.D. degrees in Electronics Engineering from the Bursa Uludag University, Bursa, in 1996, 2002, and 2009 respectively. From 2000 to 2013, she was a Research Assistant with the Department of Electronics Engineering, EM Laboratory. She was with the EM and Microwave Laboratory, Texas Tech University as a research assistant in 2006. Since 2013, she has been an Assistant Professor with the Electronics Engineering Department, Bursa Uludag University. Currently, she serves as Vice-Chair in the Electrical and Electronics Engineering Department. Dr. Karpat currently has been working as a researcher in a number of ongoing national and international projects, of which many are related to electromagnetics, electronic design for experimental studies, and software. Her research has been supported by the Council of Higher Education and Technology of Turkey (CoHE), The Scientific and Technological Research Council of Turkey (TUBITAK), the Bursa Uludag University (BUU), and the Turkish Aircraft Industries Corporation. Her research interests include high-antenna design, wave propagation, and microwave imaging.

CHAPTER 5

Comprehensive Review of Karanja & Jatropha Biodiesel Fuelled Diesel Engines

D. D. Palande, N.C.Ghuge, Rakesh Shrivastwa

Article citation information: (2022), *TJES*, Vol. SP-2, pp. 85-96, doi:10.22545/2022/00201

The globe has been compelled to develop other fuels due to emission restrictions, the depletion of oil reserves, and rising prices of petroleum fuels. The rapid development of the automobile sector has resulted in an increase in demand for petroleum-based fuels. Petroleum-based fuels have a finite number of reserves. Biodiesel is a viable alternative fuel and has qualities that are similar to diesel fuel. By combining it with diesel, it can be a suitable fuel in diesel engines. Biodiesel, which is usually made from non-edible oils like jatropha and karanja, has sparked a lot of interest as a diesel engine alternative fuel. When compared to edible oil, non-edible oil are not used in human nutrition and could grow in barren lands. The goal of this study is to provide a review of the performance, combustion, and emission characteristics of jatropha and karanja biodiesel fuels as alternative fuels for diesel engines.

Keywords: Biodiesel, non-edible oil, karanja, jatropha, diesel engine.

5.1 Introduction

It is not a new concept to utilise biodiesel in diesel engines. Rudolph Diesel experimented with using vegetable oil as an alternative fuel [1]. However, because diesel was abundant and vegetable oil fuel was more costly than diesel, as a result, biodiesel research was not taken seriously. Biodiesel's key advantages are its portability and ready availability. It is non-toxic, biodegradable, and ecologically friendly, has a high flash point, and may be mixed with diesel due to similar properties. When vegetable oil is used as a fuel in a diesel engine, there are no serious issues. The transesterification procedure has proven to be one of the most effective ways to accomplish this. Various vegetable oils can be used to make biodiesel. Edible oil is in high demand as a food source. The use of non-edible oils will help to tackle the problem of fuel shortages while also reducing the demand for edible oils. Biodiesel is one of the most important alternative sources for diesel fuel, and it may be manufactured from a range of non-edible plants. [2] Engine trials and experiments have already been performed on a vast variety of nonedible and edible oils. Non-edible oils such as jatropha,karanj, neem, cottonseed, etc., on the other hand, are not acceptable for human consumption. Due to the presence of flavonoid constituents, karajin, the seed of karanja, includes pongam oil, which is bitter and non-edible with an unpleasant flavour. [6] Recent comprehensive analyses of biodiesel synthesis from diverse feedstocks demonstrate that non-edible oils have a number of advantages over edible oils. Biodiesel production from non-edible oil feedstocks can address the challenges of food vs. fuel, as well as environmental and economic concerns about edible vegetables [7]. They can also be planted along trains,

roads, and irrigation canals, as well as on farmers' field boundaries, fallow fields, and public land. Various oils derived from non-edible crop seeds or kernels could be used as biodiesel feedstocks. jatropha [3], karanja [4], and other non-edible oil plants are essential. The oils of jatropha and karanja are the most commonly utilised feedstocks in biodiesel production.Edible oils are not produced in sufficient quantities in many countries to suit human needs, so they must be imported. As a result, biodiesel made from edible oils is substantially more expensive than petrodiesel. India is an intriguing case study in biodiesel generation from edible vegetable oils, where roughly 46% of the required amounts for domestic needs are imported [5]. Balat and Balat argued for non-edible vegetable oils such as jatropha, karanja, and mahua oils, which were briefly discussed in their summary of biodiesel processing development. [9]. Non-edible oilseed crops have numerous advantages including the fact that they require less water and can be grown on marginal or low fertility soil. [13] They can also be cultivated not only from seed but also from cuttings. They offer huge potential for creating rural jobs and lowering CO_2 emissions. The liquid form, portability, rapid availability, renewability, higher heat content, reduced sulphur content, lower aromatic content, and biodegradability are all advantages of non-edible oil. [10] Researchers are looking for new sources since there is a desire for renewable energy sources that are clean, dependable, and economically viable. Non-edible oils like jatropha and karanja are widely available and are simple to turn into biodiesel. A viable replacement for diesel fuel for diesel engines in this situation is biodiesel made from Jatropha and Karanja oil. The various results have been analysed and summarised while using Jatropha and Karanja oil and their mixes as the primary sources of fuel. The main objective of this work is to introduce its derivatives as efficient alternatives to traditional diesel fuels for CI engines.

5.2 Advantages of Karanja and Jatropha Plant

These trees occur in India, the United States, Sri Lanka, Indonesia, Australia, Pakistan, the Philippines, and Malaysia [33]. In India, karanja oil, which can be converted to biodiesel, is available abundantly. Karanja may be grown on every type of soil, including unproductive fields and degraded woods, irrigation channels, and road borders, and it is a simple plant to grow [15]. This plant only requires a small amount of water. Karanja is a medium-sized tree that looks like a neem tree and may be found all over India. Figure 5.1 depicts a karanja tree.

Figure 5.1: *Karanja (Pongamia pinnata) [30].*

With remarkable medical benefits and many uses, the karanja tree has gained a lot of attraction. Karanja wood is widely used as a fuel source and can also be used to make agricultural equipment. Many traditional medicines include the fruit and sprouts, as well as seeds. It is used in the medical field. The oil of the karanja or pongam is useful in agriculture and pharmacy. [14] The oil derived from the karanja seed has received a lot of attention as a diesel engine alternative fuel. The oil of karanja is a pale yellow liquid having antibacterial and medicinal properties. Because of its high phosphorous, nitrogen potash, potassium NPK

content, it also performs well as a fertilizer. [20] Karanja is a 15–25 m tall, medium-sized evergreen, and a fast-growing medium-sized tree. Three to four years after planting, flowering begins and lasts for another four to seven years. Karanja oil contains a number of hazardous compounds that prevent it from being used as cooking oil.[8]

The jatropha is a small to medium-sized tree with a height of 3–5 metres. In some cases, the plants have a height of 8–10 metres. The bark of the tree is smooth and grey when it is chopped. When the stems are dry, they release a whitish-colored liquid latex that hardens and discolours [12]. The Indian government promotes jatropha biodiesel mostly because of its high oil content (66.4%) and ability to thrive in non-agricultural areas. The oil content of the seeds is 35–40%. Jatropha oil is commonly used to produce soap in India and other countries. Other than as a biodiesel feedstock, jatropha oil has a variety of uses, including soap manufacturing and biocides (molluscicides, insecticides, nematicides, and fungicides). Jatropha is a plant that has the ability to produce certain productive assets, the ability to boost village-based industries, and most importantly, the ability to develop wastelands. The methods for generating jatropha oil are straightforward, and the necessary apparatus is easily available. Figure 5.2 shows the jatropha plant.

Figure 5.2: *Karanja (Pongamia pinnata) [30].*

Jatropha curcas can be grown in both deserts and higher rainfall zones. In all forms of waste land, jatropha curcas can be an excellent plant material for eco-restoration. Plant cuttings of Jatropha curcas grow quickly. Jatropha curcas isn't thought to be a suitable forage plant. The plant is resistant to pests and diseases. Jatropha curcas helps to build soil carbon by collecting carbon from the atmosphere and storing it in its woody tissues.It is now the primary fuel for biodiesel manufacturing in poor nations such as India, where yearly production is around 15,000 t [5]. It can grow practically everywhere, on waste, sandy, and saline soils, in a variety of climatic situations, including low and heavy rainfall, as well as cold. Its cultivation is simple, requiring little attention and effort. Its 30 to 50 year healthy life cycle eliminates the need for yearly replanting. The oil content of jatropha varies depending on the species, although it is typically 40–60% in the seeds and 46–58% in the kernels [6]. Some living species, such as the tusser silk worm, feed on jatropha leaves. The leaves are high in protein, but they contain poisonous chemicals that prevent them from being used as cattle fodder. According to studies, the oil's toxic component is found in the alcohol-soluble portion. [11]

5.3 Properties of Karanja and Jatropha biodiesel

The most crucial fuel qualities taken into account while using non-edible biodiesels in diesel engines include density, viscosity, flash point, cetane number, cloud and pour point, and calorific value, among others. Numerous studies have revealed that non-edible biodiesels have favourable fuel characteristics. Consequently, it is required to measure the fuel quality of a few selected biodiesels before employing non-edible-based biodiesels in diesel engines. The fuel properties of karanja and jatropha non-edible biodiesels are shown in Table 1.

Table 1: Fuel properties of various non-edible biodiesel. [8]

Properties	Karanja	Jatropha
Density at40 ^{0}C (kg/m^3)	970-928	901-940
Viscosity at40 ^{0}C (mm^2/s)	27.8-56	24.5-52.76
Flash point (^{0}C)	198-263	180-280
Pour point (0C)	-3 to 6	-3 to 6
Cloud point (0C)	13-15	8-10
Cetane number	45-67	33.7-51
CalorificValue (MJ/kg)	34–38.8	38.20–42.15

5.4 Experimental Investigation on Karanja and Jatropha

Srivastava et al. [16] used a two-cylinder CI engine to test several karanja biodiesel mixes. They found that the thermal efficiency of karanja oil biodiesel is lower than that of diesel, but that the thermal efficiency of blending is higher than that of biodiesel. When comparing 100% biodiesel to a blend of 5%, 10%, 20%, and 30% biodiesel by volume, the thermal efficiencies are higher. They also found that HC, CO, and NOx emissions from the methyl ester of karanja oil were somewhat greater than those from ordinary diesel fuel. Almost all of the properties of the methyl ester of karanja oil are found to be very comparable to those of diesel oil with 5%, 10%, 15%, and 20% blends. The NOx emissions of biodiesel were higher than those of karanja biodiesel blends.Bajpai et al. [17] tested various diesel and karanja oil fuel blends(from 5% to 20%) at varying loads (from 0 to 100 %) to determine brake specific fuel consumption (BSFC), brake thermal efficiency (BTE), and exhaust emissions in a single-cylinder DI constant speed CI engine. It was discovered that a gasoline blend containing 10% karanja oil (K10) improved brake thermal efficiency at 60% load.

Baiju et al. [18] used methyl and ethyl esters of karanja oil to conduct a comparative study of CI engine characteristics. According to the results of the performance test, methyl esters have slightly higher power than ethyl esters. The exhaust emissions of both esters were almost the same. When compared to conventional diesel fuel, NOx emissions from pure biodiesel and diesel–biodiesel fuel blends increased by 10–25% at part loads. NOx emissions, on the other hand, decreased when the engine was fully loaded. Exhaust pollutants such as CO, HC, and smoke were reduced when neat biodiesel and mixes were used.P.K. Sahoo et al. [19] determined the proper blend for optimum performance, minimal emissions, and the best combustion characteristics. This is determined by the feedstock and subsequent biodiesel formulation. According to the findings, biodiesel made from unrefined jatropha, karanja, and polanga seed oils is a viable alternative to diesel.A.K.Agarwal et al. [20] Even without preheating, a single-cylinder diesel engine performed effectively during tests on karanja oil and its blends, requiring no changes to the engine components. Engine efficiency improved marginally when preheated gasoline was used. The engine's thermal efficiency is approximately 30% when using preheated oil blends and 24–27% while using unheated oil blends like K10, K20, and K50. With warmed lower mixes, the BSFC and brake specific energy consumption of the engine improved. Unheated and preheated lower blends (K10 and K20) have lower HC emissions than mineral diesel. As a result, karanja oil blends with diesel up to 50% (v/v) without or with preheating might be used to substitute diesel in CI engines, resulting in fewer emissions and better performance.

By combining karanja oil with Petro-Diesel and preheating the karanja-Diesel blend, Kamal Kishore Khatri et al. [21] have created an experimental setup to minimise the viscosity of the fuel. On a constant speed direct injection C.I. engine, experiments are conducted utilising a Petro-Diesel and a warmed karanja-Diesel blend (in a ratio of 40:60 by volume). On the warmed karanj-Diesel blend, the influence of injection timing is examined. On the basis of the findings, the best injection timing for the karanj-Diesel blend is determined to be 19° BTDC. It has been discovered that a 40 percent substitution of diesel oil by karanj oil works best in the temperature range of 55-60°C, as the viscosity of the blend equals that of pure diesel. As

a result, it is possible to conclude that preheating and blending vegetable oils with diesel can significantly lessen the issues associated with straight vegetable oils, making them a viable option for diesel fuel.P. V. Rao [22] investigated the impact of karanja methyl ester characteristics on diesel engine combustion and nitrogen oxide emissions. The study takes into account the various properties like viscosity, density, calorific value, iodine value, cetane number, and oxygen % of the karanja methyl ester. The engine trials were conducted with karanja methyl ester (with and without preheating) and baseline diesel. Methyl ester had somewhat higher peak pressures and peak heat release rates than diesel fuel. The nitrogen oxides of karanja methyl ester increased by 6% at maximum load, according to the findings. The use of warmed methyl ester results in a considerable reduction in nitrogen oxide emissions..

Atul Dhar et al.[23] conducted trials on direct injection CI engines at various engine loads and constant engine speed with various karanja oil blends (K10, K20, K50, and K100) with mineral diesel in unheated conditions. When compared to mineral diesel, all karanja oil blends have lower fuel consumption and thermal efficiency. The amount of HC emitted was reduced. When compared to diesel, NOx emissions were greater and smoke opacity was lower for all mixes. They recommended using a 20% blend with diesel in a diesel engine.Naveen Kumar et al. [24] compare the performance, emissions, and combustion properties of biodiesel made from non-edible karanja oil. One of the performance characteristics assessed in this study is the brake thermal efficiency of karanja biodiesel with varied compositions at 5%, 10% , 20%, 30%, and 100% with mineraloil. Diesel is one of the performance characteristics assessed in this study. In comparison to diesel, BTE was roughly 3% to 5% lower with karanja biodiesel and its blends. With karanja biodiesel fuel, the amount of unburned hydrocarbons, CO, CO_2, and smoke was reduced. The NOx emissions of karanja biodiesel and its blends, on the other hand, were higher than those of diesel.

A.K. Agarwal et al. [25] tested 10%, 20%, and 50% blends of karanja oil (viscosity-35.98 cSt) with diesel to compare the performance to baseline mineral diesel. It is observed that all karanja oil blends have lower fuel consumption and thermal efficiency. HC emissions were lower for karanja oil blends than mineral diesel. Higher karanja oil mixes resulted in slightly higher CO and NOx emissions. They concluded that a 20 % karanja oil/diesel combination produces satisfactory engine performance.Ting Zhao and Mohammed Takase [26] have focused on the use of non-edible resources. Evergreen multipurpose non-edible plants such as neem, karanja, rubber, and jatropha are widely available and may be grown in a variety of socioeconomic and environmental situations. As a result, this research was conducted to investigate the multipurpose nature of these four non-edible tree species. According to the findings, these four multipurpose non-edible tree species (neem, karanja, rubber, and jatropha) have significant potential as non-edible biodiesel feedstocks for ensuring long-term bioenergy production.L. Karikalan et al.[27] conducted experimental analysis on the CI engine to evaluate the performance and emissions with various compositions of karanja biodiesel and their blends at 5% to 100% with mineral diesel. The HC, CO, CO_2, and smoke levels were reduced when using karanja biodiesel gasoline, but the NOx level increased compared to diesel. The results show that an engine running on karanja biodiesel and its blends with diesel fuel performs similarly to a pure diesel engine.

Rupesh L. Patela et al.[28] studied Transesterification, pyrolysis, micro emulsion, and blending are the four major methods for manufacturing biodiesel that have been researched. The best blend for a diesel engine (B20) is a 20% mixture of karanja oil methyl ester and diesel. The BTE and BSFC of B20 are comparable to those of diesel. When more karanja oil methyl ester is mixed with diesel, CO, HC, and smoke emissions are reduced while NOx emissions are increased.A.M. Ashraful et al. [30] analysed the numerous experimental findings and concluded that CO and HC emissions rise with EGR operation due to the high engine load, but then fall due to the high percentage of biodiesel in fuel blends. CO emissions are reduced by 5.5-35.2% and HC emissions are reduced by 14.91-32.28% as a result of the high biodiesel percentage in gasoline blends. NOx emissions rise with increased engine load and biodiesel content in fuel blends, which fall with EGR operation but rise with increased engine load and biodiesel content in fuel blends. In some cases, NOx emissions can increase by 3.29-10.75%. However, in a full load condition, it lowers.

K. Acharya et al. [31] the performance and emission characteristics of a compression ignition engine fueled with warmed karanja oil and its blends (10% and 20%) with diesel were investigated. The viscosity of unheated 10%, 20% mix, and preheated oil has been demonstrated to be appropriate for diesel engines. The performance of blended karanja oil under the above settings, according to the results of the experimental

investigation, is comparable to that of diesel in a diesel engine with no operating concerns. It was also determined that, when compared to diesel and the aforementioned mixes, preheated karanja oil at 120°C can be used in a diesel engine with somewhat inferior performance and emissions.Md. Nurun Nabi et al.[32] discuss the work production of KME in Bangladesh and the characterization of KME (B100) and its blends. B100 and similar blends emit less CO, smoke, and engine noise, but they emit more NOx. When compared to diesel fuel, the B100 reduced CO and smoke emissions by 50% and 43%, respectively, while increasing NOx emissions by 15% using the same fuel. KME reduced CO, smoke, and engine noise while increasing NOx emissions due to the presence of oxygen in its molecular structure.

Y.C. Sharma et.al. [33] studied the production of biodiesel from the karanja tree, which is primarily found in rural India. The biodiesel was created using oil extracted from the tree's seeds. The oil's molecular weight was calculated and found to be 892.7. After that, both acid and alkaline esterification were used to create the final product.L.M. Das et al.[35] carried out studies on non-edible methyl esters generated from jatropha karanja and polanga oil, which were developed and blended with regular diesel containing less than 10 mg/kg sulphur. They used a water-cooled three-cylinder tractor engine with various different fuel blends (diesel, B20, B50, and B100). It is found that a 50% jatropha biodiesel and diesel combination produces the most power boost at rated speed. For all biodiesel mixes, brake specific fuel consumption increases with speed. L.M. Das and P.K. Sahoo [36] Biodiesel made from oil crops has the potential to be a renewable and carbon-neutral substitute for petroleum fuels. Biodiesel is a chemical compound made up of monoalkyl esters of long-chain fatty acids generated from renewable feedstocks such as vegetable oils and animal fats. The viscosity and freezing point of biodiesel increase with the length of the carbon chain and decrease with the length of the double bond chain.

K. Pramanik [37] studied jatropha curcas oil and efforts were made to reduce the viscosity in order to make it suitable for use in a CI engine. The viscosity of vegetable oil was significantly reduced when it was diluted with diesel in various amounts. The viscosity of the blended products, including 70% and 60% vegetable oil, got close to that of diesel at temperatures of 70–75°C and 60–65°C. Acceptable braking thermal efficiency and SFCs were achieved with blends containing up to 50% jatropha oil. Following the engine tests, it was discovered that up to 50% jatropha curcas oil can be used as a diesel alternative in a CI engine without producing severe complications.Deepak Agarwal et al. [38] conducted an experiment on the measuring of jatropha oil viscosity at different temperatures in the range of 40–100°C to evaluate the performance of the CI engine with preheated jatropha oil. The use of waste heat from exhaust fumes to warm jatropha oil (JO) is sufficient to reduce viscosity to levels comparable to diesel fuel.When compared to clean jatropha oil, warmed JO had lower BSFC and exhaust gas temperatures. Heated jatropha oil has a better thermal efficiency than raw jatropha oil. Preheated jatropha oil had CO_2, CO, HC, and smoke opacity that were comparable to diesel fuel. They came to the conclusion that heating jatropha oil in CI engines can be employed in rural regions for agricultural and irrigation purposes.

Jindal et al. [39] performed the trial with three values of injection pressure and compression ratio. The engine's best performance is achieved at 250 bar injection pressure and a compression ratio of 18, where BSFC improves by 10% and BTE improves by 8.9%.The emissions of HC, NOx, smoke opacity, and exhaust temperature are lower with pure bio-diesel than with diesel fuel for all combinations of compression ratio and injection pressure.Hao Chen et al. [40] studied the combustion process and temperature, biodiesel properties, and engine operation circumstances that have a large impact on NOx emissions. The NOx emissions of biodiesel are lower than those of diesel for low loads and low and medium engine speeds. At medium and high loads, the BTE of the B100 is higher than that of the D100, and the difference grows with engine load. Between B100 and D100, the rise in NOx emissions increases with engine load. The main influencing factors are engine loads, engine speeds, and biodiesel characteristics. The impact of these parameters on NOx emissions is not isolated, but rather complex and interacting.

Determine the acceptability of jatropha curcas oil (unheated and warmed) as an extended fuel for CI engines, as well as the engine's performance and emission characteristics, are the main objectives of this study by Bhupendra Singh Chauhan et al. [41]. In a performance and emission study of preheated jatropha oil on CI engines, the ideal fuel input temperature was found to be 80°C when considering BTE, and gaseous emissions in a performance and emission study of preheated jatropha oil on CI engines. As the percentage

of biodiesel in the diesel–biodiesel blend increases, HC emissions drop. When compared to diesel fuel, increasing the percentage of biodiesel reduces HC emissions by 14.91-27.53%. HC emissions were found to be lower at full load. As the amount of biodiesel in the blend increases, CO emissions decrease by 6.51-12.32%. CO emissions are reduced as compared to diesel fuel. CO emissions are reduced by 10–40% when the system is fully loaded. The increase in CO emissions is noted as the load percentage increases. NOx emissions can rise by 3.29-10.75% in some cases. However, at maximum load, it drops by 5–10%. The opacity of the smoke decreases as the percentage of biodiesel in the blend increases, but increases as the load increases. [27,43].F.K. Forson et al. [42] examine the performance of jatropha oil and its blends with diesel in a single-cylinder DI diesel engine. It was observed that pure jatropha, pure diesel, and mixes of jatropha and diesel oil all operated similarly and had broadly similar emission levels under identical operating conditions. The most important conclusion is that a 97.4% diesel/2.6% jatropha fuel blend produces the greatest brake power and thermal efficiency, as well as the least specific fuel consumption.

Paul et al. [44] studied the numerical and experimental performance of JOME fuelled with a twin-cylinder diesel engine and found that the thermo-physical properties of JOME, such as density, cetane number, flash point, and fire point, are higher than those of diesel fuel. The brake thermal efficiency of jatropha biodiesel is less than diesel fuel. The particulate matter and smoke emissions were all lowered, but there was an increase in NOx emissions [40]. The acceptability and long-term viability of jatropha biodiesel in diesel engines were investigated by Kuber Singh Mehra et al. [45]. BTE increases when braking power increases for the complete combination of fuels. The maximum thermal efficiency of pure diesel (B0) is 29.8%, while the maximum thermal efficiency of pure biodiesel (B100) is 19.2%. As the percentage of biodiesel in blends grows, NOx emissions rise. Biodiesel with a 10% blend (B10) produces a product that is remarkably similar to pure diesel. While hydrocarbon emissions have decreased, NOx emissions have risen as the percentage of biodiesel in various blend compositions has grown. A mixture of 10-20% jatropha biodiesel and mineral diesel (B10 and B20) has been discovered to be suitable for use as a fuel in CI engines. The benefits of employing non-edible oils in biodiesel production are demonstrated by Ivana B. Bankovic-Ili et al. [46]. Under low loads and low and medium engine speeds, biodiesel produces a slight reduction in NOx emissions when compared to diesel. On the basis of biodiesel combustion characteristics, a full experimental investigation of NOx emission was carried out. At low loads and medium speeds, the negative effects of high viscosity and distillation temperature on the spray quality and homogeneity of the air fuel mixture are obvious. Biodiesel emits less NOx than diesel because it has a lower BTE and combustion temperature..

Anu Kumar Das et al. [47] offer a comparative analysis of jatropha curcas-based insulating oil based on experimental results from previous investigations, as well as the current state and future development needs. Jatropha curcas oil is non-edible, so it won't add to the food scarcity, and the jatropha plant is less susceptible to weather extremes. In terms of thermal capability, the results of this study reveal that jatropha curcas oils have high thermal stability. However, the long-term performance of the jatropha Curcas oil must be investigated in order to learn more about its material compatibility, partial discharge behaviour, stray gassing tendencies, and ageing performance.According to Dhandapani Kannan et al. [48] a 20% biodiesel blend has a 0.09-2.64% higher engine power than diesel fuel. Engine output decreases as the percentage of biodiesel in the fuel blend rises. At medium engine speeds, BTE improves minimally, whereas at high engine speeds, BTE improves by 0.1–6.7%.

Diesel engines can operate with minimal to no changes when using biodiesel made from vegetable and animal fats. Compared to diesel fuel, biodiesel emits less CO, HC, and PM but more NOx. Although biodiesel creates more CO_2 than other fuels, it is regarded as carbon-neutral to offset the CO_2. According to research, because they are less compressible, more viscous, and have a higher cetane number than diesel fuel, most biodiesel fuels (with the exception of eucalyptus and pine oil) and their mixes with diesel have an earlier start of combustion and a shorter ignition delay. P. Tamilselvana et al. [49]. It is also concluded that diesel engines can operate with minimal to no modifications using biodiesel blends up to 20%.M.Suresh et al. [50] examined the performance and emission studies of biodiesel on VCR. Without requiring any modifications, biodiesel may replace diesel in the VCR engine. By switching to a VCR engine, you can get improved performance, lower emissions of dangerous gases including HC, CO, CO_2, and NOx, and faster combustion. It was amply demonstrated that VCR engines have the ability to boost combustion efficiency,

decrease ignition latency, and deliver higher compression ratios under a variety of loads. According to the reviews listed above, it was discovered that the VCR engine has greater management at peak cylinder pressure, which lowers fuel consumption. Other benefits of using biodiesel in the VCR engine include a decrease in power usage and noise levels, among others.

5.5 Conclusion

This paper provides a detailed overview of the substantial contributions made by researchers working on biodiesel derived from non-edible oil, particularly karanja and jatropha, and its blend with diesel.Several investigations were conducted to measure the power output, BSFC, and BTE of an engine running on non-edible oil-based biodiesel. With brake thermal efficiency and brake specific fuel consumption approximately comparable to diesel, the performance of an engine running on a blend fuel (20% biodiesel and 80% diesel) was found to be superior to that of other blend fuels. The most optimal Karanja/diesel blend, B20, has BTE and BSFC levels that are practically identical to diesel. According to the findings of multiple experiments, using karanja biodiesel in CI engines can decrease CO, HC, and smoke emissions while increasing NOx emissions. With enhanced blending, CO, HC, and smoke emissions are decreased while NOx emissions are raised. Jatropha biodiesels showed higher BSFC but better thermal efficiency than other biodiesels in most circumstances. The thermal efficiency of jatropha oil blends was also shown to be comparable to diesel. In comparison to petroleum diesel, it has been discovered that jatropha biodiesel and its mixes with diesel fuel generally cause an increase in NOx emissions and a decrease in HC, CO, and PM emissions. Jatropha biodiesel performs satisfactorily when utilised in C.I. engines. When diesel fuel is blended with 20% jatropha biodiesel, a comparable improvement in fuel efficiency is seen. Numerous studies using jatropha biodiesel reveal variations in brake thermal efficiency (BTE) and brake specific fuel consumption (BSFC). In some circumstances, mixed biodiesel offers superior brake power (BP) to regular diesel fuel. Some research found that Jatropha biodiesel use was associated with a reduction in BTE. Engine power falls as the percentage of biodiesel in the fuel blend rises. BTE marginally improves for blends of B20. But as the percentage of jatropha biodiesel in the fuel blend rises, BTE falls. The majority of studies have found significant NOx emissions. Meanwhile, several authors have verified that using biodiesel results in fewer NOx emissions. The results are better with heated jatropha and karanja oil. More research is needed on long-term storage of karanja oil-diesel blends, NOx emissions reduction, and engine wear. Diesel engines may operate with minimal to no modification when using biodiesel blends up to 20%. According to the literature, the majority of engine tests are performed on single-cylinder diesel engines, with very few on multicylinder engines. In addition to engine performance and emission characteristics, the properties of non-edible biodiesel demonstrate that there is a high possibility of manufacturing biodiesel from non-edible sources in the future. Non-edible biodiesel has good potential as an alternate fuel for diesel engines in the near future.

Abbreviations

BSFC: Brake specific fuel consumption
BTE: Brake Thermal Efficiency
BP:Brake Power
DI:Direct injection
CI: Compression ignition
K10:10 % karanja oil
B10: Biodiesel with a 10% blend
B100: Pure biodiesel
D100:Pure diesel
BTDC: Before top dead center

CO: Carbon monoxide
HC: Unburned hydrocarbons
NOx: Oxides of nitrogen
JOME: Jatropha methyal ester
JO: Jatropha oil
KME: Karanja methyl ester
VCR :Variable compression ratio

Funding: This research received no external funding.

Conflicts of Interest: The authors declares no conflict of interest.

Authors Contributions: Authors contributed equally.

References

1. AyhanDemirbas(2008).*Biodiesel A Realistic Fuel Alternative for Diesel.* Engines.Springer.
2. S.Madiwalea,V. Bhojwani (2016). An Overview on Production, Properties, Performance and Emission Analysis of blends of Biodiesel. *Procedia Technology,* 25, 963 – 973.
3. Tiwari AK, Kumar A, Raheman H. (2007). Biodiesel production from jatropha oil (Jatropha curcas) with high free fatty acids: an optimized process. *Biomass Bioenergy,* 31,569–75.
4. Naik M, Meher LC, Naik SN, Das LM (2008). Production of biodiesel from high free fatty acid karanja (Pongamia pinnata) oil. *Biomass Bioenergy,* 32,354–7.
5. Jain S, Sharma MP. (2010) Prospect of biodiesel from Jatropha in India: a review. *Renew Sustain Energy Rev,* 14,763–71.
6. Kumar A, Sharma S. (2011) Potential non-edible oil resources as biodiesel feedstock: an Indian perspective. *Renew Sustain Energy Rev,* 15,1791–800.
7. Gui MM, Lee KT, Bhatia S. (2008). Feasibility of edible oil vs. non-edible oil vs. waste edible oil as biodiesel feedstock. *Energy,* 33,1646–53.
8. Soo Young No (2011). Inedible vegetable oils and their derivatives for alternative diesel fuels in CI engines: a review. *Renew Sustain Energy Rev,* 15,131–49.
9. Balat M, Balat H. (2010). Progress in biodiesel processing. *Appl Energy,* 87(6),1815–35.
10. Srivastava PK. Reply to letter by J.C. Jones (2008). Methyl ester of karanja oil as an alternative energy source" Letter to the Editor. *Fuel,* 87,2846.
11. King AJ, He W, Cuevas JA, Freudenberger M, Ramiaramanana D, Graham IA. (2009). Potential of Jatropha curcas as a source of renewable oil and animal feed.*J Exp Bot,* 60,2897–905.
12. Ariza-Montobbio P, Lele S.(2010). Jatropha plantations for biodiesel in Tamil Nadu, India: viability, livelihood trade-offs, and latent conflict. *Econ,* 70,189–195.
13. A.E. Atabani a,n , A.S. Silitonga (2013). Non-edible vegetable oils: A critical evaluation of oil extraction, fatty acid compositions, biodiesel production, characteristics, engine performance and emissions production.*Renewable and Sustainable Energy Reviews,* 18, 211–245.

14. Abhishek Sharma .NutanKaushik (2020). HimanshiRathoreKaranja (Milletiapinnata (L.) Panigrahi): a tropical tree with varied applications", Phytochem Rev.
15. Bobade S.N.1 and KhyadeV.B. (2012) .Detail study on the Properties of PongamiaPinnata (Karanja) for the Production of Biofuel. *Research Journal of Chemical Sciences,* 2(7), 16-20
16. Srivastava P.K.and Madhumita Verma (2008). Methyl ester of karanja oil as an alternative renewable source energy. *Fuel*, 87, 1673–1677.
17. S. Bajpai, P.K. Sahoo, L.M. Das (2009). Feasibility of blending karanja vegetable oil in petro-diesel and utilization in a direct injection diesel engine. *Fuel,* 88, 705–711.
18. B. Baiju, M.K. Naik, L.M. Das (2009). A comparative evaluation of compression ignition engine characteristics using methyl and ethyl esters of Karanja oil. *Renewable Energy,* 34, 1616–1621.
19. P.K. Sahoo, L.M. Das (2009). Combustion analysis of Jatropha, Karanja and Polanga based biodiesel as fuel in a diesel engine. *Fuel,* 88,994–999.
20. Avinash Kumar Agarwal , K. Rajamanoharan (2009). Experimental investigations of performance and emissions of Karanja oil and its blends in a single cylinder agricultural diesel engine. *Applied Energy,* 86, 106–112.
21. Kamal Kishore Khatri , Dilip Sharma (2010). Investigation of Optimum Fuel Injection Timing of Direct Injection CI Engine Operated on Preheated Karanj-Diesel Blend. *Jordan Journal of Mechanical and Industrial Engineering*, 4, 629 – 640.
22. P. V. Rao (2011). Effect of properties of Karanja methyl ester on combustion and NOx emissions of a diesel engine. *Journal of Petroleum Technology and Alternative Fuels,* Vol. 2(5), 63-75.
23. Atul Dhar, Avinash Kumar Agarwal (2014). Performance, emissions, and combustion characteristics of Karanja biodiesel in a transportation engine. *Fuel,* 119, 70-80.
24. Bhupendra Singh Chauhan Naveen Kumar (2013). A study on the performance and emission of a diesel engine fueled with Karanja biodiesel and its blends. *Energy*, 56.
25. Avinash Kumar Agarwal, AtulDhar (2013). Experimental investigations of performance, emission and combustion characteristics of Karanja oil blends fuelled DICI engine. *Renewable Energy,* 52 ,283-291.
26. Mohammed Takase a, Ting Zhao (2015). An expatriate review of neem, jatropha, rubber and karanja as multipurpose non-edible biodiesel resources and comparison of their fuel, engine and emission properties. *Renewable and Sustainable Energy Reviews,* 43,495–520.
27. L. Karikalan And M. Chandrasekaran (2015). Karanja Oil Biodiesel: A Potential Substitution For Diesel Fuel In Diesel Engine Without Alteration. *Arpn Journal Of Engineering And Applied Sciences,* 10, No. 1.
28. Rupesh L. Patela,,C.D. Sankhavarab (2017). Biodiesel production from Karanja oil and its use in diesel engine: A review. *Renewable and Sustainable Energy Reviews,* 71,464-474.
29. Abhishek Sharma.NutanKaushik (2020). HimanshiRathoreKaranja (Milletiapinnata (L.) Panigrahi): a tropical tree with varied applications", Phytochem Rev.
30. A.M. Ashraful , H.H. Masjuki, M.A. Kalam (2014). Production and comparison of fuel properties, engine performance, and emission characteristics of biodiesel from various non-edible vegetable oils: A review. *Energy Conversion and Management,* 80, 202–228.
31. S. K. Acharya, R. K. Swain,M. K. Mohantyand A. K. Mishra (2014). Preheated and Blended Karanja Oil as Diesel Engine Fuel. *Energy Sources Part A,* 36:1325–1334.
32. Md. Nurun Nabi, S.M. Najmul Hoque, Md. Shamim Akhter (2009). Karanja (Pongamia Pinnata) biodiesel production in Bangladesh, characterization of karanja biodiesel and its effect on diesel emissions. *Fuel Processing Technology*, 90, 1080–1086.
33. Y.C.Sharma, B.Singh (2008). Development of biodiesel from karanja, a tree found in rural India. *Fuel,* 87,1740-1742
34. Sanghoon Lee, Chang Sik Lee (2017). Sungwook Park Spray characteristics, engine performance and emissions analysis for Karanja biodiesel and its blends. *Energy,* 119, 138-151.

35. P.K. Sahoo, L.M. Das (2009). Comparative evaluation of performance and emission characteristics of jatropha, karanja and polanga based biodiesel as fuel in a tractor engine. *Fuel,* 88, 1698-1707.

36. P.K. Sahoo, L.M. Das (2009). Process optimization for biodiesel production from Jatropha, Karanja and Polanga.*Fuel,* 88, 1588-1594.

37. K. Pramanik (2003). Properties and use of jatropha curcas oil and diesel fuel blends in compression ignition engine. *Renewable Energy,* 28, 239–248.

38. Deepak Agarwal,Avinash Kumar Agarwa l(2007). Performance and emissions characteristics of Jatropha oil (preheated and blends) in a direct injection compression ignition engine. *Applied Thermal Engineering,* 27, 2314–2323.

39. S. Jindal,B.P. Nandwana, N.S. Rathore , V.Vashistha (2010). Experimental investigation of the effect of compression ratio and injection pressure in a direct injection diesel engine running on Jatropha methyl ester. *Applied Thermal Engineering,* 30, 442–448.

40. Hao Chen,Bin Xie, Jinqiu Ma, Yisong Chen (2018). NOx emission of biodiesel compared to diesel: Higher or lower? . *Applied Thermal Engineering,* 137, 584–593.

41. Bhupendra Singh Chauhan ,Naveen Kumar,Yong Du Jun,Kum Bae Lee (2010). Performance and emission study of preheated Jatropha oil on medium capacity diesel engine. *Energy,* 35, 2484-2492.

42. F.K. Forson , E.K. Oduro, E. Hammond-Donkoh (2004). Performance of jatropha oil blends in a diesel engine. *Renewable Energy,* 29 ,1135–1145.

43. Chauhan BS, Kumar N, Cho HM (2012). A study on the performance and emission of a diesel engine fueled with Jatropha biodiesel oil and its blends. *Energy,* 37(1),616–22.

44. Gaurav Paula, Ambarish DattabBijan Kumar MandalcAn (2014). Experimental and Numerical Investigation of the Performance, Combustion and Emission Characteristics of a Diesel Engine fueled with Jatropha Biodiesel. *Energy Procedia,* 54, 455 – 467.

45. Kuber Singh Mehra, Satyendra Singh, Amit Kumar Singh, Himanshi Kharkwal , Shwetank Avikal (2021). Performance, energy, emission and cost analysis of Jatropha (Jatropha Curcas) oil as a biofuel for compression ignition engine. *Materials Today: Proceedings*,43, 348-354.

46. Ivana B. Bankovic etal (2012). Biodiesel production from non-edible plant oils. *Renewable and Sustainable Energy Reviews,*16, 3621–3647.

47. Anu Kumar Das, Aniket Shivaji Chavan , Dayal Ch. Shill , Saibal Chatterjee (2021). Jatropha Curcas oil for distribution transformer – A comparative review. *Sustainable Energy Technologies and Assessments*,46, 1012-59.

48. Dhandapani Kannan,Senthilkumar Pachamuthu (2012). Theoretical and experimental investigation of diesel engine performance, combustion and emissions analysis fuelled with the blends of ethanol, diesel and jatropha methyl ester. *Energy Conversion and Management,* 53, 322–331.

49. P. Tamilselvana , N. Nallusamy , S. Rajkumar (2017). A comprehensive review on performance, combustion and emission characteristics of biodiesel fuelled diesel engines. *Renewable and Sustainable Energy Reviews,* 79, 1134–1159.

50. M. Suresh, C.P. Jawahar,Arun Richard (2018). A review on biodiesel production, combustion, performance, and emission characteristics of non-edible oils in variable compression ratio diesel engine. *Renewable and Sustainable Energy Reviews,* 92, 38–49.

About the Authors

Dr.D.D.Palande is currently working as an Associate Professor in the Mechanical Engineering Department at Matoshri College of Engineering and Research center Nasik. He is B.E (Mechanical) M.E.(Thermal Power Engineering) and Ph.D (Mechanical Engineering). He is having 21 years of experience in teaching and administration. He is a member of Professional Societies such as the Institution of Engineers (India), and Indian Society for Technical Education (ISTE), He has published many research papers in various national and international Journals.

Dr.Nilesh C.Ghuge is currently working as an Associate Professor in the Mechanical Engineering Department at Matoshri College of Engineering and Research center Nasik. He is B.E (Mechanical) M.E.(Mechanical Engineering) and Ph.D. (Mechanical Engineering). He is a member of Professional Societies such as the Institution of Engineers (India), and Indian Society for Technical Education (ISTE), He is having 22 years of experience in Industry and teaching and administration. He has published many research papers in various national and international Journals.

Dr.Rakesh Shrivastva is currently working as Professor in Electrical Engineering Department at Matoshri college of Engineering and Research centre Nasik

CHAPTER 6

Energy and Carbon Loss Management in an Electric Bus Factory for Energy Sustainability

Özcan Yavaş, Efe Savran, Berrak Erol Nalbur, Fatih Karpat

Article citation information: (2022), *TJES*, Vol. SP-2, pp. 97-110, doi:10.22545/2022/00207

Increasing energy need brings people one step closer to energy saving and alternative sources. The search for reliable and sustainable resources also contributes greatly to technological progress. Thanks to advanced technology, energy use becomes more efficient. However, the concept of sustainability emerges in the field of energy as in other sectors. It is expected that electric vehicles, which have started to increase in interest in recent years, will make a positive contribution to issues such as environmental protection and sustainable energy. In addition, production centers for electric vehicles should also be sustainable and sensitive to carbon emissions. In this study, energy and carbon loss assessment was carried out in an electric bus manufacturing factory. With the help of linear regression analysis, the data of the last 3 years were evaluated. Moreover, as a result of internal audits, energy loss points were determined. As a result of this study, sustainability, carbon loss, and energy management issues in an electric vehicle production factory were evaluated and guiding qualities for today's and future technology companies were revealed.

Keywords: Energy management, carbon loss, sustainability, energy sources, electric bus.

6.1 Introduction

The increase in energy demand due to the growth in human population all over the world drives people to both find new renewable energy types and decrease the usage of energy. Besides the energy demand, the scarcity of conventional energy sources can play a significant role in energy research. While applying various energy decrease methods, the phenomenon of energy efficiency appears. The phenomenon of energy efficiency can be defined as a decrease in energy usage with unchanged financial positivity, prosperity, and compromise in products [1]. Alternative energy sources that today's research can be sorted as wind, water, solar, natural gas, petroleum, wave, hydrogen, and geothermal. Each of these energy sources produces the electricity that is recent years' favorite energy type. Sustainability, the strong dominator of the 21st century forces several areas such as energy, design, manufacturing, and automotive to be more flexible and innovative. Besides the beneficial results of being sustainable, humanity and a livable environment are strong triggers of this phenomenon. The energy sector looking for new sources that are renewable and sustainable, designers take into account long-live products and also they pay attention to new and sustainable designs, the automotive sector has much know-how on lightweight cases so mass reduction corresponds to less CO2 release which

is a more sustainable product. A case study [2] that is focused on the lightweight of a commercial seat is a reliable example of this issue. This weight reduction study benefited from the finite element method and innovative design technics with state-of-art materials. Correlation of different materials and thickness variation was conducted to get light and reliable seats. Results of this study revealed 20 % more light seats. Thus, 20% weight reduction will be achieved in the vehicle in which this seat is mounted, thus reducing overall fuel consumption and reducing carbon emissions in terms of the environment. Another study [3] aimed at light door hinges for the vehicle. This study is also related to lightweight vehicles. Three different aluminum hinges were compared to steel one in finite element analysis. As a result of analyzes carried out without compromising safety standards, 65% weight reduction was achieved with aluminum alloy. The same as the previous example, reduced weight provides more sustainable products.

Energy sources that rely on fossil fuels are the main environmental contaminators and they cannot promise the future. In view of sustainability, renewable energy sources such as wind and water are good candidates for this issue. Electric vehicles are in recent years the most discussed topic. Besides the usage of these vehicles providing sustainable energy consumption, the meeting of the energy demand of these vehicles from renewable sources seems "Yin-Yang" figure. Otherwise, the dream of a clean environment, energy sustainability, and low carbon release cannot come true. In view of sustainability, EPI [4] sorts 180 countries on various performance indicators and releases annual environmental performance reports. These annual reports are like exam papers for countries and are good for the process of taking action for sustainability. While stating sustainability, it is good to mention that climate change is also a significant result of this. United Nations meet for climate change (UNFCCC) [5] and this is called as COP. The last meeting COP 26 was held in England in 2021 so this meeting is the continuation of COP 21 that is the meeting which is the Paris agreement [6] was signed by countries. In this meeting, countries saw their status since Paris agreement was signed.

The aforementioned climate change is associated with carbon emissions. Carbon emission is defined as the diffusion of carbon dioxide that the production of combustion reaction to the atmosphere [7]. Also, it is stated that carbon dioxide emission is associated with financial growth, energy consumption, and population growth [7]. Regardless of its type, energy use is essential in every production process. In general, electricity is the main supporting energy type for production areas. The source of the energy used in production should be the responsibility of the producers. There is also a production history of internal and external manufactured goods. Obtaining the energy used at any stage of this production process has the potential to release carbon to the environment. Monthly or annual audits are a good trigger for carbon emission consciousness in factories.

Electric vehicles generally known, are used since 19th century. Although vehicles with an internal combustion engine in early times took over the electric vehicles by facilities of mass production and financial prons, electric vehicles started to appear again due to sustainable environment worries. Some features such as quietness, user-friendliness, environmentalist, and high efficiency make electric vehicles more attractive when compared to vehicles with internal combustion engines. Commercial vehicles like public transportation vehicles or trucks play a critical role in the transportation of people and goods. Due to their high fuel consumption, their carbon emission and harmfulness to the environment are much higher than passenger cars. From this perspective, electrification of commercial vehicles is more beneficial and effective for both decrease in carbon emission and an increase in energy usage efficiency and sustainability.

In the literature, there are several energy management and efficiency-related study. Özer and Güven [1] studied on energy efficiency of dyeing factories. Evaluation of production and energy consumption by regression analysis was conducted. As a result of the improvement of this study, the efficiency of energy consumption was increased by 49%. Also, it is worth mentioning that production planning show 23% decrease in energy consumption. Katchasuwanmanee, Bateman, and Cheng [8] studied on energy management in an automotive manufacturing plant. For this, they examined temperature in the manufacturing area, evaluated HVAC control system, observed manufacturing information, and simulated smart energy management. By conducting these, it was revealed that simulation of energy management reduced the energy consumption in summer by 15% and in winter by 10%. Öztürk [9] studied on energy consumption in the production of textile goods. He states that electricity, oil, LPG, and coal are energy sources for the textile industry. He

highlighted the electricity usage for production, lighting, and HVAC. Results of this study state that increase in electric consumption and heat energy when there is an increase in production. The author states that by these results, an estimation can be provided for any production level and a decrease in production cost for any energy saving. Taner, Sivrioğlu, Topal, Dalkılıç, and Wongwises [10] studied on energy management in sugar production. They generally focused on energy consumption analysis, production quantity, and energy efficiency. To achieve this energy management, they production and energy consumption were controlled, and then energy usage was obtained. A numerical reliability study was conducted. In the results of this study, energy usage and production quantities of the last 3 years was listed and evaluated for finding the relation between energy consumption and sugar production. It has been seen that energy-saving results will be achieved for this study with energy optimization.

Energy consumption graphics constantly hit milestones every year. Turkish Ministry of Energy and Natural Sources [11] declares that electric consumption went up by 8,1% as 331,5 billion kWh in 2021 according to 2020. This consumption will be 370 kWh in 2025 and 591 kWh in 2040 according to a prediction study [11]. Such a significant increase in consumption will bring along the growth in the need for energy production. Thus, both energy production methods should rely on renewable sources, and energy consumption should be taken into account. Therefore, energy consumption and efficiency are the included issues in this study.

In 2011, International Standards Organization (ISO) released the ISO 50001, which describes the features and implementation of the energy management system [12], [13]. ISO 50001 is also referring to other standards such as ISO 9001 and ISO 14001 [12]. This standard was designed regardless of the conditions of the company to be applied and does not impose a set target for the optimization of energy consumption in the company [13]. The company can apply the ISO 50001 standard if it wants to establish a basis for energy management [13]. The energy management standard is created in companies to integrate with production processes and increase energy efficiency. Companies and business partners are expected to reduce energy intensity and carbon emissions in their work environments by using ISO 50001 as a tool [14]. ISO 50001 leads to continuous improvement of consumption efficiency, without specifying an evaluation criterion in terms of energy. at the same time, the specified standard is based on the Plan-Do-Check-Do (PDCA) framework in energy management [15]. This study includes specific energy consumption, specific carbon consumption, and examination of energy–carbon loss in electric bus manufacturer companies. Energy & carbon consumption predictions for 2022 were accomplished by the regression analysis. Carbon reduction studies are very important for electrified commercial vehicles so carbon prediction and sustainability management will be acquired with the help of advanced analysis methods. This study is providing a unique aspect of electric vehicle production with the methods mentioned.

6.2 Methodology

The automotive industry has been activated in an industrial area at Bursa since 1999. The specified electric bus manufacturing factory is located in a total area of 200.000 m2 and a covered area of 96.000 m2 with approximately 1500 workers. This factory produces electric vehicles with welding, painting, and assembly stages at this location. The capacity of the facility is 30.000 vehicles per year.

In this study, the energy consumer points have been detected and have been assigned to energy efficiency projects. Also, the relationship between energy consumption and carbon consumption was reviewed by using linear regression analyses and was detailed with the graph as a cumulative summary (CUSUM). Eventually, Specific Energy Consumption (SEC) was used in all scientific data. This section includes subheadings as Energy Management, Linear Regression analysis, and finding Energy Losses, and carbon Losses respectively. The flow of the methodology can be seen in Figure 6.1.

6.2.1 Energy Management

This study comprises that electric consumption evaluation will be conducted that obtained and evaluated between 2019 and 2021 in electric bus manufacturer factory.

Figure 6.1: *Flow of the methodology.*

In view of usage, two types of sources such as electricity and natural gas were benefited. For this reason, energy values should be calculated for these two different sources separately. In view of energy consumption, SCADA values for the last three years were used with the software of Power Studio. SEC values are an important Key Performance Indicator (KPI) for following the energy consumption of the automotive factory. SEC values can be calculated.

$$SEC = \frac{\mathrm{TotalEnergyConsumption}}{\mathrm{TotalNumberofProduct}} \tag{6.1}$$

In addition, energy efficiency will be calculated at the end of energy projects energy efficiency can be calculated as;

$$Efficiency\% = \frac{\mathrm{consumption_f} - \mathrm{consumption_e}}{\mathrm{consumption_e}} \times 100 \tag{6.2}$$

6.2.2 Linear Regression Analysis

Linear regression analysis is a reliable numerical method to see the energy consumption evaluation and prediction. This method is a modeling type that predicts the desired values by handling easily detectable variables. Variables that were wanted to define should be continuously sorted numerically. Also, it is stated that regression analysis is affected by extreme values and distribution properties [16]. Linear regression analysis is a useful tool to indicate the value correlations and future prediction. Since this study aimed the energy management for electric bus manufacturing, the authors focused on energy consumption per year.

The usage of regression analysis for energy predictions has increased with ISO 50001 EnS. In this study, regression analysis was used to determine the Energy Performance Indicator (EnPI) according to the energy consumption over the last 3 years. For calculating regression analysis, the amount of produced vehicle number was selected as the dependent variable, and energy consumption was preferred as the independent variable.

6.2.3 Finding Energy Losses

This study will be used the loss analysis method in factory dynamics. While creating the loss analysis method 7 energy sub-loss types were determined. They are as;

- Losses due to useless consumption
- Losses due to overconsumption
- Losses due to non-optimization
- Losses due to not using recoverable energy
- Transmission losses
- Transformation losses
- Lack of renewable energy use

A loss collection system was created by Supervisory Control and Data Acquisition (SCADA) and employee cooperation in the factory. Thus, losses and leakages in energy can be prevented immediately.

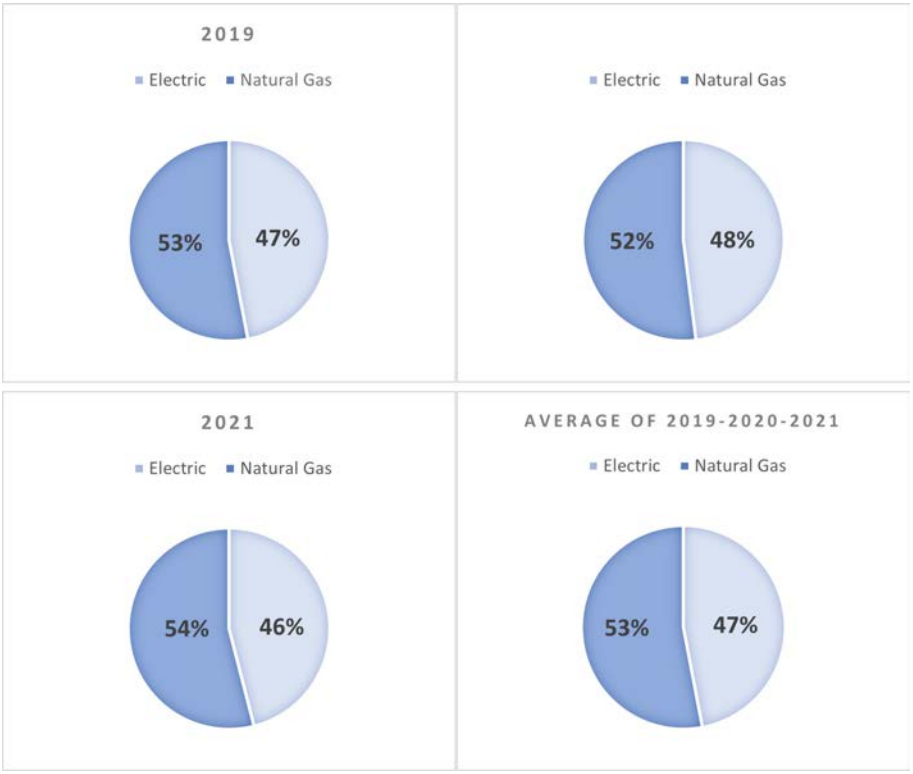

Figure 6.2: *Energy consumption rates between 2019 and 2021.*

6.2.4 Carbon Losses

In this study, the internal methodology of the factory was used for carbon losses as Scope 1 and Scope 2 emissions reduction were followed by associating with energy losses:

$$CO_2 = \sum_{k-1}^{n} Dak\ NCVk\ EFk\ 1 - BRk\ OFk \tag{6.3}$$

In equation 3, parameters as Da, NCV, EF, BR, and OF correspond to Activity of Data, Calorific Value, Emission Factor, Rate of Biomass, and Oxidation Factor.

6.3 Results and Discussion

6.3.1 Energy Management

Energy studies were started with the energy consumption definition including the kind of energy type of the factory. These studies provide the opportunity to the related product and efficiency of energy and carbon emissions. Especially, when the loss analysis and product relationship are determined correctly, energy projects will be prioritized and efficiency will be increased. Thus, the carbon efficiency of electric vehicle producer companies will be increased, and carbon-neutral targets throughout its life cycle will be achieved.

Production mainly depends on two main energy sources that are electricity and natural gas in the factory. Types of energy resources that used in the factory for the last 3 years are given in Figure 6.2.

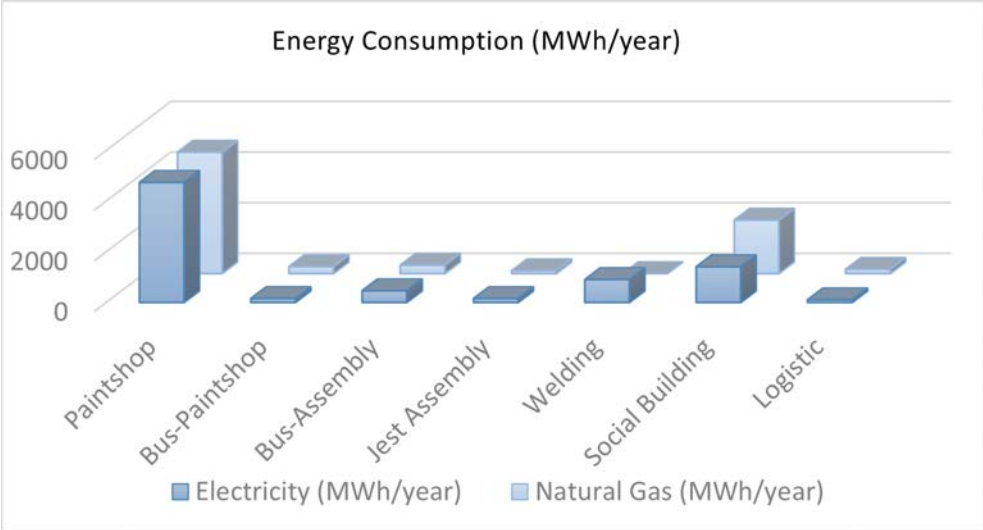

Figure 6.3: *Energy consumption according to units (MWh/year).*

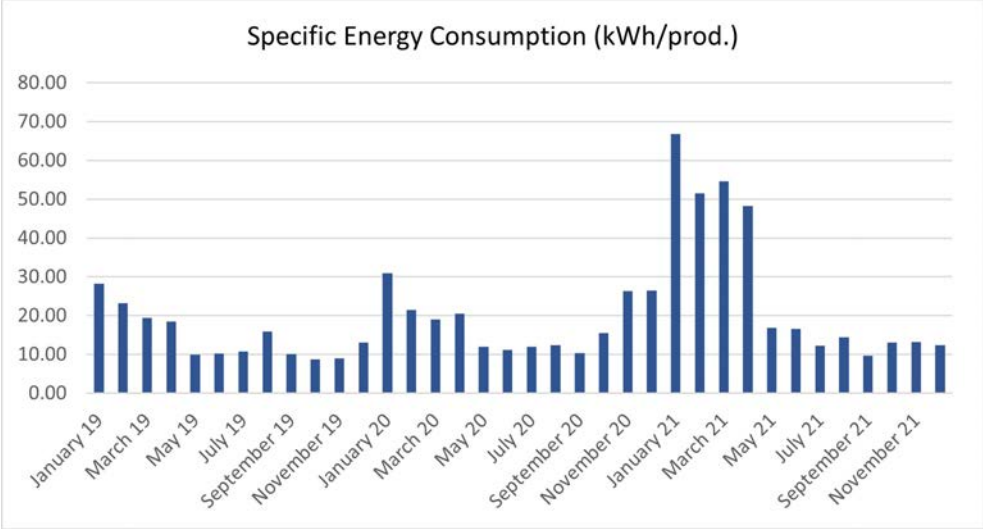

Figure 6.4: *Specific energy consumption (2019 to 2021).*

Total energy consumption may not always show the correct prediction of the energy performance of the factory. Specific Energy Consumption (SEC) is another preferable supporter for this reason. SEC graphics can be seen in Figures 6.3 and 6.4. According to SEC values, the energy and carbon consumption per product are calculated through regression analysis in Figure 6.4 for energy consumption and Figure 6.5 for carbon consumption.

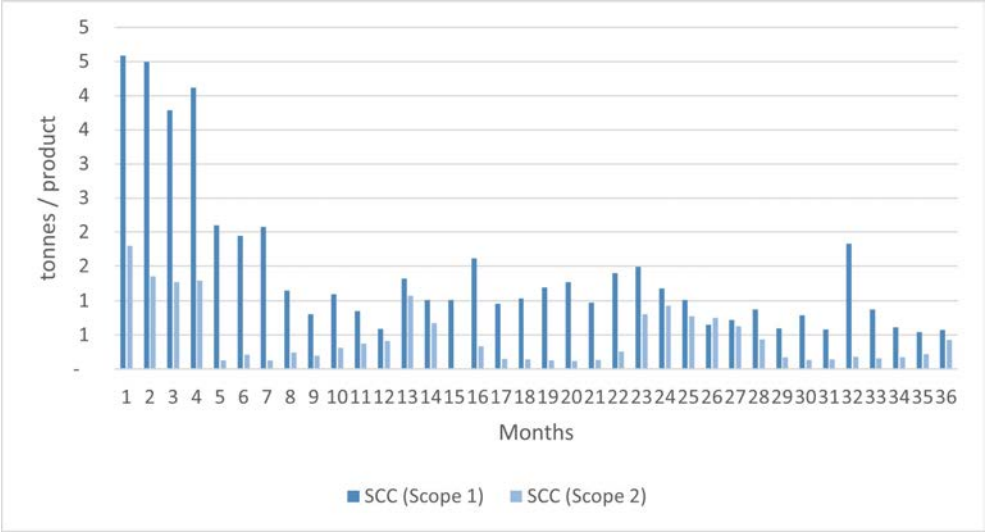

Figure 6.5: *Specific carbon consumption for scope 1 and scope 2 emissions (2019 to 2021).*

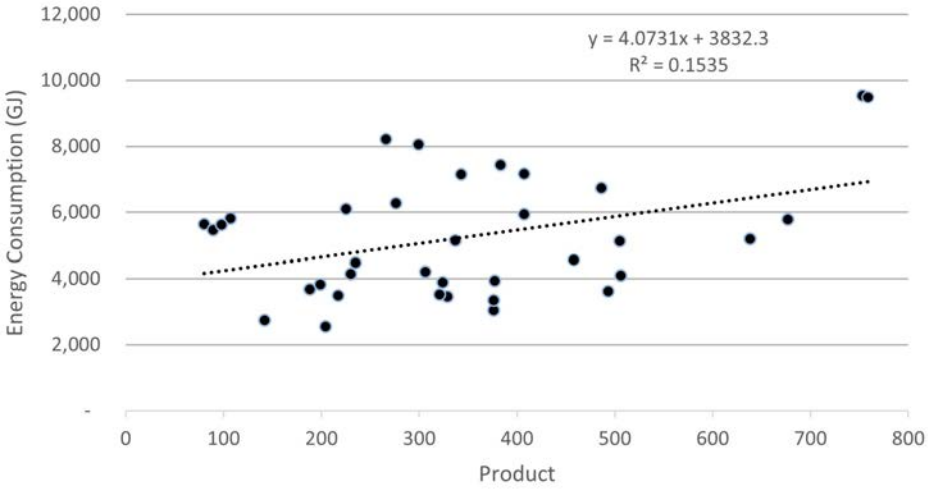

Figure 6.6: *Regression analysis for energy consumption.*

6.3.2 Linear Regression Analysis

The aforementioned regression analysis study results were illustrated in Figures 6.6 and 6.7

In Figure 6.7, it is seen that R2 values for Scope 1 and Scope 2 emissions are quite low (3% and 13% respectively). This shows that direct and indirect carbon emissions in electric bus production are not directly related to the production of the vehicle. For this reason, a carbon loss system has been created. In the carbon loss analysis, it is expected that 'Type 1 – Useless Consumption' and 'Type 7 – Lack of Renewable Energy Use' will be high and these losses are expected to be intervened. Thus, the study was focused on

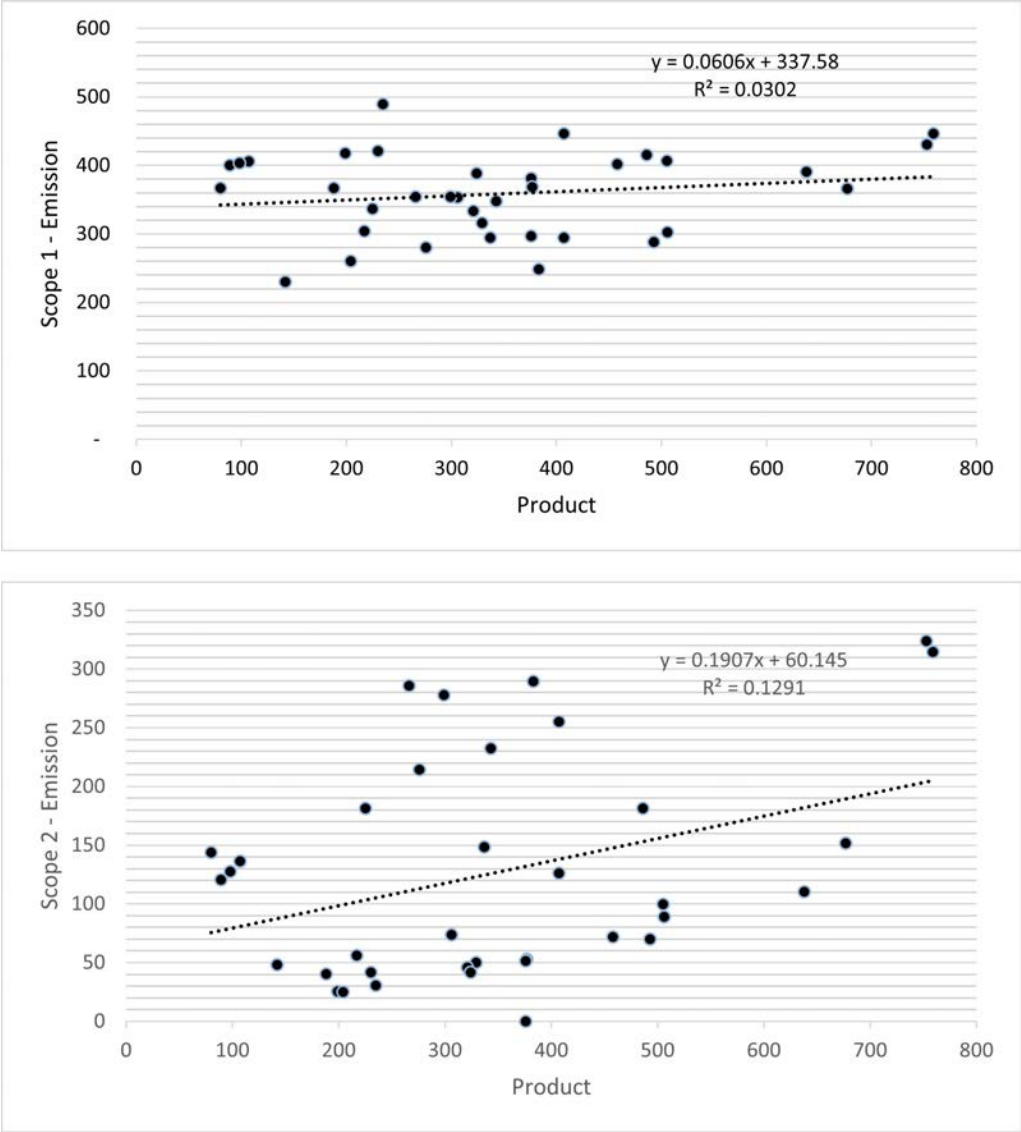

Figure 6.7: *Regression Analysis for Scope 1 Emissions (above) and Scope 2 Emissions (below).*

non-production energy and carbon loss projects.

6.3.3 Energy and Carbon Loss Analysis

When the loss structure for automotive companies is analyzed, energy losses are among the top 10 losses. Energy and carbon losses per product are given in Figure 6.8.

Considering the directions about sustainability, electric vehicle producers should consider carbon tax and other carbon costs. For this reason, in this study, the carbon costs of the energy projects determined for feasibility are included. İdentified carbon costs can be listed as;

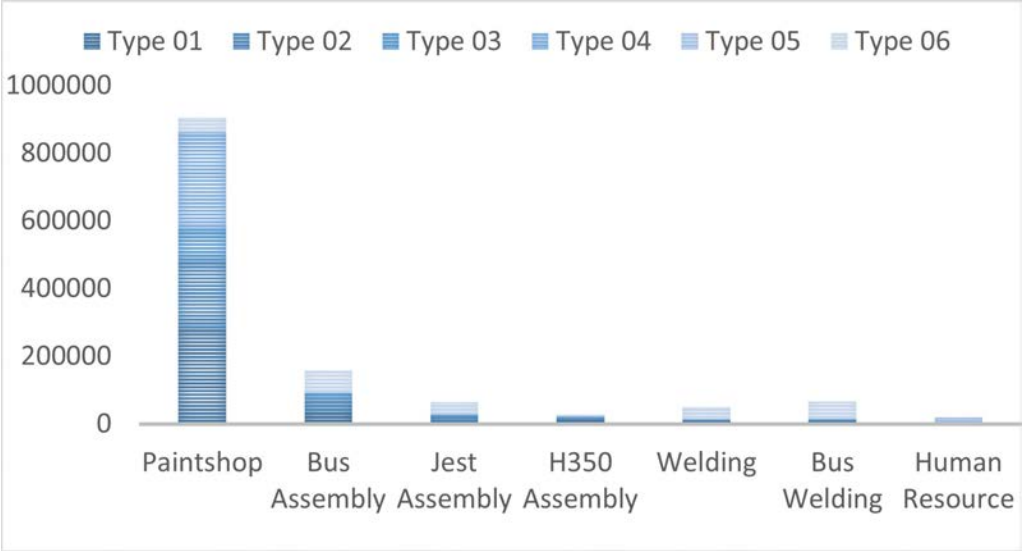

Figure 6.8: *Energy and carbon losses per unit (Average).*

- Unnecessary Consumption
- Overconsumption
- Lack of Optimization
- Lack of Recoverable Energy Use
- Transmission Losses
- Transformation Losses
- Lack of Sustainable Energy Use

Energy loss identification and Significant Energy User (SEU) are followed by energy project creation. In this context, energy-saving improvements include;

- Pump/motors
- Compressors
- Lightning
- Cabins and drying ovens

Cabins and drying ovens are stated as the most used and lost energy in the automotive industry. Therefore, it is significant to priority according to energy consumption. These projects include prevention of energy consumption due to air leaks, recovery of waste heat, boiler efficiency, transformation to less consumer lighting technologies, and efficient operation at the pump or/and motor systems.

The numerical values determined according to the aforementioned equations are shown in the following sub-headings, near the values are indicated in parentheses from which equation they are obtained.

Unnecessary Consumption

The losses are related to unnecessary consumption. In the cataphoresis tank, unnecessary consumption was determined as 86.3 kWh with help of SCADA. Wrong-designed equipment is defined as the root cause of this loss. Energy loss due to useless consumption was prevented and 384.312 kWh energy saving was achieved (eq.2) by adding an inverter. Finally, 191 tonnes of carbon saving was achieved as scope 2 emissions (eq.3).

Over Consumption

The overconsumption creates a loss. 80 kWh energy overconsumption was determined in the air preparation unit of the heating system with the help of SCADA. Lack of system knowledge was defined as the root cause. It was defined from SCADA data that there is still consumption for the levels of upper 22 OC. Also, it is possible to use outside air by adding a valve system. 70.400 kWh/year (eq.2) and 14 tonnes carbon saving as Scope 1 (eq.3) was gained.

Lack of Optimization

The losses are related to also deficiency of optimization. Lack of optimization was revealed with the evaluation of the pump and 19 kWh energy consumption was saved by increasing the efficiency of pumps. Lack of equipment was defined as the root cause. By changing pumps with brand new, 98.000 kWh/year (eq.2) and 49 tonnes/year carbon saving as Scope 2 (eq.3) were achieved.

Lack of Renewable Energy Use

The losses are also related to the lack of recoverable energy using in the compressor units. 181 kWh energy recovery was detected with an analysis. Lack of technology was defined as the root cause. The addition of heat recovery unit to the output of compressors resulted in the factory saving 452.500 kWh/year (eq.2) and 84 tonnes/year of carbon as Scope 1 (eq.3).

Transmission Losses

Cooling chiller overload brings about loss. This loss was detected with the help of SCADA as 47 kWh energy consumption for the cooling chiller. Lack of knowledge is the root cause of this loss as well. By changing the water transmission line instead of the cooling unit and it was a disabled cooling unit in summer. This modification made the factory save 48.465 kWh/year (eq.2) and 24 Tonnes/year as Scope 2 (eq.3).

Transformation Losses

Energy consumption during the time of rest is a significant loss. It was detected with the help of theoretical calculation and 40 kWh energy consumption in the lighting system. 36.000 kWh/year (eq.2) and 18 tonnes carbon emissions as scope 2 (eq.3) gained by adding a field scanner sensor that reduces the magnitude of lighting automatically when area usage is reduced.

Lack of Sustainable Energy Use

Renewable energy technology usage affects the loss. It was detected as 7.000 MWh/year with the help of a feasibility report. The root cause is lack of technology in this scenario. This project is not yet completed and at the end of this process, 7,000 MWh/year (eq.2) will be used from renewable energy. Also, it will be a carbon-neutral factory for Scope 2 emissions. Total carbon and energy gained are given in Table 1 below.

Table 1: Energy and Carbon Savings in Types of Losses

Losses	Electric (kWh/year)	Natural Gas (kWh/year)	Scope 1 (tonnes/year)	Scope 2 (tonnes/year)
Unnecessary Cons.	384.312	-	-	191
Over Cons.	-	70.400	14	-
Lack of Optimization	98.000	-	-	49
Lack of Renewable Energy Use	-	452.500	84	-
Transmission Losses	48.465	-	-	24
Transformation Losses	36.000	-	-	18
Lack of Sustainable Energy Use	7.000.000	-	-	3.481
Total	7.566.777	522.900	98	3.763

6.4 Conclusions

In this study, studies on energy management and carbon loss in the electric vehicle production factory were carried out and the findings were evaluated. In addition, the energy consumption values between 2019 and 2021 were gained and illustrated. Regression analysis for energy consumption per product number showed increase in product number corresponding to an increase in energy consumption as expected. With this issue, some fluctuation was observed on graphics. Environmental status has an effect on the production process thus consumption values were varied. For instance, while the number of 677 vehicles produced in figure 1 required approximately 6590 GJ, the real amount was revealed as 5782 GJ. This is because the variable environmental conditions such as weather, internal temperature, and mental state of employees. Electric and natural gas consumption between 2019 and 2021 averaged 53% and 47% for electric and natural gas respectively. Electricity consumption is dominant at this rate, and therefore, the use of sustainable energy sources will have a significant impact on the financial budget of the factories. In view of resource usage per unit, while the welding unit was expected as the most consumer, the PaintShop was seen on the top of the list among the other specified units. It was thought that compressors are critical equipment for energy consumption in this unit. Moreover, the internal temperature is important by qualified production. Paintshop was followed by social building. For sustainable and quality production, it is necessary for employees to have sufficient rest time. Making necessary improvements without sacrificing social units will provide financial savings. When the revealed energy loss points are evaluated, it has been revealed that the lack of information about the equipment used or the system has a significant effect on the energy loss issue. In this context, providing training on hardware knowledge and process mastery throughout the company and increasing energy consumption awareness will provide significant advantages on an annual basis.

Acknowledgments

Efe SAVRAN who is the bursary of the TUBITAK 2244 Industrial doctorate program (Project code 119C154) presents his appreciation to the supporter institution. All authors would like to thank KARSAN AUTOMOTIVE for data support and assistance in the preparation of this study.

Funding: This research received no external funding.

Conflicts of Interest: All authors declare that no conflict of interest exists in the submission of this manuscript, and the manuscript is approved for publication.

Authors Contributions: In this study, data collection and evaluation, sections of methodology, and results & discussion have been conducted by Özcan Yavaş. Abstract, introduction, literature review, conclusion, and edit of sections have been prepared by Efe Savran. General examination and revisions for quality-enhancing have been accomplished by Fatih Karpat and Berrak Erol nalbur.

References

1. Özer, B., Güven, B. (2021). Energy efficiency analyses in a Turkish fabric dyeing factory. *Energy Sources, Part A Recover. Util. Environ. Eff.,* vol. 43, no. 7, pp. 852–874, doi: 10.1080/15567036.2020.1755392.

2. Yuce, C., Karpat, F., Yavuz, N., Sendeniz, G. (2014). A case study: Designing for sustainability and reliability in an automotive seat structure. *Sustain.,* vol. 6, no. 7, pp. 4608–4631, doi: 10.3390/su6074608.
3. Yilmaz, T. G., Tüfekçi, M., Karpat, F. (2017). A study of lightweight door hinges of commercial vehicles using aluminum instead of steel for sustainable transportation. *Sustain.,* vol. 9, no. 10, doi: 10.3390/su9101661.
4. Wolf, M. J., Emerson, J. W., Esty, D. C., Wending, Z. A. (2022). 2022 Environmental Performance Index, *New Haven, CT: Yale Center for Environmental Law & Policy.* https://epi.yale.edu/
5. UNCC. (2022). What is a COP?, https://ukcop26.org/uk-presidency/what-is-a-cop/ (reachable: 15.09. 2022)
6. Europian Comission. (2022). Paris Agreement. https://ec.europa.eu/clima/eu-action/international-action-climate-change/climate-negotiations/paris-agreement_en (reachable: 15.09.2022)
7. Özer, B., Güven, B. (2021). Energy efficiency analyses in a Turkish fabric dyeing factory, Energy Sources, Part A Recover. Util. Environ. Eff., vol. 43, no. 7, pp. 852–874, doi: 10.1080/15567036.2020.1755392.
8. Yuce, C., Karpat, F., Yavuz, N., Sendeniz, G. (2014). A case study: Designing for sustainability and reliability in an automotive seat structure, Sustain., vol. 6, no. 7, pp. 4608–4631, doi: 10.3390/su6074608.
9. Yilmaz, T. G., Tüfekçi, M., Karpat, F. (2017). A study of lightweight door hinges of commercial vehicles using aluminum instead of steel for sustainable transportation, Sustain., vol. 9, no. 10, doi: 10.3390/su9101661.
10. Wolf, M. J., Emerson, J. W., Esty, D. C., Wending, Z. A. (2022). 2022 Environmental Performance Index, New Haven, CT: Yale Center for Environmental Law & Policy. https://epi.yale.edu/
11. UNCC. (2022). What is a COP?, https://ukcop26.org/uk-presidency/what-is-a-cop/ (reachable: 15.09. 2022)
12. Europian Comission. (2022). Paris Agreement. https://ec.europa.eu/clima/eu-action/international-action-climate-change/climate-negotiations/paris-agreement_en (reachable: 15.09.2022)
13. Güllü M., Yakışık, H. (2017). Karbon Emisyonu Ve Enerji Tüketiminin Büyüme Üzerindeki Etkileri: MIST Ülkeleri Karşılaştırması, Sosyoekonomi, vol. 25, no. 32, pp. 239–239, doi: 10.17233/sosyoekonomi.289930.
14. Katchasuwanmanee, K., Bateman, R., Cheng, K. (2017). An Integrated approach to energy efficiency in automotive manufacturing systems: quantitative analysis and optimisation, Prod. Manuf. Res., vol. 5, no. 1, pp. 90–98, doi: 10.1080/21693277.2017.1322539.
15. Ozturk, H. L. (2005). Energy usage and cost in textile industry: A case study for Turkey, Energy, vol. 30, no. 13, pp. 2424–2446, doi: 10.1016/j.energy.2004.11.014.
16. Taner, T., Sivrioğlu, M., Topal, H., Dalkılıç, A. S., Wongwises, S. (2018). A model of energy management analysis, case study of a sugar factory in Turkey, Sadhana - Acad. Proc. Eng. Sci., vol. 43, no. 3, doi: 10.1007/s12046-018-0793-2.
17. Ministry of Energy and Natural Sources, (2022). Elektrik, https://enerji.gov.tr/bilgi-merkezi-enerji-elektrik (reachable: 15.09.2022)
18. Marimon, F., Casadesús, M. (2017). Reasons to adopt ISO 50001 Energy Management System, Sustain., vol. 9, no. 10, pp. 1–15, doi: 10.3390/su9101740.
19. Fiedler T., Mircea, P. M. (2012). Energy management systems according to the ISO 50001 standard - Challenges and benefits, 2012 Int. Conf. Appl. Theor. Electr. ICATE 2012 - Proc., pp. 31–34, doi: 10.1109/ICATE.2012.6403411.
20. McKane, A., Desai, D., Matteini, M., Williams, R., Risser, R. (2009). – Thinking Globally: How ISO 50001–Energy Management can make industrial energy efficiency standard practice, Environ. energy Technol., pp. 1–16,

21. Kanneganti H., Gopalakrishnan, B., Crowe, E., Al-Shebeeb, O., Yelamanchi, T., Nimbarte, A., Currie, K., Abolhassani, A. (2017). Specification of energy assessment methodologies to satisfy ISO 50001 energy management standard, Sustain. Energy Technol. Assessments, vol. 23, no. June, pp. 121–135, doi: 10.1016/j.seta.2017.09.003.
22. Kilic, S. (2013). Linear regression analysis, J. Mood Disord., vol. 3, no. 2, p. 90, doi: 10.5455/jmood.20130624120840.

About the Authors

Özcan Yavaş, responsible for environment, health, and occupational safety at Karsan Automotive. He is currently a Ph.D. student in environmental engineering department of Bursa Uludag University. After receiving his MSc. from Bursa Uludag University, he worked on the subject of sustainable management for electric vehicles. He focused on environment and energy management systems, WCM management, carbon footprint per vehicle and sustainable management systems as a researcher. He has national and international academic publications on research subjects.

Efe Savran, Ph.D. student in mechanical engineering department of Bursa Uludag University. He received B.Sc. from Balikesir University. After graduation he worked as manufacturing engineer and he started Ph.D. in 2020. As a scholarship holder of The Scientific and Technological Research Council of Turkey (TUBİTAK), he is co-worker of Karsan Automotive. His research areas are electric vehicles, e-powertrain, biomedical implants and applications, finite element methods. He has national and international academic publications on his research areas.

Dr. Berrak Erol Nalbur, assistant professor in Environmental Engineering at Bursa Uludag University. She received her B.Sc. in 1995, M.Sc. in 1997 from Istanbul Technical University and Ph.D. in 2008 from Bursa Uludag University. He worked as research assistant at Namık Kemal University between 1996 and 1999. She gained the title of assistant professor in 2008. She has 14 academic conference publications and she managed efficiency, water recycle, water purification, electro-regulation related several theses. Her research area focused on engineering and technology.

Dr. Fatih Karpat, Professor and head of mechanical engineering department at Bursa Uludag University. He received his B.Sc. in 1998, M.Sc. in 2001, and Ph.D. in 2005 from Bursa Uludag University. He joined the academic community as research assistant in 1998 and he continued his success by gaining the title of associate professor in 2015 and professor in 2020. He has been to Texas Tech University and University of Central Oklahoma between 2006 and 2015 for postdoctoral and guest researcher. His professions based on machine elements, energy, biomedical engineering, sustainability, MEMS, technological innovations. He has more than 20 science citation indexed publications, 5 book chapters, more than 70 academic conference publications. Beside the academic side, he also managed more than 20 industrial projects.

CHAPTER 7

Electromagnetic Energy Harvester Design for Power Transmission Line

M. Ş. Balcı, S. Sakar, and A. Dalcalı

Article citation information: (2022), *TJES*, Vol. SP-2, pp. 111-123, doi:10.22545/2022/00211

Parallel to the increase in energy demand, the importance of energy transmission lines is also increasing. In order for energy transmission to be carried out correctly, transmission lines must operate uninterruptedly. Therefore, it is important to inspect and monitor the lines and to intervene immediately in case of any fault. The use of Unmanned Aerial Vehicles (UAV) for the inspection and monitoring of these lines provides advantages in terms of both safety and cost. In the study, the design and analysis of electromagnetic energy harvesters have been made in order to provide energy to UAVs. Firstly, the mathematical modeling of the core has been presented. Electromagnetic energy harvesters designed based on this model have been analyzed using the Finite Element Method (FEM). The performances of toroidal magnetic energy harvesters have been investigated according to core size, material properties, air gap and line current. According to the results obtained from the analyzes, the harvester with the best size/energy density has been determined.

Keywords: Electromagnetic energy harvesters, transmission line, UAV, FEM.

7.1 Introduction

The importance of power transmission lines increases with the increasing energy demand nowadays. It is important to monitor and inspect power transmission lines for energy sustainability and quality. Most power transmission lines are located in places with difficult transportation and access. These lines are monitered by manpower, helicopters, or airplanes. UAVs are used in these duties due to costs and harsh environmental conditions. The most significant disadvantage of UAVs is their insufficient batteries. Therefore, when UAVs are about to run out of charge, they can be charged by harvesting magnetic energy from an appropriate nearby line instead of withdrawing them from their duty stations for charging or periodically changing the battery. Thus, the UAV, which will perform the duty, can continue to work from where it is left off after charging without leaving the duty area [1, 2].

Energy harvesting can be defined as the capture of small amounts of energy available by thermal, mechanical, and electromagnetic methods and its conversion into electrical energy [1]. An electromagnetic energy harvester can be likened to a transformer, with the transmission line being primary windings and windings on the core being secondary windings [3]. In this harvester, voltage is induced using the magnetic field around the line, and energy is obtained from transmission lines. The method of energy harvesting from electromagnetic fields has some advantages over other energy harvesting methods. These advantages can be listed as not being dependent on weather conditions, not having maintenance costs, and working as long as current flows through the transmission line [4].

In electromagnetic energy harvesters, factors such as core material, core geometry, and core saturation are very important for the harvester's efficiency. Numerous studies have been conducted in the literature to optimize the harvester and overcome various problems [5, 6]. The saturation of the core material used in the harvester significantly impacts the output power obtained. Harvesting can be done effectively when the core is unsaturated, in other words, the core operates in the linear region. When the core is saturated, the output power decreases excessively with the reduction in the induced voltage. A comprehensive study investigating the effect of core geometry determined that a decrease in the magnetic flux leakage increased the output power due to the reduced inner radius of the core, the increased core height, and the air gap being as small as possible. Furthermore, it was revealed that windings should be optimized according to the line current value [7]. In the study in which harvesters using ferrite cores with different relative permeabilities were examined, the effects of 1000 and 2500 spiral windings and core material were investigated. The study found that the harvester having a core with a high relative permeability obtained the highest energy with the highest number of windings [8]. Therefore, it can be concluded that the obtained energy increased as the relative permeability of the core material and the number of windings increased. Different solutions have been proposed in the literature to prevent the core from reaching saturation in harvesters. A harvester with dual core was designed to avoid the magnetic resistance caused by the air gap added to the core to prevent the magnetic core's saturation. This two-piece core designed was compared with a single-piece core of the same size, with the same material and the same number of windings. Magnetic flux leakage was significantly reduced in the harvester with dual core compared to the harvester with single core, and more output power of up to 53% was achieved [9]. Another study, designed and tested an energy harvester with a desaturation controller. In this model, a secondary winding was added in addition to windings on the core to eliminate the saturation effect of the magnetic core, and it was attempted to eliminate the saturation effect by running the secondary winding while the core was about to be saturated. The study, obtained 13.8% more power than the harvester without secondary winding [10].

A magnetic energy harvester providing wireless charging for UAVs used in the monitoring and inspection of power transmission lines was designed in this study. In the structure to be designed, the system should be optimized in terms of size and high energy density to obtain energy from power transmission lines with an UAV. The optimum design was achieved in the study by focusing on factors such as core material, size, and core saturation while designing the harvester.

7.2 Energy Harvesting Methods

Energy harvesting is collecting of small amounts of energy available in the environment, such as solar energy, wind energy, mechanical energy, kinetic energy, and magnetic field energy, and its use by converting it into electrical energy. The term energy harvesting is used since the amount of energy obtained is low. Regarding energy conversion, people have long been using the current energy harvesting technologies in the form of windmills, watermills, geothermal and solar energy [11].

Energy harvesting techniques have become highly important due to the limited availability of conventional power sources, increasing demands for systems such as wireless sensor networks, the increased number of in electrical devices working with very low power with the development of technology, and their environmental friendliness. With recent developments in wireless and micro electro-mechanical systems, energy harvesting stands out as an important alternative to conventional batteries [11]. Conventional batteries are used as power sources for portable electronic devices and wireless sensors with low power requirements. However, battery life is quite short compared to the working life of devices, and batteries must be replaced or recharged periodically, which is very costly, especially for sensors in inaccessible locations [12].

Numerous studies have been conducted on portable devices or wireless sensor network systems harvesting their energy independently of conventional batteries. In a study conducted to power UAVs, a mixed energy harvester containing radio frequency and solar energy was proposed, and an output voltage of 23.2 V, sufficient to meet the battery requirement of the aerial vehicle, was obtained [13]. A study on piezoelectric energy harvesters tested the designed harvester theoretically and experimentally. An output voltage of 5.99

V theoretically and 3.65 V experimentally at 35 Hz was obtained. This difference between theoretical and experimental results was originated from the fact that variables such as frequency and material properties differed from their real values in the simulation environment [14]. In the study in which energy was harvested from an electric field on a 765 kV high-voltage line, a Zigbee-based temperature sensor was successfully operated with the power obtained [15]. In a comprehensive study on thermoelectric energy harvesters, a low-power harvester was tested without any booster circuit, and a maximum power of 64.59 mW was obtained at a temperature change of 105 °C. It was indicated that the power obtained could be increased significantly by increasing the amount of change in heat with better heat sink designs and using booster circuits [16]. A piezoelectric energy harvester allowing electrical energy to be obtained from low-frequency bridge vibrations was designed in another study. In the mentioned study, measurements were taken from an overpass used in the city, and the harvester was tested by generating the vibration measured in the laboratory environment. The test results, showed that 0.20 µW power was obtained at a frequency of 4 Hz and an amplitude of 4 V. Irregular structural vibrations were the reason for this low power [17]. In other words, continuous and regular vibrations are required to ensure the efficiency of this type of energy harvesters. Obtaining electrical energy from solar and wind energy, which are among the renewable energy sources, can be considered an energy harvesting method. However, energy harvesting from solar energy can only be performed in daylight. Wind turbines have been developed for large-scale energy generation with wind energy [18]. Since solar and wind energy is unavailable due to weather conditions and in some situations, such as indoor environments, vibrational energy comes to the forefront as an alternative to these sources. There are three conversion mechanisms, piezoelectric, electrostatic, and electromagnetic, to convert vibrational energy into electrical energy [19].

In particular, harvesting energy from the electric field is one of the energy harvesting methods studied to provide energy to sensors used in monitoring transmission lines. The method of harvesting energy from the electric field is one of the most appropriate techniques for transmission lines since electric fields around power lines are under open circuit conditions are independent of the line current and are relatively rich and continuous. An electric field is emitted when a certain voltage is applied to a conductor. The electric field energy harvesting technique is based on the principle of this emission. The capacitive displacement current flowing from the conductor to the ground can harvest this emitted energy [20]. The most significant advantages of energy harvesting from the electric field are not requiring current flow on the line and the ease of installation. The disadvantages of these harvesters are their large size and the necessity of being short-circuited under some conditions [21, 22]. Table 1 summarizes the comparison of energy harvesting techniques.

7.3 Methodology

In this study, the method of harvesting energy from the magnetic field, one of the energy harvesting methods, was chosen to charge UAVs. A toroidal model was preferred as the core geometry since it is easy to install on lines and allows higher power to be obtained than other geometric shapes [30]. In the design of electromagnetic energy harvesters, some analyses should be performed to achieve a design that meets the desired properties by taking into account some problems, such as core saturation, core geometry, and ease of installation. In this section, the harvester will be examined theoretically, and its analytical model will be derived. In the structures of electromagnetic energy harvesters, there is a core consisting of soft magnetic material and a conductor wound on the core, as seen in Figure 7.1. The windings on the core are secondary windings, and the line to which the toroid will be connected is primary windings. The equivalent circuit of these harvesters operating based on the current transformer logic is shown in simple Figure 7.2, and these harvesters can be considered electrical machines.

The method of harvesting energy from the magnetic field works in line with the principles of Faraday's and Lenz's laws. The current flowing through a transmission line creates a magnetic field around the wire. Sufficient power can be obtained to charge the UAV by inducing voltage from this magnetic field.

Table 1: Comparison of energy harvesting systems.

Energy Harvesting Method	Advantage	Disadvantage
Solar Energy [22-24]	It has a high potential.	There is dependence on weather conditions. There is a need for storage. It cannot be used in closed environments. Photovoltaic cells have low efficiency.
Heat Energy [25-27]	Any system or device that generates heat in nature and industry can be utilized.	Thermoelectric materials have low efficiency.
Vibrational Energy [17]	It is easily available in the surrounding area.	Vibrations in the environment are usually not continuous and constant, which reduces efficiency.
Wind Energy [18,24]	It has a high potential.	There is dependence on weather conditions. The maintenance cost is high. It is difficult to install. It cannot be used in indoor environments.
Electric Field Energy [28]	It is always available on high-voltage lines or near the equipment.	It has low energy conversion due to high reactance.
Magnetic Field Energy [3,4,29]	Current is always present in every flowing conductor. Its efficiency is high, there is no maintenance cost, and the structure is quite simple.	The current flowing through the conductor should be sufficient. Energy losses occur inside the ferromagnetic core.

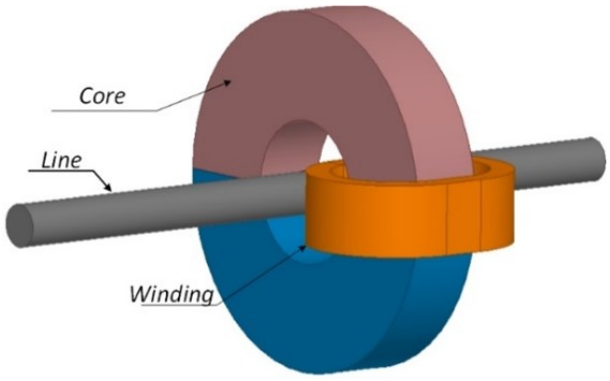

Figure 7.1: *Toroidal energy harvester.*

7.3.1 Numerical Model

When Ampere's law is applied to the toroidal model, the magnetic flux density at any radius r inside the toroid is given in Equation 1 [8]:

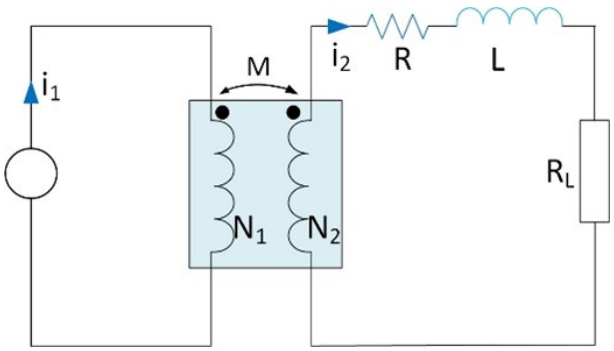

Figure 7.2: *Equivalent circuit of the electromagnetic energy harvester.*

$$\bar{B} = \frac{\mu i}{2\pi r} \tag{7.1}$$

where B represents the magnetic flux density, i represents the current passing through the line, μ represents the product of the magnetic permeability (μ_r) of the core material and the magnetic permeability of the air (μ_0). Based on the value of magnetic flux density, the flux in the toroid (ϕ_{21}), and based on it, the common inductance of the toroid and the line (L_{21}) and the self-inductance of the toroid (L_{22}) can be calculated. Through common and self-inductance, the voltage induced by the toroid (V_2) and the magnetic energy stored at the magnetic flux density in the harvester can be reached. Inductance can be expressed as an inductor's capacity to store energy as magnetic flux density. It can be said that there is a significant correlation between inductance values, induced voltage, power density, and energy obtained. The magnetic flux in the toroid;

$$\Phi_{21} = B_1 ds_2 = \frac{\mu i}{2\pi} \ln bah \tag{7.2}$$

Common inductance:

$$L_{21} = L_{12} = M = N_2 \frac{d\Phi_{21}}{di} = \frac{\mu}{2\pi} h N_2 \ln ba \tag{7.3}$$

Self-inductance:

$$L_{22} = \frac{\mu}{2\pi} h N_2^2 \ln ba \tag{7.4}$$

and the voltage induced in the toroid according to Faraday's law:

$$V_2 = N_2 \mu f i t \sin wt \ln bah \tag{7.5}$$

As seen from the equation, the voltage induced by a toroidal electromagnetic energy harvester is affected by the following variables [31];

Number of windings around toroid N_2,

Magnetic permeability of core μ,

Amount of the current flowing through transmission line$i$,

Inner and outer diameters of core a and b,

Core height h.

The following equation expresses the magnetic energy stored at the magnetic flux density:

$$W = \frac{1}{2}Li^2 \tag{7.6}$$

As mentioned previously and seen in Figure 2, toroidal electromagnetic energy harvesters operate based on a transformer logic in which the transmission line is considered the primary winding and windings on the toroid are considered the secondary winding. In this case, the magnetic energy stored at the magnetic flux density in the harvester can be expressed by the following relation.

$$W = \frac{1}{2}L_{11}i_1^2 \;\; L_{22}i_2^2 \;\; 2Mi_1i_2 \tag{7.7}$$

According to this relation, the energy obtained by the harvester is affected by the values of the current on the line (i_1), current induced in the windings (i_2), common inductance (M), and self-inductance (L_{22}). Therefore, it can be said that inductance values are very important for the harvested energy and power density. Thus, the common inductance and self-inductance values should be calculated to design the energy harvester most appropriately in terms of power density and energy obtained.

7.4 Design and Comparative Analysis

7.4.1 Designed Model

The electromagnetic energy harvesters designed were analyzed by FEM. This method is intensively used in many engineering fields such as electrical - electronic, construction, and biomedicine fields. FEM has been put forward to solve problems whose changes over a given area can be represented by partial differential equations. Through FEM, complex and time-consuming problems are solved with high accuracy and in a short time [32]. Thus, there is a significant advantage in terms of time and economy. Models were analysed using a magnetostatic and transient solution type in Ansys/Maxwell package program. Figure 7.3 displays the mesh model of the toroid core with a size of 30x10x10 mm. This core model, used 184309 tetrahedral mesh structures.

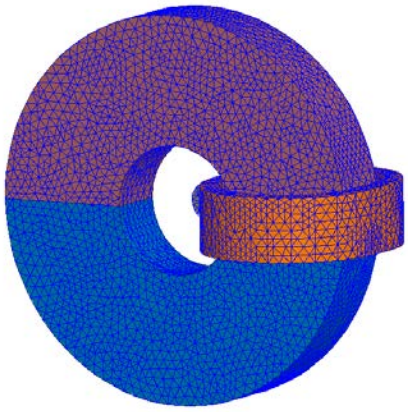

Figure 7.3: *Mesh structure of the core.*

Toroidal cores were determined as the core geometry for analysis. These cores were analyzed separately with different magnetic materials and in different sizes. Since soft magnetic materials form the harvester's magnetic circuit, these materials are expected to have high relative permeability, high saturation, and low core loss. Mu Metal, Steel 1010, and M19 were used as core materials in the study. Figure 7.4 shows the B-H curves of these materials.

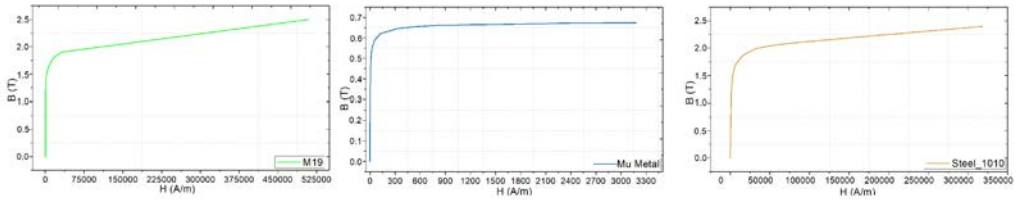

Figure 7.4: *BH curves of the materials used.*

Due to the weight problem, which can be considered the biggest disadvantage of UAVs, harvesters are limited size and weight during the design. Therefore, it is necessary to provide the most optimum design regarding harvester weight and performance. The sizes of the cores used for toroidal models in the study were chosen as 25x10x10, 25x10x20, 25x15x10, 25x15x20, 30x10x10, 30x10x20, 30x15x10, and 30x15x20, respectively. The variables represent the outer diameter (mm), the inner diameter (mm), and the height (mm) of the toroid, respectively.

7.4.2 FEM Analysis

In the analyses, the common inductance (M) and self-inductance (L_{22}) values of the harvesters were first calculated. While inductance values are important for the voltage induced by the harvester, with an increase in the inductance value, the voltage induced by the harvester and the power density in the harvester increase to the same extent. In this respect, there is a significant correlation between power density and inductance. Moreover, the power density in the harvester and the energy obtained depend on inductance values, as seen in Equation 7. However, the weight of the harvester limits the designs. A larger core provides higher inductance and power density, resulting in a heavier core. Therefore, it is necessary to compromise one of the weight or inductance values during design. According to Equations 3 and 4, the common inductance and self-inductance values depend on the core's height, inner and outer diameters, the number of windings, and the material's relative permeability. According to the results of the analyses conducted with cores of different sizes, the harvester with the highest inductance values was the harvester with a 30x10x20 mm sized M19 core with a small inner diameter, large outer diameter, and large height, as seen in Table 2. Therefore, this is the most appropriate model in terms of induced voltage and, thus, harvested energy. No air gap was used during these analyses, and the current value was determined as constant 60 A.

Table 2: Common inductance and self-inductance values.

Core Dimensions(mm)		25x10x10	25x10x20	25x15x10	25x15x20	30x10x10	30x10x20	30x15x10	30x15x20
M19	L_{22} (mH)	820.13	1633.6	542	1070.5	1074.2	2158.9	792.34	1585.1
	M (mH)	1.6211	3.246	1.067	2.1214	2.124	4.2891	1.5631	3.1447
Mu Metal	L_{22} (mH)	418.18	828.46	280.87	552.61	555.71	1104.9	417.31	826.53
	M (mH)	0.81718	1.636	0.54488	1.0857	1.0871	2.1817	0.81301	1.6271
Steel 1010	L_{22} (mH)	436.42	864.52	248.43	489.47	517.79	1027	329.49	650.14
	M (mH)	0.85369	1.7066	0.8065	0.95968	1.0114	2.0266	0.63776	1.2751

As can be calculated from Equation 3, the outer diameter/inner diameter ratio affects the mutual inductance and self-inductance. A high ratio causes high inductances. Among the toroids with the same inner diameter, material, and height from Table 2, the inductance of the larger outer diameter is also higher.

In the continuation of the study, the effect of the current value on the harvester's performance was examined. The current values were analyzed by increasing 5 A at each step, in the range of 0-100 A. It was tried to reveal the effect of the current on harvesters by calculating magnetic flux density values at each current value. These analyses were based on the core design of a 30x10x20 mm size with the highest inductance value among the designs.

M19 was the material that reached the highest magnetic flux density value at the current values applied in the analyses. M19 also performed quite well in reaching saturation. As seen from the BH curves in Figure 7.4, Mu metal, with the highest relative permeability among the materials, started to reach saturation rapidly when the line current was just 10 A. When the flux density is examined by considering Equation 1, it is seen that mu metal with high magnetic relative permeability provides high flux density at low current compared to other materials. Although Mu metal yields quite good results at low current values, its use is limited due to saturation problems as the current value increases. Steel 1010 did not approach the saturation region at the applied current values, but it did not provide as good results as M19 at the magnetic flux density value. According to the analysis, the magnetic material that yielded the best results at low current values was Mu metal. In this study, M19 was the material that provided the best results for magnetic flux density at the applied current values, and steel 1010 came to the forefront at high current values. According to the analyses carried out by increasing the line current, as the amount of current increased, the magnetic flux density also increased in line with expectations, as seen in the graphs in Figure 7.5. However, the increase in magnetic flux density decreased, although the current increased after a certain point, and the core reached saturation. Hence, adding an air gap is one of the most common solutions for the core to operate in the linear region at high current values.

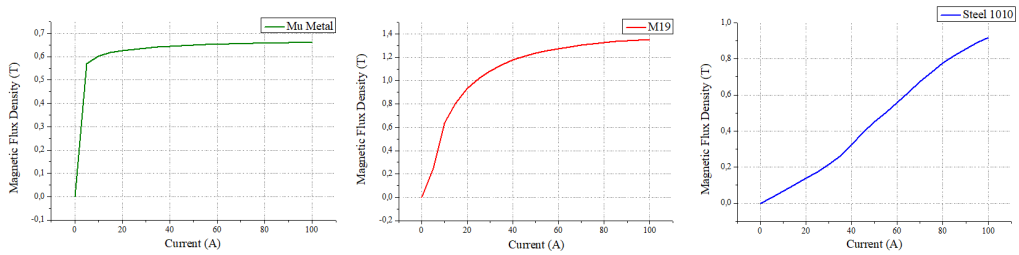

Figure 7.5: *Flux density with respect to excitation current.*

7.4.3 Air-gap Effect

In this section, analyses were performed to see how the air gap affected the harvester performance and saturation problem. The air gaps added to the cores were tested in the range of 0-2 mm by increasing them by 0.1 mm at each step. These analyses were also based on the design of 30x10x20 mm in size.

According to the analysis conducted by increasing the air gap in the core in 0.1 mm steps, as the air gap increased, the magnetic flux density decreased due to the increase in reluctance and took a constant value close to zero after a certain point, as seen in the graph in Figure 7.6. Therefore, attention should be paid to ensuring that the air gap should not be more than necessary to prevent core saturation. Figure 7.7 demonstrates magnetic flux density distributions of the cores with no air gap and an air gap of 0.1 mm at a 60 A. In this part, the effect of both material and air gap on the flux density distribution is obtained by magnetostatic analysis. In order to create an air gap in the toroid core, the core was designed in two parts and an air gap of 0.1 mm was created between the parts according to the first model.

While the mu metal core was at saturation point in case of no air gap, it operated in the linear region when the air gap was added. Likewise, in case of no air gap, the M19 core operated close to this region, although it was not in the saturation region. However, it operated in the linear region with an air gap. Although the

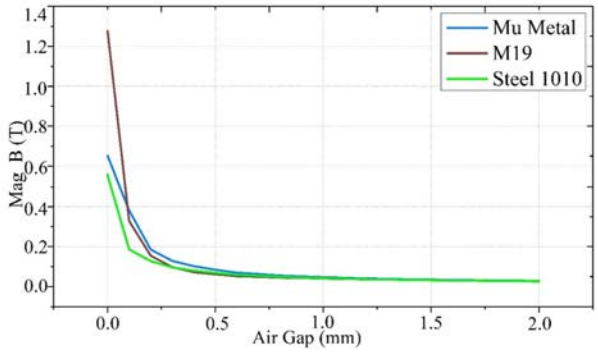

Figure 7.6: *Graphs of change in the air gap and magnetic flux density.*

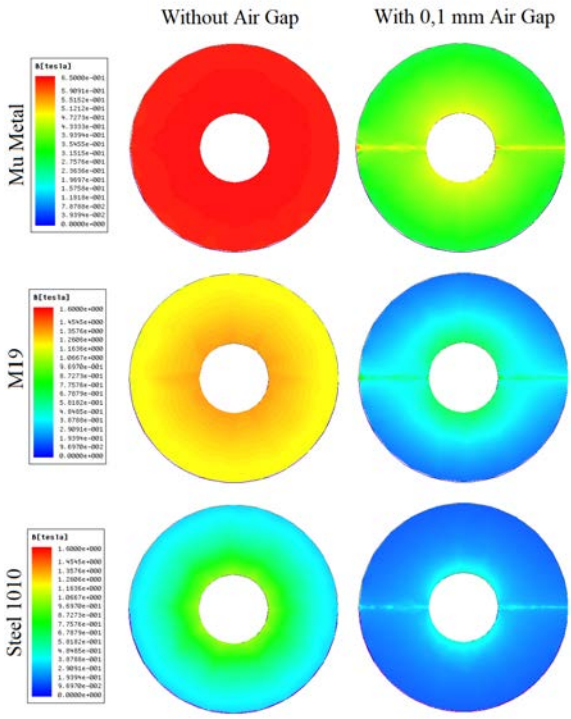

Figure 7.7: *Magnetic flux density distributions in the cores with and without air gap.*

steel 1010 core had no air gap at this current value, adding an air gap did not make any sense since it was operating in the linear region.

7.5 Conclusions

In this study, magnetic energy harvesters providing wireless charging for UAVs used to monitor and inspect power transmission lines were designed. The harvesters were analyzed with M19, Mu metal, and steel 101 materials at different currents and air gaps. The design with the highest inductance values among the designs was the harvester with a 30x10x20 mm core having a self-inductance of 2158.9 mH and a common inductance of 4.2891 mH. According to the analysis carried out by increasing the line current in the range of 0 – 100 A with 5 A steps, the highest magnetic flux density value was obtained with the M19 core. The Mu metal core reached saturation rapidly, and the steel 1010 core lagged behind the M19 core in the magnetic flux density value, although it did not reach saturation. According to above-mentioned results, while Mu metal was the material that yielded the best results at current values less than 10 A, the steel 1010 core was the core that provided the best results at high current values. M19 had the best results in the 0 – 100 A current range.

According to the analyses conducted with air gaps, the magnetic flux densities of the cores decreased with the increase in the reluctance of the magnetic circuit as the air gap increased, and it approached 0 for each material when the air gap was above 0.1 mm. Mu metal, which reached saturation rapidly, and M19, which approached the saturation region, started to operate in the linear region when an 0.1 mm air gap was added. According to the results from the overall study, the harvester which had the highest magnetic flux density and inductance values and therefore could reach the highest voltage, power, and energy density values was the 30x10x20 harvester with a core of M19 material without adding an air gap. With the results from the analyses performed by FEM, the performance of toroidal magnetic energy harvesters was investigated according to size, material properties, air gap, and line current variables, and it was attempted to reveal the harvester with the best size/energy density.

Funding: The authors did not receive support from any organization for the submitted work.

Conflicts of Interest: The authors declare that they have no conflicts of interest.

Authors Contributions: This work is Mr. Balcı' thesis. Dr. Dalcalı is Mr. Balcı' advisor. In study literature review, model and analysis have been prepared by M. Şamil Balcı. Abstract, introduction, numerical model and conclusion have been prepared by Selcuk Sakar and Adem Dalcalı.

References

1. Júnior, T., Rodriguez, Y., Melo, E., Santos, M., and Souza, C. (2013). Energy Harvesting Based on Magnetic Dispersion for Three-Phase Power System. *Energy and Power Engineering,* 5 (3B), 20-23. DOI: 10.4236/epe.2013.53B005.
2. Özer, İ., Efe, S. B., & Özbay, H. (2021). CNN/Bi-LSTM-based deep learning algorithm for classification of power quality disturbances by using spectrogram images. *International Transactions on Electrical Energy Systems*, 31(12), e13204. https://doi.org/10.1002/2050-7038.13204.
3. Kabakulak, M. (2020). Energy harvesting from electromagnetic fields around overhead power lines. M. Sc. *Thesis, Harran University.*

4. Zhuang, Y., Xu, C., Yuan, S., He, C., Chen, A., Lee, W. W., and Huang, Y. (2017). An improved energy harvesting system on power transmission lines. Paper presented at Wireless Power Transfer Conference, Taipei, 10-12 May 2017. https://doi.org/10.1109/WPT.2017.7953847.
5. Dos Santos, M. P., Vieira, D. A., Rodriguez, Y. P. M., de Souza, C. P., de Moraes, T. O., and Freire, R. C. S. (2014). Energy harvesting using magnetic induction considering different core materials. Paper presented at International Instrumentation and Measurement Technology Conference, Montevideo, (pp. 942-944). DOI: 10.1109/I2MTC.2014.6860881.
6. de Moraes Júnior, T. O., Rodriguez, Y. P. M., de Souza Melo, E. C., and de Souza, C. P. (2013). Experimental results on magnetic cores for magnetic induction-based energy harvesting. Paper presented at IMEKO TC 4 Symposium and 17th IWADC Workshop Advances in Instrumentation and Sensors Interoperability, Barcelona, (pp. 625-630).
7. Wang, W., Huang, X., Tan, L., Guo, J., and Liu, H. (2016). Optimization design of an inductive energy harvesting device for wireless power supply system overhead high-voltage power lines. *Energies,* 9(4). https://doi.org/10.3390/en9040242.
8. Gaikwad, A. A., and Kulkarni, S. B. (2019). Energy harvesting based on magnetic induction. *Smart Innovation, Systems and Technologies,* 106, 363–370. https://doi.org/10.1007/978-981-13-1742-2_35.
9. Zhang, J., Tian, X., Li, J., and Yan, D. (2020). A Novel Electromagnetic Energy Harvester Based on Double-Ring Core for Power Line Energy Harvesting.*Journal of Circuits, Systems and Computers,* 29(16). https://doi.org/10.1142/S0218126620502655.
10. Wang, J., Kim, J., and Ha, D. S. (2021). Powerline Energy Harvesting Circuit with a Desaturation Controller for a Magnetic Core. Paper presented at International Midwest Symposium on Circuits and Systems, Lansing (pp. 220–223). https://doi.org/10.1109/MWSCAS47672.2021.9531890.
11. Kim, H. S., Kim, J. H., and Kim, J. (2011). A review of piezoelectric energy harvesting based on vibration", *International Journal of Precision Engineering and Manufacturing,* 12(6), 1129–1141. https://doi.org/10.1007/s12541-011-0151-3.
12. Li, S., Peng, Z., Zhang, A., Luo, D., and Wang, F. (2016). Dual resonant structure for energy harvesting from random vibration sources. Paper presented at 11th Annual International Conference on Nano/Micro Engineered and Molecular Systems, Sendai, (pp. 255-259). DOI: 110.1109/NEMS.2016.7758245.
13. Quyen, T. V., Nguyen, C. V., Le, A. M., and Nguyen, M. T. (2020). Optimizing Hybrid Energy Harvesting Mechanisms for UAVs. *EAI Endorsed Transactions on Energy Web,* 7(30), 1–8. https://doi.org/10.4108/eai.13-7-2018.164629.
14. Jayarathne, W. M., Nimansala, W. A. T., and Adikary, S. U. (2018). Development of a Vibration Energy Harvesting Device Using Piezoelectric Sensors. Paper presented at Moratuwa Engineering Research Conference, Moratuwa, (pp. 197-202). DOI: 10.1109/MERCon.2018.8421913.
15. Kang, S., Kim, J., Yang, S., Yun, T., and Kim, H. (2017). Electric field energy harvesting under actual three-phase 765 kV power transmission lines for wireless sensor node.*Electronics Letters,* 53(16), 1135–1136. https://doi.org/10.1049/el.2017.1794.
16. Nadaf, N., and Preethi, A. (2021). Review on Waste Heat Energy Harvesting using TEG: Applications and Enhancements. Paper presented at 8th International Conference on Smart Computing and Communications, Kerala, (pp. 334-339). DOI: 10.1109/ICSCC51209.2021.9528196.
17. Balguvhar, S., and Bhalla, S. (2018). Green Energy Harvesting Using Piezoelectric Materials from Bridge Vibrations. Paper presented at 2nd International Conference on Green Energy and Applications, Singapore, (pp. 134-137). DOI: 10.1109/ICGEA.2018.8356282.
18. Wen, Q., He, X., Lu, Z., Streiter, R., and Otto, T. (2020). A comprehensive review of miniatured wind energy harvesters. *Nano Materials Science,* 3, 170-185. https://doi.org/10.1016/j.nanoms.2021.04.001.
19. Uddin, M. N., Islam, M. S., Sampe, J., Ali, S. H. M., and Bhuyan, M. S. (2016). Design and simulation of piezoelectric cantilever beam based on mechanical vibration for energy harvesting

application. Paper presented at International Conference on Innovations in Science, Engineering and Technology, (pp. 1-4). DOI: 10.1109/ICISET.2016.7856532.

20. Rodríguez, J. C., Holmes, D. G., McGrath, B. P., and Wilkinson, R. H. (2014). Maximum energy harvesting from medium voltage electric-field energy using power line insulators. Paper presented at Australasian Universities Power Engineering Conference, (pp. 1-6). DOI: 10.1109/AUPEC.2014.6966633.

21. Moghe, R., Yang, Y., Lambert, F., and Divan, D. (2009). A scoping study of electric and magnetic field energy harvesting for wireless sensor networks in power system applications. Paper presented at Energy Conversion Congress and Exposition, San Jose, CA, USA, 20-24 September 2009. DOI: 10.1109/ECCE.2009.5316052.

22. Najafi, S. A. A., Ali, A. A., Sozer, Y., and De Abreu-Garcia, A. (2018). Energy Harvesting from Overhead Transmission Line Magnetic fields. Paper presented at IEEE Energy Conversion Congress and Exposition, Portland, (pp. 7075–7082). https://doi.org/10.1109/ECCE.2018.8558356.

23. Yuan, S., Huang, Y., Zhou, J., Xu, Q., Song, C., and Thompson, P. (2015). Magnetic Field Energy Harvesting under Overhead Power Lines.*IEEE Transactions on Power Electronics,* 30(11), 6191–6202. https://doi.org/10.1109/TPEL.2015.2436702.

24. Roscoe, N. M., and Judd, M. D. (2013). Harvesting energy from magnetic fields to power condition monitoring sensors.*IEEE Sensors Journal,* 13(6), 2263–2270. https://doi.org/10.1109/JSEN.2013.2251625.

25. Zhou, J., He, L., Liu, L., Yu, G., Gu, X., and Cheng, G. (2022). Design and research of hybrid piezoelectric-electromagnetic energy harvester based on magnetic couple suction-repulsion motion and centrifugal action. *Energy Conversion and Management,* 258. https://doi.org/10.1016/j.enconman.2022.115504.

26. Yeesparan, S., Bin Baharuddin, M. Z., Din, N. B. M., and Haron, M. H. (2018). A review of energy harvesting methods for power transmission line monitoring sensors.*International Journal of Engineering and Technology* (UAE), 7(4), 153–161. https://doi.org/10.14419/ijet.v7i4.35.22348.

27. Camboin, M. M., Baiocchi, O., Villarim, A. W. R., Catunda, S. Y. C., de Souza, C. P., and Moreira, C. D. S. (2019). An Automatic Emulation System for Environmental Thermal Energy Harvesting. Paper presented at International Instrumentation and Measurement Technology Conference, New Zealand, May 2019, (pp. 1-6). DOI: 10.1109/I2MTC.2019.8827004.

28. Yuan, S. (2019). Magnetic Field Energy Harvesting for Smart Grid Application. PhD thesis, University of Liverpool.

29. Najafi, S. A. (2019). Energy Harvesting from Overhead Transmission Line Magnetic Fields. M. Sc. Thesis, Graduate Faculty of the University of Akron.

30. Zhang, Y., Wang, Z., Li, Y., Tian, B., Huang, X., and Zhang, P. (2021). Optimized Design and Simulation Study of Helical Core Suitable for Non-invasive Energy Harvesting. Paper presented at 16th Conference on Industrial Electronics and Applications, Chengdu, (pp. 1016–1019). https://doi.org/10.1109/ICIEA51954.2021.9516123.

31. Park, B., Kim, D., Park, J., Kim, K., Koo, J., Park, H. H., and Ahn, S. (2018). Optimization design of toroidal core for magnetic energy harvesting near power line by considering saturation effect. *AIP Advances,* 8(5). https://doi.org/10.1063/1.5007772.

32. Dalcalı, A. (2019). Influence of Rotor Magnet Material and Stator Winding Geometry on Output Torque in Spherical Actuator.*Journal of Engineering Sciences and Design,* 7 (1), 145-151. DOI: 10.21923/jesd.437980.

About the Authors

M. Şamil Balcı received the B.Sc. degree from Kırıkkale University in 2015. He is M.Sc student and Research Assistant with the Department of Electrical-Electronics Engineering, Bandırma Onyedi Eylül University, Türkiye. His research interests are electromagnetic fields and electrical machinery.

Selcuk Sakar received the B.Sc. and M.Sc. degrees from the Graduate School of Natural and Applied Sciences, Gazi University, Ankara, Türkiye, in 2010 and 2012, respectively. In 2021, completed his Ph.D. degree in electrical power engineering at the Lulea University of Technology, Sweden. He is currently working in Hitachi Energy as an R&D engineer.

Adem Dalcalı received the B.Sc. and M.Sc. degrees from Gazi University in 2010 and 2013, respectively, and the Ph.D. degree in electric and electronics engineering from Karabük University in 2017. His research interests include wind energy and the numerical analysis of the electromagnetic field in electrical machinery.

CHAPTER 8

Investigation of Energy Efficiency of Servo Motor Drive Hybrid Press Brake System: A Comparative Study with a Traditional Application

Özkan Pehlivanoğlu, Elif E. Topçu, Engin C. Çelik

Article citation information: (2022), *TJES*, Vol. SP-2, pp. 125-136, doi:10.22545/2022/00214

In this study, an energy consumption comparison of the conventional valve-controlled and variable speed pump-controlled press brake systems was carried out experimentally. The envisaged studies have been applied to the 80-ton press brake. In conventional valve-controlled systems, the flow rate is adjusted with the help of a proportional valve while the required flow in the variable-speed pump-controlled system is provided by changing the pump speed with using of a servo motor. From the results obtained, it has been seen that 54% energy saving can be achieved in 100 cycles, and the amount of oil used has also been reduced.

Keywords: Energy efficiency, hydraulic system, pump control, valve control, press brake.

8.1 Introduction

Hydraulic systems are used widely in industry because of their high power density, energy storage capability, safe against overloads, shock-free, ability to keep force and torque constant, and at the same time being a closed and protected system [1]. Pressing and cutting presses, plastic injection machines, robots, spacecraft, airplanes, and machine tools are some places where hydraulic systems are used.

The valves used for controlling the hydraulic actuators change the fluid flow areas to provide appropriate control. Due to these area changes during the hydraulic fluid flow in the valves, high-pressure losses and heat generation problems occur. These situations cause energy losses and also heat generation in the system creating the need for cooling, increasing costs, and shortening the service life of the hydraulic fluid due to viscosity changes. Today, due to the difficulties and costs of obtaining energy, it is expected that the systems to be energy efficient and reach high values in terms of performance. For this reason, researchers have done many studies to increase efficiency and reduce costs in hydraulic systems by eliminating the inefficiency caused by energy losses in valve-controlled systems and the need for cooling due to heat generation.

Shang (2004) used a pump-controlled hydraulic circuit with higher efficiency compared to valve-controlled systems to increase the performance of the energy-efficient hydraulic system. PID control algorithm was used as the controller, and the rotational speed overshoot of the pump is reduced by 50%, thus reducing the flow fluctuation [2]. Gao et al. (2005) analyzed the mechanism of the variable displacement

pump and the driving force of this swashplate and designed a new variable displacement mechanism with a DC servo motor. With the new design, the displacement change in the pump has been achieved faster, the pump structure has been simplified, and a solution has been provided to the contamination problem encountered in traditional pump systems [3]. Çalışkan et al. (2008) carried out a position control study of the servo-hydraulic system with the variable speed pump. As a result of the study, it has been determined that in valve-controlled systems, there is a loss of 42.3% in the pressure valve and 19.2% in the proportional directional valve. As an alternative, a pump-controlled hydraulic circuit has been suggested. It was stated that the heat loss was reduced, and the position control could be done as precisely as the valve-controlled systems [4]. Çelikayar (2008) carried out a study of servo-driven pump control systems and energy saving. A servo motor and fixed displacement piston hydraulic pump were used. 25% energy saving was achieved by applying the designed system in the plastic injection machine [5]. In the study of Deng (2016), a double-way pump was connected to a single motor for energy saving. At the same time, it is aimed to provide energy to be used again in the supply line, with the pump operating in a hydraulic motor mode in the return line by providing reverse operation in the system. According to the test results, 93% energy efficiency and a 67% increase in volumetric efficiency were achieved [6]. Li et al. (2017) investigated an analysis of the double-actuated energy-saving system for the hydraulic press. The system is modeled in which the return line of one of the actuators is synchronized with the feed line of the second actuator. When the experimental results of the study are analyzed, 20.61% energy savings and 26.09% efficiency increase due to the improvements in the realization time of the processes were obtained [7].

In addition to various studies on the design criteria and efficiency analysis in hydraulic systems, various applications have been made for controlling hydraulic power systems using classical and modern control techniques such as artificial neural networks, fuzzy control, and PID control [8-15]. In addition, different studies examined the effect of valve characteristics on the system dynamics, and the energy flows [16-20]. It can be said that with the increase in energy demand in the world, the concept of energy recovery, energy efficiency, and sustainability has gained importance, and studies on these issues have increased in recent years [22-25].

In this study, the energy efficiency of the hydraulic system used in the press brake system to form sheet metal materials by pressing was discussed. Due to the high energy losses in the study, a pump-controlled system was proposed instead of a valve-controlled system. According to the system requirements, the components of the system were selected, experimental studies were carried out on the bench and the analysis results were evaluated. The position, speed, pressure, energy consumed, and instant hydraulic fluid amount of the piston in the system was investigated. As a result of the study, the efficiency and cost values of the pump-controlled system were compared with the classical valve-controlled system.

8.2 Methodology

8.2.1 Experimental Equipment of Press Brake System

Press brakes are machines defined as C-Type presses used for bending sheet metal and composite materials. In Figure 8.1, a press brake and its main components, in addition to these, the experimental setup is shown schematically. The Control unit, hydraulic actuators, upper jaw, upper mold, lower mold, lower jaw, and side safety devices are the main components of the system. In order to obtain the desired form during the bending process, lower mold and upper mold are used according to the material type and the desired shape.

Controlled movement of the upper jaw is required for the desired bending operations. The one-cycle loop of an example operation is shown in Figure 8.2.

During the pressing process, the piston, which is the hydraulic actuating element, moves 0.5 m. The amount of hydraulic oil required by the system is 0.24 lt. However, in the classical valve-controlled system, since the engine rotates at 1500 rpm, there are 34.5 liters of hydraulic oil in the system, and an extra 34.26 liters of oil is sent to the hydraulic tank under pressure. This indicates the amount of heat and the resulting extra wasted energy. In other states, as here, the oil is under pressure and at the same time, the required position control is obtained by reducing the valve flow areas in the proportional valves. In this case, an

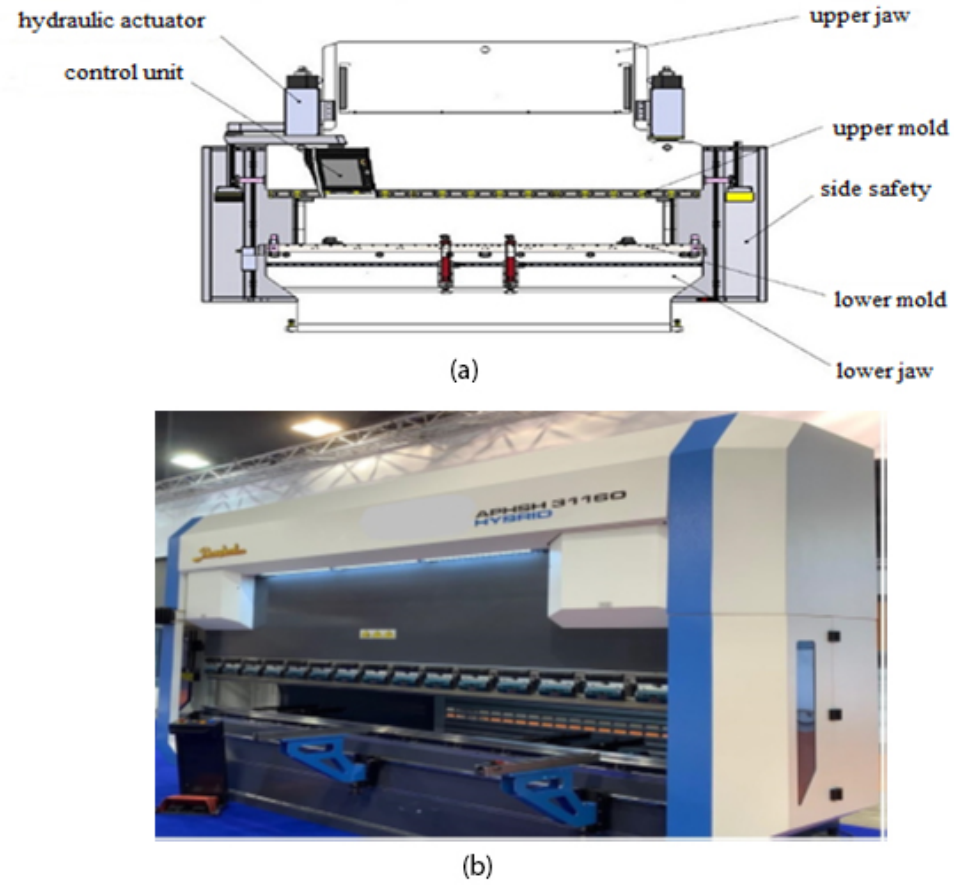

Figure 8.1: *(a) Schematic representation of the press brake and its main components, (b) Photo of the press brake system.*

excessive amount of heat is generated in the system and at the same time, the oil viscosity value changes over time. Therefore, due to the change in the structure of the oil, the service life is reduced. Changing the deteriorated oil in an average of six months according to the catalog values shows how important this situation is for environmental pollution.

Due to these negativities, in this study, the realization of position control with pump control in hydraulic systems has been examined. Basically, with the pump-controlled system, the oil was supplied to the system as much as desired [1]. During this process, a high-efficiency fixed displacement pump and a servo motor were used, which can rotate in both directions. Pressurized oil as much as the system needs were provided by adjusting the speed of the servo motor according to the position of the hydraulic actuator measured with the linear transducer. With the double-way rotational pump, the circulation of extra oil and heat losses in the system were prevented. At the same time, the amount of oil needed was reduced and the service life of the oil was increased. The hydraulic circuit of the proposed system can be seen in Figure 8.3.

In the designed system, the P-1 component consists of a servo motor and a bidirectional fixed displacement pump. P-2 is the main directional valve, P-3 is the pressure relief valves, P-4 is the directional valve, P-5 is the hydraulic accumulator and pressure relief valve, and finally, P-6 is the pre-charge valve. P-2 is valves that operate as on-off and only used to direct the oil. The amount of oil in the system and the adjustment of

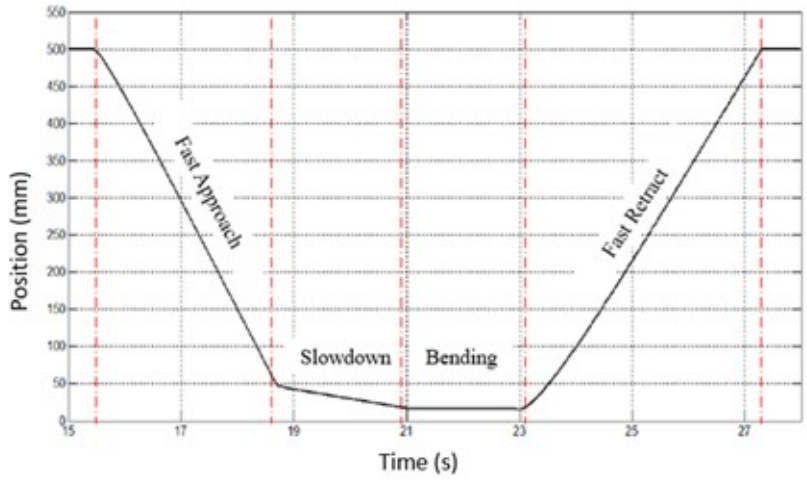

Figure 8.2: *Working stages of press brake system.*

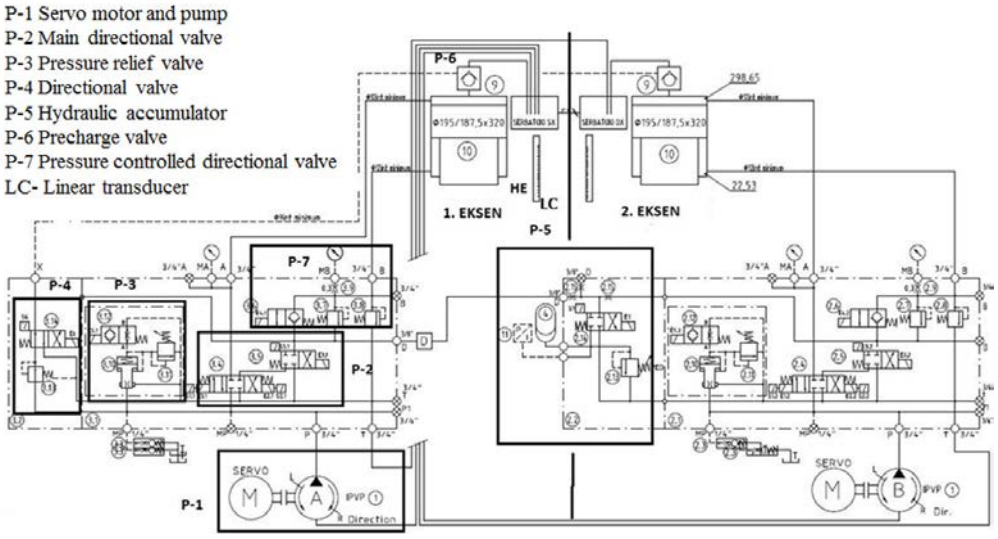

Figure 8.3: *Hydraulic circuit of proposed pump-controlled system.*

the pressure are carried out by the pump. P-4 directional and pressure relief valves are primarily used for pressure relief. P-3 activates in case of overpressure. P-5 hydraulic accumulator and pressure relief valves are used to return the generated energy to the system by accumulating it in the hydraulic accumulator. At the same time, a pressure relief valve is used in this part to prevent damage to the system in case of excessive pressure or excessive oil flow. The P-6 pre-charge valve performs oil suction from the tank by working based on vacuum during the downward movement in the cylinder. The hydraulic cylinder represents the working part of the designed electro-hydraulic system. The P-7 is a directional valve that works with pressure relief valves.

8.2.2 Sizing of the Pump-Controlled System

As with most processes in the industry, there are certain requirements from a press brake system used for bending sheet metals in order to perform the process appropriately. The requirements related to the process discussed in this study are given in Table 1.

Table 1. Desired requirements in bending process

Requirements	Symbol	Value	Units
Hydraulic actuator force	F_{HA}	80	ton
System pressure	P_{system}	270	bar
Downward velocity of hydraulic actuator	V_{down}	0,15	m/s
Pressing velocity of hydraulic actuator	V_{press}	0,01	m/s
Upward velocity of hydraulic actuator	V_{up}	0,15	m/s
Displacement of hydraulic actuator	L	0,5	m

According to the requirements in Table 1, the hydraulic cylinder cross-sectional area can be found with the formula below depending on the hydraulic actuator force value and the system pressure;

$$F_{HA} = \Delta P_{system} \times A_{cylinder} \tag{8.1}$$

Based on this equation, the cylinder piston diameter is found as 0,192 (m), but this value is determined as 0,195 (m) in order to choose from standard products. The required flow rate during the up and down movement of the cylinder can be calculated by the following equation;

$$Q_{1,2} = V_{1,2} \times A_{piston} \tag{8.2}$$

Where $Q_{1,2}$ (lt/min) are flow rate required for up and down movement and $V_{1,2}$ (m/sn) are velocity required for up and down movement. Accordingly, it is found as $Q_{1,2} = 4,48.10^{-3} m^3 s = 268,7$ (lt/min). Thus, the required pre-charge valve capacity for the system is determined. The pre-charge valve with a maximum 500 lt/min flow capacity was selected for the pre-charging process. When the flow required during the pressing process is calculated with equation (3) for the desired pressing speed, Q_{press} =17,91 (lt/min) is found. The power of the electric motor, which will provide torque to the pump, can be calculated by the following equation;

$$P = \frac{Q \times \Delta P_{system}}{\eta_v \times 600} \tag{8.3}$$

Where, P (kW) represents the power of the electric motor, η_v (-) represents the motor efficiency value that usually taken 0,95. Accordingly, the required electric motor power is calculated as 9,6 kW. In this case, the sizing process of the basic elements of a hydraulic power transmission system is completed. The dimensioned basic elements can be seen in Figure 8.4.

8.3 Results and Discussion

8.3.1 Test Results for One Loop (Pressure, Flow Rate and Velocity Variations)

In this section, the proposed pump-controlled system is examined in terms of the flow rate of the fluid circulating in the system and the power values of the process steps. The results of the experimental validation

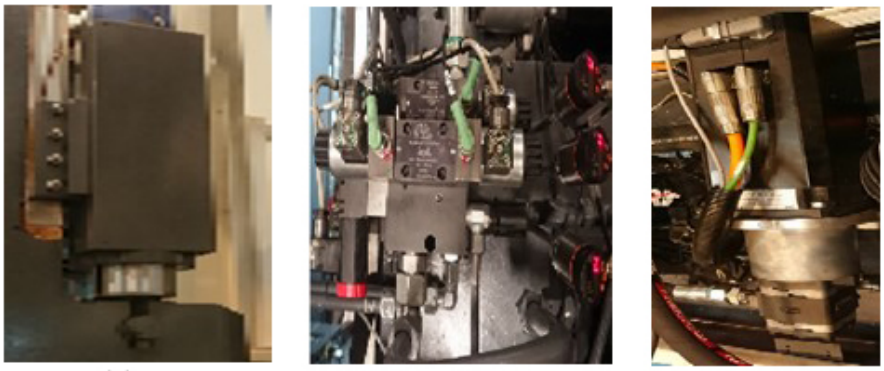

Figure 8.4: *Basic components of the proposed pump-controlled system: (a) hydraulic actuator (b) directional valve and pressure sensors (c) servo motor and pump.*

studies that carried out were analyzed. According to the results of the equations given in the previous section, the machine to be used in the experimental studies was dimensioned and the equipment selection was made based on the results obtained from these equations. The general characteristics of the machine are shown in Table 2.

Table 2. General Characteristics of the Experimental Setup

Servo Motor		**Pump**		**Valve**		**Cylinder**	
Maximum Velocity	3000 (rpm)	Maximum Pressure	345 (bar)	Working Pressure	315 (bar)	Maximum Force	80 (ton)
Maximum Torque	40 (Nm)	Maximum Speed	3600 (dev/dk)	Maximum Flow	80 (lt/dk)	Pressing Velocity	1 (cm/s)
Maximum Current	26 (A)	Maximum Flow	74,5 (lt/dk)	Response Speed	40 (ms)	Displacement	50 (cm)

Tests were carried out on thin specimens with a thickness of 1.5 mm and thick specimens with a thickness of 6 mm in the experimental setup composed of the elements in Table 2. The results obtained after the bending tests can be output from the controller result and analysis page. In Figure 8.5, the pressure, flow, and velocity curves obtained as a result of bending tests on thin parts of the test setup can be seen. According to the results obtained, as expected, the system pressure reached its maximum value of 285 bar at the time of bending, the flow rate provided by the pump remained at the lowest level at the time of bending, and the maximum flow rate was obtained as 24 lt/min during the retraction of the cylinder. In addition, it is seen that the speeds are 15,2 cm/s in the approach movement, 0,85 cm/s in the bending, and 16 cm/s in the retraction movement. Here, the desired maximum flow value during the approach and retraction movement of the cylinder is not provided by the pump alone. Unnecessary high-power pump usage is prevented by obtaining a high flow rate through the pre-charge valve. Thus, the motor adjusted the flow according to how much flow is required during the bending process and significantly preventing the losses in the valve-controlled system and increasing the efficiency.

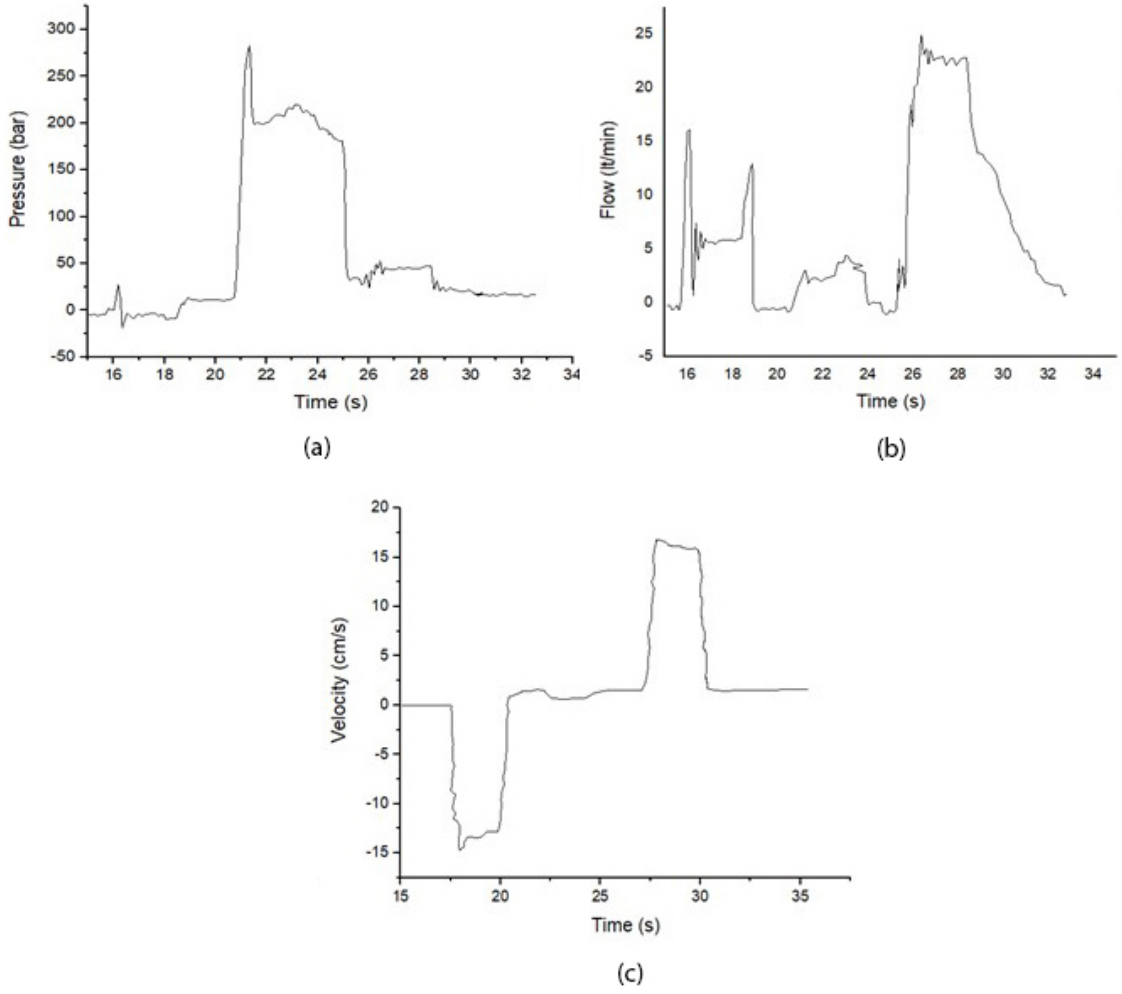

Figure 8.5: *Results obtained from experimental study: (a) Pressure change (b) Flow change (c) Velocity change.*

8.3.2 Energy Efficiency Analysis

In order to obtain the energy consumption of the tests carried out on the experimental setup, the average energy consumption of the two systems as a result of 100 cycles of bending tests at 9 cm position change is given in Table 3. Dimensions of the bent test piece with St42 material; 1 cm thickness, 20 cm wide, and 300 cm tall.

The energy consumed at the beginning of bending (W_0) and the energy consumed at the end of the bending process (W_1) were obtained with a measuring device on the experimental panel as in Figure 8.6. According to the measurement results, when the energy efficiency in the proposed pump-controlled system is compared with the energy efficiency in the traditional valve-controlled system, it is concluded that the proposed system is 54% more efficient.

Table 3: Energy consumptions of the conventional (valve-controlled) system and the proposed (pump-controlled) system.

	Valve-Controlled System		**Pump-Controlled System**	
Power (kWh)	Thin specimen (1,5 mm)	Thick Specimen (6 mm)	Thin Specimen (1,5 mm)	Thick Specimen (6 mm)
W_0	4,86	6,44	6,44	7,25
W_1	8,23	8,56	7,76	8,45
$W_1 - W_0$	3,37	2,12	1,32	1,2
Average	**2,74 kWh**		**1,26 kWh**	

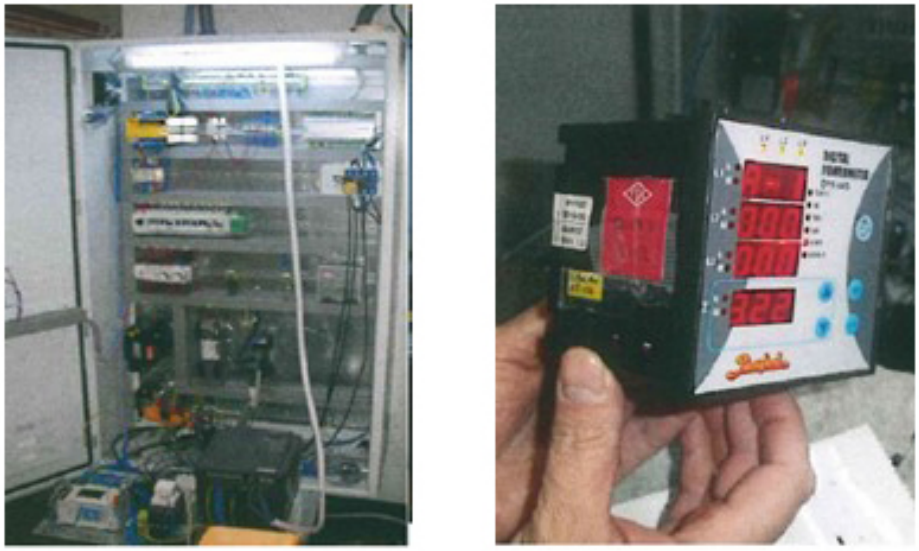

(a) (b)

Figure 8.6: *(a) Experimental measurement panel (b) Power consumption measuring device.*

The energy efficiency of the systems used in the industry is important as well as the initial investment costs for the manufacturers. In this context, the cost of pump-controlled and valve-controlled systems used in this study was compared. Due to the energy efficiency of the pump-controlled system, which has a higher initial investment cost, the time to amortize the cost difference between the two systems is discussed. The cost of the main components and the sum of the components used in both systems are given in Table 4.

Two scenarios are set up taking into account the initial investment and the cost of energy consumption for the same pressing conditions, and it is assumed that a press brake machine work for 15 hours/day, and 24 hours/day respectively with one cycle of 15 seconds. According to the information in Table 3 and the current electricity prices of 0.187 €/kWh [21], it is obtained as in Figure 8.7 that the pump-controlled and the valve-controlled system's costs will be equal approximately 3,5, and 2 years. Maintenance costs are not taken into account when making the calculations, only the costs of the components are calculated.

Table 4: Cost information of the conventional (valve-controlled) system and the proposed (pump-controlled) system

Pump-Controlled System		**Valve-Controlled System**	
Component	**Cost (€)**	**Component**	**Cost (€)**
IPVP-20 pump	5488	Vane pump	504
Servo motor ESA-142	3920	Asynchronous motor	252
Servo driver ESA-143	2464	Esa graphic unit	504
Main valve group	1232	Main valve group	616
Directional valve group	2691	Directional valve group	1521
Pressure valve group	900,9	Pressure valve group	900,9
Pre-charge valves	643,5	Pre-charge valves	643,5
Other equipments	491,4	Other equipments	491,4
Hydraulic accumulator	409,5		
Total	**18240,3**	Total	**5432,8**

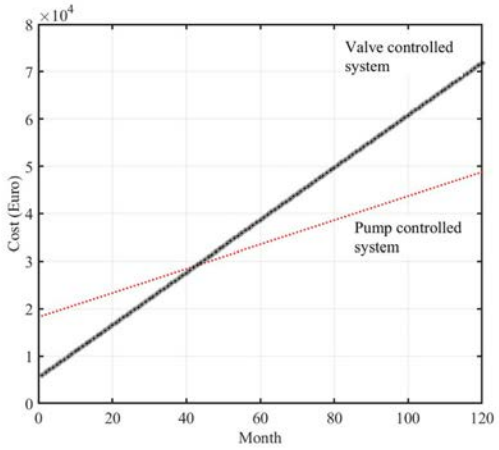

(a) working 15 hours/day

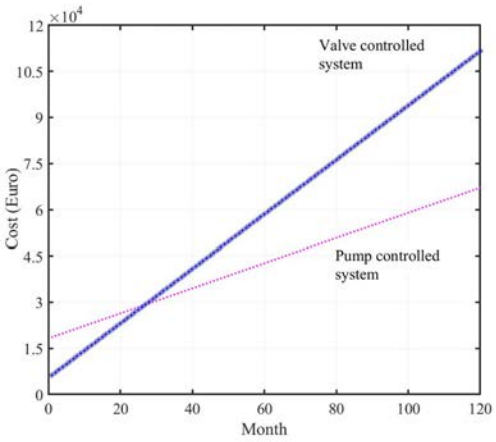

(a) working 24 hours/day

Figure 8.7: *Amortization period of proposed pump-controlled system.*

8.4 Conclusions

In this study, position control and analysis with pump control of a double-acting actuator are examined. It is aimed to comparatively examine valve-controlled conventional systems and servo motor-controlled pump systems in terms of energy efficiency. In the tests carried out in the experimental setup, the efficiency was found to be 54% higher than the classical valve-controlled system according to the number of 100 cycles of bending. The hydraulic tank capacity used in the traditional system is 135 liters in order not to overheat the oil and due to the extra circulation. In the pump-controlled system, the hydraulic tank for each axis is 34 lt. In total, the volume of the two hydraulic tanks is 68 liters. About half of the hydraulic oil is used in the pump-controlled system. In this case, the pump-controlled system can be accepted as an advantageous system in terms of preventing environmental pollution. In addition to energy efficiency, the amount of oil used in the pump-controlled system is approximately 50% less and it has been seen that it can be recommended as a more environmental solution. Since the oil is not exposed to the throttling in the valves, it heats up less, so it is also advantageous that there is no need to use extra energy for cooling. Based on these results, it

has been observed that the double-acting actuator can be precisely controlled with pump control, it can be successfully applied in press brakes used in sensitive bending processes, and the cost difference can be met at the appropriate time with energy efficiency.

In addition to the advantage in electricity consumption of a hybrid press brake system, it also has the features of ease of maintenance and needs less maintenance time. Decreasing energy costs and maintenance easiness provides a competitive advantage to companies in the production and use of products. Considering these results, high-volume system design and efficiency can be studied in the future, where high forces provided by hydraulic systems will be obtained.

Acknowledgments

All authors would like to thank BAYKAL MACHINE for data support and assistance in the preparation of this study Engin Can ÇELİK, who is the bursary of the TUBITAK 2244 Industrial doctorate program (Project code :118C120) presents his appreciation to the supporter institution.

Funding: It was carried out with the project number 1170141 within the scope of TUBITAK 1511 Priority Areas Research, Technology Development and Innovation Projects Support Program carried out by Baykal Machine, and certain parts of it were discussed as thesis topic.

Conflicts of Interest: The authors declare that they have no conflicts of interest.

Authors Contributions: Methodology, management of experimental studies, preparing results and analysis has been conducted by Ö.P. Sections of methodology, results & discussion have been conducted by E.E.T. Abstract, introduction, literature review, conclusion, and edit of sections have been prepared by Ö.P. and E.E.T. Literature review and last revisions of the manuscript have been accomplished by E.C.Ç. All authors edited and agreed to the manuscript.

References

1. Pehlivanoglu, Ö. Analysıs of servo motor drıve hybrıt press brake system. Msc. Thesis, Bursa Uludag University, 2019. https://avesis.uludag.edu.tr/yonetilen-tez/01eb9489-70de-4c0d-9b70-e3ff08f9e4fd/servo-motor-tahrikli-hibrit-abkant-pres-sisteminin-analizi
2. Shang, T., Submitted, T., & Fulfillment, P. (2004). Improving Performance of an Energy Efficient Hydraulic Circuit. *Ph. D. Thesis,* University of Saskatchewan Saskatoon, Saskatchewan. https://central.bac-lac.gc.ca/.item?id=TC-SSU-04242004151248&op=pdf&app=Library&oclc_number=1007592909
3. Gao Bo, Fu Yong-ling, & Pei Zhong-cai. (2005). Research of the Servo Pump's Electrically Driven Variable Displacement Mechanism. *IEEE International Conference Mechatronics and Automation,* 2005, 4(July), 2130–2133. https://ieeexplore.ieee.org/document/1626892
4. Çalışkan, H., Balkan, T., Platin, E. B., & Demirer, S. (2008). Değişken Devirli Pompa ile Servo Hidrolik Konum Kontrolü. *V. Ulusal Hidrolik Pnömatik Kongresi,* 359–375. http://www.hpkon.net/wp-content/uploads/mdocs/2008-30.pdf

5. Çelikayar, G. (2008). Servo Motor Tahrikli Pompa Kontrol Sistemleri ve Enerji Tasarrufu. *V. Ulusal Hidrolik Pnömatik Kongresi,* 151–159. http://www.hpkon.net/wp-content/uploads/mdocs/2008-12.pdf
6. Deng, Y., Wu, Y., & Xu, Y. (2016). Energy Recovery of Testing Bed for High-Speed Hydraulic Pumps. *AUS 2016- 2016 IEEE/CSAA International Conference on Aircraft Utility Systems,* 1122–1127. https://ieeexplore.ieee.org/document/7748227
7. Li, L., Huang, H., Zhao, F., Triebe, M. J., & Liu, Z. (2017). Analysis of a Novel Energy-Efficient System with Double-Actuator for Hydraulic Press. *Mechatronics,* 47, 77–87. https://www.sciencedirect.com/science/article/abs/pii/S0957415817301162
8. Li, M., Shi, W., Wei, J., Fang, J., Guo, K., & Zhang, Q. (2019). Parallel Velocity Control of an Electro-Hydraulic Actuator with Dual Disturbance Observers. *IEEE Access,* 7, 56631–56641. https://ieeexplore.ieee.org/document/8707088
9. Detiček, E., & Kastrevc, M. (2016). Design of Lyapunov Based Nonlinear Position Control of Electrohydraulic Servo Systems. *Strojniski Vestnik/Journal of Mechanical Engineering,* 62(3), 163–170. https://www.sv-jme.eu/article/design-of-lyapunov-based-nonlinear-position-control-of-electrohydraulic-servo-systems/
10. Liang, L., Le, Z., & Li, J. (2017). Frequency Analysis and PID Controller Design for a Pump-Controlled Electrical Hydraulic System. 2017 *IEEE International Conference on Mechatronics and Automation, ICMA* 2017, 1150–1155. https://ieeexplore.ieee.org/document/8015979
11. Kocabıçak, Z. K., Topçu, E. E., & Yüksel, İ. (2011). Bir Plastik Enjeksiyon Makinesinin Hidrolik Sisteminde Değişken Hız Denetimli Motor Kullanımının Enerji Verimi Açısından Kuramsal İncelemesi. VI. *Ulusal Hidrolik Pnömatik Kongresi,* 25–33. http://www.hpkon.net/wp-content/uploads/mdocs/2011-03.pdf
12. Topçu, E.E. (2017). PC-Based Control and Simulation of an Electro-Hydraulic System. *Computer Applications in Engineering Education,* 1-13. https://onlinelibrary.wiley.com/doi/abs/10.1002/cae.21831
13. Sun C, Fang J, Wei J, Hu BO (2018) Nonlinear Motion Control of a Hydraulic Press Based on an Extended Disturbance Observer. IEEE Access 6:18502–18510. https://ieeexplore.ieee.org/document/8308715
14. Lyu, L., Chen, Z., & Yao, B. (2019). Development of Pump and Valves Combined Hydraulic System for Both High Tracking Precision and High Energy Efficiency. *IEEE Transactions on Industrial Electronics,* 66(9), 7189–7198. https://ieeexplore.ieee.org/document/8495014
15. Yao Z, Yao J, Yao F et al (2020) Model reference adaptive tracking control for hydraulic servo systems with nonlinear neural networks.*ISA Trans.* 100:396–404. https://www.sciencedirect.com/science/article/abs/pii/S001905781930521X.
16. Noskievip, P. (2019). Identification of Linear Hydraulic Actuator using Self-excited Oscillations. *2019 20th International Conference on Research and Education in Mechatronics (REM),* 5, 1–6. https://ieeexplore.ieee.org/document/8744107
17. Quan, Z., Quan, L., & Zhang, J. (2014). Review of energy efficient direct pump-controlled cylinder electro-hydraulic technology. *Renewable and Sustainable Energy Reviews,* 35, 336–346. https://doi.org/10.1016/j.rser.2014.04.036
18. D., Li, Y., Li, Y., Zhang, P., Dong, S., & Yang, L. (2018). Study on PMSM power consumption of dual-variable electro-hydraulic actuator with displacement-pressure regulation pump. *IEEE/ASME International Conference on Advanced Intelligent Mechatronics, AIM,* 2018-July 1172–1177. https://ieeexplore.ieee.org/document/8452426
19. Filo, G., Lisowski, E., Kwiatkowski, D., & Rajda, J. (2019). Numerical and Experimental Study of a Novel Valve Using the Return Stream Energy to Adjust the Speed of a Hydraulic Actuator. Strojniški Vestnik – *Journal of Mechanical Engineering,* 65, 103–112. https://www.sv-jme.eu/article/numerical-and-experimental-study-of-a-novel-valve-using-the-return-stream-energy-to-adjust-speed-of-hydraulic-actuator/

20. Navatha, A., Bellad, K., Hiremath, S. S., & Karunanidhi, S. (2016). Dynamic Analysis of Electro Hydrostatic Actuation System. *Procedia Technology, 25(Raerest),* 1289–1296. https://doi.org/10.1016/j.protcy.2016.08.223
21. https://www.uludagelektrik.com.tr/2022-guncel-elektrik-tarifeleri (accessed October 26, 2022)
22. Balcı, M.Ş., Sakar, S., Dalcalı, A., (2022). Electromagnetic Energy Harvester Design for Power Transmission Line, *Transdisciplinary Journal of Engineering & Science,* 13. https://doi.org/10.22545/2022/00211
23. Palande, D. D., Ghuge, N., & Dapase, C. R. (2022). Waste Heat Recovery from The Hot Water Boiling Plant Analysis using CFD. *Transdisciplinary Journal of Engineering & Science,* 13. https://doi.org/10.22545/2022/00182
24. Li, Z., Wang C., Quan, L., Hao, Y., Ge, L., & Xia. L. (2021). Study on energy efficiency characteristics of the heavy-duty manipulator driven by electro-hydraulic hybrid active-passive system. Automation in Construction. 125, https://doi.org/10.1016/j.autcon.2021.103646
25. Savran, E., Yavaş, Özcan, Erolnalbur, B., & Karpat, F. (2022). Energy and Carbon Loss Management in an Electric Bus Factory for Energy Sustainability. *Transdisciplinary Journal of Engineering & Science,* 13. https://doi.org/10.22545/2022/00207

About the Authors

Ozkan Pehlivanoĝlu received his B.Sc. from Eskişehir Osmangazi University in 2002, and M.Sc. from Bursa Uludaĝ University in 2019. He has been working Baykal Machine since 2006.

Dr. Elif E. Topçu, associate professor in Mechanical Engineering at Bursa Uludag University. She received her B.Sc. in 1998, M.Sc. in 2000, and Ph.D. in 2005 from Bursa Uludaĝ University. She joined the academic community as research assistant in 1998 and she continued her success by gaining the title of associate professor in 2018. Her professions based on fluid power systems and their control, electromechanical system design and control, mechatronics, system modeling and analysis.

Engin C. Çelik is a Ph.D. student in mechanical engineering department of Bursa Uludag University. He received B.Sc. degree from Bursa Uludaĝ University. He started Ph.D. in 2020 as a scholarship holder

of The Scientific and Technological Research Council of Turkey (TUBITAK), His research areas are fluid power systems and automatic control.

CHAPTER 9

Exploring Grassroots Renewable Energy Transitions: Developing a Community Scale Energy Model

L. Codrington, E. Haghi, K. Moo Yi and M. McPherson

Article citation information: (2022), *TJES*, Vol. SP-2, pp. 137-163, doi:10.22545/2022/00215

Decarbonizing energy systems through the integration of decentralized renewable energy generators creates opportunities for community-scale actors to participate in energy system decision-making. However, typical modelling approaches exclude community stakeholders, causing a loss of local knowledge. This exclusion is problematic for Indigenous peoples in so-called Canada where the natural resource industry harms their land and communities. The Exploring Grassroots Renewable Energy Transitions (EGRET) platform introduced in this work presents an alternative to typical energy system modelling because it facilitates community participation throughout the model development and application process. This platform was developed in partnership with a local First Nation's energy specialist to assess whether solar panels could increase community energy sovereignty. The platform's user interface, visualization suite, and high-speed machine learning models make energy system modelling accessible to community members through interactive workshops. In the future, the EGRET approach could be generalized for stakeholder-led renewable energy exploration in other community settings.

Keywords: Decarbonization, variable renewable energy integration, community energy, Indigenous energy, energy system modelling, participatory modelling, machine learning.

9.1 Introduction

Mitigating climate change is an urgent global issue. In 2015, the United Nations Framework Convention on Climate Change agreed upon a "safe" maximum global temperature increase of 2°C above pre-industrial levels, with an ideal upper limit of 1.5°C later set by the Intergovernmental Panel on Climate Change (IPCC) to further reduce the negative effects of global warming [1]. A 2018 report by the IPCC found that this 1.5°C limit could be reached as soon as 2040 [2]. Maintaining global temperatures within this threshold requires that net-zero greenhouse gas emissions be reached by 2050 [3]. The International Energy Agency (IEA) has urged the widespread, immediate deployment of every clean energy and energy efficiency technology available to make net-zero possible over the next 30 years [3]. In response, the Canadian government is targeting a two- to three-fold increase in national clean power production by 2050 [4].

Towards this effort, variable renewable energy (VRE) generators are the technologies most commonly associated with clean energy. These generators, such as wind turbines and solar photovoltaic panels, transform abundant natural resources into energy with a relatively small carbon footprint. However, there are two issues

that make integrating VRE generators into electricity networks a challenge. First, as their name implies, VRE generators provide an inconsistent source of energy because operators have no control over when wind or sunlight is available. Electricity systems that incorporate VRE generators must have sources of flexibility, such as storage devices, available to provide energy when the weather is cloudy and still [3]. Second, VRE generators are often widely spatially distributed as they must be placed wherever their powering resource is most abundant [5]. Current electricity systems are designed around centralized power plants to simplify control and transmission.

The first challenge highlights the need for complex energy system modelling when integrating VRE into the grid. Every region will have different characteristics — such as the flexibility of the existing power system and the seasonal variability of wind and solar resources — that will dictate how much VRE can be reliably integrated. The second challenge heralds an upcoming shift in energy system structure. The decentralization of VRE generators brings new actors and new priorities into the energy space, redistributing the power of traditional energy systems (in both senses of the word) to local actors through energy democracy [6].

Looking at these two challenges simultaneously, a third issue emerges. Communities, individuals, and other local actors in the energy democracy movement may not have the resources to design and model a VRE-integrated grid in-house. Energy system models are computationally expensive to run, and often require experience and training to operate [7]. Typical industry three-step scenario modelling frameworks only include stakeholders in the scenario development phase, leading to the overrepresentation of modeller perspectives and exclusion of local knowledge during model development and results analysis [8]–[10]. For example, two of the most commonly applied tools for modelling decentralized energy systems, the Hybrid Optimization of Multiple Energy Resources (HOMER) software and EnergyPLAN, exclude most stakeholders because they require users to have prior knowledge of energy system analysis [11]–[13]. These tools are also not open source, blocking even experienced users from adapting them to reflect community priorities through model (re)development. An open source tool, called the Open Energy Modelling Framework (oemof), was developed to address this barrier, but it is still designed for users with an understanding of energy system modelling and analysis [14], [15]. oemof developers also list the communication of model results as an ongoing challenge, further limiting the ability of inexperienced users to interact with the tool in the results analysis step of the modelling process [15].

While available tools do not facilitate accessible engagement, community input into the energy system design process is crucial. Frameworks for change that bring individuals and communities into the decision-making process through participatory governance are key to ensuring an equitable transition [16]. For example, transdisciplinary approaches that include diverse stakeholders could help mobilize society to achieve the United Nation's sustainable development goal of affordable clean energy, which Canada has not yet achieved [17]. The exclusion of stakeholders from renewable energy decision-making is particularly damaging for Indigenous communities in so-called Canada because the natural resource industry and renewable energy developments have inflicted harm on Indigenous lands and communities [18]. Decarbonization presents an opportunity for reconciliation through Indigenous ownership over renewable energy production, but barriers make ownership challenging for some communities [19], [20]. One common barrier is the need for outside consultation when navigating energy technologies and modelling tools because of community capacity strains, leading to the exclusionary modelling process outlined above [20].

The Exploring Grassroots Renewable Energy Transitions (EGRET) platform introduced in this work aims to make all stages of the modelling process accessible to stakeholders. The guiding concept behind the platform is the participatory system dynamics framework described in [21], which recommends the inclusion of stakeholders at all stages of model development, use, and analysis to promote deep learning about the system in question. Designed for use in collaborative workshop settings, the EGRET platform is powered by high-speed machine learning models to support dynamic conversation and a broad exploration of the renewable energy design space. These models are packaged with a user interface and visualization suite to make the platform accessible to use and interpret. The EGRET platform was designed and developed in collaboration with Musqueam band's community energy specialist to ensure the platform would meet the needs of the community in which it would be applied.

9.1.1 xʷməθkʷəy̓əm Energy Context

xʷməθkʷəy̓əm (Musqueam) are traditional hən̓q̓əmin̓əm speaking people living in their territory (currently called Vancouver and the surrounding areas) for thousands of years [22]. Musqueam Indian Reserve number 2, located at the mouth of the Fraser River to the north of Sea Island, is a small portion of Musqueam Nation's traditional territory. Musqueam Nation has a vision of self-sufficiency and self-government as stated in the Nation's comprehensive community development plan [23]. To achieve these goals, Musqueam band and members have engaged in multiple projects focused on:

- Improving the energy efficiency of Musqueam homes and public buildings
- Reducing greenhouse gas (GHG) emissions from energy consumption in the community
- Investigating the feasibility of renewable energy generation on Musqueam reserve

Currently, Musqueam homes, public buildings, and vehicles are the major energy consuming sectors and sources of GHG emissions in the community. Figure 9.1 shows the estimated shares of the community's top GHG emissions sources.

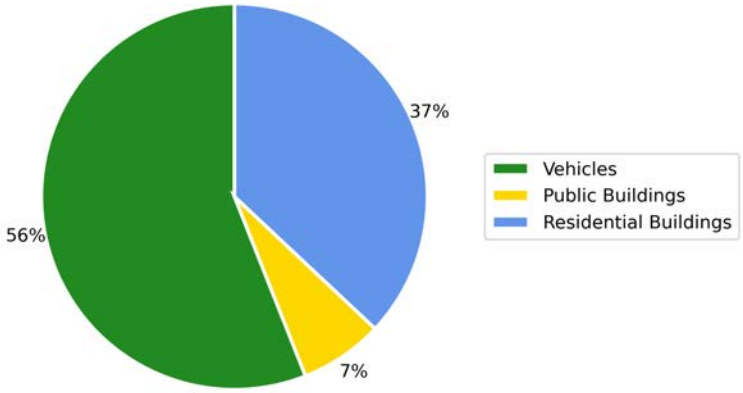

Figure 9.1: *The estimated share of different GHG emissions sources in the Musqueam community.*

As shown in Figure 9.1, vehicles are the most significant source of GHG emissions in the community. Residential buildings are the second largest source of GHG emissions, with a total of 37% of annual GHG emissions, while public buildings account for 7% of the annual GHG emissions.

As stewards of their land, Musqueam people are exploring options that enable their transition to a net-zero community. One of the most promising technologies that enables such a transition is solar power. Solar power is a commercially available technology that can provide clean electricity to the community and reduce energy bills for both Musqueam members and the band. The development of renewable energy generation capacity in the community also aligns with the self-sufficiency and self-governance goals of the Nation [23].

The EGRET platform provides a tool for Musqueam departments and leadership to engage with community members regarding a renewable energy development project. The EGRET platform enables Musqueam members and staff to investigate different aspects of a renewable energy project including the cost to the community and GHG emission reduction potential. The EGRET platform also allows comparing different renewable energy technologies as well as storage system sizes. The EGRET platform eases the process of consultation with Musqueam members which is an integral step in any community-based project in Musqueam.

The remaining three sections in this paper outline how the EGRET platform was constructed and evaluated, highlight the key results of the evaluation process, and discuss these results in the context of the platform's goals. The methodology section focuses on the technical development of the platform, including the machine learning approaches used and the data processing steps needed to apply them. The results section considers both community feedback and objective measures of the platform's effectiveness. Finally, the discussion section draws conclusions about the platform's ability to engage community members in the energy modelling process, addresses the limitations of this project, and makes recommendations for future work.

9.2 Methodology

The EGRET platform consists of three components: an interface where the user selects an energy system scenario, a visualization suite that compares results, and the machine learning surrogate models that transform the user's inputs into these visualized results. The user interface and two visualization views are shown later in figures 9.11 to 9.13. In essence, surrogate models use supervised learning to understand and replicate the connection between the inputs and outputs of an established model. The concept is applied here to maximize user interactivity; surrogate models can be evaluated much faster than the optimization-based models they replicate due to the absence of a time-consuming optimization loop.

The EGRET surrogate model replicates the results of the Strategic Integration of Large-capacity Variable Energy Resources (SILVER) model developed by the Sustainable Energy Systems Integration and Transitions group at the University of Victoria [24]. SILVER takes a theoretical energy system — made of user-specified generators and their characteristics — and simulates its operation based on given demand and VRE potential data. The results are hourly generation profiles for each asset on the system as well as an operational cost break down over the specified period. By creating a large dataset of inputs and associated outputs from the SILVER model, EGRET can be trained to replicate these results in a fraction of the time.

This section focuses on the development and testing of the surrogate model and the data upon which it was trained, but it will also touch on the compilation of the platform and the final evaluation process. The University of Victoria human research ethics board approved the original research project, code 21-0553-01, on April 1st, 2022, with amendments accepted on October 6th, 2022.

9.2.1 Data Processing

Developing a surrogate model requires a dataset of inputs and outputs from the model being replicated; in this case, that model is SILVER. The following paragraphs outline the data processing steps taken to obtain SILVER inputs, as well as how those steps were repeated to build the full dataset. Figure 9.2 shows an overview of these inputs and the data flow through both SILVER and the EGRET surrogate model, as well as how the data is transferred from one to the other through the machine learning model's training process.

The first input needed to run SILVER is electricity demand for the region being modelled. Monthly electricity demand values for 39 residential and 6 public buildings in the community were available. The residential data came from an energy audit process previously done in the community using the building energy modelling tool HOT2000. These results were scaled up to represent the 250 total homes in the community. The public building consumption data is actual electricity use measured from December 2017 to August 2021 and averaged per month. While these monthly totals are useful data points, the SILVER model requires hourly demand resolution.

Two methods of increasing resolution from monthly to hourly were explored. The first method uses hourly normalized internal gains specified by the National Building Council of Canada (NBCC) to scale electricity demand [25]. In this method, the total community electricity consumption per month is divided by the number of hours in the month to obtain an average hourly consumption value. This number is then multiplied by the NBCC's normalized hourly internal gain factor for each hour in the day. This process results in twelve 24-hour representative load profiles — one for each month — which are then repeated to

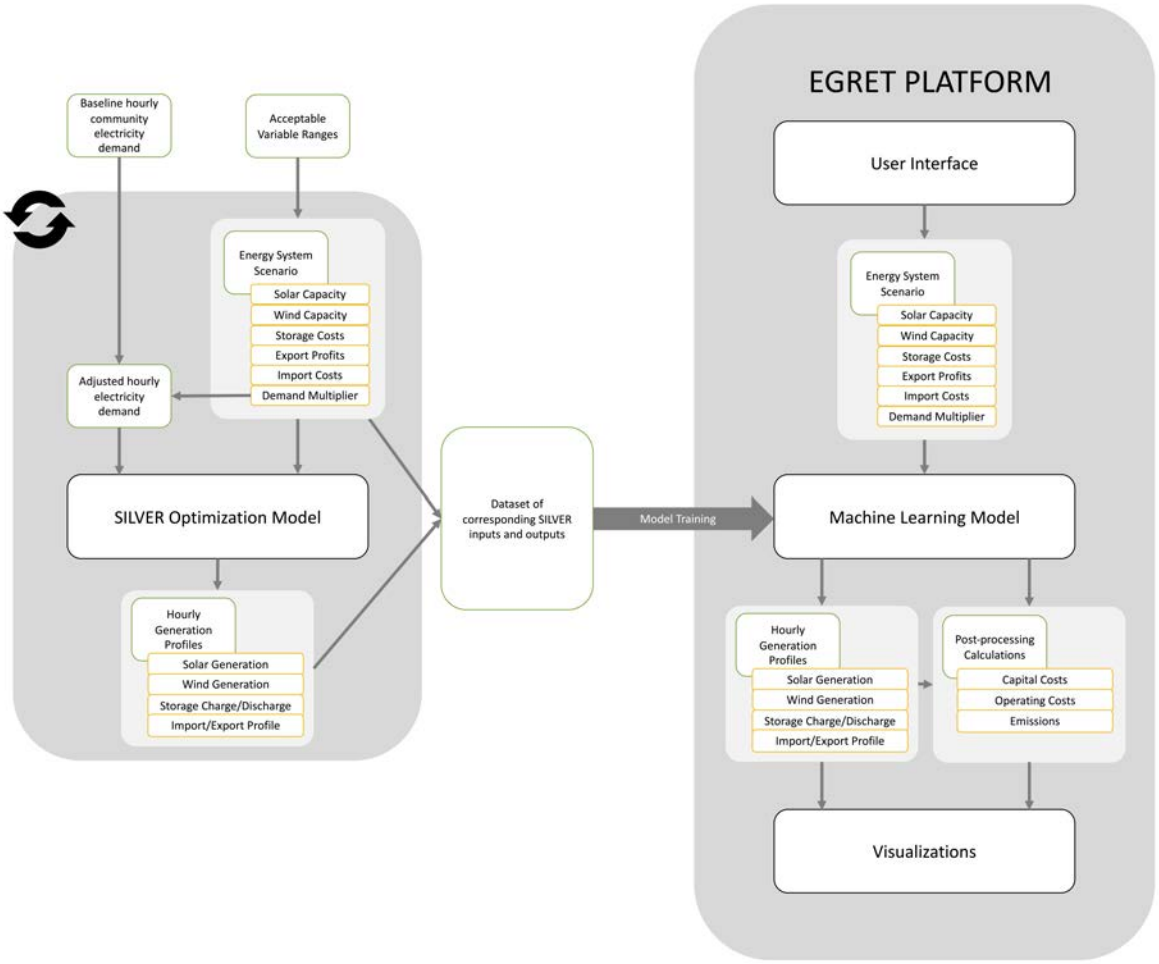

Figure 9.2: *The SILVER model is run repeatedly for randomly generated energy system scenarios to create a dataset of inputs and outputs. In turn, this dataset is used to train the machine learning models behind the EGRET platform.*

build an annual curve. Because SILVER breaks the year into twelve thirty-day periods, the representative days were each repeated thirty times to create a "year" of 360 days.

The second method adjusts an annual electricity demand curve with hourly resolution from a community in Northern Quebec, Kangiqsualujjuaq, with a similar population to Musqueam Indian Reserve number 2. This publicly accessible demand curve was provided by Natural Resources Canada (NRCAN). The Kangiqsualujjuaq demand curve was scaled to match Musqueam community's monthly demand. This scaling process addressed population and climate differences between the two communities. In this method, the total demand of the reference community is summed over each thirty-day period. Each hourly demand value is then normalized by the corresponding thirty-day total to obtain hourly factors, which are in turn multiplied by Musqueam community's corresponding thirty-day demand to obtain an annual curve. Because

of the normalization steps in both methods, both 360-day "annual" curves have the same thirty-day total demand, allowing for comparison. Figure 9.3 shows an annual comparison of the demand curves as well as a snapshot of January demand values for better understanding of day-to-day variation.

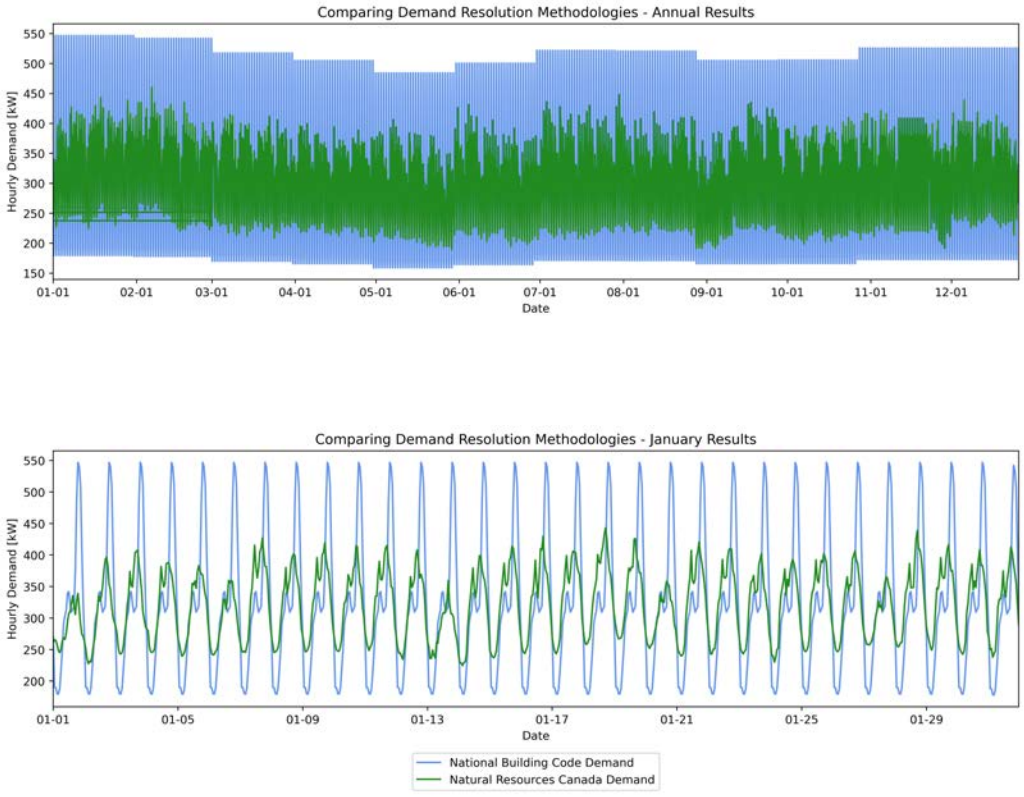

Figure 9.3: *These plots compare the demand curves produced by the NBCC and NRCAN demand methodologies. The top figure shows the full annual profiles, and the bottom figure zooms in to show daily fluctuations through the month of January.*

These two methods were tested by modelling the scenarios shown in table 9.1 using SILVER over a one-year period. Each scenario was modelled twice; once with the NBCC demand, and a second time with the NRCAN demand. Variables not shown in table 9.1 were kept constant across all scenarios. Figure 9.4 compares the total generation by technology type resulting from the two demand methodologies for each scenario.

Table 9.1: *SILVER scenarios used to test demand curve options.*

Scenario	Solar Capacity kW	Wind Capacity kW	Storage Power kW	Storage Energy kWh	Import Cost $/kWh	Export Profit $/kWh
1 - Baseline	-	-	-	-	0.093	0.093
2 - Solar	100	-	-	-	0.093	0.093
3 - Wind	-	500	-	-	0.093	0.093
4 - Solar & Storage	1000	-	130	232	0.1	0.093

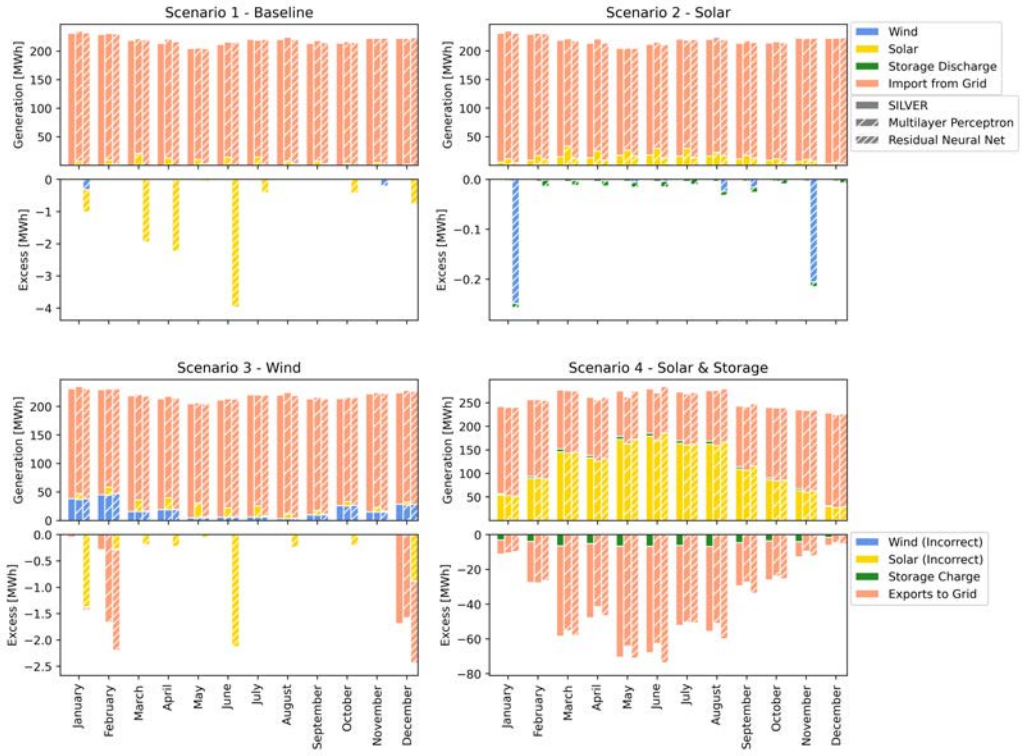

Figure 9.4: *Total monthly energy generation by technology type is shown for each scenario. The solid bars on the left resulted from the NBCC demand methodology, and the hatched bars on the right resulted from the NRCAN demand methodology.*

As shown in Figure 9.4, Scenario 1 produced the same total monthly generation for both demand methodologies. This behaviour was expected as no variable generators were present in the scenario. The same behaviour was observed in Scenario 2, showing that temporal demand discrepancies do not have an effect when only limited VRE generation capacity is present. However, the total electricity exported per month varies between demand methodologies when modelling Scenario 3. This behaviour shows that differences in temporal demand values have an impact on SILVER's results when VRE generation exceeds consumption. As the amount of generation increases further beyond demand, the difference in outputs from the two demand methodologies also increases, as shown in the modelled Scenario 4 results.

In the case of these two demand profiles, the first method has lower load values at midday, when solar generation is most active, than the second method. As a result, the scenarios with solar generation capabilities export more to the grid with the first demand profile. The first method also has lower demand values at night when wind resources are typically most abundant. As a result, the scenarios with wind generation capability also export more to the grid with the first demand profile. These findings highlight the importance of accurate community hourly demand data in situations where the community is looking to sell excess electricity back to the grid.

For the purposes of this study, the demand curve produced by the second method was selected for use in the EGRET training process because it is based on the demand of a real community and has more day-to-day variability, as shown in Figure 9.3.

Another data component needed to run SILVER is VRE potential. VRE potential is the amount of electricity a given generator type would produce at every hour in the time series under typical weather

conditions. These datasets were obtained from Renewables.ninja for Musqueam community's geographical position using the Modern Era Retrospective-Analysis for Research and Applications (MERRA) 2019 weather file [26], [27]. Solar potential was calculated assuming the South-facing, 1kW panels were oriented 35 degrees from horizontal. Wind potential was calculated assuming a Vestas V47 660 turbine.

Table 9.2: *Range of acceptable inputs to the SILVER model and their justification.*

Variable	Range	Justification
Solar Capacity	1-6300kW	The minimum reflects a small, one-residence installation. The maximum assumes the whole area Musqueam community is considering for development is converted into a solar farm [28].
Wind Capacity	10-1200kW	The minimum reflects the smallest turbine available on the market. The maximum assumes the whole area Musqueam community is considering for development is used for wind turbines [29].
Storage Power Capacity	5-130kW	This range is based on commercially available battery technologies.
Storage Energy Capacity	1-230kWh	This range is based on commercially available battery technologies.
Import Price	0.05-0.25 $/kWh	This range is based on current BC rates of about 0.1$/kWh and projected provincial increases with a bias towards rising energy prices [30].
Export Profit	0.05-0.25 $/kWh	This range is based on current BC rates of about 0.1$/kWh and projected provincial increases with a bias towards rising energy prices [30].
Number of Households	50-500 households	There are currently about 250 homes in the community. This range is biased towards growth due to the community's long housing waitlist.

SILVER also requires several inputs which together define the available electricity generation assets and the overall energy system scenario. As shown in Figure 9.2, these inputs include the capacity of any solar generation assets, the capacity of any wind generation assets, the power and energy capacity of any storage assets, and the cost of importing electricity from the grid. The researchers adapted SILVER to include a separate price for electricity being exported to the grid, so Musqueam members can explore the financial impact of selling excess power generated by VRE technologies. The researchers also incorporated the number of households in the community as an extra input, which is used to adjust the baseline electricity demand curve and explore how future community growth could affect Musqueam's energy system.

To create a dataset of SILVER inputs and outputs, the above-mentioned inputs were randomly generated within a variable-specific acceptable range as defined by the researchers. These ranges and their justification are summarized in Table 9.2. SILVER was run a total of 1996 times with randomly generated inputs to produce the dataset, which covered generation profiles for an entire year. However, preliminary attempts at training a machine learning model on a whole year's worth of data were less accurate than those trained

on a single month. The annual dataset was divided into twelve monthly datasets to facilitate the training of separate monthly machine learning models. These twelve datasets were each split into training, validation, and testing subsets each with 1434, 281, and 281 SILVER runs, respectively. All features and labels were normalized using the mean and standard deviation of the corresponding feature or label in the training dataset.

9.2.2 Surrogate Model Development

The machine learning surrogate model was developed in Python using PyTorch Lightning [31]. PyTorch Lightning is a deep learning framework with built-in functions to simplify the machine learning process. These tools were used to construct two different machine learning model architectures: a typical artificial neural net (ANN) composed purely of fully connected layers or multilayer perceptrons (MLP), and a residual neural net (ResNet) [32]. MLP models are very flexible in terms of architecture, size, and hyperparameter selection. As such, they are good candidates for energy system model applications [33]. However, particularly complex data relationships (typically image recognition) can require neural nets that are very deep for good accuracy [34], and these additional layers can make training difficult with traditional MLPs [32]. ResNet architectures can alleviate these challenges [32]. The authors chose to investigate the use of ResNet in case a deep neural net was required to predict the large number of time series outputs produced by SILVER. Basic representation of the MLP and ResNet architectures are shown in Figures 9.5 and 9.6, respectively.

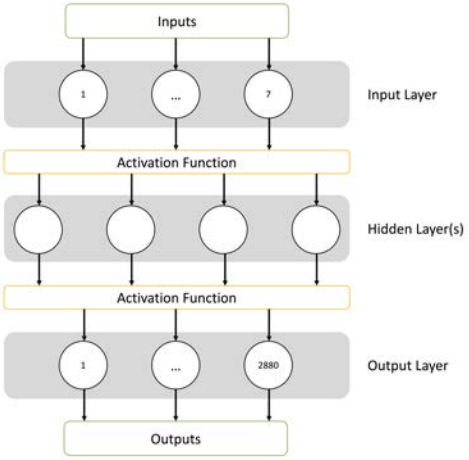

Figure 9.5: *Basic MLP architecture with an input layer, hidden layers, and an output layer.*

Both the MLP and ResNet architectures were tuned using the hyperparameter optimization framework Optuna [35]. To do so, a skeleton model with optimizable parameters is trained with the provided training dataset. The trained skeleton model then predicts outputs for the inputs in the testing dataset. These predictions are compared to the actual outputs from the testing dataset using a loss function, resulting in a loss value. Optuna then repeats this process with a new set of parameter values.

For the MLP architecture, the number of layers, number of neurons in each hidden layer, and activation function applied to each layer, as well as hyperparameters like batch size, learning rate, and the loss function used to evaluate model performance were identified as optimizable parameters. For the ResNet architecture, the number of groups, number of blocks in a group, number of nodes in a layer in each group, activation function, batch size, learning rate, and loss function were identified as optimizable parameters.

Because of limited computational availability, the importance of having a unique model architecture for each month versus using a shared model architecture for all months was tested. Each approach has its own

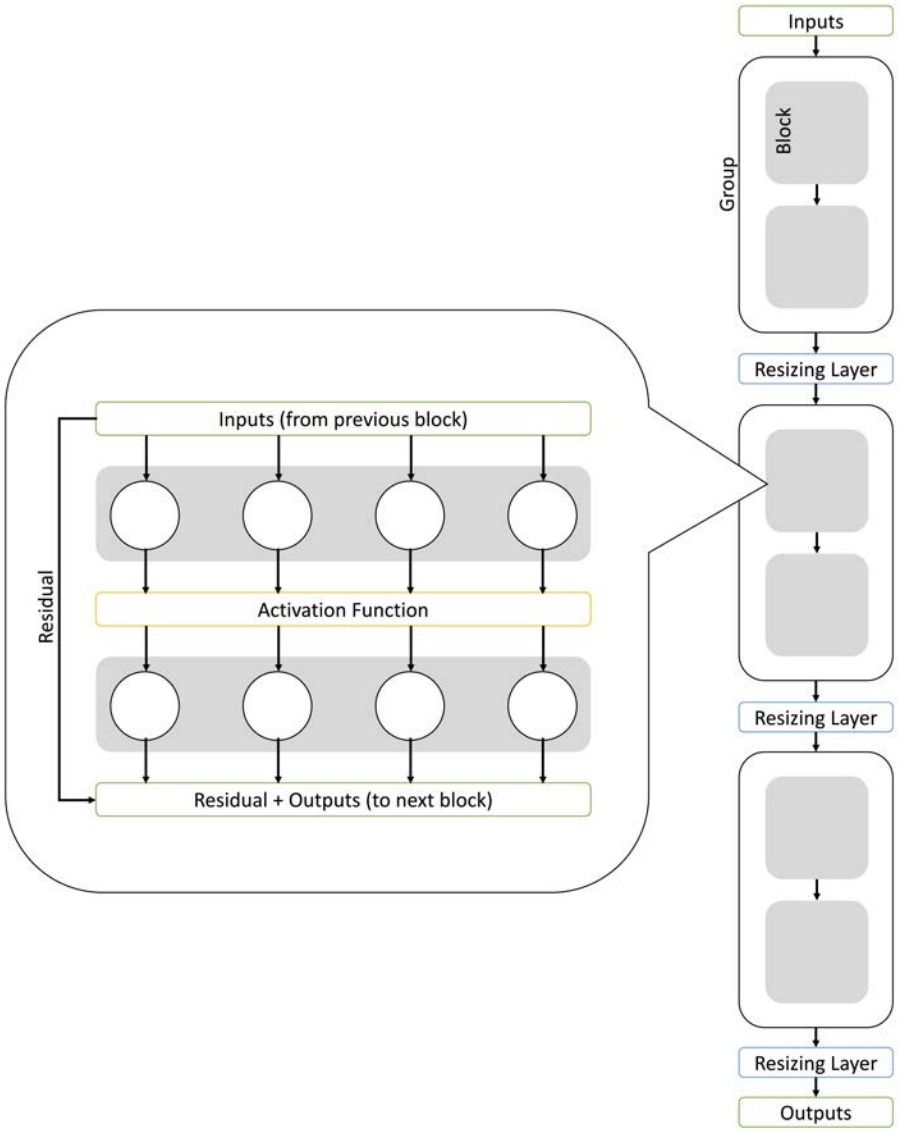

Figure 9.6: *Basic ResNet architecture made of groups of blocks. Each block is made of two layers, and every block in a group has the same number of neurons per layer.*

benefits; creating twelve unique models would optimize each architecture for the given 30-day data subset, while a single, shared model architecture would allow for broader hyperparameter space exploration and reduced optimization and training loads. Using the MLP architecture as a test, twelve Optuna hyperparameter optimizations were conducted. Each optimization was trained on the corresponding monthly data subset and consisted of 100 parameter trials. Each trial could take a maximum of 500 steps. A single optimization was conducted on the January data subset with 1000 trials of 1000 steps each. Both optimizations could prune trials with poor results after 25 steps.

To compare, the parameter values from the best trial for each optimization were used to construct MLP models. The twelve unique monthly models and twelve copies of the shared model architecture were trained and tested on their corresponding data subsets. The mean absolute error (MAE) loss and loss variance for each test were recorded and visualized in Figure 9.7. The lines represent the average MAE loss across all test predictions for each architecture type, and the shaded areas represent the variance in loss across these test predictions. The shared MLP architecture performed better across all months, likely due to deeper parameter space exploration and therefore better parameter optimization.

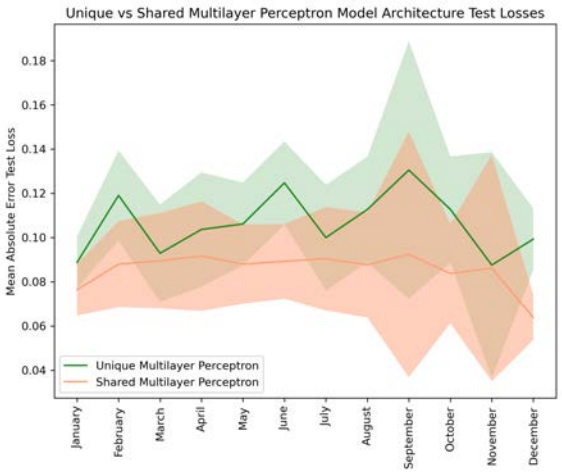

Figure 9.7: *Comparing the MAE losses of unique and shared monthly model architectures. The shaded areas represent the variance of the MAE loss for each architecture.*

The shared architecture approach was carried forward to test the MLP and ResNet architectures' ability to learn the SILVER dataset. The Optuna tuning process was repeated for an MLP and a ResNet architecture using the January data subset. A total of 1000 trials of maximum 1000 steps each were completed for each architecture. The parameters values from the best trials of the MLP and ResNet optimization processes are shown in Tables 9.3 and 9.4, respectively. The average MAE losses across all test predictions and the associated variances were recorded and visualized in Figure 9.8. The ResNet architecture provided consistently lower losses across all months.

Table 9.3: *Optimal parameter values as determined by Optuna for the MLP architecture.*

	Number of Layers	Neurons in Hidden Layers	Dropouts	Activation Functions	Batch Size	Learning Rate	Loss Function
Optimal Value(s)	2	84, 92	0.22, 0.20	Tanh, Sigmoid	96	5.85e-4	MAE

Table 9.4: *Optimal parameter values as determined by Optuna for the ResNet architecture.*

	Number of Groups	Number of Blocks	Neurons per Group Layer	Activation Functions	Batch Size	Learning Rate	Loss Function
Optimal Value(s)	2	2	56,56	ReLU	224	6.02e-2	MAE

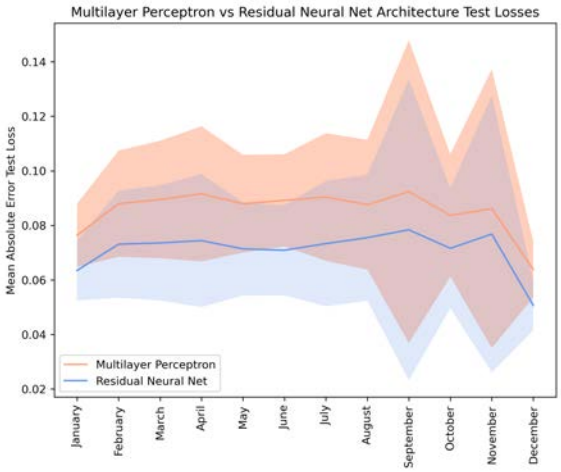

Figure 9.8: *Comparing the MAE losses of MLP and ResNet shared model architectures. The shaded areas represent the variance of the MAE loss for each architecture.*

To further test the MLP and ResNet architectures, each machine learning model was used to predict generation values for the four scenarios described above. The monthly by-technology generation totals for the MLP and ResNet architectures were compared against the actual generation values produced by SILVER for the same scenarios. The comparison is summarized in Figure 9.9. The ResNet model was selected for the EGRET platform because it predicted positive generation values more accurately than the MLP model (Figure 9.9) and had lower average loss values in testing (Figure 9.8).

While Figure 9.9 shows that the ResNet architecture produces similar monthly totals to the original SILVER model, further analysis was needed to assess the machine learning model's hourly performance relative to the computational model. The June hourly generation predictions from the ResNet machine learning model were visualized against the computed values from SILVER for each of the four scenarios. Figure 9.10 shows this visualization for Scenario 4. Unfortunately, a lack of community data made further benchmarking against real measured values impossible.

9.2.3 User Interface and Visualizations

To make the machine learning model user friendly, it was packaged with an interface and visualization suite constructed in Bokeh [36]. This package also includes post-processing scripts that calculate the costs and emissions associated with the modelled scenario. To calculate costs, the input capacity of each generator type is multiplied by an associated capital cost constant, and hourly generation values are multiplied by associated operating costs constants. Capital costs and operational costs are then summed for each generator. To calculate emissions, the hourly generation from each generator type is multiplied by an associated emissions constant and summed across the whole year. The cost and emissions constants are summarized in table 5.

These scripts also rescale the outputs into more familiar units — equivalent car use for emissions and equivalent household consumption for generation — at the recommendation of the community energy

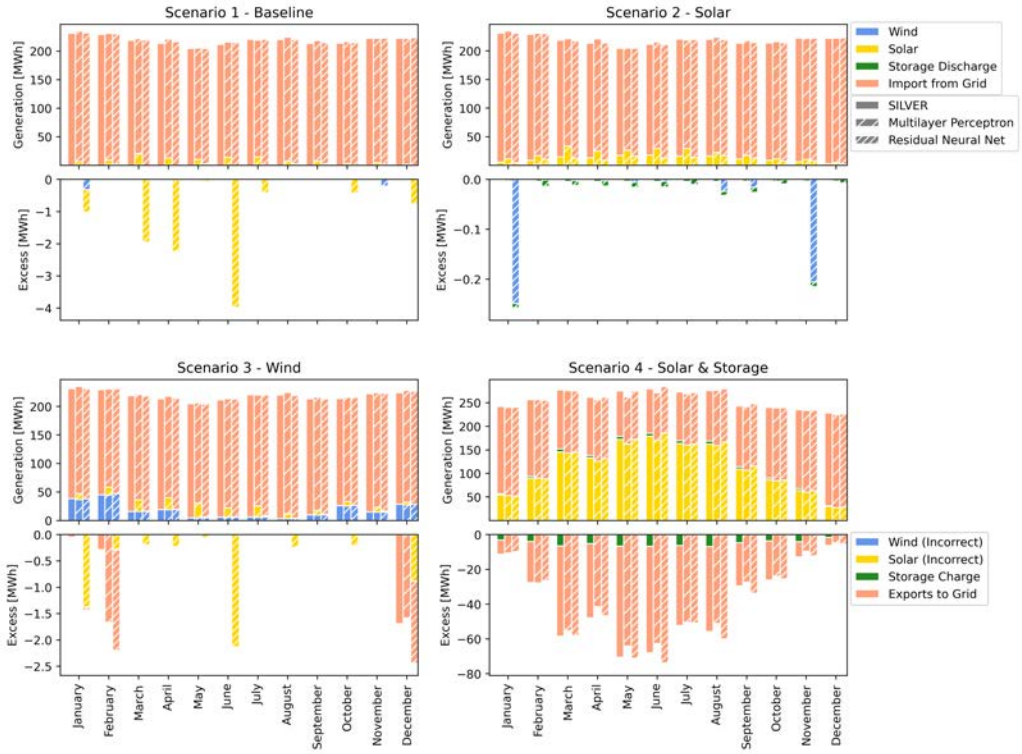

Figure 9.9: *Comparing MLP and ResNet monthly generation totals against the actual totals computed by SILVER for the four test scenarios.*

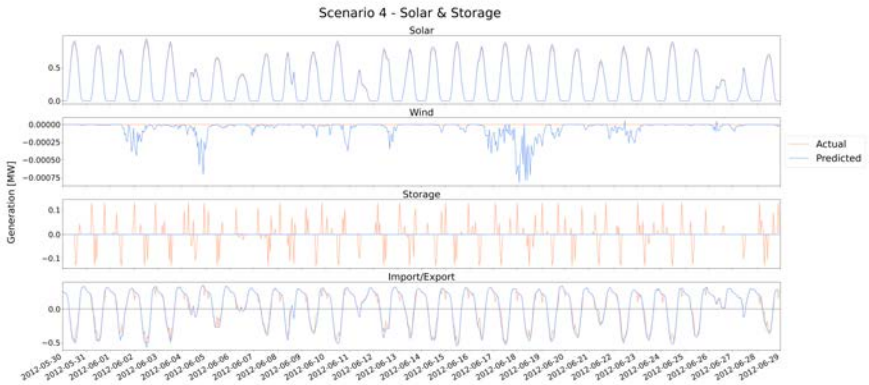

Figure 9.10: *June hourly generation comparison between the ResNet model and SILVER for Scenario 4 – Solar & Storage.*

Table 9.5: *Cost and emissions constants used to calculate financial and environmental impacts of each energy system.*

	Solar	Wind	Storage	Imports/Exports
Capital Costs ($/MW)	2,600,000 [37]	8,000,000 [38]	700,000 [39]	0
Operating Costs ($/MWh)	11.4 [40]	13 [40]	2.8 [40]	Variable Input
Emissions (tCO2/MWh)	0	0	0	0.04 [41]

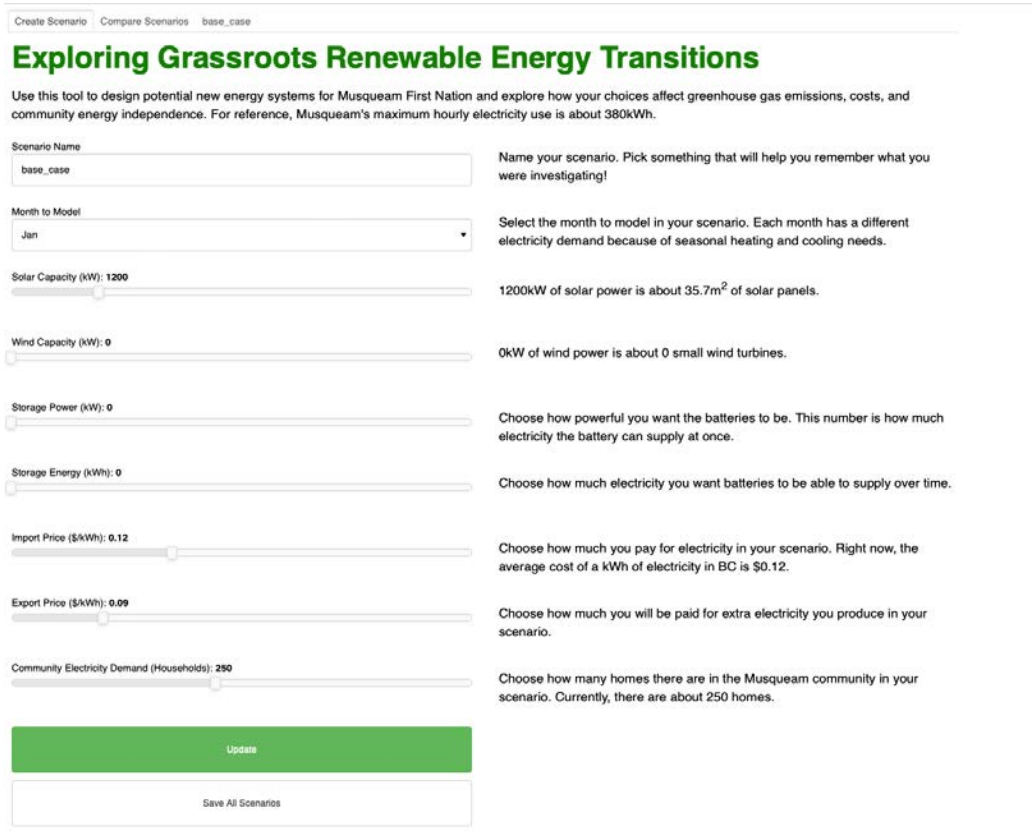

Figure 9.11: *EGRET user interface.*

specialist. Figure 9.11 shows the interface that users manipulate to define an energy system scenario. Figure 9.12 shows the scenario-specific visuals representing the generation profiles predicted by the machine learning model. Figure 9.13 shows the comparison visuals that illustrate the cost and emissions of each modelled scenario.

Figure 9.12: *EGRET visualizations showing hourly generation by technology type.*

9.2.4 Community Feedback

To gather feedback, community members were asked to participate in an informal workshop. Each participant completed a pre-interaction questionnaire, investigated the costs and benefits of community solar generation using the EGRET platform, and then completed a post-interaction questionnaire. These questionnaires evaluated EGRET for both utility and usability. The utility aspect considered the platform's ability to answer the identified community energy question, while usability looked at the accessibility and ease of use of the platform.

To evaluate utility, participants were asked the same set of questions both pre- and post-modelling to assess the impacts of the platform. The questions focused on the participants' understanding of the local electricity system in terms of cost, emissions, and sources as well as whether the participants had ideas for how the electricity system's costs and emissions could be reduced. The set also included questions about the participants' opinions on solar panels and whether they felt comfortable sharing their thoughts with others. All questions used a Likert scale [42]. Through these questions, the researchers hoped to evaluate how the platform affected the participants' energy system knowledge, opinions on potential future changes, and confidence in their position.

To evaluate usability, the participants were asked whether the user interface was easy to use, whether the available inputs provided adequate flexibility, and whether the visualization suite presented the information needed to explore the community energy question. These questions also used a Likert scale [42]. Participants were also given opportunities to suggest additional inputs or visualizations and provide general feedback on the platform. Through these responses, the researchers aimed to understand the platform's ease of use and accessibility.

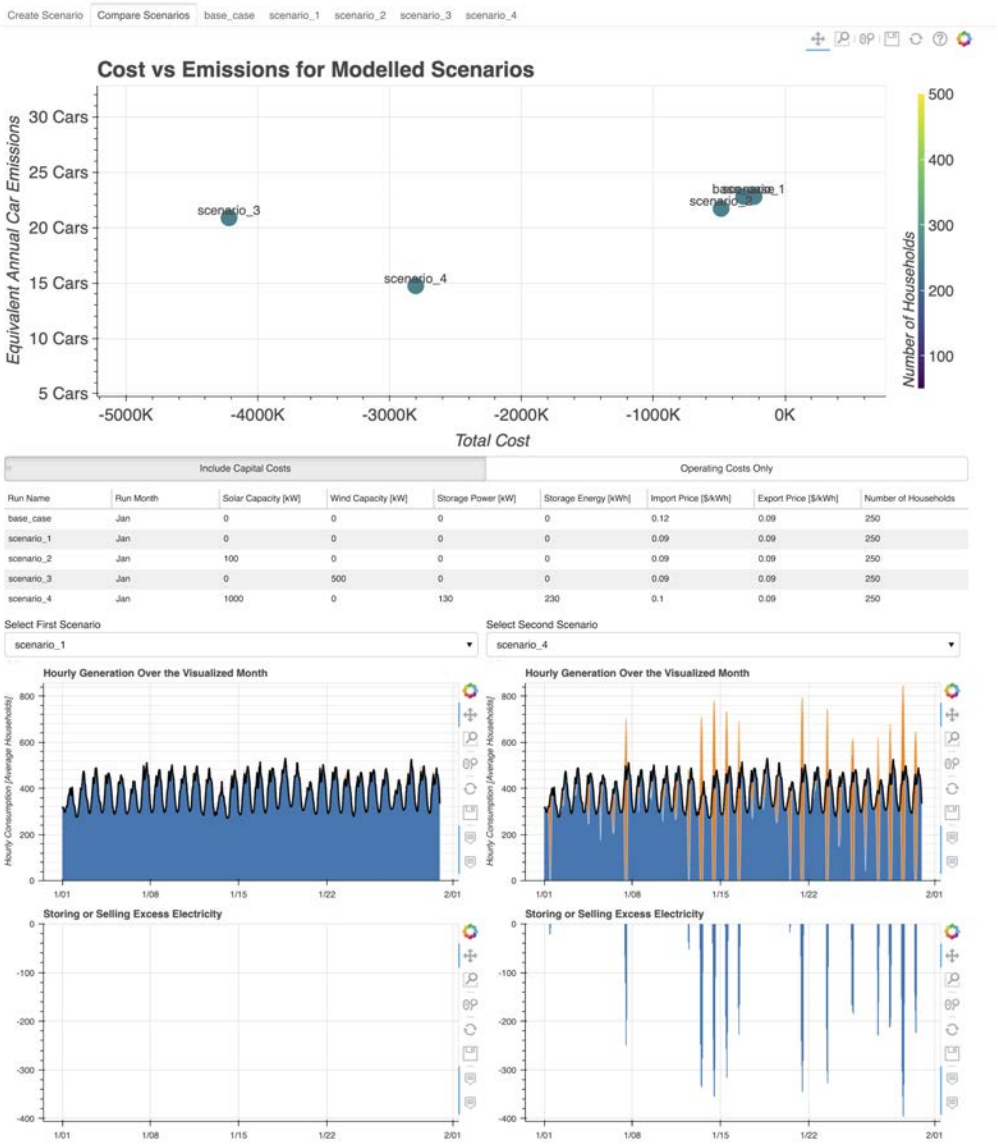

Figure 9.13: *EGRET visualization comparing cost and emissions across modelled scenarios.*

9.3 Results

Three members of the community administration team participated in the interactive workshop. These participants were the target audience for the EGRET platform because it is important to include community decision-makers such as planners and elected officials in modelling initiatives to support policy discussions [43]. The participants' responses were coded into numeric values for visualization with Strongly Disagree corresponding to a score of 1, and Strongly Agree corresponding to a score of 5. Each participant's pre- and post-modelling responses to the utility portion of the questionnaires are summarized in Figure 9.14. The

participants' scores on the platform's usability are summarized in Figure 9.15.

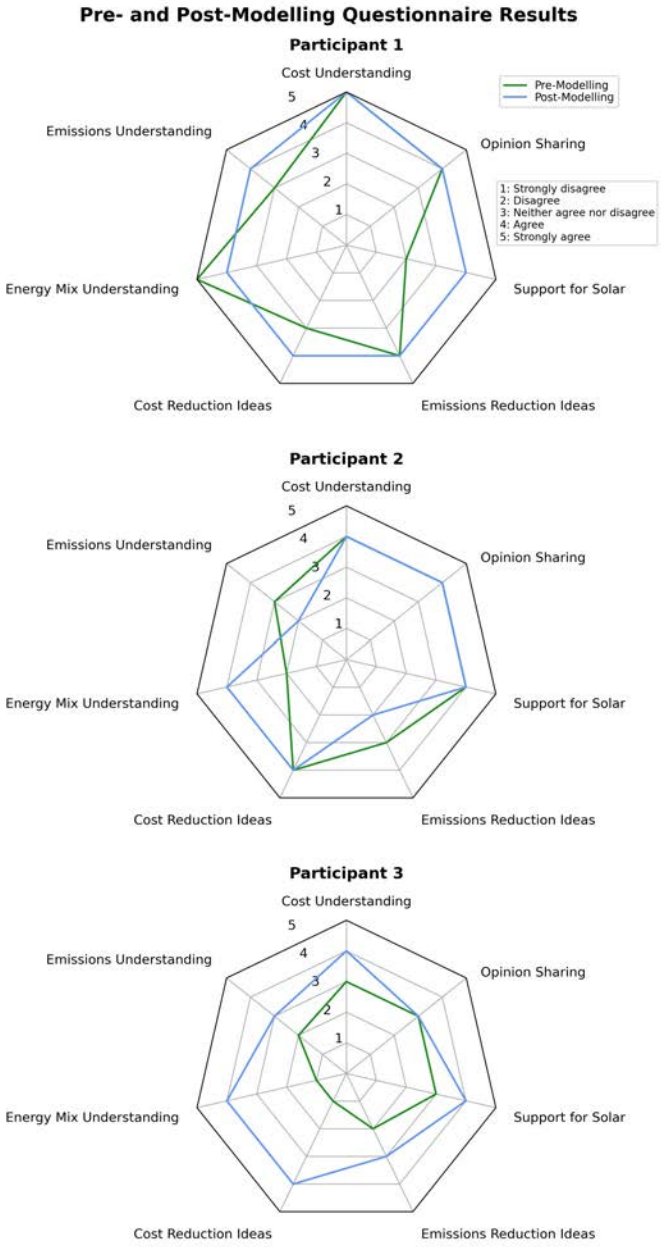

Figure 9.14: *Participants' pre- and post-modelling scores for their energy system understanding, ideas for the future, support for solar panels, and confidence in sharing their opinion on solar panels with others.*

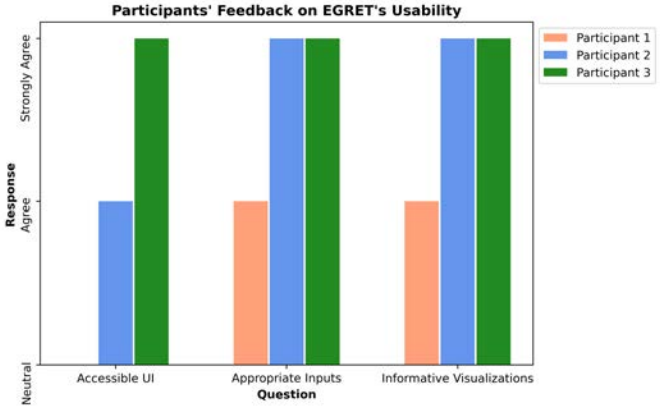

Figure 9.15: *Participants' feedback on whether the platform's user interface was easy to use, the available options allowed for exploration, and the visualizations provided adequate information. All participants answered neutrally or positively.*

Although the participants' usability scores were all neutral or positive —- and open-ended feedback questions were left blank — participants provided oral suggestions to improve both the user interface and visualization suite. These suggestions included the addition of local annual capacity factors for wind and solar as reference information on the user interface page, references for potential funding options that might offset capital costs, modelling options for single home scenarios, the ability to show production from a single generator type on the hourly generation plots, and a pie chart of total monthly generation by generator type.

In addition to participant feedback, the EGRET platform was evaluated based on its speed. Figure 9.16 compares run times for the computational model (SILVER), the machine learning models, and the EGRET platform (which combines the machine learning model run times with additional data processing and visualization steps). Run times were recorded for each of the four scenarios described previously. All runs were completed on the same computer with a Dual-Core Intel Core i7CPU 3.1 GHz and 16 GB RAM memory storage.

9.4 Discussion

The following section evaluates the EGRET platform against its goals for utility, usability, reduced computational burden, and output accuracy, and it also discusses the platform's limitations and potential next steps for improvement.

9.4.1 Utility

Responses to the utility questions varied greatly between the limited number of participants. All participants felt the same level of comfort sharing their opinions on solar panel installations before and after using the EGRET platform, suggesting that the experience did not improve self-confidence in or ownership over their energy system ideas. The overall change in ideas for energy system emissions reduction across all participants was also zero, likely because the British Columbian grid already has low emissions due to hydro integration. A different measure of environmental impact, such as land use or displacement, might be better suited to the provincial context. In general, the participants felt they had a better understanding of the local energy system's costs, emissions, and electricity sources after interacting with the platform, and supported the installation of solar panels in the community more strongly. EGRET created a positive knowledge building

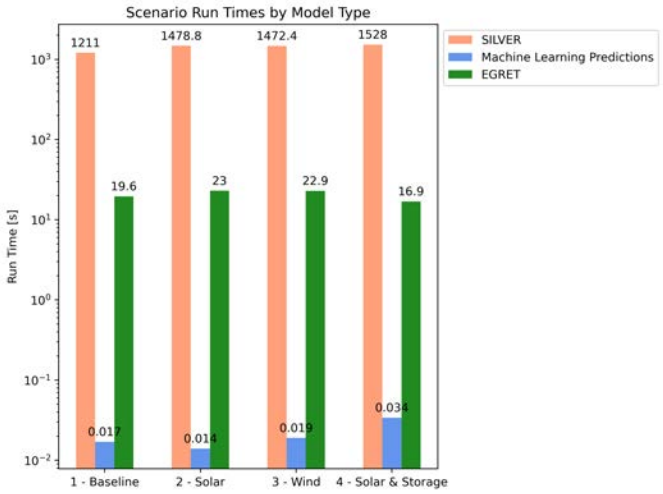

Figure 9.16: *Test scenario run times for each model type. The EGRET run times include the machine learning predictions, data post-processing, and visualization times.*

experience about energy system costs and the effectiveness of solar panels, but it did not facilitate learning about emissions or emissions reduction.

9.4.2 Usability

Participants' usability scores suggest that interacting with the EGRET platform was accessible and provided suitable flexibility and information to explore community energy questions. The participants were also able to learn how to use the platform and model and discuss three scenarios within an approximately one-and-a-half-hour workshop. Most energy system models require days or weeks of training to use [7]. However, the one neutral score for user interface accessibility and the numerous verbal suggestions for improvements highlight the need for additional work on the platform's usability.

9.4.3 Computational Burden

The machine learning models behind the EGRET platform are approximately five orders of magnitude faster than the original computational model. It takes some additional time to process and visualize these results on the platform. However, the overall run time of all three steps — modelling, processing, and visualization — is still short enough to facilitate live workshops and broad design space exploration that would be tedious with the original computational model.

It should be noted that although the EGRET platform is faster at run time, the machine learning model development process is extensive. Essentially, the computational burden is shifted from the actual modelling to the dataset creation, hyperparameter optimization, and model training steps needed to create the surrogate model. The accessibility of computing facilities limits who can develop platforms like EGRET. Further, communities looking to pursue ideas generated through the EGRET platform must complete additional modelling with other tools to finalize their designs due to EGRET's limitations as described below. EGRET does not reduce the computational expense needed to integrate renewable energy generators; rather, it shifts the expense such that community members can be included in the decision-making and scenario exploration phases of the process.

9.4.4 Accuracy

Although the machine learning models provide significant run time speed benefits, these benefits come at the cost of decreased accuracy. Figure 9.10 highlights two reductions in accuracy that could be improved through further experimentation with machine learning architectures. First, the EGRET models predict small outputs from generator types with zero capacity. Second, the models' predictions for storage activity do not fully capture the charge and discharge spikes in the actual results.

A third, hidden source of inaccuracy is the lack of hourly community electricity demand data. As shown in Figure 9.4, the shape of the hourly demand curve impacts monthly export totals. Because exporting only occurs when generation exceeds demand, the difference between production and demand at every time step affects how much electricity is used or sold. Hourly electricity demand profiles were not available for the Musqueam community, so the predicted export quantities may not be accurate. Further, a lack of community electricity cost and supply data prevented benchmarking of the computational model against the current scenario. As a result, the researchers had to assume that the SILVER model was accurate in the community context based on previous benchmarking exercises at different scales [24].

9.4.5 Model Limitations

Several other assumptions inherent in the SILVER model introduced limitations to the EGRET platform. The first limitation is the parameters defining the VRE potential time series used to calculate hourly VRE generation. For both wind and solar, these time series are dependent on the selected technology model and its specifications. In the case of solar, the time series is also dependent on the orientation of the panel installation. Although the assumptions made for solar panel orientation reflects best practices for Musqueam community's location, members might want to orient their panels differently (eg. on the roof of homes).

SILVER was also constructed with larger scale electricity applications in mind. As a result, transmission infrastructure is modelled as long distance direct current transmission. At the community scale, the transmission infrastructure would use alternating current flow. Alternating current flow produces higher losses due to capacitance. There is a need for better distribution-scale modelling to understand how these factors impact community energy planning.

9.4.6 Institutional Limitations

While the EGRET platform contains several internal limitations, the institutional context in which the platform is used can present additional challenges. One of the initial goals of the EGRET platform was to promote a sense of ownership over community energy decisions. Ideally, community members should have actual ownership over renewable energy developments to realize the development's benefits, but a simple modelling tool cannot provide that [44]. Several barriers, such as inequitable access to financing and a lack of long-term clarity on incentives, can make ownership difficult in the current energy context [20]. [44]. For example, the EGRET platform assumes that Musqueam Nation could secure a power purchase agreement with BC Hydro, but these contracts are difficult to obtain. The application of the EGRET platform in this context could create feelings of "misempowerment" as community members are encouraged to engage with a system that does not value their input [10]. There is a risk that if "the tool falsely suggests free access to the machinery of plan making", it will cause a loss of trust in institutions of power [10]. There is a need to refine policies that support Indigenous ownership in renewable energy development so communities can implement and benefit from the systems they envision with tools like the EGRET platform.

9.4.7 Future Work

Focusing back on the EGRET platform itself, there are several areas of future work that would increase the scope of the tool's abilities. First, SILVER only considers the operating costs of the energy system being modelled. Capital costs were an important consideration for community decision makers, so a simplistic capital cost calculation as described in the methodology section was included in the post processing steps

and optionally included in scenario comparisons. In future versions, capacity expansion modelling could be integrated into the platform to better capture capital costs.

Second, demand-side technologies will play an important role in the energy system transition alongside renewable energy generators, but SILVER does not currently include non-electric sources of energy like natural gas or gasoline. Demand-side considerations can only be integrated if they use technologies like heat pumps or electric vehicles. Expanding the suite of computational models behind the EGRET surrogate models to integrate building energy and transportation tools would expand the application of the platform into demand-side management strategies.

Third, further development of the machine learning model architecture is needed to accurately predict storage charge and discharge profiles. Although the Musqueam community is grid connected, the community energy specialist expressed an interest in having storage technology available in case of an outage. In the larger context, some Indigenous communities in Canada are off-grid, making storage a critical component of their energy systems. These off-grid communities typically use diesel generators to produce electricity, which introduce another layer of complexity when integrating renewable energy generators due to diesel generators' minimum capacities. Introducing diesel generator capacity as an input to EGRET would make the tool useful for off-grid communities.

While the above-mentioned improvements would make EGRET applicable in broader contexts, the way that EGRET is currently constructed would require the underlying machine learning models to be retrained on local data for each community that wishes to use it. Including VRE potential and demand time series as variable inputs to the machine learning models would make EGRET applicable to any location without the retraining requirement. Including time series data as inputs would necessitate restructuring of the machine learning model architectures to something more complex. This approach has already been applied by Westermann to the building energy space; the authors constructed a geographically flexible surrogate model that recreates building energy simulations using temporal convolutional neural networks [45]. Applying such an approach to the EGRET platform to create an open-source tool would further increase the accessibility of energy system modelling.

9.5 Conclusion

The EGRET platform looked to restructure typical energy system modelling approaches to better suit a future with decarbonized and decentralized power sources. By facilitating community-scale engagement in renewable energy development initiatives, the EGRET platform supports the decentralized governance structures needed for an equitable transition to sustainable power systems. The application of machine learning to create an interactive model for use in a community workshop setting was successful in that the EGRET platform provides reasonable predictions for wind and solar generation and grid connection electricity flow in a timeframe that promotes conversation. The speed at which EGRET makes these predictions relative to the original computational model shows strong potential for using machine learning in participatory system dynamics modelling approaches. The user interface and visualization suite also received positive feedback on their utility and usability from a limited number of community testers, further supporting the use of ongoing collaboration through the model development process to ensure the finished product's applicability in the community context. However, the EGRET platform's storage predictions could benefit from further development of the machine learning architecture, and several other factors limit its application beyond the Musqueam community. Future work to generalize the platform for use by other communities would provide additional support for Indigenous engagement in renewable energy decision-making and an equitable transition to sustainable energy sources at a local scale.

Acknowledgments: The authors would like to acknowledge the financial support of the Natural Sciences and Engineering Research Council of Canada and the Tyler Lewis Clean Energy Research Foundation. The authors would also like to thank Evan Dungate and Keegan Griffiths for their visualization support and Brittany Point and Lenny Kishi for their feedback.

Funding: This work was supported by a Natural Sciences and Engineering Research Council of Canada (NSERC) New Frontiers in Research — Exploration grant [NFRFE-2018-00338] as well as an NSERC Canada Graduate Scholarship. Financial support was also provided by a 2021 Tyler Lewis Clean Energy Research Foundation Grant.

Conflicts of Interest: The authors declare there are no known conflicts of interest — either financial or personal — that have influenced the work discussed in this paper.

Authors Contributions: Lia Codrington: Conceptualization, Methodology, Data Curation, Software, Investigation, Visualization, Writing – Original Draft. Ehsan Haghi: Conceptualization, Methodology, Project Administration, Writing – Original Draft. Kwang Moo Yi: Methodology, Writing – Review and Editing. Madeleine McPherson: Conceptualization, Funding Acquisition, Resources, Supervision, Writing – Review and Editing.

References

1. United Nations Framework Convention on Climate Change, (2015). The Paris Agreement. doi: 10.4324/9789276082569-2.
2. Allen, M. R., Pauline Dube, O., Solecki, W., Aragón-Durand, F., Cramer France, W., Humphreys, S., Dasgupta, P., and Millar, R., (2018). Framing and Context, in *Global Warming of 1.5C: An IPCC Special Report on the impacts of global warming of 1.5C above pre-industrial levels and related global greenhouse gas emission pathways, in the context of strengthening the global response to the threat of climate change,* I. E. Idris, A. Fischlin, and X. Gao, Eds. Intergovernmental Panel on Climate Change, 2018.
3. International Energy Agency, (2021). Net Zero by 2050: A Roadmap for the Global Energy Sector, 222.
4. Environment and Climate Change Canada, (2020). A Healthy Environment and a Healthy Economy: Canada's strengthened climate plan to create jobs and support people, communities and the planet. [Online]. Available: https://www.canada.ca/en/services/environment/weather/climatechange/climate-plan/climate-plan-overview/healthy-environment-healthy-economy.html
5. Bridge, G., Bouzarovski, S., Bradshaw, M., and Eyre, N., (2013). Geographies of energy transition: Space, place and the low-carbon economy,*Energy Policy,* 53, 331–340, doi: 10.1016/j.enpol.2012.10.066.
6. Burke, M. J. and Stephens, J. C., (2017). Energy democracy: Goals and policy instruments for sociotechnical transitions. *Energy Research and Social Science,* 33, 35–48, doi: 10.1016/j.erss.2017.09.024.
7. Connolly, D., Lund, H., Mathiesen, B. V., and Leahy, M., (2010). A review of computer tools for analysing the integration of renewable energy into various energy systems, *Applied Energy,* doi: 10.1016/j.apenergy.2009.09.026.
8. Fortes, P., Alvarenga, A., Seixas, J., and Rodrigues, S., (2015). Long-term energy scenarios: Bridging the gap between socio-economic storylines and energy modeling. *Technological Forecasting and Social Change,* 91, 161–178, doi: 10.1016/j.techfore.2014.02.006.
9. Varho, V. and Tapio, P., (2013). Combining the qualitative and quantitative with the Q2 scenario technique - The case of transport and climate. *Technological Forecasting and Social Change,* 80(4), 611–630, doi: 10.1016/j.techfore.2012.09.004.

10. Senbel, M. and Church, S. P., (2011). Design empowerment: The limits of accessible visualization media in neighborhood densification. *Journal of Planning Education and Research,* 31(4), 423–437, doi: 10.1177/0739456X11417830.
11. Lilienthal, P. and Lambert, T., (2004). HOMER: The Micropower Optimization Model. [Online]. Available: http://www.nrel.gov/homer
12. Lund, H., Thellufsen, J. Z., Østergaard, P. A., Sorknæs, P., Skov, I. R., and Mathiesen, B. V., (2021). EnergyPLAN - Advanced analysis of smart energy systems. *Smart Energy,* 1, 100007, doi: 10.1016/j.segy.2021.100007.
13. Weinand, J. M., Scheller, F., and McKenna, R., (2020). Reviewing energy system modelling of decentralized energy autonomy. *Energy,* 203, 117817, doi: 10.1016/j.energy.2020.117817.
14. Hilpert, S., Kaldemeyer, C., Krien, U., Günther, S., Wingenbach, C., and Plessmann, G., (2018). The Open Energy Modelling Framework (oemof) - A new approach to facilitate open science in energy system modelling. *Energy Strategy Reviews,* 22(0), 16–25, doi: 10.1016/j.esr.2018.07.001.
15. Hilpert, S., Günther, S., Kaldemeyer, C., Krien, U., Plessmann, G., Wiese, F., and Wingenbach, C., (2017). Addressing Energy System Modelling Challenges: The Contribution of the Open Energy Modelling Framework (oemof), *Preprints,* (February), 1–26, doi: 10.20944/preprints201702.0055.v1.
16. Komendantova, N., Riegler, M., and Neumueller, S., (2018). Of transitions and models: Community engagement, democracy, and empowerment in the Austrian energy transitio. *Energy Research and Social Science,* 39(November 2017), 141–151, doi: 10.1016/j.erss.2017.10.031.
17. Aguilar, H., Suazo López, F., and Arturo Domínguez Pacheco, F., (2022). Sustainable Development Goals index: An analysis (2000-2022).*Transdiciplinary Journal of Engineering and Science,* SP-1, 111–128, doi: 10.22545/2022/00213.
18. King, H. and Pasternak, S., (2019). Land Back Red Paper. [Online]. Available: https://redpaper.yellowheadinstitute.org/wp-content/uploads/2019/10/red-paper-report-final.pdf
19. Scott, K. A., (2020). Reconciliation and energy democracy. *Canadian Journal of Program Evaluation,* 34(3), 480–491, doi: 10.3138/cjpe.68844.
20. Krupa, J., (2012). Identifying barriers to aboriginal renewable energy deployment in Canada. *Energy Policy,* 36, 710–714, doi: 10.1016/j.enpol.2011.12.051.
21. Antunes, P., Stave, K., Videira, N., and Santos, R., (2015). Using participatory system dynamics in environmental and sustainability dialogues. *Handbook of Research Methods and Applications in Environmental Studies,* 346–376, doi: 10.4337/9781783474646.
22. Musqueam Indian Band, Musqueam. https://www.musqueam.bc.ca/ (accessed Oct. 17, 2022).
23. Musqueam First Nation, (2011). Musqueam First Nation: A Comprehensive Sustainable Community Development Plan.
24. McPherson, M. and Karney, B., (2017). A scenario based approach to designing electricity grids with high variable renewable energy penetrations in Ontario, Canada: Development and application of the SILVER model. *Energy,* 138, 185–196, doi: 10.1016/j.energy.2017.07.027.
25. Brideau, S. A., (2020). Estimating hourly heating and cooling loads from monthly results. *ASHRAE Transactions,* 126, 166–173.
26. Staffell, I. and Pfenninger, S., (2016). Using bias-corrected reanalysis to simulate current and future wind power output. *Energy,* 114, 1224–1239, doi: 10.1016/j.energy.2016.08.068.
27. Pfenninger, S., Hawkes, A., and Keirstead, J., (2014). Energy systems modeling for twenty-first century energy challenges. *Renewable and Sustainable Energy Reviews,* 33, 74–86, doi: 10.1016/j.rser.2014.02.003.
28. Ong, S., Campbell, C., Denhold, P., Margolis, R., and Heath, G., (2013). Land-Use Requirements for Solar Power Plants in the United States, Golden, Colorado.
29. NREL, (2016). Land Use by System Technology. *Energy Analysis.* https://www.nrel.gov/analysis/tech-size.html

30. Ministry of Energy Mines and Petroleum Resources, Comprehensive Review of BC Hydro, [Online]. Available: https://www2.gov.bc.ca/assets/gov/farming-natural-resources-and-industry/electricity-alternative-energy/electricity/bc-hydro-review/final_report_desktop_bc_hydro_review_v04_feb12_237pm-r2.pdf

31. Falcon, W. and The PyTorch Lightning Team, (2019) PyTorch Lightning. doi: 10.5281/zenodo.3828935.

32. He, K., Zhang, X., Ren, S., and Sun, J., (2016). Deep residual learning for image recognition, in *Proceedings of the IEEE Computer Society Conference on Computer Vision and Pattern Recognition,* 2016(December), 770–778. doi: 10.1109/CVPR.2016.90.

33. Köhnen, C. S., Nolting, L., Praktiknjo, A., and Robinius, M., (2021). The potential of deep learning to reduce complexity in energy system modeling, (August), 1–22, doi: 10.1002/er.7448.

34. Simonyan, K. and Zisserman, A., (2015). Very deep convolutional networks for large-scale image recognition. *3rd International Conference on Learning Representations, ICLR 2015 - Conference Track Proceedings,* 1–14.

35. Akiba, T., Sano, S., Yanase, T., Ohta, T., and Koyama, M., (2019). Optuna: A Next-generation Hyperparameter Optimization Framework. in *Proceedings of the 25rd International Conference on Knowledge Discovery and Data Mining,* 2019.

36. Bokeh Development Team, (2018). Bokeh: Python library for interactive visualization. 2018. Accessed: Oct. 19, 2022. [Online]. Available: http://www.bokeh.pydata.org

37. Urban, R., (2021). Cost of Solar Power in Canada 2021, Energy Hub. https://www.energyhub.org/cost-solar-power-canada/#: :text=The%20average%20installation%20cost%20of,province%20that%20you%20live%20in (accessed Oct. 13, 2022).

38. Clarke, S., Electricity generation using small wind turbines for home or farm use. https://www.ontario.ca/page/electricity-generation-using-small-wind-turbines-home-or-farm-use#: :text=Understanding wind turbine costs,$ 80,000 and C$ 110,000. (accessed Oct. 13, 2020).

39. Cole, W. and Frazier, A. W., (2020). Cost Projections for Utility-Scale Battery Storage: 2020 Update, *National Renewable Energy Laboratory (NREL)*, (June), 21.

40. United States Energy Information Administration, (2014). Levelized Cost and Levelized Avoided Cost of New Generation Resources in the Annual Energy Outlook. [Online]. Available: http://www.eia.gov/forecasts/aeo/pdf/electricity_generation.pdf

41. Government of British Columbia, Electricity emission intensity factors for grid-connected entities. https://www2.gov.bc.ca/gov/content/environment/climate-change/industry/reporting/quantify/electricity (accessed Oct. 13, 2022).

42. Likert, R., (1932). A technique for the measurement of attitude. , *Archives of Psychology,* 22(4), 55, [Online]. Available: files/325/1933-01885-001.html

43. McGookin, C., Ó Gallachóir, B., and Byrne, E., (2021). Participatory methods in energy system modelling and planning – A review. *Renewable and Sustainable Energy Reviews,* 151(November 2020), doi: 10.1016/j.rser.2021.111504.

44. Savic, K. and Hoicka, C. E., (2021). Reconciliation and self-determination through renewable energy? The perspective of economic development corporations of grid-connected First Nations communities. *Clean Economy Working Paper Series,* (January).

45. Westermann, P., Welzel, M., and Evins, R., (2020). Using a deep temporal convolutional network as a building energy surrogate model that spans multiple climate zones. *Applied Energy,*278(July), 115563, doi: 10.1016/j.apenergy.2020.115563.

About the Authors

Lia Codrington is a Masters student in the Civil Engineering Department at the University of Victoria. She graduated from the University of Toronto in 2020 with a BASc in Engineering Science and a minor in Environmental Engineering. Her focus during her undergraduate degree was energy efficient housing design, particularly for remote Indigenous communities. She has completed work terms at the National Research Council's Flight Research Lab and Construction portfolio, and she spent a summer in Accra, Ghana, as an Engineers Without Borders Junior Fellow.

Ehsan Haghi is currently working as the community energy specialist at Musqueam Indian Band. In this role, he works with housing and public works departments to implement energy efficiency measures in Musqueam homes and public buildings. Additionally, Ehsan leads energy studies and energy awareness campaigns in the community. Ehsan has a background in engineering and has received his PhD in chemical engineering from University of Waterloo in 2020.

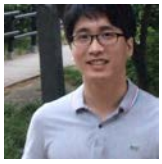

Kwang Moo Yi is an assistant professor in the Department of Computer Science at the University of British Columbia (UBC), and a member of the Computer Vision Lab, CAIDA, and ICICS at UBC. Before, he was at the University of Victoria as an assistant professor, where he is currently an adjunct professor. Prior to being a professor, he worked as a post-doctoral researcher at the Computer Vision Lab in École Polytechnique Fédérale de Lausanne (EPFL, Switzerland), working with Prof. Pascal Fua and Prof. Vincent Lepetit. He received his Ph.D. from Seoul National University under the supervision of Prof. Jin Young Choi. He also received his B.Sc. from the same University. He serves as area chair for top Computer Vision conferences (CVPR, ICCV, and ECCV), as well as AAAI. He is part of the organizing committee for CVPR 2023.

Madeleine McPherson is an Assistant Professor in the Civil Engineering department at the University of Victoria and principal investigator of the Sustainable Energy Systems Integration & Transitions Group. Previously, McPherson worked as a Post-Doctoral researcher in the Grid Systems Analysis group at the National Renewable Energy Laboratory (NREL) in Golden, Colorado. McPherson obtained her PhD in Civil Engineering from the University of Toronto in 2017. Her research focuses on integrating high penetrations

of wind and solar PV onto electricity systems around the world. She has explored questions ranging from the impact of renewable resource characteristics on integration strategies, storage assets remuneration and integration in electricity system markets, and the interaction between electric vehicle charging profiles and grid decentralization. More recently, McPherson has developed and applied a methodology for exploring the role of demand response for facilitating increasing renewable penetrations. McPherson is the lead-author on numerous peer-reviewed journal articles, conference proceedings, reports, and presentations. Currently, McPherson is developing an integrated modelling framework to explore the sustainable energy transition in Canada.

CHAPTER 10

Implementation of Taguchi Method for Designing a Robust Wind Energy System – A Wind Turbine

Vishal Kaushik, R. Naren Shankar, N. I. Haroon Rashid, P. B. Khope

Article citation information: (2022), *TJES*, Vol. SP-2, pp. 165-185, doi:10.22545/2022/00216

The current paper demonstrates the design parameters and tolerances for a horizontal axis wind turbine which is used to extract the energy from the wind. Here in the present work, one of the DOE (design of experiment) methods namely Taguchi method, a traditional approach for designing a robust wind turbine is adopted. For optimization purpose, the evaluation and estimation of various problems i.e; constrained as well as unconstrained have been done using Taguchi method. For the derivation of design parameters like lift coefficient (C_L), drag coefficient (C_D) and power coefficient (C_P), the L-9 Orthogonal array (OA) comprising of 4 parameters each with three levels (NACA aerofoil type, Mach number, Reynolds number and angle of attack) is considered. Open source Q-Blade designing software is used for determining the power, lift and drag coefficients of the wind turbine. The combination of GRA and orthogonal arrays are used for attaining the optimized parameters. In this paper an investigation has been carried out on the specific NACA aerofoils 4412, 4712, and 4421. Among all the aerofoils NACA 4712 has shown impressive results in terms of a maximum lift coefficient of 0.9491and minimum drag coefficient of 0.02601. Also from signal-to-noise plots it can be inferred that the most influenced parameter for C_L and C_D is Mach number and Aerofoil for C_P.

Keywords: Taguchi method, HAWT, SN ratio, GRA, optimization, Q-blade, optimization.

10.1 Introduction

Renewable energy is an urgent need in today's world so as to minimize the need for energy from natural resources to some extent. We know that lot of advancements are going on in the field of renewable energy and one of it is wind energy, which is used for sustainable development[1]. For extraction of wind energy, there are two types of wind turbines, horizontal and vertical based on their axis of rotation. The wind turbine industries are emerging day by day in which the share of HAWT is impressive. To enhance the efficiency and performance of these turbines the need of blade optimization has become an important factor. The main interest in this paper is to obtain optimized performance variables which directly or indirectly affect the efficiency of HAWT.

A robust design includes tolerance as well as parameter designing. [2] has presented a methodology by considering various tolerations along with multiple design parameters for a HAWT robust design using Taguchi approach as one of the methods of DOE. For the utilization of wind turbines, both in urban and

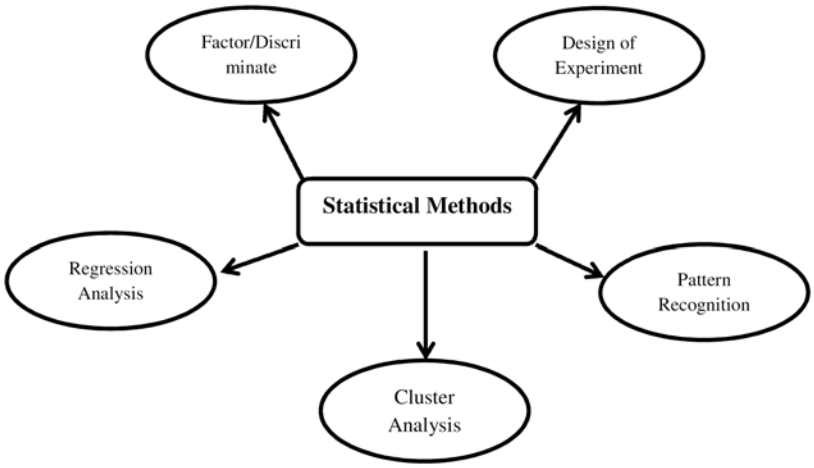

Figure 10.1: *Classification of statistical method.*

rural areas lot of research are being carried out in the field of both types of wind turbines[3]. Desired quality values within the acceptance range can be achieved by using a design of experiment Taguchi method [4].

In the year 1956, a method of optimization for improving the quality of manufactured goods was developed by Genichi Taguchi an engineer and statistician from Japan. A statistical method has various kinds of analysis like Factor/Discriminate analysis, Regression Analysis, Pattern Recognition, Cluster Analysis, and Design of Experiments. Taguchi method is one of the methods in DOE which has concluded the experiments with quality characteristics.

Competence of providing the combination of optimized design parameters and having implementation in almost every engineering field, Taguchi method has evolved in past few years. Single and double objective functions for optimization and to operate both the positive and negative objective values of the function Taguchi method has become widened [5]. A module of wind capacity and heat sink of a CPU design was carried out by utilizing Taguchi and ANOVA [6]. A robust HAWT design in view of both parameter and toleration using Taguchi method and its extension has been proposed by [7].

Various types of research have been done for predicting the aerodynamic performance of wind turbines over the years. By using Q-blade and CFD simulations, various analysis has been carried out for obtaining various coefficients of aerodynamics for horizontal axis wind turbines with SG6043 aerofoil [8]. Taguchi method has an implementation in various fields of engineering for determining the optimum process for a single response[9].

Some of the merits related to Taguchi method are as i) handling of parameters required for design is simple when it has discrete values rather than mixed discrete values, ii) it does not need derivatives for the functions unlike genetic algorithm, iii) minimum functions are enough for the optimal and robust designs unlike the approaches having large functions for nonlinear programming, iv) results obtained from this method can be directly implemented as the physical designs[7]. Figure 10.1 comprises various methods of the statistical approach in OR (Operation Research), which can be classified as cluster analysis, regression analysis, pattern recognition, design of experiments, and factor/discriminate analysis. Taguchi method falls under the category of statistical analysis of operation research.

Various types of research have been carried out in past by different investigators, where they have used Q-blade software for designing and simulation of wind turbines and very few have utilized the Taguchi method for the optimization purpose. In this paper, the authors have tried to fulfill this research gap so as to get the most optimized design based on the combination of variables derived. Many analyses have

been carried out on various NACA aerofoils for horizontal and vertical wind turbines using freely available open-source Q-blade designing and simulation software. For the prediction and valuation of various wind turbine parameters like the coefficient of lift, drag, and power, implements the use of blade element theory and empirical equation. For determining and exploration of wind turbine parameters' effect on NACA 4412, 4421, and 4712, a grey-based Taguchi method has been utilized.

10.2 Taguchi Method of Statistical Analysis

A Statistical method is one of the methods used in operation research for obtaining the relation between the input and output parameters which also affects the whole process. It is very convenient for optimizing the complex characteristics of aerodynamics comprising different variables[10]. One of the statistical methods is the Taguchi approach which consists of the various steps which are depicted in Figure 10.2 below.

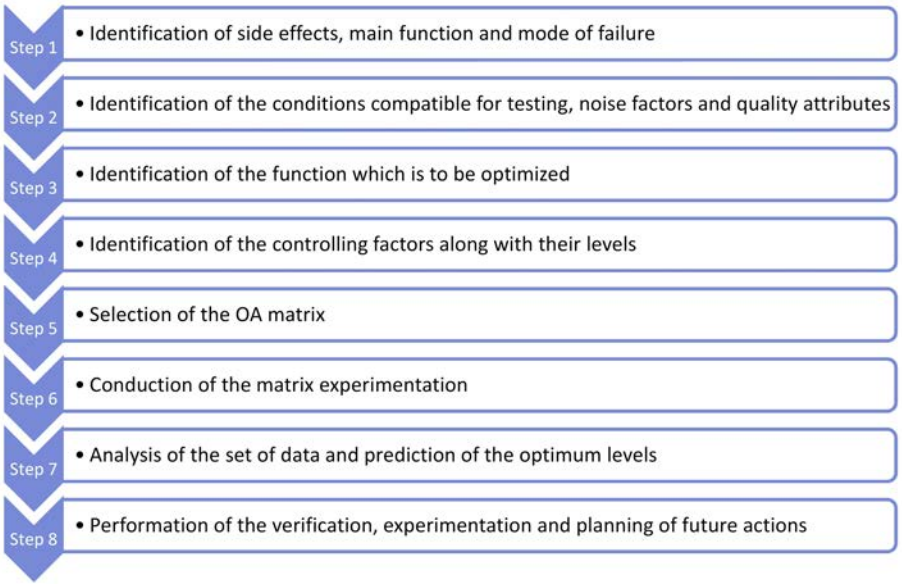

Figure 10.2: *Various steps in Taguchi method.*

In this paper, the parameters related to wind turbine aerodynamics are aerofoil type, angle of attack, Mach number, and Reynolds number. For obtaining and determining the influence and effect of the considered parameters and their combination on the wind turbine performance, we have considered the Taguchi method with L9 – orthogonal array having three sets of levels having four parameters.

Tables 1 and 2 include information on the number of considered parameters with their level of experimentation ranging from low to high and Taguchi L9 OA representation as ($Level\ design^{No.of factors}$) that is 34. For the analysis, Minitab 19 statistical package is used in which Taguchi method was chosen for obtaining the effect on quality response. [11] had carried out experimentation using Taguchi by considering the orthogonal array of L9, along with one interaction and three parameters to examine the effects which will be of prime importance for the designing process, which ultimately affects the performance of the turbine.

10.2.1 Robust Design

The Taguchi method can be used to determine the influence of aerodynamic parameters. For the experimental run, the numbers of quality responses considered are lift coefficient, drag coefficient, and power coefficient.

Table 1: Designing parameters levels

Design variables	**Levels**		
	1 (Low)	**2 (Intermediate)**	**3 (High)**
NACA Aerofoils	4412	4421	4712
Mach Number	0.0087	0.0146	0.0204
Reynolds Number	50000	75000	100000
Angle of attack	2 degree	4 degree	6 degree

Table 2: L-9 OA (orthogonal array) Mapping

Experiment No.	**NACA Aerofoil**	**Mach No.**	**Reynolds No.**	**AOA**
1	4412	0.0087	50000	2 degree
2	4412	0.0146	75000	4 degree
3	4412	0.0204	100000	6 degree
4	4421	0.0087	75000	6 degree
5	4421	0.0146	100000	2 degree
6	4421	0.0204	50000	4 degree
7	4712	0.0087	100000	4 degree
8	4712	0.0146	50000	6 degree
9	4712	0.0204	75000	2 degree

Lift and power coefficients are very crucial parameters for deciding the aerodynamic characteristics of a wind turbine and thus these parameters must be kept as high as possible. On the other hand, the drag coefficient must be kept as low as possible to enhance the performance of the turbine, due to this fact drag coefficient is taken as lower is better, and lift and power coefficients are considered as higher is better. For lift coefficient and power coefficient, the following equation 1 is used, which gives the relation for signal-to-noise ratio (SNR). For the maximum SNR, there must be an improvement in the mean value and variance[12].

$$\frac{S}{N} = -\log_{10}\{\frac{1}{n}\left[\sum_{i=1}^{n}\frac{1}{y_i^2}\right]\} \tag{10.1}$$

Where,

S- Signal

N - Noise
y_i - Response experiment
n - Number of runs

Here in the present paper, the input Mach number (velocity) is taken as a factor of noise, as it affects the HAWT performance.

Researchers utilized one of the DOE methods i.e; Taguchi approach for determining the optimal output responses related to the deflector which is used as an augmenter for their wind turbine setup. An experiment based on a matrix can be designed by defining the controlling factors like noise and control, followed by the performance of experiments based on the matrix. Below is Table 3 represents the factors and levels that were considered by an investigator to determine the effect of 5 factors of deflector on the output power coefficient of the vertical axis wind turbine[13].

Table 3: Number of factors and levels for the deflector[13]

Factors	**Levels**			
	1	**2**	**3**	**4**
Horizontal distance from the axis to top edge of deflector (X)	0	$^1/_2 D$	D	$^3/_2 D$
Vertical distance between top and bottom edge of a blade (Y)	0	$^1/_3 H$	$^2/_3 H$	H
Angle of deflection w.r.t turbine rotation (ϕ)	0 degree	30 degree	45 degree	60 degree
Deflector Length (L)	$^1/_2 H$	H	$^3/_2 H$	2H
Deflector Width (W)	$^1/_3 D$	$^2/_3 D$	D	$^4/_3 D$

10.2.2 Validation

A similar study has been conducted by Yi Hu et al. [7] and Kriswanto et al. [14] for designing a robust wind turbine using the Taguchi approach. For the present investigation, a detailed procedure is followed by considering the past research, based on Taguchi method for the optimization purpose. For parameters like lift coefficient and power coefficient "higher is better" and for drag coefficient "lower is better," SNR is considered for the present research and accordingly, all the related plots like main effect plot, SN response table and SN plots were generated and analyzed by considering L9 orthogonal array for parameters like aerofoil type, angle of attack, Mach number and Reynolds number, each having three levels as low, intermediate and high.

10.3 Q-Blade Simulation Software

Q-blade is a simulation tool that is available freely and facilitates the designing and simulation of vertical as well as horizontal axis wind turbines. This software uses the principle of the Blade element momentum method and doubles multiple stream tube algorithm for analyzing horizontal and vertical axis wind turbines[15][16][17].

For calculations, an inbuilt methodology of Q-blade software is utilized, which is based on blade element momentum theory (blade element and momentum) theories, which accounts for the angular momentum of the turbine rotor. These theories are utilized for calculating the local forces acting on a propeller or turbine blade. Angular momentum is included in the model in BEM theory. Here in our calculations, the turbulence consideration was not taken into account.

Figure 10.3 shows the algorithm associated with Q-blade software which enables the designing and simulation of customized aerofoils, along with their respective polar computations, and polar data extrapolation to 360 degrees. This software consists of various modules namely XFLR5, XFoil Analysis, Polar extrapolation, designing of blade, and analysis of turbine[18].

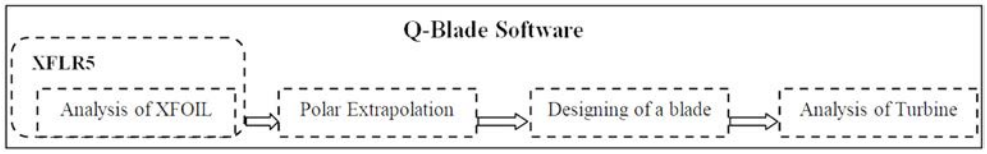

Figure 10.3: *Different Modules of Q-blade software.*

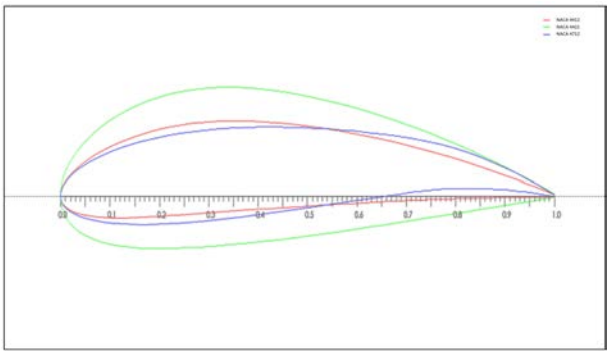

Figure 10.4: *NACA 4412, 4421 and 4712 aerofoil profiles.*

Figure 10.4 depicts the profiles of three NACA aerofoils namely NACA4412, 4421, and 4712 which have been generated using the Q-blade software by taking chord length as 1 m. Also, it can be concluded that for all the aerofoils the maximum thickness is there at the location of 0.3 m from the leading edge of an aerofoil and NACA 4421 aerofoil has the maximum thickness among all of them. Also, NACA4421 shows the highest camber among all the aerofoils.

Figure 10.5, depicts the plot generated using the Q-blade software for all three aerofoils at M = 0.0087 and Re = 50000. For the lift coefficient and Cl/Cd versus angle of attack plots, it can be seen that NACA4712 aerofoil shows impressive results over the wide range of angles in comparison with the other two aerofoils. At AOA 8 degree NACA4712 aerofoil has the maximum value of lift coefficient and Cl/Cd ratio. For the lift coefficient versus Transition point (Xtr) plot, all the aerofoils show a similar down falling trend.[19] has presented the optimization of HAWT by considering different parameters like AOA, aerofoil type, and speed of the wind. The investigators considered various NACA aerofoils namely 4412, 2412, modified 4412, and modified NACA2412 for the analysis using Q-blade software and optimization by using Taguchi method. They concluded that for obtaining the optimal power, the conditions found were aerofoils – Mod NACA 4412 and 2415 placed at 3 degrees AOA for the wind speed of 8 meters per sec. On the basis of ANOVA analysis, the most and least significant factors found were the speed of the wind and AOA respectively.

Table 4 comprises the details of the S/N ratio graph for the rotor power.

A study has been made on a small capacity HAWT by using Q-blade software which is based on a BEM theory. Also, the effect of chord and angle of twist design was deeply investigated by considering SG6043 aerofoil at 10 varying locations along blade length and the maximum obtained value for the C_L/C_D was at the AOA of 2 degrees. Below is Figure 10.6 depicting the modified and unmodified blades of the wind turbine with SG6043 aerofoil[20].

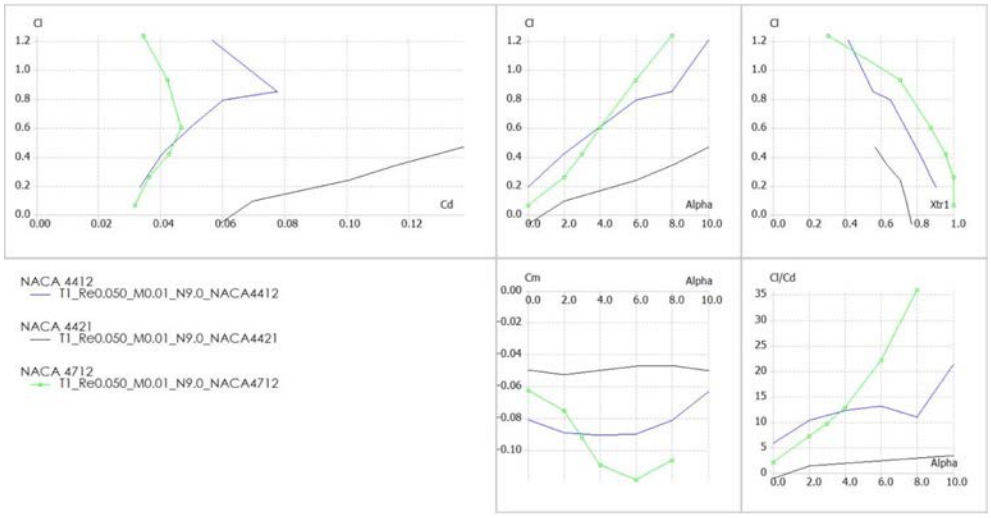

Figure 10.5: *Plots between various parameters at Mach 0.0087 and Re 50000 for NACA4412, 4421 and 4712 using Q-blade software.*

Table 4: S/N Ratio response of Roundness of Effect of Factor[19]

Level	Aerofoil	AOA	Wind Speed
1	57.51	57.84	51.27
2	57.56	57.78	56.00
3	57.90	57.70	60.10
4	57.93	57.58	63.53
Delta	0.42	0.26	12.26
Rank	2	3	1

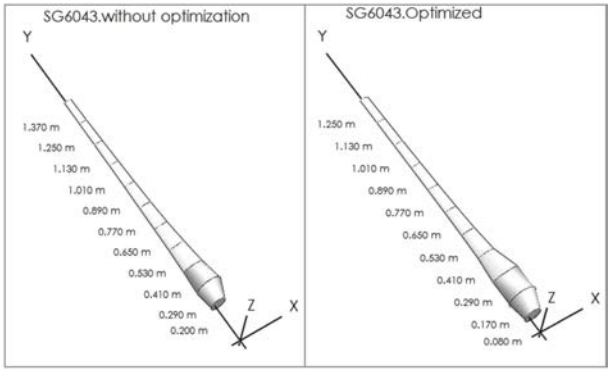

Figure 10.6: *Wind turbine blades (Source: Q-blade)[20].*

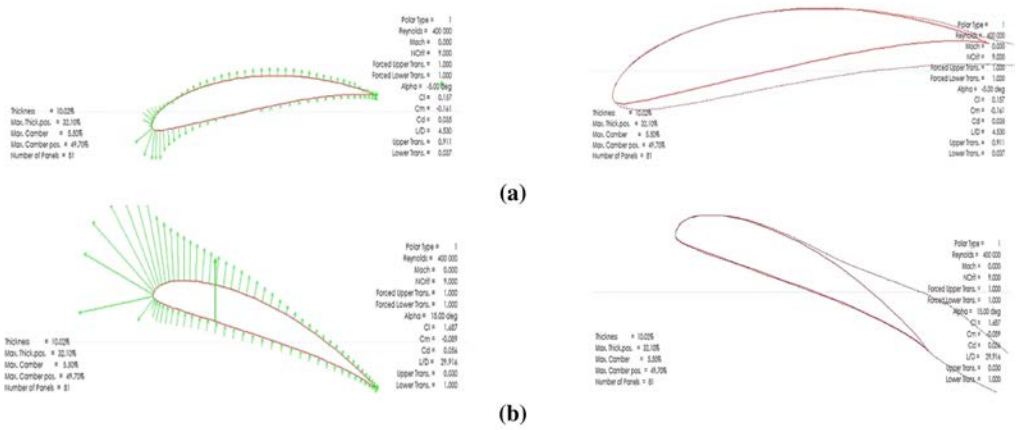

Figure 10.7: *Pressure distribution and boundary layer of SG6043 aerofoil at (a) AOA of – 5 degree (Re 4 x 104) and (b) AOA of 15 degree (Re 4 x 104) [21].*

Based on BEM theory research has been carried out on a small-scale HAWT setup. For experimentation and simulation purpose SG6043 aerofoil was selected and its corresponding parameters like the coefficient of lift and drag was taken as a reference. The investigation has been done on the variable chord length and a rotor diameter of 2.5 m by varying the pitch from 5 to 25 degrees. Pressure vector and boundary layer of the selected aerofoil at AOA of – 5 degrees and 15 degrees at Reynolds number of 4 x 10^5 is depicted in Figure 10.7 [21].

A study has been carried out to investigate the performance of HAWT both with non-yawing and yawing mechanism using Q-blade software. It has been concluded that there was a significance of yaw angles on the turbine performance. It has been observed that there is a decrement in power output by around 15% after 25-degree yawing angle in non-yawed flow and there is almost ½ of the power generation at a yawing angle of more than 45 degrees[22].

In the present study our main focus is to find out the impact of various parameters i.e. Reynolds number, Mach number, angle of attack, and type of aerofoil on the aerodynamic characteristic variables like lift coefficient C_L, drag coefficient C_D, and power coefficient C_P. For that, the value of turbulence considered is the default value in the software tool utilized for the simulation purpose.

10.3.1 Validation of Q-Blade Simulation Results

An investigation has been carried out by Bili Darnanto Susilo et al.[23] on NACA 4712 and NACA 4412 aerofoils using Q-blade software and CFD simulations at various angles of attack to obtain the results like lift coefficient, drag coefficient, C_L/C_D ratio. It has been concluded that NACA4712 showed higher lift, power coefficients, and C_L/C_D ratios in comparison with NACA4412. Also, the maximum lift coefficients obtained for both aerofoils were 1.696 for NACA4712 and 1.628 for NACA4412. And similar trends can be seen in Figure 10.8, among the present study which demonstrates the close agreement with the past research. In the present research also NACA4712 aerofoil showed impressive results over a wider range of angles in comparison with the other two aerofoils namely NACA4412 and NACA0021.

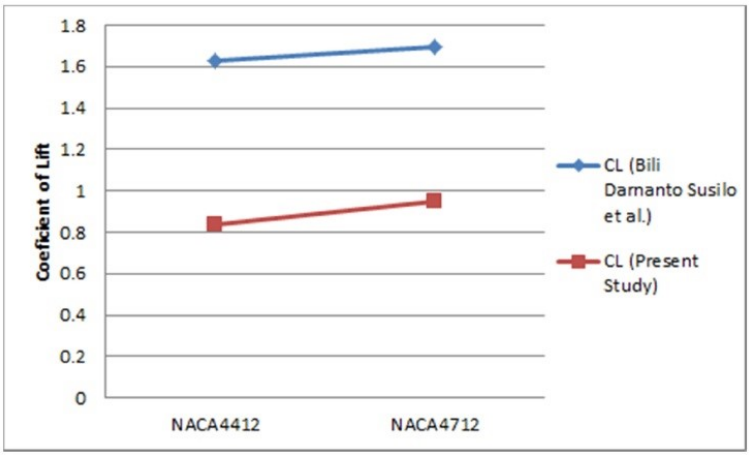

Figure 10.8: *Comparison of lift coefficients of NACA4412 and NACA4712.*

10.3.2 Mathematical Formulation Related to Q-Blade

Lift and Drag Coefficients (C_L and C_d)

Lift and drag coefficients are the dimensionless variables of aerodynamic forces and can be formulated by the following mathematical equations (2) and (3)

$$C_L = \frac{L}{0.5\rho A v^2} \tag{10.2}$$

$$C_L = \frac{D}{0.5\rho A v^2} \tag{10.3}$$

Where,

L is Lift force in (N)
D is Drag force in (N)
ρ is air density in (kg/m^3)
v is airflow velocity in (m/s)
A is swept area in (m^2)

Lift and Drag Force Extrapolation of an Aerofoil

Each and every section of an aerofoil can be extrapolated by using Montgomerie and Viterna techniques, which are very popular methods among all for extrapolation purposes [24].

Viterna technique: By utilizing the set of aerofoils data obtained from the analysis of XFOIL. The performance of extrapolation for stalling angle of attack to a 90-degree angle of attack is done with the help of the following mathematical equations [24].

$$C_D = B_1 \sin^2 \alpha \;\; B_2 \cos \alpha \tag{10.4}$$

$$C_L = A_1 \sin 2\alpha \;\; A_2 \cos^2 \alpha \sin \alpha \tag{10.5}$$

$$C_{D_{max}} \cong 1.11 \;\; 0.018AR \tag{10.6}$$

Where

AR is the aspect ratio of wind turbine

$$A_1 = C_{Dmax}2 \tag{10.7}$$

$$B_1 = C_{Dmax} \tag{10.8}$$

$$A_2 = C_L - C_{Dmax} \sin\alpha_{stall} \cos\alpha_{stall} \frac{\sin\alpha_{stall}}{\cos^2\alpha_{stall}} \tag{10.9}$$

$$B_2 = \frac{C_{D_{stall}} - C_{D_{max}} \sin^2\alpha_{stall}}{\cos\alpha_{stall}} \tag{10.10}$$

Montgomerie technique: At a higher angle of attack aerofoil behaves like a thin plate. Here in this technique, the assumption is considered around an aerofoil placed at 00. Below is the equation which defines the curve of potential flow[24]

$$C_L = f \times 1 \ \ fs \tag{10.11}$$

Where,

t – Straight tangent to $C_L\alpha = 0$

f – Transformation function

$$f = \frac{1}{1f_2 - 1\frac{1}{\alpha_2 - \alpha_m{}^4} \times \Delta\alpha^4} \tag{10.12}$$

where,

α_m – deviation of C_L from potential flow curve angle

$$\alpha_m = \frac{\alpha_1 - \sqrt[4]{\frac{1}{f_1} - 1\frac{1}{f_2} - 1 \times \alpha_2}}{1 - \sqrt[4]{\frac{1}{f_1} - 1\frac{1}{f_2} - 1}} \tag{10.13}$$

Coefficient of Power of Wind Turbine

The analysis of power coefficient of wind turbines can be done for the wide range of tip speed ratios (TSR)[25]. Mathematically the power coefficient and tip speed ratio are given as follows

$$C_P = \frac{P}{0.5\rho A v^3} \tag{10.14}$$

$$TSR\lambda = \frac{wR}{\nu} \tag{10.15}$$

where,

w -Angular velocity of a wind turbine

v - Linear velocity

R - Radius of wind turbine

10.4 Result and Discussion

10.4.1 Single Response Taguchi Method

Lift Coefficient (C_L)

ANOVA is a simplified effect of the column method of Taguchi which stipulates columns with a large influence on a particular response. The experimental data of the lift coefficient is demonstrated in below

Table 5.

Using the Q-Blade simulation tool results have been obtained for NACA 4412, 4421, and 4712 aerofoils for the given parameters like angle of attack, Reynolds number, and Mach number.

Table 5: Table for Mean C_L and SN ratio for L-9 OA

Exp No.	NACA Aerofoil	Mach No.	Re	AOA	MEAN1 C_L	SNRA1
1	4412	0.0087	50000	2 degree	0.4193	-7.5495
2	4412	0.0146	75000	4 degree	0.8337	-1.5798
3	4412	0.0204	100000	6 degree	0.7865	-2.08603
4	4421	0.0087	75000	6 degree	0.4174	-7.58895
5	4421	0.0146	100000	2 degree	0.7152	-2.91145
6	4421	0.0204	50000	4 degree	0.2341	-12.612
7	4712	0.0087	100000	4 degree	0.8117	-1.81209
8	4712	0.0146	50000	6 degree	0.9491	- 0.45376
9	4712	0.0204	75000	2 degree	0.3966	- 8.03295

It can be observed from Table 5 that the C_L max value (Max coefficient lift) is 0.9491 for the experimental run 8 for NACA 4712 aerofoil kept at 6 degrees AOA, 0.0146 Mach number for Reynolds number of 50000. And similarly, the min value of lift coefficient C_L min 0.2341 for the experimental run 6 where the corresponding Mach number is 0.0204, AOA is 4 degrees, and Reynolds number is 50000 for the NACA 4421 aerofoil.

By considering larger is better for C_L, Figure 10.9 depicts the impact of aerofoil type, Reynolds number, Mach number, and AOA on CL mean along with SNR main effect plots for C_L. Table 6 depicts that the major impact on C_L is due to the Mach number followed by the Reynolds number, and type of aerofoil, and the least influence is due to the angle of attack. Also, the delta value helps us to decide about the variable which has the greater amount of noise (error) associated with it and hence majorly influences the output, here we have a Mach number with a delta value of 5.929, and the least influenced one is AOA with a delta value of 2.788.

Table 6: Signal/Noise response for C_L

Level	Aerofoil	Mach No.	Re	AOA
1	-3.738	-5.650	-6.872	-6.165
2	-7.704	-1.648	-5.734	-5.335
3	-3.433	-7.577	-2.270	-3.376
Delta	4.271	5.929	4.602	2.788
Rank	**3**	**1**	**2**	**4**

Coefficient of Drag (C_D)

The experimental results for the coefficient of drag is presented below in Table 7 which states that the maximum and minimum values of C_D and the corresponding experiment number are $C_{D_{max}}$ = 0.10066

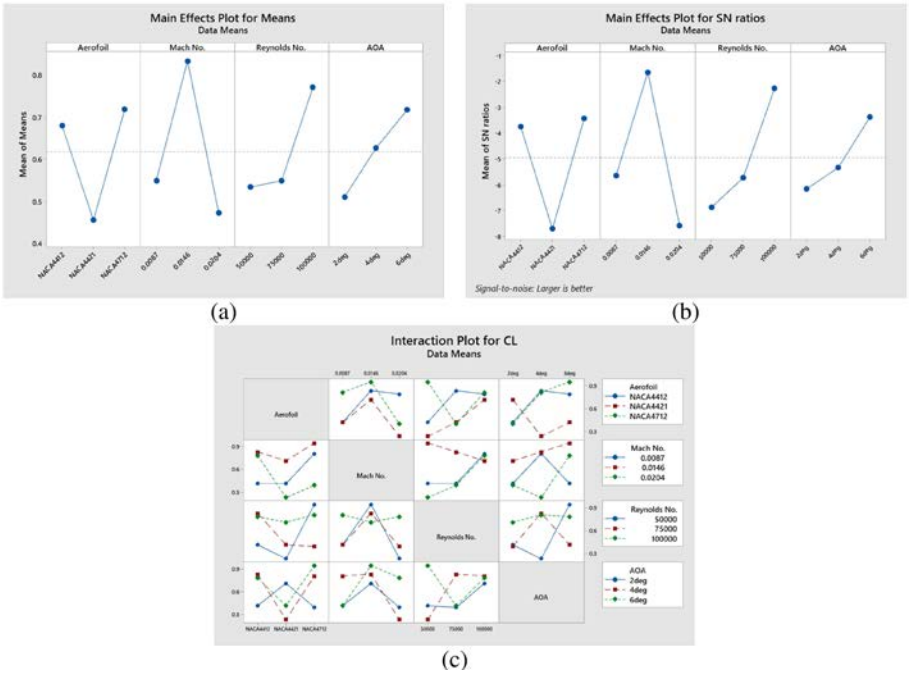

Figure 10.9: *(a) Effect of Aerofoil, Re, M and AOA on mean C_L, (b) Signal to Noise effect plot for C_L and (c) Plot for interaction of aerofoil, M, Re and AOA.*

Table 7: Table for Mean C_D and SN ratio for L-9 OA

Exp No.	NACA Aerofoil	Mach No.	Re	AOA	MEAN1 C_D	SNRA1
1	4412	0.0087	50000	2 degree	0.04056	27.8380
2	4412	0.0146	75000	4 degree	0.02754	31.2007
3	4412	0.0204	100000	6 degree	0.06018	24.4110
4	4421	0.0087	75000	6 degree	0.08034	21.9014
5	4421	0.0146	100000	2 degree	0.02627	31.6108
6	4421	0.0204	50000	4 degree	0.10066	19.9429
7	4712	0.0087	100000	4 degree	0.02601	31.6972
8	4712	0.0146	50000	6 degree	0.04053	27.8445
9	4712	0.0204	75000	2 degree	0.0339	29.3960

for experiment number 6 and $C_{D_{min}}$ = 0.02601 for experiment number 7. For experiment 7, the set of parameters influencing the response is NACA 4712 aerofoil (level 3) which is kept at 4 degrees angle of attack (level 2) at an inlet Mach number of 0.0087 (level 1) and corresponding Reynolds number taken as 100000 (level 3).

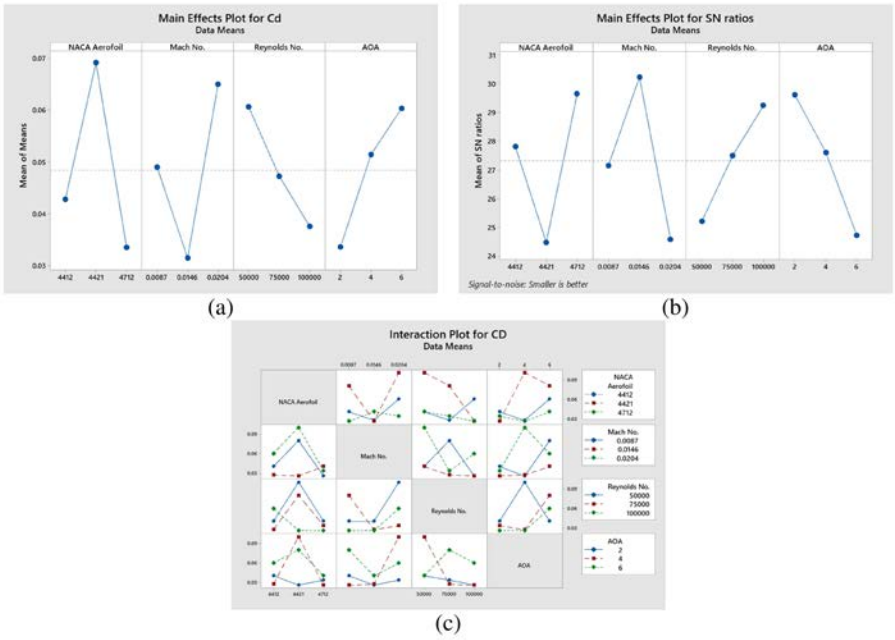

Figure 10.10: *(a) Effect of Aerofoil, Re, M and AOA on mean C_D, (b) Signal to Noise effect plot for C_D and (c) Plot for interaction of aerofoil, M, Re and AOA.*

Table 8: Signal/Noise response for C_D

Level	Aerofoil	Mach No.	Re	AOA
1	27.82	27.15	25.21	29.61
2	24.49	30.22	27.50	27.61
3	29.65	24.58	29.24	24.72
Delta	5.16	5.64	4.03	4.90
Rank	**2**	**1**	**4**	**3**

By considering smaller is better for C_D, Figure 10.10 depicts the impact of aerofoil type, Reynolds number, Mach number, and AOA on C_D mean along with SNR main effect plot for C_D. Table 8 depicts that the major impact on C_D is due to the Mach number followed by the type of aerofoil, angle of attack, and least influence by the Reynolds number.

Power Coefficient (C_p)

It is one of the significant aerodynamic parameters for a wind turbine. For the same, it has to be optimized to a greater extent to provide the maximum value of efficiency.

For finding the power coefficient of a wind turbine, the following empirical formula is used, which is expressed as follows [26]:

$$C_{pmax} = 0.593\frac{\lambda B^{0.67}}{1.48\ \ B^{0.67} - 0.04\lambda\ \ 0.0025\lambda^2} - \frac{1.92\lambda^2 C_D}{1\ \ 2\lambda B C_L} \tag{10.16}$$

Where,

λ - Tip speed ratio

B - Blade number

C_D and C_L is coefficient of drag and lift respectively.

For analysis purposes, we have considered the value for TSR = 5 and B = 3. For C_P which supposes to be the maximum for a wind turbine, we have considered "larger is better". The results obtained are demonstrated in Table 9. In an experiment run 7, it can be observed that the set of parameters influencing the response is NACA 4712 aerofoil (level 3) which is kept at a 4-degree angle of attack (level 2) at an inlet Mach number of 0.0087 (level 1) and corresponding Reynolds number taken as 100000 (level 3).

Table 9: Table for Mean C_P and SN ratio for L-9 OA

Exp No.	NACA Aerofoil	Mach No.	Re	AOA	C_P	SNRA1
1	4412	0.0087	50000	2 degree	0.440379	-7.1234
2	4412	0.0146	75000	4 degree	0.495263	-6.1032
3	4412	0.0204	100000	6 degree	0.455753	-6.8254
4	4421	0.0087	75000	6 degree	0.356283	-8.9641
5	4421	0.0146	100000	2 degree	0.492102	-6.1589
6	4421	0.0204	50000	4 degree	0.168278	-15.479
7	4712	0.0087	100000	4 degree	0.496196	-6.0869
8	4712	0.0146	50000	6 degree	0.486258	-6.2626
9	4712	0.0204	75000	2 degree	0.450588	-6.9244

Figure 10.11 comprises various graphs for CP depicting the signal-to-noise graph, interaction plot and main effects plot and Table 10 depicts the most influencing parameter for CP is the Aerofoil followed by Mach number, Reynolds number, and the least influencing parameter is the angle of attack.

***Table 10*:** Signal/Noise response for C_P

Level	Aerofoil	M	Re	AOA
1	-6.684	-7.392	-9.622	-6.736
2	-10.201	-6.175	-7.331	-9.223
3	-6.425	-9.743	-6.357	-7.351
Delta	3.776	3.568	3.265	2.488
Rank	**1**	**2**	**3**	**4**

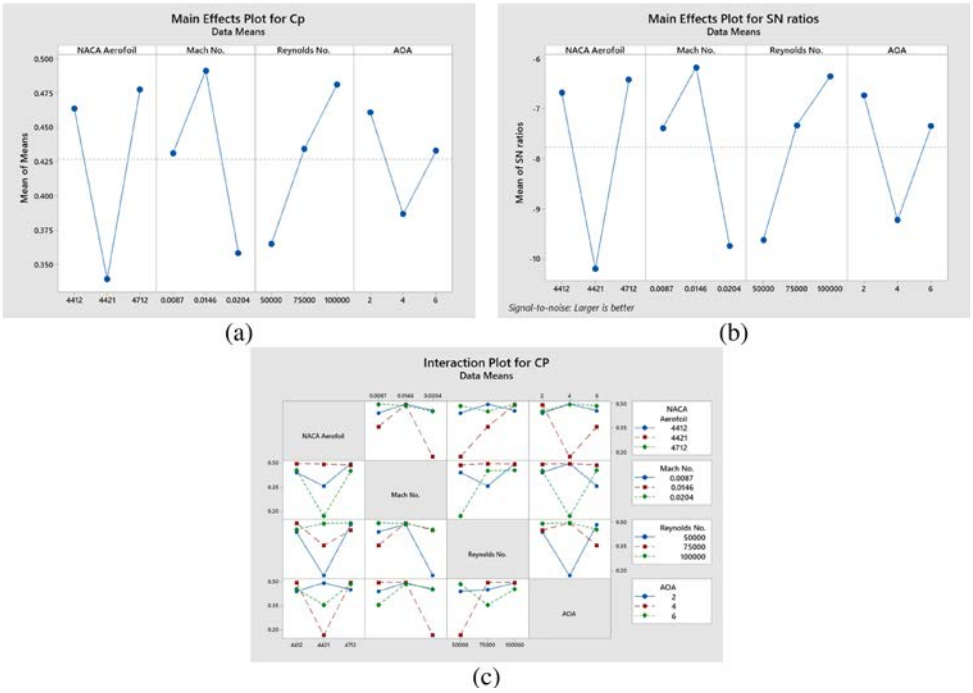

Figure 10.11: *(a) Effect of Aerofoil, Re, M and AOA on mean C_P (b) Signal/Noise ratio effect plot and (c) Plot for aerofoil, M, Re and AOA interaction.*

10.4.2 Multi response Grey- Based Taguchi Method

[27] had stated that for GRA (grey relational analysis) first step is normalizing the results (output) obtained from the experimentation of simulation and GRA has 0 as a minimum value and 1 as the maximum value.

The response value normalization has concluded by considering the lift coefficient and power coefficient as "higher is better" and the drag coefficient as "lower is better". It can be obtained by considering the following equation. Equation 3 is used for lower is better whereas for higher is better Equation (18) is taken into consideration.

$$X_{ij} = \frac{x_{max} - x_{ij}}{x_{max} - X_{min}} \qquad \text{Lower is better} \tag{10.17}$$

$$X_{ij} = \frac{x_{ij} - x_{min}}{x_{max} - X_{min}} \qquad \text{Higher is better} \tag{10.18}$$

Where

X_ij – normalized value for i^{th} experiment for j^{th} performance

x_{max} – value for maximum response

x_{min} – value for minimum response

x_{ij} – response value for i^{th} experiment for j^{th} performance

Table 11 comprises the values of GRA along with normalized values of C_L, C_D and C_P also consisting of GRG (grey relational grade) which can be evaluated by using Equation (20) along the ranking of various parameters.

Table 11: Normalized Values and Calculated GRC for coefficient of lift, drag and power for L-9 OA and Main effects on mean Grey Relational Grade (GRG)

Exp No.	NACA Aerofoil	Mach No.	Re	AOA	Normalized Values			Grey Relational Coefficient			GRG	Rank
					C_L	C_D	C_P	C_L	C_D	C_P		
1	4412	0.0087	50000	2 degree	0.25902	0.80509	0.82978	0.40290	0.71951	0.74602	0.6228	7
2	4412	0.0146	75000	4 degree	0.83860	0.979504	0.99715	0.75597	0.96062	0.99434	0.9036	2
3	4412	0.0204	100000	6 degree	0.72587	0.542264	0.87666	0.68738	0.52206	0.80214	0.67052	5
4	4421	0.0087	75000	6 degree	0.25636	0.272204	0.57332	0.40204	0.40723	0.53956	0.4496	8
5	4421	0.0146	100000	2 degree	0.67286	0.99651	0.98751	0.60449	0.99308	0.97563	0.8577	4
6	4421	0.0204	50000	4 degree	0	0	0	0.33333	0.33333	0.33333	0.3333	9
7	**4712**	**0.0087**	**100000**	**4 degree**	**0.80783**	**1**	**1**	**0.7223**	**1**	**1**	**0.9074**	**1**
8	4712	0.0146	50000	6 degree	1	0.80549	0.9696	1	0.7199	0.9428	0.8875	3
9	4712	0.0204	75000	2 degree	0.2272	0.89430	0.8609	0.3928	0.8255	0.7823	0.6669	6

Followed by the normalized values, grey relational coefficient (ξ_{ij}) is evaluated by taking β as 0.5 in Equation 19.

$$\xi_{ij} = \frac{min_i min_j \mid X_i^0 - X_{ij} \mid \beta max_i max_j \mid X_i^0 - X_{ij} \mid}{\mid X_i^0 - X_{ij} \mid \beta max_i max_j \mid X_i^0 - X_{ij} \mid} \tag{10.19}$$

Where,

ξ_{ij} - Grey relational coefficient

X_i^0 - Ideal normalized value

X_ij - Response value for ith experiment for jth performance

$$\Gamma = \frac{1}{n} \sum_i^n w_i \xi_{ij} \tag{10.20}$$

Where, w_i is the factor of weighting

In the present work, the multi-response Grey based approach is taken into consideration which is used to solve the practical problems within the limited set of data and gives us the normalized values and GRC i.e; grey relational coefficient. GRC helps us to determine the ranking of all the factor combinations i.e; (Aerofoil, Mach number, Reynolds number and angle of attack). Here we are considering the multiple responses for the optimization process of output by considering input factors/parameters. On the other hand, the single response considers only single output parameter for optimization purposes.

From Table 11, an inference can be drawn that for experimental run 7, the overall rank for all the combined responses is rank 1 with Grey relational grade (GRG) of 0.9074 for the corresponding factors as NACA4712 aerofoil kept at 4 degrees AOA and Mach number 0.0087 for Reynolds number of 100000 and the least ranking i.e; rank 9 was there for the experimental run 6 with GRG of 0.3333.

In comparison with other methods like RSM, regression analysis, ANOVA analysis, etc.. Taguchi approach for experimental designing has supremacy in various aspects like cost reduction, quality improvement, ability to optimize various factors simultaneously along with the extraction of more information through minimum experimental runs, for example, a process having 8 variables each with 3 levels, would require 6561 i.e; 3^8 experimental runs. But by implementing Taguchi approach to this, it would require only 18 experimental runs to get the most optimal result or less than 0.3% of 6561 runs which come to be 19.683. Moreover, this method of DOE is very simple but powerful tool that can be applicable in almost all engineering fields.

10.5 Conclusions

This research paper presents the implementation of Taguchi method for designing a robust horizontal-axis wind turbine. Designing and simulation were done using Q-blade software. A Design of Experiment method namely Taguchi approach with L-9 orthogonal array mapping was utilized for studying the effect and influence of individual parameters like Reynolds number, aerofoil type, angle of attack, and Mach number on the aerodynamic performance of a wind turbine. Both single and multi-response Taguchi approaches are utilized in the present work.

From the wind turbine designing and simulation software the results obtained are: The maximum lift coefficient obtained is 0.9491 in an experiment run 8 for an input Mach number of 0.0146 when NACA4712 aerofoil was kept at 6 degrees angle of attack at Re of 50000 and on the other hand, the minimum drag coefficient value obtained was 0.02601 for an experiment run 7, for the NACA4712 aerofoil which was placed at 4-degree angle of attack when the input Mach number was 0.0087 with 100000 Re. The inferences are drawn from the obtained signal/noise response for various aerodynamic parameters of wind turbine are:

a) For the coefficient of lift the most and least influenced parameters are Mach number and angle of attack respectively, whereas Reynolds number and aerofoil type are the second and third most influenced variables respectively,
b) Similarly, for drag coefficient, Mach number and Reynolds number are the most and the least influenced parameters, and
c) Aerofoil type followed by Mach number is the prime influenced parameter, whereas the angle of attack is the least one for the power coefficient.

By considering the plot for main effects, the major influencing individual parameters that affect the wind turbine performance are NACA 4712 Aerofoil at (L3), input Mach number of 0.0146 at (L2), and Re of 100000 for all the three coefficients of lift, drag and power, whereas the AOA of 2 degrees is for both drag and power coefficient respectively. And for lift coefficient, the most influenced AOA is 6 degrees.

Funding: The authors did not receive support from any organization for the submitted work.

Conflicts of Interest: The authors declare that they have no conflicts of interest.

Authors Contributions: VK and RNS had the idea for this analysis and to optimize the results with Taguchi approach. RNS has supervised the research work. NIHR and PBK supported the research as an expert. All authors critically revised and edited the text and results, and finally approved the manuscript.

References

1. Aguilar, C. H., López, F. S., & Pacheco, F. A. D. (2022). Sustainable Development Goals index: An analysis (2000-2022). *Transdisciplinary Journal of Engineering and Science*, 13, 111–128. https://doi.org/10.22545/2022/00213.
2. Rao, S. S. (2015). Robust design of horizontal axis wind turbines using Taguchi method. *ASME International Mechanical Engineering Congress and Exposition, Proceedings (IMECE)*, 6B-2015, 1–9. https://doi.org/10.1115/IMECE201552093

3. Kaushik, V., & Shankar, R. N. (2021). Review of Experimental Approaches for the Analysis of Aerodynamic Performance of Vertical Axis Wind Turbines. In N. Gascoin & E. Balasubramanian (Eds.), *Innovative Design, Analysis and Development Practices in Aerospace and Automotive Engineering* (pp. 473–480). Springer Singapore.
4. Kackar, R. N. (1989). Off-Line Quality Control, Parameter Design, and the Taguchi Method. *Quality Control, Robust Design, and the Taguchi Method,* 51–76. https://doi.org/10.1007/978-1-4684-1472-1_4.
5. Ku, K. J., Rao, S. S., & Chen, L. (1998). Taguchi-aided search method for design optimization of engineering systems. *Engineering Optimization,* 30(1), 1–23. https://doi.org/10.1080/03052159808941235.
6. Chiang, K.-T. (2005). Optimization of the design parameters of Parallel-Plain Fin heat sink module cooling phenomenon based on the Taguchi method.*International Communications in Heat and Mass Transfer,* 32(9), 1193–1201. https://doi.org/10.1016/j.icheatmasstransfer.2005.05.015.
7. Hu, Y., & Rao, S. S. (2011). Robust Design of Horizontal Axis Wind Turbines Using Taguchi Method. *Journal of Mechanical Design,* 133(11). https://doi.org/10.1115/1.4004989.
8. Emre Koç, Onur Günel, T. Y. (2016). Mini-Scaled Horizontal Axis Wind Turbine Analysis By Qblade and Cfd.*International Journal of Energy Applications and Technologies,* 3(2), 87–92. https://doi.org/ https://dergipark.org.tr/en/pub/ijeat/issue/28204/299500.
9. Roy, R. K. (2010). *A Primer on the Taguchi Method.* Society of Manufacturing Engineers (SME), USA
10. Khanjanpour, M. H., & Javadi, A. A. (2021). Optimization of a Horizontal Axis Tidal (HAT) turbine for powering a Reverse Osmosis (RO) desalination system using Computational Fluid Dynamics (CFD) and Taguchi method. *Energy Conversion and Management,* 231, 113833. https://doi.org/10.1016/j.enconman.2021.113833.
11. Hwas, A. M., Lect, P. D., & Hatab, A. M. (2020). *Effects of Design Parameters of Wind Turbine on Airfoil Coefficients Using Grey-Based Taguchi Method.* 7(12), 13103–13109.
12. Dhamotharan, V., Meena, R., Jadhav, P., Ramu, P., & Prakash, K. A. (2015). Robust Design of Savonius Wind Turbine. In *Renewable Energy in the Service of Mankind,* Vol I (Vol. 1, Issue September, pp. 913–923). Springer International Publishing. https://doi.org/10.1007/978-3-319-17777-9_82.
13. Qasemi, K., & Azadani, L. N. (2020). Optimization of the power output of a vertical axis wind turbine augmented with a flat plate deflector.*Energy,* 202, 117745. https://doi.org/10.1016/j.energy.2020.117745.
14. Kriswanto, Romadlon, F., Al-Janan, D. H., Aryadi, W., Naryanto, R. F., Anis, S., Sukoco, I., & Jamari. (2022). Rotor Power Optimization of Horizontal Axis Wind Turbine from Variations in Airfoil Shape, Angle of Attack, and Wind Speed. *Journal of Advanced Research in Fluid Mechanics and Thermal Sciences,* 94(1), 138–151. https://doi.org/10.37934/arfmts.94.1.138151.
15. Suresh, A., & Rajakumar, S. (2019). Design of small horizontal axis wind turbine for low wind speed rural applications. *Materials Today: Proceedings,* 23(July 2019), 16–22. https://doi.org/10.1016/j.matpr.2019.06.008.
16. Altmimi, A. I., Alaskari, M., Abdullah, O. I., Alhamadani, A., & Sherza, J. S. (2021). Design and optimization of vertical axis wind turbines using qblade. *Applied System Innovation,* 4(4), 1–11. https://doi.org/10.3390/asi4040074.
17. D. Marten, J. Wendler, G. Pechlivanoglou, C.N. Nayeri, C. O. P. (2013). QBLADE: an open source tool for design and simulation of horizontal and vertical axis wind turbines. *International Journal of Emerging Technology and Advanced Engineering,* 3(3), 264–269.
18. D. Marten, J. Wendler, G. Pechlivanoglou, C.N. Nayeri, C. O. P. (2013). QBLADE: an open source tool for design and simulation of horizontal and vertical axis wind turbines.*International Journal of Emerging Technology and Advanced Engineering,* 3(3), 264–269.
19. Kriswanto, Romadlon, F., Al-Janan, D. H., Aryadi, W., Naryanto, R. F., Anis, S., Sukoco, I., & Jamari. (2022). Rotor Power Optimization of Horizontal Axis Wind Turbine from Variations in Airfoil Shape,

Angle of Attack, and Wind Speed.*Journal of Advanced Research in Fluid Mechanics and Thermal Sciences,* 94(1), 138–151. https://doi.org/10.37934/arfmts.94.1.138151.

20. Alaskari, M., Abdullah, O., & Majeed, M. H. (2019). Analysis of Wind Turbine Using QBlade Software. *IOP Conference Series: Materials Science and Engineering,* 518(3). https://doi.org/10.1088/1757-899X/518/3/032020.
21. Nabil, T., Dawood, M. K., & ... (2018). Design and Implementation of the Rotor Blades of Small Horizontal Axis Wind Turbine. *Journal of Renewable Energy and Environment,* 5(2), 41–51.
22. Husaru, D. E., B rsănescu, P. D., & Zahariea, D. (2019). Effect of yaw angle on the global performances of Horizontal Axis Wind Turbine - QBlade simulation.*IOP Conference Series: Materials Science and Engineering,* 595(1). https://doi.org/10.1088/1757-899X/595/1/012047.
23. Susilo, B. D., Jatisukamto, G., & Kustanto, M. N. (2019). Characteristic Analysis of Horizontal Axis Wind Turbine Using Airfoil NACA 4712. *Journal of Mechanical Engineering Science and Technology,* 3(2), 96–108. https://doi.org/10.17977/um016v3i22019p096.
24. Mahmuddin, F., Klara, S., Sitepu, H., & Hariyanto, S. (2017). Airfoil Lift and Drag Extrapolation with Viterna and Montgomerie Methods. *Energy Procedia,* 105, 811–816. https://doi.org/10.1016/j.egypro.2017.03.394.
25. Battisti, L., Benini, E., Brighenti, A., Dell'Anna, S., & Raciti Castelli, M. (2018). Small wind turbine effectiveness in the urban environment. *Renewable Energy,* 129, 102–113. https://doi.org/10.1016/j.renene.2018.05.062.
26. Spera, D.A. (2009). *Wind Turbine Technology: Fundamental Concepts in Wind Turbine Engineering, Second Edition* (David A. Spera (ed.); second edi). ASME Press. https://doi.org/10.1115/1.802601.
27. Tarng, Y. S., Juang, S. C., & Chang, C. H. (2002). The use of grey-based Taguchi methods to determine submerged arc welding process parameters in hardfacing.*Journal of Materials Processing Technology,* 128(1–3), 1–6. https://doi.org/10.1016/S0924-0136(01)01261-4.

About the Authors

Mr. Vishal Kaushik is a Ph.D. Scholar in the Department of Aeronautical Engineering at VelTech Rangarajan Dr. Sagunthala R&D Institute of Science and Technology, Chennai, India. He is currently working as an Assistant Professor in Department of Aeronautical Engineering, PCE Nagpur with an experience of nearly 7 years. He has received his B.E. degree in Aeronautical Engineering from Nagpur University in 2013 and M.Tech Degree in Aerospace Engineering from JNTU University, Hyderabad, in 2016, respectively. He has published 15 research articles in various International Journals/Conferences and has 6 professional bodies' memberships. ORCID ID: 0000-0001-9007-5636.

Dr. R. Naren Shankar is currently working as an Associate Professor (Research) in Department of Aeronautical Engineering at VelTech Rangarajan Dr. Sagunthala R&D Institute of Science and Technology,

Chennai, India. He has received Ph.D. in Gas Dynamics from MIT Campus Anna University, Chennai, India. He is having 13.5 years of experience. He has He has completed two funded projects of NSTL-DRDO and Preethi Kitchen Appliances Pvt. Ltd and working on funded projects from SERB-TARE and VEL TECH SEED FUND. He has published 20 research papers in high impact factor Journals indexed in Scopus and SCI. He has also filed 3 patents and is having research collaboration with 5 organizations. Also, he is a book editor of "Aspects and Applications of Incompressible and Compressible Aerodynamics", IGI Global. He is an Associate member of Aeronautical Society of India (AM7400). Also he is a reviewer of International Journal of Turbojet and Journal of Aerospace (Institute of Mech Engg. Part- G). His main area of interest is in High Speed Jet Flows, Shock waves, Computational analysis of high speed jets, Wind turbine Aerodynamics. ORCID ID: 0000-0002-3363-4478.

Dr. N. I. Haroon Rashid is currently working as an Associate Professor in Department of Aeronautical Engineering at B.S. Abdur Rahman Crescent Institute of Science and Technology, Chennai, India. Prior, he has worked as HoD, Department of Aeronautical Engineering, Mohamed Sathak Engineering College, Kilakarai, Tamil Nadu, India. He has received Ph.D. in Aerospace Engineering from Anna University, Chennai, India. He is having nearly 24 years of experience in Academics. He has published several research papers in high indexed International/National Journals. He has also worked as a reviewer for Journal of Mechanical Science and Technology, Seoul. His main areas of interest are Aerodynamics, Aircraft General Engineering & Maintenance Practices, Airframe Maintenance and Repair, Wind Engineering etc. ORCID ID: 0000-0002-0444-2880.

Dr. P. B. Khope is currently working as HoD of Aeronautical Engineering Department, PCE Nagpur. He has received his Ph.D. in Mechanical Engineering from Nagpur University in 2014. He is having nearly 30 years of experience in Academics. He has published over 35 research papers in International/National Journals/Conferences. In addition to this, he has filed 6 patents and is an author of 2 books. He is having 10 professional bodies' memberships. ORCID ID: 0000-0002-5491-476X.

CHAPTER 11

Modified Lewis Correlation for Desiccant Dehumidification Process

M. H. Gurses, A. Ertas

Article citation information: (2022), *TJES*, Vol. SP-2, pp. 1-21, doi:10.22545/2022/00172

Using effective tower design utilized in the dehumidification of air has potential applications in many fields,e.g., air-conditioning, crop-drying, meat, and fish drying, to reduce energy consumption. One of the most important parameters for packed tower design is the correct calculation of the Lewis Correlation. In this study, the Lewis Correlation method is summarized, and the agreements and disagreements are discussed. The Lewis Correlation method is modified for packed tower applications. This modification is based on the assumption that the water layer is thick and therefore the change in the interfacial temperature with tube length varies. The resulting equations are applied to water and liquid desiccants.

Keywords: Packed tower, Lewis correlation, liquid desiccant, vapor pressure equilibrium.

11.1 Introduction

Using effective tower design utilized in the dehumidification of air has potential applications in many fields, e.g., air-conditioning, crop-drying, and meat, and fish drying, to reduce energy consumption. One of the most important parameters for packed tower design is the correct calculation of the Lewis Correlation. Walker, Lewis, and McAdams [1] proposed a basic theory for cooling tower operation in 1923. Lewis [2] proposed an approximate relation for cooling water systems by assuming the interface temperature along the height of the cooling tower and Merkel [3] developed the first practical use of Lewis' relation in 1925. The Lewis relation was based on the assumption that the interface temperature is equal to the liquid temperature, and states that the ratio of the heat transfer coefficient to the coefficient of vapor diffusion through the gas film is constant and equal to the heat capacity of the humid air which can be expressed by a constant. In 1933, Lewis [4] found, through experimentation, that this ratio was greater than twice the initial estimate. Hensel and Treyball [5] determined that the interface temperature was not equal to the liquid temperature and noted that the apparent psychometric ratio for a packed tower is neither constant nor equal to the heat capacity of the humid air, as previously postulated. Lof, et al. [6] supported this result and concluded that until additional data was available, the design of packed towers should be based on a heat/mass transfer coefficient ratio of about 0.5 rather than 0.24 Btu/lb $^{\circ}$F.

Many experiments have been performed in the past to correlate relations concerning heat and mass transfer between air and water. The air in the atmosphere contains 0%-4% water vapor. There are several applications of air-water vapor mixtures. One such application in engineering is air conditioning. Although

the amount of water in the air is small, it plays a major role in human comfort. Temperature, humidity, mass transfer, dust, clearness, and sound can affect comfort. Dehumidification of air can be achieved by refrigeration, mechanical compression, or using desiccants. To condense the excess moisture, air is cooled below the saturation temperature, compressed mechanically, or desiccants are used. Of these three operations, desiccant dehumidification has two major advantages over the other three operations. These are low drying temperatures and low cost. Desiccants are chemicals that have the ability to absorb moisture from different media. To reuse the desiccants or in other words, to evaporate the absorbed moisture from the desiccant, regeneration is necessary. The desiccant regeneration process requires the application of heat to drive off the moisture. There are two kinds of desiccants: Solid desiccants and liquid desiccants. Many chemicals can be used as liquid desiccants. e.g. lithium chloride, sodium or potassium hydroxide, mono ethylene, sulphuric acid, phosphoric acid, etc. Liquid desiccants have low vapor pressure, are nontoxic, and have the ability to be regenerated at low temperatures. Moreover, liquid desiccants clean up the air from contaminants and disinfect it. When the liquid desiccant and air are brought into contact with each other, depending on the concentration of the liquid desiccant, moisture tends to move from the gas phase to the liquid phase. The driving force in this phase change is the difference between the vapor of the liquid desiccant and the vapor pressure of the air.

In liquid desiccant systems, air and liquid desiccant can be brought into contact by flowing them through a counter flow tower such as a spray tower, a packed tower, or a wetted–wall tower. To regenerate the liquid desiccant, either the air or the desiccant is heated. A packed tower, vertical columns filled with packing or other devices to provide a large interfacial surface area, keeps the air and liquid desiccant in contact continuously. The liquid desiccant is distributed over the packing as a thin liquid film and it then flows downward under the influence of gravity. The air, which is moved upward through the wet packing by fans experiences a considerable pressure drop. Strigle [7] developed equations for the air side pressure drop related to the air velocity for counterflow towers. The pressure drop in packed towers is dependent on both the air and liquid flow rates. If the gas velocity is fixed, the gas pressure drop increases with increased liquid flow rate. Treybal [3] discusses problems due to the large pressure drop across the packed column. The selection of packing materials is important to minimize the pressure drop and to provide maximum interface surface area.

Lof et al. [6] examined a cooling system, combined with and operated by a solar air heating process, based on the concept of an open–cycle LiCl absorption air conditioning system. A packing made from 1–inch ceramic rashing rings was utilized. The resultant heat transfer coefficient was found to be within the expected range as predicted by the correlation of McAdams et al. [8] for pure water flowing in a column packed with 1–inch rings. The difference between the measured heat transfer coefficient and the McAdams correlation was about 10 percent. However, Lof et al. [6] were not satisfied with the mass transfer coefficient found by McAdams et al. [8].

Sherwood and Holloway [9] did the first extensive investigation relating to liquid mass transfer coefficients for packed towers. They studied the desorption of carbon dioxide, oxygen, or hydrogen from water using a variety of packing materials. They used different size ceramic rasching rings and berl saddles, and found that the volumetric mass transfer is the most widely used correlation because of its simplicity and its requirement of well–documented physical properties. In 1942, Molstad et al. [10] collected data for a square tower with approximately the same cross–sectional area of the study of Sherwood and Holloway [9]. Molstad et al. [10] used Sherwood and Holleway's correlation to determine the constants. Vivian and Whitney [11] also employed a similar process to find additional data for the desorption of oxygen from water in packed columns. Vivian and Whitney's [11] results were found to agree well with those of Sherwood and Holloway [9]. Norman [12] used the same data as Sherwood and Holleway [9], and Molstad [10] for different packings and found smaller values for the volumetric mass transfer. Sherwood and Pigford [13] reported that one of the equations did not give accurate data for absorption as reported by Sherwood and Holleway [8]. Puranik and Vogelpohl [14] developed a correlation for predicting values of the effective interfacial area based on the concepts of static and dynamic area. With these three equations, all values of the interfacial area during vaporization, absorption with and without chemical reaction, and wetted surface area can be predicted within a range of $\pm$ 20 percent accuracy. However, many investigators concluded that further investigations are

necessary for the contact of air and liquid at the interface.

Because of the difficulty of measurements, the interfacial temperature is usually assumed to be equal to the bulk temperature of the liquid. In 1922, Lewis [2] established an important relationship for calculating the humidity of air from wet– and dry–bulb thermometer readings, and showed that the ratio of the heat transfer coefficient to the diffusion coefficient is equal to the heat capacity of the humid air. This constant numerical value is about 0.26 to 0.27 for a wet bulb thermometer with water. The purpose of this paper is to show that this value changes with some properties and investigate the correct value for a liquid desiccant. Hence, the Lewis correlation will be summarized, and the agreements and disagreements will be discussed. Then the Lewis correlation will be modified to include the effect of the change in the interfacial temperature with the height of the tower.

11.2 Materials and Methods

11.2.1 Correction of Lewis Relation

The basic theory of cooling tower operation was proposed in 1923 by Walker, Lewis, and McAdams [1]. Lewis [2], by assuming the interface temperature to be constant with respect to tower height, was able to develop an approximate relation to describe cooling water systems. Merkel [3] combined Lewis' relation with the equations for heat and water vapor transfer to show that total heat or enthalpy could be used as a driving force to potentially provide both sensible and latent heat transfer. Merkel's work explained the insignificance of inlet air dry–bulb temperature in determining the cooling obtained in a given tower with specified air and water rates. Merkel's relationship,

$$\frac{h_g}{k_G} = c_s = 0.2355 \pm 0.0006,$$

states that the heat transfer coefficient divided by the coefficient of vapor diffusion through the gas film is constant and equal to the heat capacity of the humid air. This ratio can be calculated from the wet–bulb and dry–bulb temperatures for any vapor—gas mixture of known gas humidity. Clearly h_G and k_G depend on the air film thickness.

In 1933, Lewis [4] noted that the equations derived in 1922 were correct, but in comparing them it was mistakenly assumed that the absolute humidity of water and the temperature of the water was constant, whereas, in fact, they are functions of the air absolute humidity and temperature (Lewis [15]). The assumption by Lewis that the interface temperature is always equal to the liquid temperature is incorrect because the interfacial temperature depends on the air temperature. After many difficulties, he solved the problem through experimentation. He concluded that the ratio of the heat transfer coefficient of the gas to the vapor coefficient of diffusion is 0.60, a value more than 2.5 times greater than the heat capacity of the humid air. Simpson and Sherwood [16] agreed with this value of the psychrometric ratio and with Lewis' assumptions regarding work for a compact cooling tower used for air conditioning. They assumed that the ratio $h_G k_G$ for the water surfaces in a cooling tower was the same as for a wet–bulb thermometer. However, for a packed tower the mass and heat transfer areas are not equal thus Simpson and Sherwood assumed the psychrometric ratio to be $h_G a_H k_G a_M$, where a_H is the area of heat transfer and a_M is the interfacial mass transfer area.

Hensel and Treybal [5] also found that the interface temperature and the humidity vary considerably which required that the experimental coefficients had to be corrected before being used to generate a correlation. Further, they noted that the psychrometric ratio for a packed column is neither constant nor equal to the heat capacity of the humid air. They found the same values as Hensel and Treybal [5] reported in air–water systems. This ratio also varies in a packed column in which lithium chloride solutions are concentrated. They concluded that until additional data becomes available, it is recommended that the design of packed columns for this application is based on heat/mass transfer coefficient ratio of about 0.5 Btu/lb$^\circ$F rather than 0.24 Btu/lb$^\circ$F.

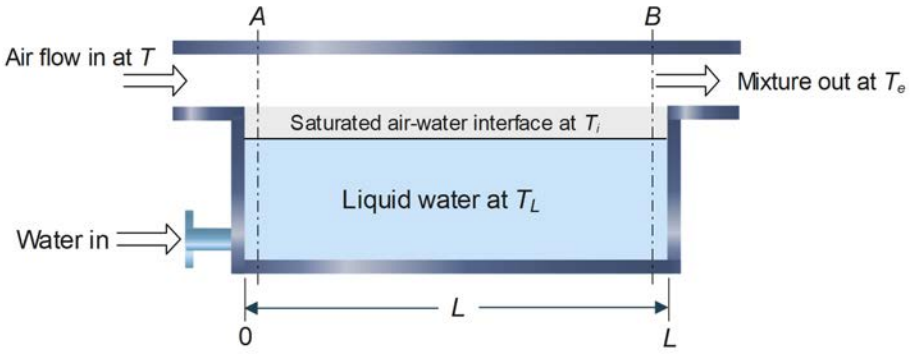

Figure 11.1: *Configuration considered for analysis (not scaled).*

11.2.2 New Psychrometric Ratio Value

Consider a long insulated horizontal pipe, as shown in Figure 11.1 (a detailed experimental setup of this figure will be introduced later), where liquid and air are in contact. The liquid, which is added as needed to maintain a constant level in the container, is stirred constantly to ensure that its concentration and temperature remain the same throughout the container. An air stream is introduced at one end of the container (pipe) over-flows over the liquid and allows the inlet temperature of the liquid to be less than the inlet air temperature. If the channel is long enough, the air stream will exist as saturated air at the adiabatic saturation temperature. The process can be analyzed as a steady–flow process with the mass velocity of the air over the liquid constant and sufficiently low so that heat generated by friction may be neglected. This process involves no heat or work interactions; therefore, the kinetic and potential energy changes may be neglected.

Lewis [2] derived this correlation with a thin layer for humidifier cooler (1922). Because the process is adiabatic and the only substance getting in and out is air, the following equations can be written for the mass and energy balances at the air and saturated gas layer interface at point A (see Figure 11.1). The weight of evaporated liquid is

$$-dW = k_G^{'} a_M P_i - P dt \tag{11.1}$$

where $k_G^{'}$ is the mass of liquid vapor transferred across the interface area, P is the partial pressure of the air, P_i is the partial pressure of the liquid-vapor in the interface, t is time, and a_M is the mass transfer interface area. The sensible and latent heats can be expressed as

$$dQ = h_G a_H T - T_i dt \tag{11.2}$$

and

$$dQ = -\lambda_o dW \tag{11.3}$$

In Equation (11.2), h_G is the heat transfer coefficient and a_H is the heat transfer interface area and λ_o in Equation (11.3) is the latent heat of vaporization at the base temperature of 90°F.
The absolute humidity is given by

$$w = 0.622\phi \frac{P_s}{P_t} \tag{11.4}$$

where ϕ is the relative humidity ($\phi = P_v P_s$), P_v is the partial liquid vapor pressure and P_s is the saturated steam vapor pressure at the air temperature. Rearrangement Equation (11.4) yields,

$$w = 0.622\frac{P_v}{P_t}, \quad \text{and} \tag{11.5a}$$

$$P = P_v = \frac{1}{0.622}P_t w \tag{11.5b}$$

Combining and rearranging Equations (1), (2), and (3) yields,

$$P_i - P = \frac{h_G a_H}{\lambda_o k_G^{'} a_M}T - T_i \tag{11.6}$$

If the interface is fully wetted, the heat transfer and mass transfer interface areas will be equal to each other ($a_M \approx a_H$). As the liquid temperature is constant throughout the pipe, the condition is fully wetted. Substituting Equation (11.5b) into Equation (11.6), rearranging and applying, $a_M \approx a_H$ gives

$$\frac{1}{0.622}k_G^{'}P_t w_i - w = \frac{h_G}{\lambda_o}T - T_i \tag{11.7}$$

The product of the first three terms on the left–hand side of Equation (11.7) is the mass transfer coefficient

$$k_G = \frac{1}{0.622}k_G^{'}P_t \tag{11.8}$$

Substituting Equation (11.8) into Equation (11.7) yields,

$$w_i - w = \frac{h_G}{k_G \lambda_o}T - T_i \tag{11.9a}$$

$$\lambda_o dw = -\frac{h_G}{k_G}T_i - T \tag{11.9b}$$

The heat given up by cooling the air must correspond to the heat of the vaporization of water. Hence, it becomes

$$-c_s dT = \lambda_o dw \tag{11.10}$$

where c_s is the humid air heat capacity, $c_s = 0.24\ \ 0.45w$ (Btu/lb dry air $^\circ$F). By assuming c_s and λ_o are constant throughout the pipe and then integrating Equation (11.10) from point A to point B (see Figure 11.1), it can be shown that,

$$w_e - w = \frac{c_s}{\lambda_o}T - T_e \tag{11.11}$$

where the subscript e indicates the exit. Rewriting Equations (11.9) and (11.11) generates the main equation of the Lewis correlation

$$w = w_i - \frac{h_G}{k_G \lambda_o}T - T_i = w_e - \frac{c_s}{\lambda_o}T - T_e \tag{11.12}$$

Lewis assumed that the interface temperature did not vary across the tube length. In other words, the interface temperature was equal to the liquid temperature, T_L, everywhere, and he also assumed that at the exit there was a thermal and vapor pressure equilibrium, namely

$$T_i = T_L = T_e, \quad \text{and}$$

$$w_i = w_e$$

By using Equation (11.12), and the above definitions, we obtain

$$\frac{h_g}{k_G} = c_s \tag{11.13}$$

The psychrometric ratio, Equation (11.13), is the same as Lewis' correlation obtained in 1922.

11.2.3 Modified Lewis Correlation

As previously mentioned, the interface temperature may not necessarily be equal to the liquid temperature. Hensel and Treybal [5], and Lof et al. [6] concluded that the psychrometric ratio varies between 0.23 and 0.58. Hensel and Treybal [5] found the psychrometric ratio equal to 0.58 by assuming an extrapolated tower height. Their results imply that there should be a constant in front of the heat capacity of humid air, c_s. By introducing a correlation constant A to the right side of Equation (11.15), the modified Lewis correlation can be rewritten in the form of,

$$\frac{h_g}{k_G} = Ac_s \tag{11.14}$$

In light of the conclusions presented by Hensel and Treybal [5], and Lof et al. [6], A fluctuates between 1 and 2.32. When the layer of the liquid is very thin, it can be assumed that the interface temperature is equal to the liquid temperature. Compared to packed tower applications, the water layer is not thin. Considering the assumption of that the interface temperature depends on the air and liquid temperatures, the following assumption can be made:

$$T_i = A_1 T \;\; A_2 T_L \quad \text{and} \quad \mathrm{A}_1 \;\; \mathrm{A}_2 = 1 \tag{11.15}$$

For instance, choosing $A_1 = 0$, Equation (11.15) concludes to $T_i = T_L$. The correlation for the interface temperature may be obtained through experimentation. As mentioned previously, the Lewis correlation was found for a thin water layer, so for a thick water layer Equation (11.12) must be modified. The liquid film resistance to heat and mass transfer in the air–liquid system can be assumed negligible. The following equation relating to the height of a packed column and the film coefficient in the gas phase were obtained by Lof et al. [6].

$$h_G a_H = \frac{G^{'} c_s}{Z} \ln\left(\frac{T - T_i}{T_e - T_i}\right)$$

Taking into account of the long horizontal pipe, the above equation can be written as:

$$h_G a_H = \frac{G^{'} c_s}{L} \ln\left(\frac{T - T_i}{T_e - T_i}\right) \tag{11.16}$$

where $G^{'}$ is the flow rate of air, and L is the length of the tube. However, in regard to the tower, the basic differential equation for heat transfer is [6]

$$G^{'} c_s dT = -h_G a_H T_G - T_i dz \tag{11.17}$$

The heat transfer coefficient of the liquid phase is very small compared with the heat transfer coefficient of the gas phase, hence assuming

$$h_{overall} \approx h_G \quad \text{and} \quad a_{H\,overall} \approx a_{HG} \tag{11.18}$$

Now considering the overall heat transfer, Equation (11.17) can be modified to

$$-h_{overall} a_{H\,overall} T_G - T_L dz = G^{'} di_G \tag{11.19}$$

where air enthalpy difference is given by

$$di_G = c_s dT_G \;\; \lambda_o dw_G$$

The temperature difference between air and liquid will change throughout the tower, namely;

$$\Delta T \neq \Delta T z$$

The temperature difference throughout the pipe is

$$\Delta T_{DF} = \left(\frac{T_e \;\; T_p}{2}\right) - \left[\frac{T_{Le} \;\; T_{Lp}}{2}\right]$$

where the subscript p indicates a particular point at the pipe and the subscript e represents the pipe exit. Integrating Equation (11.19) throughout the pipe (see Figure 11.1),

$$\int_0^L -h_{overall} a_{Hoverall} T_G - T_L dz = \int_p^e G^{'} di_G \tag{11.20}$$

yields,

$$-h_{overall} a_{Hoverall} \Delta T_{DF} L = G^{'} \left\{ \left[c_s T_e - T_o \;\; \lambda_o w_e \right] - \left[c_s T - T_o \;\; \lambda_o w \right] \right\} \tag{11.21}$$

where T_o is the base temperature (90°F). Rearranging Equation (11.21)

$$-h_{overall} a_{Hoverall} \Delta T_{DF} L = G^{'} \left[c_s T_e - T \;\; \lambda_o w_e - w \right] \tag{11.22}$$

From Equation (11.22), absolute humidity difference can be written as

$$w_e - w = \frac{c_s}{\lambda_o} T - T_e \;\; \frac{1}{G' \lambda_o} \left[-h_{overall} a_{Hoverall} L \Delta T_{DF} \right] \tag{11.23}$$

Substituting Equations (11.16) and (11.18) into Equation (11.23), we obtain

$$w_e - w = \frac{c_s}{\lambda_o} T_e - T \;\; \frac{c_s}{\lambda_o} \Delta T_{DF} \ln \left(\frac{T - T_i}{T_e - T_i} \right) \tag{11.24}$$

Equation (11.9) is just for the conditions where the gas temperature is greater than the liquid temperature. Taking the absolute value of the temperature difference of Equation (11.9) makes valid for $T_L > T_G$. Relating this and Equation (11.24), the modified main equation of the Lewis correlation becomes:

$$w = w_i - \frac{h_g}{k_G \lambda_o} |T - T_i| = w_e \;\; \frac{c_s}{\lambda_o} T_e - T - \frac{c_s}{\lambda_o} \Delta T_{DF} \ln \left(\frac{T - T_i}{T_e - T_i} \right) \tag{11.25}$$

Equation (11.25) is valid for long horizontal pipe. Substituting Equations (11.5a) and (11.5b) into Equation (11.25), the modified psychrometric ratio of packed tower for water can be obtained as

$$\begin{aligned} \frac{0.622}{P_t} c_2 T_{ip} \quad - \quad & \frac{h_G}{k_G \lambda_o} |T_p - T_{ip}| = \frac{0.622}{P_t} c_2 T_e \;\; \frac{c_s}{\lambda_o} T_e - T_p \\ & \frac{c_s}{\lambda_o} \left\{ \left[\frac{T_{Le} \;\; T_{Lp}}{2} \right] - \left(\frac{T_e \;\; T_p}{2} \right) \right\} \ln \left| \frac{T_p - T_{ip}}{T_e - T_{ie}} \right| \end{aligned} \tag{11.26}$$

Rearranging Equation (11.26) yields

$$\frac{h_G}{k_G} = \frac{\frac{0.622}{p_t} c_2 \left[T_{ip} - T_e \right] \;\; \frac{c_s}{\lambda_o} T_p - T_e - \Delta T_{DF} \ln \left| \frac{T_P - T_{ip}}{T_e - T_{ie}} \right|}{|T_p - T_{ip}|} \lambda_o \tag{11.27}$$

where c_2 = 4.622E–2 and λ_o = 1042 for the saturated pressure between 90°F and 145°F and P_t = 13.05 psi. Constant A, for this case, can be found by dividing Equation (11.27) by c_s.

11.2.4 Determination of Coefficient A for a Liquid Desiccant

Desiccants are used to absorb moisture from the air, thus keeping the humidity level in the air to A required value. Since first developed by Lof in 1955, the desiccant dehumidification system has been extensively used in industrial and agricultural sectors [17]. Many researchers investigated to improve the effectiveness of liquid desiccants [18]. Ertas et al. [19] develop a new desiccant called CELD (Cost Effective Liquid Desiccant)– is a mixture of calcium chloride and lithium chloride. The mixture solution was tested between 26.6 °C to 65.6 °C with a concentration from 20wt% to 40wt%. The testing results indicated that mixing LiCl with $CaCl_2$ reduces the vapor pressure in a nonlinear manner in the tested temperature range. They also showed that a mixture of 50% calcium chloride and 50% lithium chloride (CELD) will reduce the cost of the adsorption process. The effectiveness of liquid and solid desiccant dehumidification systems was investigated for air conditioning and agricultural product drying and compared by Naik et al. [20]. They found that the highest latent effectiveness and dehumidification ability were at the desorption temperature of 345 K, at 0.91 and 6.8 g/kg, respectively. The use of liquid desiccant for industrial applications was investigated by Ertas et al. [21, 22].

The effect of the latent heat on the performance of the desiccant dehumidification system for five different desorption temperatures of 308, 318, 328, 338, and 345 K was experimentally investigated by Yaningsih et al. [23]. Ahn and Choi [24] studied local measurement and computational fluid dynamics (CFD) employed to evaluate thermal comfort in a residential environment where desiccant cooling is performed in Korea.

Analytical and experimental investigations on liquid desiccant systems for drying air or air conditioning systems were studied by Xiaochen et al. [25], Hesam [26], and Esam [27] among the many other researchers.

Now consider the liquid pool shown in Figure 11.2 to be a liquid desiccant. For the case of a long insulated channel above the liquid, the coefficient A for a desiccant is greater than for water. This increase in A results from the increase in resistance to mass transfer which provide a decrease in the mass transfer coefficient. As the mass transfer coefficient decreases, the value of A increases. The value of A for water is in the range of 1 to 2.32; for the desiccant, A is greater than 2.32. The desiccant must be at a higher temperature than the air for regeneration to occur. If the temperature of the air throughout the long channel where the wet–bulb and dry–bulb temperatures are the same, the exit air temperature can be found. If wet–bulb and dry–bulb temperatures are equal, the air is saturated. The exit temperature of air can be assumed to be

$$T_e = c_1^{"} \; c_2^{"} T_L \tag{11.28}$$

where $c_1^{"}$ and $c_2^{"}$ are coefficients that depend on the desiccant concentration. The saturation pressure at the exit can be expressed in terms of the exit temperature as

$$P_{Se} = c_1 \; c_2 c_1^{"} \; c_2^{"} T_L$$

Rearranging the above equation provides the saturation pressure at the exit.

$$P_{Se} = c_1 \; c_2 c_1^{"} \; c_2 c_2^{"} T_L \tag{11.29}$$

Substituting Equation (11.29) into the relative humidity equation, Equation (11.5a), the absolute humidity at the exit can be expressed as

$$w_e = \frac{0.622}{P_t} c_1 \; c_2 c_1^{"} \; c_2 c_2^{"} T_L \tag{11.30}$$

Substituting Equations (11.28), (11.29), and (11.30) into Equation (11.27) produces the following psychrometric ratio for regeneration in packed towers.

$$\begin{aligned} \frac{h_G}{k_G} \;=\; & \frac{\lambda_o}{|T_p - T_{ip}|} \left\{ \frac{0.622}{P_t} c_2 \left[T_{ip} - c_2 c_1^{"} \; c_2 c_2^{"} T_L \right] \; \frac{c_s}{\lambda_o} T_p - c_1^{"} \; c_2^{"} T_L \right\} \\ & \frac{\lambda_o}{|T_p - T_{ip}|} \left\{ \left[\frac{T_{Le} \; T_{Lp}}{2} - \frac{c_1^{"} \; c_2^{"} T_L \; T_P}{2} \right] \ln \left| \frac{T_p - T_{ip}}{c_1^{"} \; c_2^{"} T_L - T_{ie}} \right| \right\} \end{aligned} \tag{11.31}$$

Constant A can be found by dividing Equation (11.31) by c_s. Equation (11.31) is the general form for the psychrometric ratio. It is obvious that the water has no concentration. Substituting $c_1^{"}$=0 and $c_2^{"} = 1$ reduces Equation (11.31) to the case for liquid water for packed towers or Equation (11.27).

11.2.5 Experimental Set-Up

To find the psychometric ratio for the water and desiccant, two experiments were performed. The tube was long enough to allow the mixture to reach the same wet and dry temperature. After measuring the temperatures for particular desiccant concentrations, a correlation for the exit air temperature as a function of the desiccant temperature was found for the range of the concentrations considered.

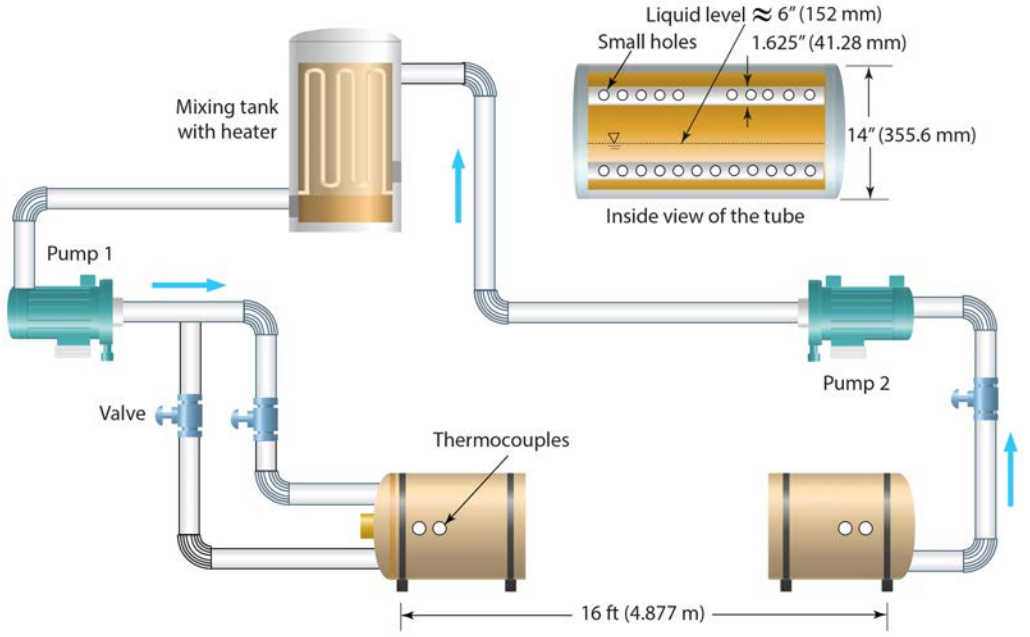

Figure 11.2: *Experimental setup (not scaled).*

A 4877 mm long pipe (tube) with 355.6 mm diameter, shown in Figure 11.2, contained a desiccant at high temperature and air at ambient temperature. The following test procedures were used to perform the experiment.

- The flow rate of the liquid was carefully adjusted.
- Two small diameter (41.28 mm), 4877 mm long pipes of an equal length as the large pipe was constructed with many small holes along their sides. These holes were used to mix the desiccant constantly, so that its concentration and temperature were nearly constant throughout the large pipe.
- The heater in the mixing tank was used to bring the desiccant to a particular temperature and then turned off while the flow continued. When the thermocouples located at ports along the tube indicated the same value, the experiment for that temperature was started.
- The pumps, which were used to pump the desiccant to and from the tube had similar characteristics to control the flow.
- Valves were used to adjust the level of the desiccant in the tube and to keep the flow rate constant.

- Regular tap water is used and the level of the water is assumed to be flat.
- Thermocouples were installed at a distance of very little over the water level of 152 mm.

The flow rate of the air, as well as the flow rate of the desiccant, during the experiment, is important. If a very high airflow rate is used, the wet and dry bulb temperatures can never be equal. Therefore, a constant low air flow rate was used. Although the air flow rate, the length of the tube, etc., are not related to the psychometric ratio, they were adjusted to find equal wet and dry bulb temperatures in the tube. Because the flow rate of air is not a parameter for the psychometric ratio, it was not measured.

One of the other major problems was to keep the concentration constant because it became higher as the temperature increased. Before making each experiment at a specific temperature, the heaters were turned off, and the concentration of the desiccant was measured and brought to the desired level.

A hydrometer, which gives reliable accuracy to the third decimal place, was used to determine the density of the CELD. The test procedure for the CELD density measurement is as follows:

1. Carefully clean and dry the hydrometer.
2. Make sure the temperature of the hydrometer is at the same temperature as the solution temperature.
3. Mix the solution well enough to ensure uniformity and pour into a graduated cylinder.
4. Place the graduated cylinder into a constant temperature bath.
5. Dip the hydrometer slowly in the solution, and then release it to float freely.
6. Record reading.

After finding the value of the density, d, the concentration equations for specific temperatures were used to find the concentration of the desiccant. Some of them are:

$$\begin{aligned}
\text{at} \quad 90^{\circ}F \qquad & C = -134.473\ 138.261d; \\
\text{at} \quad 100^{\circ}F \qquad & C = -134.197\ 138.261d; \\
\text{at} \quad 110^{\circ}F \qquad & C = -133.920\ 138.261d; \\
\text{at} \quad 160^{\circ}F \qquad & C = -132.539\ 138.261d;
\end{aligned}$$

In all these equations, the density is in SI units.

The experiment was started with a high CELD concentration of 46% and lowered to 38.2% during the experiment. In other words, the experiments were run for five concentrations (38.2%, 40%, 42%, 44%, 46%) at specific temperatures. To measure temperatures accurately, the thermocouples were calibrated. The procedure of the calibration is as follows.

- The thermocouples and an accurate thermometer were submersed in a large cup filled with water. The temperatures for each were recorded.
- The cup was heated slowly while the thermocouple and thermometer readings were recorded. The water temperature varied over the range of temperatures anticipated during the experiments.
- The data for each thermocouple was curve-fit and a graph was produced for the temperature of each thermocouple versus the temperature of the thermometer.
- For convenience during testing, a table for each thermocouple between the temperatures of 80 $^{\circ}$F and 180 $^{\circ}$F was prepared.

Along the tube, two holes (just above the liquid level of 152 mm) were drilled every 2 feet for the thermocouples. The thermocouples for dry bulb temperatures at each port were placed ahead of the thermocouples for wet bulb temperatures. One end of a section of shoestring was placed over each wet bulb temperature thermocouple and the other end was placed in a small container that contained water. Throughout the experiment, care was taken to ensure that the container was filled with water so that the hole and the string were always wet.

After considering all of the experimental parameters, the system was built and initially tested with water rather than desiccant to check for leaks, constant liquid temperature, and flow rate throughout the tube.

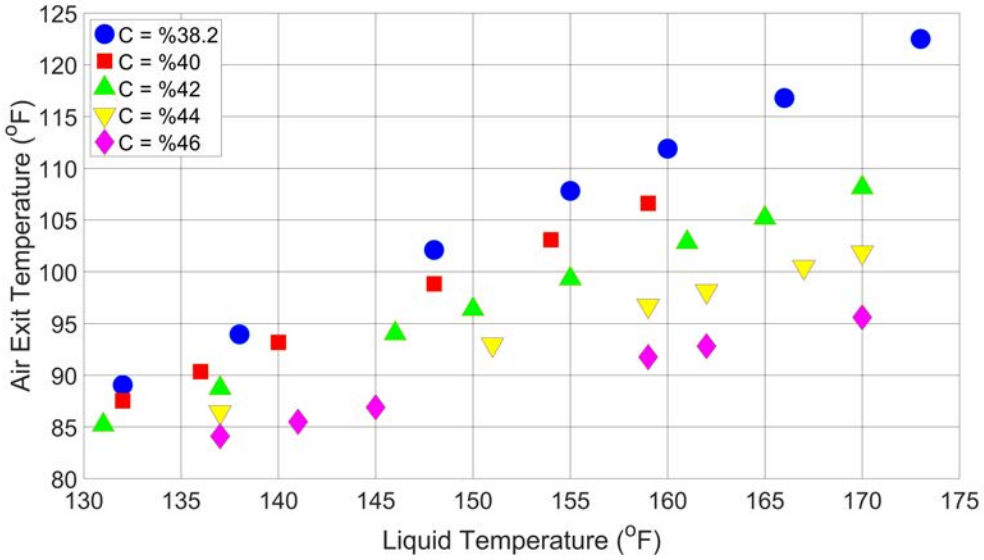

Figure 11.3: *Experimental results generated using Table 11.1.*

Table 11.1: *Experimental results depending on concentration.*

C=%38.2		C=%40		C=%42		C=%44		C=%46	
Liquid Temp	Air Exit Temp	Liquid Temp	Air Exit Temp	Liquid Temp	Air Exit Temp	Liquid Temp	Air Exit Temp	Liquid Temp	Air Exit Temp
132	89.05375	132	87.5096	131	85.20594	137	86.41856	137	84.10354
138	93.94779	136	90.3408	137	88.73358	151	92.97168	141	85.49642
148	102.1045	140	93.172	146	94.02504	159	96.71632	145	86.8893
155	107.8143	148	98.8344	150	96.3768	162	98.12056	159	91.76438
160	111.8926	154	103.0812	155	99.3165	167	100.461	162	92.80904
166	116.7867	159	106.6202	161	102.8441	170	101.8652	170	95.5948
173	122.4964			165	105.1959				
				170	108.1356				

11.3 Results and Discussions

At the completion of each test, the data for each desiccant concentration was reviewed and plotted. Data for the tests that produced the same wet and dry bulb temperatures for each desiccant concentration are tabulated in Table 11.1. Figure 11.3 shows the experimental results generated using Table 11.1.

For desiccant concentrations at low temperatures, equilibrium was expected near the ports at the exit of the tube, and as the temperatures of the liquid increased equilibrium was expected to move toward at front ports on the tube. However, for many tests equilibrium occurred at a port about 14 feet from the entrance. At low concentrations, a steady state was obtained in a short time. Increasing the percent of the concentration, especially at high temperatures, presented a great deal of difficulty in obtaining steady-state conditions due

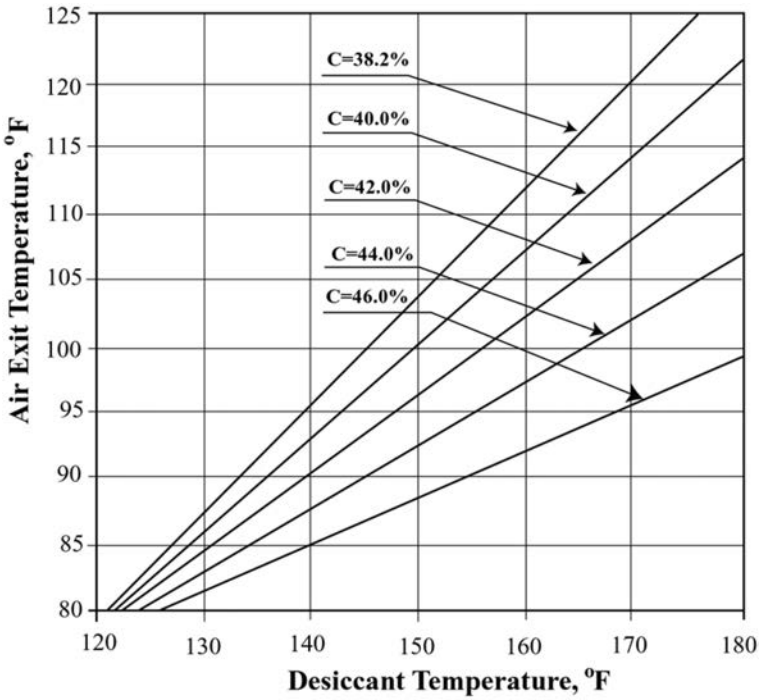

Figure 11.4: *Experimental results for exit air temperature by using correlation.*

to the time required. Therefore, tests for 46% desiccant concentration were repeated three times, and two of the results were dropped by considering the slope of the other concentrations.

From the experimental data, a correlation was obtained using the SAS software for Equation (11.28), where $c_1^{"}$ and $c_2^{"}$ depend on the concentration, C. The correlation for Equation (11.28) is:

$$T_e = -288.036\ \ 705.29C\ \ 3.105 - 5.993CT_L \tag{11.32}$$

Figure 11.4 was generated from Equation (11.32).

The second experiment was conducted, using the same experimental setup, to find a correlation for the interface temperature of the water. The air and interface temperatures were measured for a given air flow rate and different water temperatures. Thermocouples used to measure the interface temperature were fixed on a small and thin metal tab. The approximate interface temperatures were measured by placing half of the metal tab in the water and half in the air. The results of this experiment are presented in Table 11.2. The correlation obtained for the interface water temperature is

$$T_i = 0.94T_L\ \ 0.058T_G \tag{11.33}$$

Figure 11.5 was generated using experimental results shown in Table 11.2. The measured interface temperatures were approximately two degrees lower than the water temperatures. The same correlation can be used for desiccant applications because the transfer media between the air and the desiccant is water.

Case 1: By taking account of thermal and vapor pressure equilibrium at the exit, ($T_i = T_L = T_e$), and $w_i = w_e$ and rearranging Equation (11.28), the psychrometric ratio can be obtained for the case of water with thermal and vapor pressure equilibrium. The value of the constant A can then be found by dividing c_s into the psychrometric ratio. Table 3 (see Appendix A) presents the MATLAB example algorithm used to

Table 11.2: *Experimental results for interface temperature.*

Water temperature (°F)	**Air temperature (°F)**	**Interface temperature (°F)**
102.5	81.8	100.7
103.5	82.3	102.0
105.6	82.3	104.2
107.0	83.5	105.4
109.1	84.3	107.3
110.4	84.5	108.5
112.2	84.8	110.5
114.5	85.4	112.7
116.3	85.9	114.2
118.8	86.2	116.6
120.2	86.6	117.9
121.9	86.9	119.6
123.4	87.3	121.1

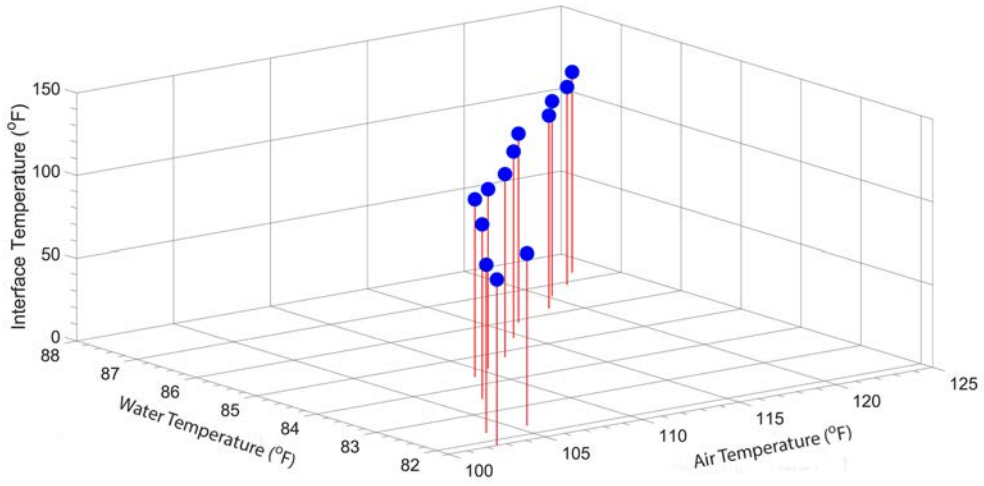

Figure 11.5: *Experimental results of interface temperatures.*

compute the value of A for this case. Using Kiris' [23] experimental data (see Appendix A, Table 7) in this algorithm for a humidifier, constant A was found to be 1.226 (see Table 3).

Typically, a tower is not tall enough to produce thermal and vapor pressure equilibrium at the exit. However, results can be found from the psychrometric ratio, determined from the interface temperature correlation. A MATLAB example algorithm to compute A=1.799 for this case is shown in Table 4 (see Appendix A) .

Case 2: Substituting Equations (11.32) and (11.33) into Equation (11.31) and using the data for regeneration (Table 6) by Kiris [29], the psychrometric ratio can be found. Dividing the value of this ratio to the heat capacity of humid air which is equal to 0.25, the constant A=13.573 can be obtained ((see Appendix A Table 5 for the MATLAB algorithm to compute constant A for CELD).

11.4 Conclusion

In this study, air and liquid contact for humidifier and regeneration applications have been carried out. Considering the psychrometric ratio change between 0.25 and 0.58, the modified Lewis correlation for water and liquid desiccant (CELD) was derived. To find the psychometric ratio for the water and desiccant, two experiments were performed. After measuring the temperatures for particular desiccant concentrations, a correlation for the exit air temperature as a function of the desiccant temperature was found for the range of the concentrations considered. The following conclusions were drawn from this study:

1. In the Lewis relation for a very thin water layer the psychrometric ratio is equal to the heat capacity of the humid air. If the layer is not thin, the psychrometric ratio will be changed in the range of 0.25 and 0.58.

2. A correlation for the interface temperature for water was found. This correlation can also be used for desiccant because the transfer media between air and desiccant is water.

3. An experiment for the desiccant was performed. A correlation for the exit air temperature depending on the concentration and liquid temperature was obtained. Using the interface temperature and air exit temperature correlations, the modified psychrometric ratio A for the following cases was obtained:

    - A= 1.226 for the case of water with thermal and vapor pressure equilibrium,
    - A= 1.799 based on the experimental interface temperature correlation, and
    - A= 13.573 for regeneration of CELD.

The followings are recommendations for future work in this research area: (a) obtain the results for different air and desiccant flow rates, (b) perform experiments by changing the air flow rate for humidifier and regeneration to obtain correlations.

Acknowledgments

We would like to take this opportunity to thank Dr. Ilker Kiris for his insightful comments.

Abbreviations

The following abbreviations are used in this manuscript:

a_H	Interfacial heat transfer area, ft^2/ft^3
a_M	Interfacial mass transfer area, ft^2/ft^3
c_s	Heat capacity of humid air, BTU/(lbm$^\circ$F)
d	Density of desiccant, lbm/ft^3
ϕ	Relative humidity of air
$G^{'}$	Dry air mass velocity, lbm dry air/(min ft^2)
h	Film heat transfer coefficient, BTU/($^\circ$F ft^2 min)
h_G	Heat transfer coefficient of gas phase, BTU/($^\circ$F ft^2 min)
$h_{overall}$	Overall heat transfer coefficient, BTU($^\circ$F ft^2 min)
i	Enthalpy of mixture of air and water vapor at given T, BTU/lbm of dry air
k	Film mass of enthalpy transfer coefficient, Btu/(min ft^2 (Btu/lbm))
k_G	Mass transfer coefficient of the liquid phase, Btu/(min ft^2 (BTU/lbm))
λ_o	Latent heat of vaporization of water at base temperature T_0, BTU/lbm
P	Partial liquid vapor pressure of the air, lbf/ft^2
P_i	Partial liquid vapor pressure of the interface, lbf/ft^2
P_v	Partial liquid vapor pressure, lbf/ft^2
P_s	Saturated steam vapor pressure, lbf/ft^2
t	Time, min
T	Air temperature, $^\circ$F
T_e	Air temperature at exit, $^\circ$F
T_G	Bulk air temperature, $^\circ$F
T_i	Interface temperature, $^\circ$F
T_L	Liquid temperature, $^\circ$F
T_p	Air temperature at particular height of the tower, $^\circ$F
ΔT_{DF}	Temperature difference throughout the pipe, $^\circ$F
T_{ie}	Interface temperature at the exit of the tower, $^\circ$F
T_{ip}	Interface temperature at the particular height of the tower, $^\circ$F
T_{Le}	Liquid temperature at the exit of the tower, $^\circ$F
T_{Lp}	Liquid temperature at the particular height of the tower, $^\circ$F
w	Absolute humidity, (lbm H2O)/(lbm dry air)
w_e	Absolute humidity at the exit tower, (lbm H_2O)/(lbm dry air)
W	Weight of evaporated liquid, lbm (H_2O)
Z	Height of packing materials, ft

Subcripts

G	Bulk gas
H	Heat transfer
I	Gas liquid interface
L	Bulk liquid (CELD)
M	Mass transfer
W	Water

Funding: This research received no external funding.

Conflicts of Interest: The authors declare no conflict of interest.

Authors Contributions: This work is Mr. Gurses' MS thesis. Dr. Ertas was Mr. Gurses' advisor.

References

1. Lewis, W. K. McAdams, W. H. (1937). *Principles of Chemical Engineering*, 3rd Edition, McGraw–Hill, New York.
2. Lewis, W. K. (1992). *Trans. American Society of Mechanical Engineers*, Vol. 44, pp.379.
3. Treybal, R. E. (1980). *Mass–Transfer Operation*, 3rd Edition, McGraw–Hill, New York.
4. Lewis, W. K. (1933). The Evaporation of a Liquid into a Gas–A Correction. *Mechanical Engineering* **1933**, Vol. 55, pp. 565–573.
5. Hensel, S. L., Jr. and Treybal, R. E. (1952). Adiabatic Humidification of Air with Water in a Packed Tower. *Chemical Engineering Progress*, pp. 362–370.
6. Lof, G. O. G., Lenz, T. G. and Rao, S. (1984). Coefficients of Heat and Mass Transfer in a Packed Bed Suitable for Solar Regeneration of Aqueous Lithium Chloride Solutions. *Journal for Solar Energy Engineering*, Vol.106, pp. 387–392.
7. Strigle, R. F., Jr. (1987). *Random Packings and Packed Towers: Design and Application.* Gulf Publishing Company, Houston, Texas.
8. McAdams, W. H., Phlenz, J. B. And John, R. C. (1949). Transfer of Heat and Mass between Air and Water in a Packed Tower. *Chemical Engineering in Progress*, Vol. 45, No. 4, pp. 241–252.
9. Sherwood, T. K. and Holloway, F. A. L. (1939). Performance of Packed Towers – Experimental Studies of Absorption and Desorption. *Transactions American Society of Engineers,* p.21.
10. Molstad, M. C., Abbey, R. G., Thompson, A. R. and McKinney, J. F. (1942). Performance of Drip–Point Grid Tower Packings II. Liquid–Film Mass Transfer Data. *Transactions American Chemical Engineering*, Vol. 38, 410–434.
11. Vivian, J. E., and Whitney, R. P. (1949). Absorption of Sulfur Dioxide in Water, *Chemical Engineering Progress,* Vol. 45, 323–337.
12. Norman W. S. (1961). Absorption, Distillation and Cooling Towers, Wiley, New York.
13. Sherwood, T. K. and Pigford, R. L. (1952). *Absorption and Extraction*, 2nd Edition, McGraw–Hill, New York.
14. Puranik, S. S. and Vogelpohl, A. (1974). Effective Interfacial Area In Irrigated Packed Columns. *Chemical Engineering Science*, Vol. 29, pp. 501–507.
15. Lewis, W. K.(1984). The Evaporation of a Liquid into a Gas–A Correction *Mechanical Engineering*, Vol. 55, pp. 153–158.
16. Simpson, W. M. and Sherwood, T. K. (1946). Performance of Small Mechanical Draft Cooling Towers. *Journal of the ASREA*, pp. 535–576.
17. GOG, L. (1955). Cooling with solar energy. Congress on Solar Energy, Tucson, Ariz, pp. 73–78.

18. Xiangjie, C., Saffa, R., Hongyu, B., Xiaofeng, Z., Reay, D. (2020). Recent progress in liquid desiccant dehumidification and air-conditioning: A review. *Energy and Built Environment*, 1, 106–130.
19. Ertas, A., Anderson, E. E., Kiris, I. (1992). Properties of a new liquid desiccant solution–Lithium chloride and calcium chloride mixture. *Solar Energy,* 49 (3), 205–212.
20. Naik,B. Kiran, Mullapudi, J., Palanisamy,M., Muhammad, S., Takahiko, M., Redmond, R. S., and Hadeed, A. 2020. Investigating Solid and Liquid Desiccant Dehumidification Options for Room Air-Conditioning and Drying Applications. *Sustainability*, 12, 10582; doi:10.3390/su122410582
21. Ertas, A., Anderson, E. E., Kavasogullari, S. (1991). Comparison of Mass and Heat Transfer Coefficients of Liquid-Desiccant Mixtures in a Packed Column. *Journal of Energy Resources,* 113(1), https://doi.org/10.1115/1.2905774
22. Ertas, A., Hoque, A. K. A., I. Kiris, I., & P. Gandhidasan, P. (1997). Low Temperature Peanut Drying Using Liquid Desiccant System Climatic Conditions. *Drying Technology*, Vol. 15, Issue 3-4.
23. Yaningsih, I., Wijayanta, T. A., Thu, K., and Miyazaki, T. (2020). Influence of Phase Change Phenomena on the Performance of a Desiccant Dehumidification System. *Appl. Sci.* 10, 868; doi:10.3390/app10030868
24. Ahn, J., and Yup Choi H.(2020). Effects of Supply Angle on Thermal Environment of Residential Space with Hybrid Desiccant Cooling System for Multi-Room Control. *Appl. Sci*. 10, 7271; doi:10.3390/app10207271
25. Liu, X., Liu, X., Zhang, T. (2018). Experimental analysis and performance optimization of a counter-flow enthalpy recovery device using liquid desiccant. *Engineering Sage Journal,* https://doi.org/10.1177/0143624418780852
26. Salarian, H. (2013). An Analysis of Packed Bed Liquid Desiccant System. *Applied Mechanics and Materials*, 390:680-DOI:10.4028/www.scientific.net/AMM.390.680
27. Elsarrag E. (2018). An Innovative Smart Liquid Desiccant Air Conditioning System for Indoor and Outdoor Cooling using Seawater Bittern. *Innovative Energy & Research,* Vol 7(1): 178.
28. Kiris, I. Experimental Development and Investigation of a New Liquid Desiccant System for Drying Operations, M. S. Thesis, Texas Tech University, 1991.
29. Mickley, H. S. (1949), Design of Forced Draft Air Conditioning Equipment. *Chemical En-gineering in Progress*, Vol.45, No.12, pp. 739–745.

About the Authors

Huseyin M. Gurses is the founding partner of GONCA OSGB, which was established in 2011. He has been the Occupational Health and Safety Director of GONCA OSGB since the day it was founded.

Dr. Atila Ertas is the director of the Academy of Transdisciplinary Studies and a professor of Mechanical

Engineering at Texas Tech University. Dr. Ertas has many years of experience in teaching transdisciplinary design courses. He is the author/co-author of over 190 technical papers that cover many engineering technical fields. His textbooks include The Engineering Design Process (co-author with J. Jones,1993, 1996), Prevention through Design (PtD): Transdisciplinary Process (2010), Engineering Mechanics and Design Applications: Transdisciplinary Engineering Fundamentals (2011), Transdisciplinarity Engineering Design Process (2018), and Managing System Complexity through Integrated Transdisciplinary Design Tools (co-author with U. Gulbulak, 2020).

Appendix A

Table 3. MATLAB algorithm to compute the value of constant A for the case of water with thermal and vapor pressure equilibrium.

```
clc                          lambda = 1042;
clear all                    n = c11 + c22 *Tlp;
                             r = cs / lambda;
syms X                       nl = c11 + c22 * Tle;
                             Tie = Tle;
Tp = 90;                     term1 = 0.5*(Tle + Tlp) - 0.5*(nl+Tp);
Tle = 120;                   term2 = log(abs((Tp - Tip)/(Tout - Tie)));
Tlp = 76;                    % p = (hg/kg)*(1/lambda)
Tout = 98;                   % (hg/kg) is defined as X in the equation.
Pt = 13.05;
m = 0.622/Pt;                s = vpasolve(m*c2*Tip-(X/lambda)*abs(Tp-Tip) == m*c2*n
Tip = Tlp;                       + (cs/lambda)*(n-Tp)-(cs/lambda)*(term1*term2),X);
c11 = 0;
c22 = 1;                     A = double(s)/0.25;
cs = 0.25;                   fprintf('A = %.9f\n',A)
c2 = 0.04622;
                             >> A = 1.225992562
```

Table 4. MATLAB algorithm to compute the value of constant *A* based on the experimental interface temperature correlation.

```
clc
clear all

syms X

Tp = 90;
Tle = 120;
Tlp = 76;
Tout = 98;
Pt = 13.05;
m = 0.622/Pt;
Tip = 0.940567*Tlp+0.058394*Tp;
c11 = 0;
c22 = 1;
cs = 0.25;
c2 = 0.04622;
lambda = 1042;
n = c11 + c22 *Tlp;
r = cs / lambda;
nl = c11 + c22 * Tle;
Tie = 0.940567*Tle + 0.058394*Tout;
term1 = 0.5*(Tle + Tlp) - 0.5*(nl+Tp);
term2 = log(abs((Tp - Tip)/(Tout - Tie)));
% p = (hg/kg)*(1/lambda)
% (hg/kg) is defined as X in the equation.
s = vpasolve(m*c2*Tip-(X/lambda)*abs(Tp-Tip) == m*c2*n
    + (cs/lambda)*(n-Tp)-(cs/lambda)*(term1*term2),X);

A = double(s)/0.2
fprintf('A = %.9f\n',A)

>> A = 1.799292219
```

Table 5. MATLAB algorithm to compute the value of constant *A* for regeneration of CELD.

```
clc
clear all

syms X

Tp = 90;
Tle = 160;
Tlp = 108;
Tout = 118;
Tlport = 0.5*(Tle+Tlp);
Tport = 0.5*(Tp+Tout);
cin = 0.378;
cout = 0.3877;
c = (cin+cout)*0.5;
C11 = -288.036 + 705.29*cin;
C22 = 3.105 - 5.993*cin;
Pt = 13.05;
m = 0.622/Pt;
Tip = 0.940567*Tlport+0.058394*Tport;
c11 = -288.036 + 705.29*c;
c22 = 3.105 - 5.993*c;
cs = 0.25;
c2 = 0.04622;
lambda = 1042;
n = c11 + c22 *Tlport;
r = cs / lambda;
nl = C11 + C22 * Tle;
Tie = 0.940567*Tle + 0.058394*Tout;
term1 = 0.5*(Tle + Tlport) - 0.5*(nl+Tport);
term2 = log(abs((Tport - Tip)/(Tout - Tie)));
% p = (hg/kg)*(1/lambda)
% (hg/kg) is defined as X in the equation.
s = vpasolve(m*c2*Tip-(X/lambda)*abs(Tport-Tip) == m*c2*n
    + (cs/lambda)*(n-Tport)-(cs/lambda)*(term1*term2),X);

A = double(s)/0.25;
fprintf('A = %.9f\n',A)

>> A = 13.572801512
```

Table 6. Data sets for regeneration of Kiris with calculated data [23].

at G=1091 CFM	TG	W	TL	C	L	kg*am	hg*ah	hl*ah	kg*am
	(in)	(in)	(in)	(in)					
	[F]	10^3	[F]	(%)	[lbm/min*f^2]	[lbm/min*f^3]	[Btu/F*min*f^3]	[Btu/F*min*f^3]	[lbm/min*f^3]
Regen-1	90	23.56	156	44.3	24.4132	5.1489	20.2677	14.9315	2.5744
Regen-2	90	27.02	161	44.3	24.4132	5.5258	20.0837	15.4722	2.7629
Regen-3	90	27.02	182	44.3	24.4132	5.0482	17.5624	17.163	2.5241
Regen-4	90	27.02	170	44.3	24.4132	4.9774	17.6749	17.42	2.4887
Regen-5	90	23.56	160	44.3	24.4132	5.3247	20.3936	14.3768	2.6623
Regen-6	90	23.56	182	44.3	24.4132	8.3792	29.8715	14.2438	4.1896
Regen-7	76	16.51	144	39.46	24.4132	4.4269	14.8976	1327.954	2.2134
Regen-8	76	16.51	160	39.46	24.4132	5.7609	18.4332	54.7202	2.8805
Regen-9	76	16.51	176	39.46	24.4132	7.5631	23.0877	34.0264	3.7815
Regen-10	90	23.56	160	44.3	18.3099	4.3044	18.0239	11.4064	2.1522
Regen-11	90	23.56	160	44.3	24.4132	3.4239	13.1134	21.2266	1.7119
Regen-12	90	23.56	160	44.3	30.5165	5.5582	20.1871	17.7862	2.7791
Regen-13	90	23.56	160	39.46	24.4132	8.32	38.339	11.6473	4.16
Regen-14	90	23.56	160	41.12	24.4132	5.995	25.8261	11.0908	2.9975
Regen-15	90	23.56	160	37.8	24.4132	10.6908	53.5614	12.828	5.3454
Regen-16	83	23.56	182	44.3	24.4132	4.0731	12.1928	41.9522	2.0365
Regen-17	90	23.56	182	44.3	24.4132	8.3792	29.8715	14.2438	4.1896
Regen-18	97	23.56	182	44.3	24.4132	13.2525	60.7527	12.8549	6.6262
Regen-19	90	20.31	182	44.3	24.4132	8.1774	30.2809	13.0838	4.0886
Regen-20	90	23.56	182	44.3	24.4132	9.5785	34.1472	15.3256	4.7892
Regen-21	90	27.02	182	44.3	24.4132	8.2204	28.5982	15.6187	4.1102
Regen-22	90	23.56	160	44.3	36.6199	2.6326	10.0827	46.0707	1.3163

Table 7. Data sets for humidifier of Kiris with calculated data [23].

at G=1091 CFM	TG (in)	W (in)	TL (in)	C (in)	L	kg*am	hg*ah	hl*ah	kg*am
	[F]	10^3	[F]	(%)	[lbm/min*f^2]	[lbm/min*f^3]	[Btu/F*min*f^3]	[Btu/F*min*f^3]	[lbm/min*f^3]
Hum-1	86	9.7	120	2.5	48.8265	1.2229	0.3057	36.6887	0.6115
Hum-2	86	9.7	120	2.5	24.4132	1.3426	0.3356	38.669	0.6713
Hum-3	86	9.7	120	2.5	30.5166	1.2931	0.3332	19.1382	0.6465
Hum-4	86	9.7	120	2.5	36.6199	1.2485	0.3121	14.9829	0.6242
Hum-5	86	9.7	120	2.5	43.5776	1.2425	0.3106	18.6382	0.6212
Hum-6	86	9.7	107.7	2.5	30.5166	1.1919	0.2979	19.4295	0.5959
Hum-7	86	9.7	120	2.5	30.5166	1.3221	0.3305	18.907	0.6611
Hum-8	84	9.7	120	3.5	24.4132	1.7099	0.4275	19.6643	0.8549
Hum-9	84	9.7	120	3.5	30.5166	1.4766	0.369	11.0739	0.7382
Hum-10	84	9.7	120	3.5	36.6199	1.1893	0.2973	8.9212	0.5946
Hum-11	84	9.7	120	3.5	39.061	1.1388	0.2847	8.4843	0.5694
Hum-12	84	9.7	120	3.5	48.8265	0.8993	0.2248	67.5433	0.4496
Hum-13	84	9.7	104.6	3.5	30.5165	1.3662	0.3408	13.768	0.6815
Hum-14	84	9.7	120	3.5	30.5165	1.4765	0.3691	11.0739	0.7382
Hum-15	90	12.1	120	4.5	24.4133	2.2627	0.5656	33.5311	1.1313
Hum-16	90	12.1	120	4.5	30.5165	1.6291	0.4072	13.9126	0.8145
Hum-17	90	12.1	120	4.5	36.6199	1.4955	0.3738	6.7899	0.7477
Hum-18	90	12.1	120	4.5	45.7748	1.0955	0.2738	5.0833	0.5477
Hum-19	84	10.4	104	4.5	30.5166	1.2981	0.3245	7.7887	0.649
Hum-20	84	10.4	122	4.5	30.5166	1.2141	0.3035	7.0421	0.607

CHAPTER 12

Current and Future Challenges of Nanomaterials in Solar Energy Desalination Systems in Last Decadee

Trupti S. Gajbhiye, Sagar D. Shelare, and Kapil R. Aglawe

Article citation information: (2022), *TJES*, Vol. SP-2, pp. 187-201, doi:10.22545/2022/00217

Renewable energy plays key role in developing any nation. Freshwater is sometimes hard to get to in places far aside or poor. Because of this, it is essential to have a cheap and effective desalination system that helps these communities grow and helps society as a whole. For example, the development of nanotechnology could help solve water problems by making it easier to get rid of viruses, bacteria, and other contaminants and lowering the cost of purification processes. Desalination is a process that uses a lot of energy and is responsible for most of the costs of running the plant. Also, a lot of the power comes from greenhouse gas emissions and traditional fossil-fuel-fired power plants, which pose a severe danger to the ecosystem. In the last few years, many studies have been done on the use of nanotechnology in desalination, the treatment of brine, and the role of renewable energy in desalination. The main goal of this paper is to look at the most important new developments in desalination nanotechnology with respect to energy. Some conclusions and suggestions for future research are made based on the progress and problems that still need to be solved.

Keywords: Water productivity; Nanoparticles; Nanofluids; Solar distillation systems Performance; Solar energy.

12.1 Introduction

Energy is one of the primary foundations supporting evolutionary changes [1]. Increases in both developed and developing nation's economies have led to higher living standards and, in turn, greater demand for energy during the past few decades. An ever-increasing global population and the ever-increasing energy demands of contemporary society have boosted the demand for alternative power sources [2]. Conventional primary energy generating techniques (such as burning fossil fuels) must be replaced with low-emission alternatives if the Paris Agreement 2°C global warming target is to be fulfilled. Figure 12(a) depicts the relationship between electricity, heating/cooling, transportation energy use, and the use of renewable energy sources. Solar energy, wind energy, geothermal energy, marine energy, hydro energy, and bioenergy are the six main types of renewable energy [3]. Global power consumption dropped significantly as a result of the Covid-19 crisis as a result of restrictions on freedom of travel, shutdowns, and economic slowdown. Renewable energy sources such as geothermal, hydropower, sun, wind, and biomass can provide sustainable energy services based on the usage of indigenous, habitually accessible resources [4]. As the cost of renewable energy sources decreases and oil and natural gas prices continue to vary, a transition to renewable energy

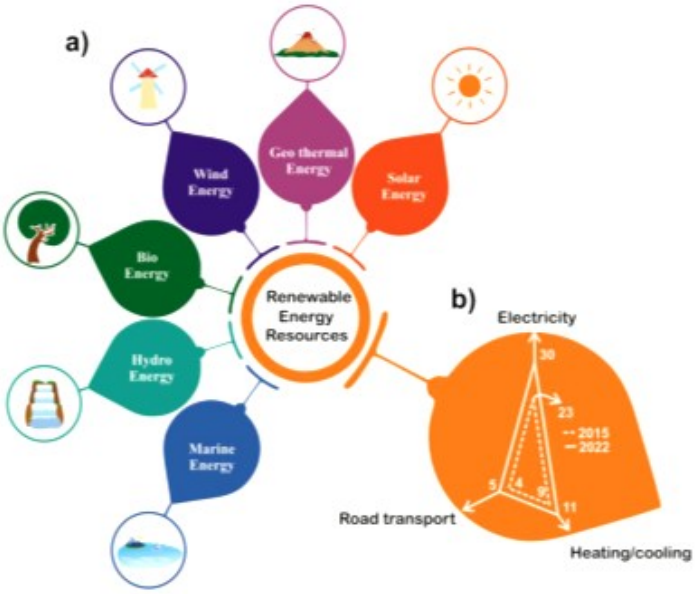

Figure 12.1: *(a) Multiple renewable energy sources (b) significance of renewable sources of energy to road transport, heating/cooling, and electricity generation.*

sources becomes highly probable [5]. For reasons such as energy security, access to cheap energy supplies, power greenhouse gas emissions, etc., it is relevant to evaluate the potential worldwide contribution of renewables to long-term energy demand [6]. In the past three decades, fossil fuel and renewable energy prices, as well as environmental and social costs, have been trending in different directions, and the political and financial mechanisms required to sustain the widely dissemination of and sustainable marketplaces for renewable energies are continually developing [7]. In April 2020, the United States saw a decrease of 5% in its electricity usage from April 2019, while Germany saw a decrease of 12%, Spain saw a decrease of 18%, and India saw a decrease of 23%. As can be seen in Figure 12.1(b), it is predicted that by 2022, the share of electrical energy supplied by renewable sources would rise to as much as 30%. In addition, by 2025, renewable energy sources will have contributed to 95 percent of the net expansion in global power capacity [8].

The advent of produced materials at the nanoscale scale is largely attributable to the development of cutting-edge scientific methods. Nanoparticles has played a significant role in the development of superior heat exchange fluids for a variety of industrial applications because of their exceptional properties. Argonne National Laboratory (ANL) in the United States introduces the concept of a "Nanofluid" [9]. Water, engine oil, ethylene glycol, and refrigerants are all examples of common base liquids that may be used to create nanofluids with the addition of nanoscaled solid particle auxiliaries. Because it allows for more efficient heating and cooling processes, this extraordinary breakthrough in nanoscale research is a tool for improving heat transfer in fluids. Indeed, many studies, some of which will be discussed here, have shown convincingly that the presence of nanofluids may plainly contribute to reducing the system size, design flexibility, and compact size [10].

Single-phase and phase change procedures are the two main types of desalination technologies [11]. Techniques that include a phase transition—from solid to gas, liquid to gas, or liquid to solid—are grouped below the umbrella term "phase change," as the name suggests. The latest desalination methods are categorized in Table 1 according to the separation mechanisms and energy utilization procedures that they employ. Desalination techniques that rely on evaporation or crystallisation experience a phase change.

Table 1: Organization of overall desalination technologies.

Desalination Process	**Energy utilized**	**Phase**	**Technologies**
Evaporation	Electrical and Thermal	Phase Change	Formation and Freezing of Hydrates (Solid/Liquid)
	Mechanical	Phase Change	Mechanical Vapour Compression (MVC) (Gas/Liquid)
Evaporation	Electrical and Thermal	Phase Change	Solar distillation, Ocean Thermal Energy Conversion (OTEC), Thermal Vapour Compression (TVC), Multi-Effect Distillation (MED), Multi-Stage Flash (MSF) (Gas/Liquid)
Evaporation and filtration	Electrical and Thermal	Phase Change	Membrane Distillation (MD)
Exchange	Chemical	Single Phase	Extraction and Ion Exchange (IX) (Electrochemical separation)
Filtration	Mechanical	Single Phase	Nanofiltration and Reverse Osmosis
Selective filtration	Electrical	Single Phase	Electro Dialysis (ED)

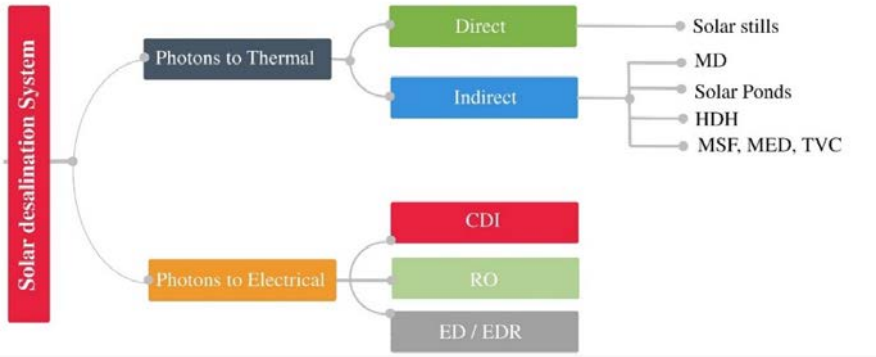

Figure 12.2: *Organization of solar water desalination methods.*

Decentralized freshwater needs are met by solar distillation units, which are commonly divided into direct and indirect processes (Figure 12.2).

In places far from civilization where regular sources of energy, such as running water, are scarce, solar desalination systems have become increasingly popular. The most significant drawbacks of solar desalination systems are their bulkiness and inability to be moved easily. Unfortunately, the absorber and glass cover sizes often seen in domestic solar desalination systems are too tiny to maximize freshwater output or plant efficiency. The pace at which water is produced from the sun in a solar distillation unit depends mostly on the strength of the sun's rays. Using solar desalination systems can help make up for the shortage of freshwater in arid places with high sun intensity and high temperatures, such as South Africa, Saudi Arabia, and the Middle East [12]. The effectiveness of solar desalination systems relies upon the evaporation of water and moisture via glass top cover [13]. Increased output may result from the large temperature difference between condensation and evaporation zones. Multiple factors, including solar desalination system water geometry,

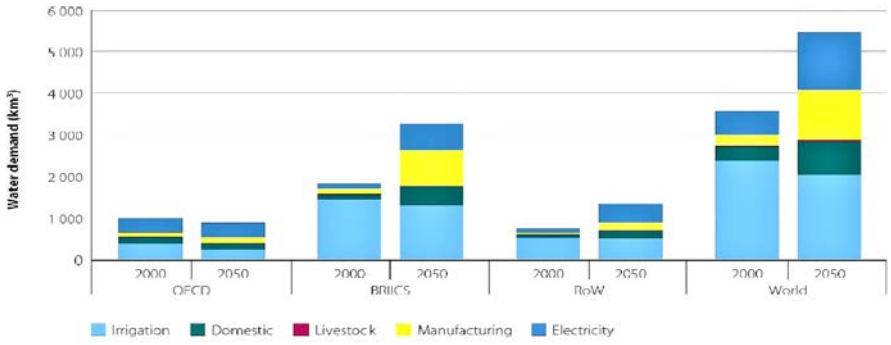

Figure 12.3: *Demand of freshwater worldwide: baseline scenario, 2000 and 2050 [16]. (BRIICS: Brazil, Russia, India, China and South Africa; ROW: Rest of the World; OECD: Organization for Economic Co-operation and Development).*

absorber material, water depth, and insulation thickness and material, might impact the water production rate [14]. Additionally, the water temperature can be raised by using nanoparticles, thermoelectric heating, Photovoltaic/Thermal, a solar collector or a phase change material; additionally, the condensation rate can be enhanced by utilizing thermoelectric cooling, water/air glass cooling, or an external condenser [15].

The goal of providing drinkable water to every person on Earth requires a significant increase in seawater desalination capacity. Figure 12.3 depicts this increase by comparing freshwater demand across industries from the years 2000 to 2050. Physical water shortage may be separated from the more economical forms of water scarcity. When it becomes too expensive to draw clean water from current sources, we have a situation known as economic water scarcity. Calculations of water stress for a number of nations suggest that it is worst in Northern Africa (at 112.2%), next in Central Asia (79%), and finally Melanesia, Micronesia, and Polynesia (together, 0.1%).

Nanofluids, a novel class through enhanced thermophysical characteristics introduced by Choi and Eastman have opened up opportunities to boost the thermal performance of various systems. Numerous studies have looked at multiple aspects of nanofluids, including their manufacturing techniques, dynamic viscosity, thermal conductivity, machine learning applications for forecasting thermophysical parameters, and heat transfer performance. Many review articles have been written to describe the developments in this emerging topic [17]–[19]. Heat transfer rates in many types of energy systems can be improved by using nanomaterials. Solar desalination systems have also made use of a variety of nanoparticles to boost efficiency [20].

To speed up the water-making process, some researchers have tried mixing nanoparticles with pure fluid. Through modifications to the fluid's physical characteristics, nanoparticles can combine with the pure fluid and accelerate evaporation heat transfer in the solar desalination system. Alternate nanoparticle application strategies that boost condensation and evaporation include incorporating nanoparticles into a coating of a glass cover and mixing nanoparticles with absorber paint. Evaporation is increased when nano-coating is combined with absorber paint, and condensation is improved when nano-coating is applied to a glass cover. Other nano-techniques have improved water production in the face of low solar intensity by increasing a heat transfer rate by the addition of nanoparticles to phase changer material. Researchers have evaluated nanofluids in a solar desalination system, researched their effects in a solar desalination system, and found that utilizing them increases mass transfer and heat [21].

This manuscript aims to examine the development of nanofluids for water desalination with solar energy during the past decade. This evaluation fills in a blank left by other studies by focusing on the relationship between NP characteristics and performance. The mechanism of energy transmission between NPs is the

central focus of this discussion. The function of NFs as heat carriers and its impact on desalination system efficiency will then be the primary topic of the following discussion. The NF's composition will also be investigated in order to investigate its bearing on desalination system efficiency. After discussing the relevant NFs and design adjustments, we will move on to the obstacles and research problem.

12.2 Various Nanomaterials in Solar Energy Desalination System

The efficiency of a solar distillation unit for producing water may be improved with the use of various nanoparticles. Solar desalination system nanomaterials are depicted in Figure 12.4.

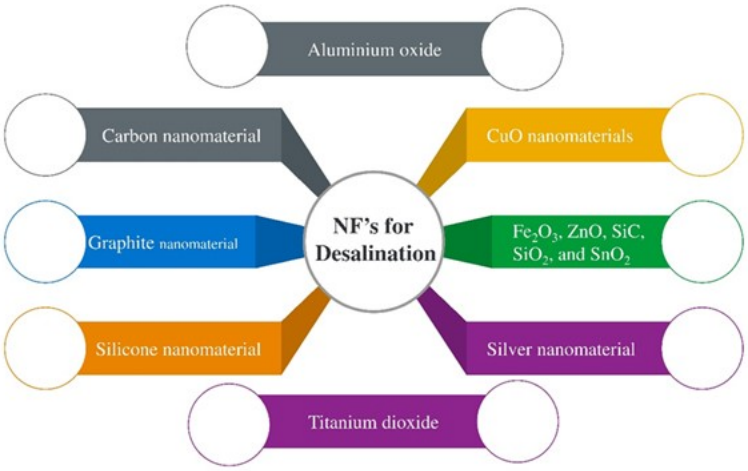

Figure 12.4: *Various nanomaterials used in the solar energy desalination system.*

12.2.1 Al_2O_3 in Solar Desalination System

Kabeel et al. investigated the effects of Al_2O_3-water nanofluids on single-slope solar performance and the role of an external condenser [22]. Rates of Production Water 76% and 116% were reported while employing nanofluid with and without an external condenser, respectively. Muraleedharan et al. looked at improved solar desalination unit that included a heat exchanger, an evacuated tube, and a Frensel lens concentrator [23]. Therminol-55 has 0.1% Al_2O_3 added to it in order to rise its heat transfer efficiency in the heat exchanger loop. Outcomes of experiments suggest that the water production rate of the modified solar desalination system is approximately 3.5 times higher than that of traditional distillation units. Karthikeyan et al. studied the efficiency of nine distinct solar desalination system designs, each of which made use of a unique combination of absorber materials [24]. As absorber material, the solar desalination system made use of a glass ball. Al_2O_3 nanoparticles, in comparison to other absorber materials, had the highest productivity. Al_2O_3 nanoparticles and gravels, respectively, increased freshwater output by around three and two and a half times additional compared to the material absorber.

When compared to a solar desalination system without Al_2O_3 nanoparticles and PCM, authors found that the efficiency of water of FWCW and CW absorber materials utilizing these additives increased by 56.7% and 79.3%, respectively. The impact of incorporating Al_2O_3 nanoparticles into the black paint and solar distillation units base fluid was investigated [25]. The water temperature and rate of evaporation rose with

both approaches. Al_2O_3 nano-coated and nano-fluid increased solar desalination system water production by around 24.3%, as shown by the output data. The efficiency of a mixture of Al_2O_3 nanoparticles and PCM in a single slope solar distillation unit was evaluated by the authors. Through the use of Al_2O_3 nanoparticles-PCM, they demonstrated the efficiency of solar desalination systems equivalent to 45%. Using nano-coated and nanofluid techniques together can have a significant effect on water evaporation and productivity.

12.2.2 Carbon Nanomaterial in Solar Desalination System

Arora et al., analyzed the efficiency of different photovoltaic/thermal systems that used SWCNT and MWCNT nanoparticles in water [26]. At a 1% concentration of nanoparticles, the component temperatures, heat transfer coefficient, and Nusselt number were studied in a modified solar desalination system. Water was heated using a PV/T-CPC system connected to a helically coiled heat exchanger. The sun desalination system produced 65.7% and 28.1% more water, respectively, as shown by the results. Sharshir et al. improved water output of a stepped double solar still. Findings revealed that using CBN nanoparticles and LW increased solar desalination system freshwater output by approximately 110.5%, and 80.57% respectively [27]. The thermo-physical effects of Al2O3-water and MWCNT-water nanofluids in a double-slope conventional solar distillation unit were studied by Sahota. In order to maximize the efficiency of the solar desalination system, the suggested thermal model was used to generate optimal concentrations of nanofluids of 0.12%, 0.08%, and 0.04%. Specifically, they discovered that the water productivity increased by 58.1% and 52.1%.

12.2.3 CuO Nanomaterials in Solar Energy Desalination System

Nazari et al. found that the CuO-water nanofluid affects the water temperature and cooling water, resulting in a lower temperature of glass cover in the solar desalination system [28]. The glass is cooled by a fan and a channel that is connected to the thermoelectric cold side. The output findings demonstrate that compared to traditional ones, the exergy, productivity, and energy were enhanced by 112.5%, 81%, and 80.6%, respectively. Bahiraei et al. forecasted water production using ANN Tool from a single-slope solar desalination system using thermoelectric cooling and CuO-water nanofluid [29]. Abdullah increased water output in another study. The solar desalination system's water temperature is greater than before while a water depth is decreased. Once again, the trials were carried out in the climate of Saudi Arabia. Based on the data, it was determined that the freshwater production was maximized at 0.1 rpm drum speed, an increase of 4.49 times above the yield of traditional solar distillation units.

Abdullah et al. investigated the efficacy of a solar desalination system. The results showed that the total solar distillation unit yield of water trays increased by 57.14%, 70.7%, and 108% [30]. The study of nighttime water production was also conducted. According to the findings, the freshwater yield of SSSS-CuO-NCAP was approximately 2.9 L/m2, SSSS-PVA about 1.9 L/m2, SSSS-SCB about 2.8 L/m2, and SSSS-pebbles about 2.6 L/m2. When used together, nanoparticles and phase change materials (PCM) drastically alter the time it takes to absorb and release heat from PCM. Behura and Gupta studied the use of a single-slope solar desalination system to distill a colorless solid mixture (wax) at varying concentrations of CuO nanoparticles [31]. The results have shown that increasing the concentration of CuO nanoparticles in PCM from 0.1 to 0.2 to 0.3% increased solar water production.

12.2.4 Graphite Nanomaterial in Solar Desalination System

Sharshir et al. studied the influence of water depth on water productivity rate as a result of employing flake graphite nanoparticles (FGN), phase change nanomaterial, and water film cooling in the solar desalination system. Sharshir investigated the performance of a single-slope solar distillation unit after introducing copper oxide and graphite nanoparticles [32]. Graphite nanoparticles and Copper oxide were shown to increase water production by 41.18%, and 32.35% respectively, associated to conservative methods.

Kabeel et al. looked at the efficiency of three different solar desalination system designs using graphene oxide nanoparticles and PCM in a tubular solar distillation unit. Experiments were conducted using a standard

solar distillation unit, a solar distillation unit including PCM, and a solar desalination system containing graphene oxide nanoparticles. Adding graphene oxide to PCM allowed for higher solar desalination system water yields. The results show that both the solar distillation unit with PCM and the solar desalination system with graphene oxide are more productive than a traditional solar desalination system by a factor of 29.3 and 216.9, respectively. By incorporating nanoparticles of GO, CuO, and TiO2 into PCM at 0.3%, concentrations, improved water production in a solar distillation unit. The paraffin PCM lines both sides of the solar distillation unit wall [33]. Results demonstrate that daily water productivity from solar distillation unit using CuO, TiO2, and GO nanofluids ranged from around 3.66 L/ m2 /day to 5.28 L/ m2 /day. Wax, a colorless solid combination, was utilized as a PCM in solar desalination systems' washbasins. As shown by the data, the productivity of solar distillation unit freshwater systems using PCM and mixed nanoparticles in PCM is much higher than that of conventional systems by 39.5% and 83.7%, respectively.

12.2.5 Fe_2O_3, ZnO, SiC, SiO_2, and SnO_2 Nanomaterial in Solar Desalination System

The effectiveness of a single slope solar distillation unit was evaluated by Elango et al. after nanoparticles of Al_2O_3, ZnO, and SnO_2 were added to water [34]. The first findings indicate that the nanofluid had a significant effect on amount of water that was made by the solar distillation unit. In comparison to a solar desalination system that did not use nanofluids, the generation of water using SnO_2-water, Al_2O_3-water, and ZnO-water nanofluids were enhanced by 18.63%, 29.95%, and 12.67%, respectively. Chen et al. evaluated the effect of SiC nanoparticles in the solar still at varying concentrations of thermal conductivity. Based on the findings, it appears that the addition of SiC nanofluid resulted in a 5.2% increase in thermal conductivity. Saleh et al. investigated the influence of the hydrothermal synthesis technique on generated ZnO nanoparticles in a solar desalination system [35]. They used a variety of solvents to do their research. Nanoparticles in the form of nanorods and nanospheres were investigated. It was discovered that the water productivity and thermal efficiency improved by 30% and 38%, respectively. Experiments were carried out with a volume fraction concentration of 10% and at two distinct water depths. They discovered that the water productivity of the absorber coated with $Fe2O_3$ nanoparticles was increased by 35.9% when compared to the water productivity of the absorber coated with microparticles.

12.2.6 SiC Nanomaterial in Solar Desalination System

Using an experimental approach, Chen et al. analyzed the characteristics of SiC nanoparticles. The study's overarching goals included examining the thermal conductivity, stability, and optical features of SiC/water nanofluid [36]. According to the findings, there is an obvious problem with the salts in the water-base fluid. The thermal conductivity of the water base fluid was significantly improved by the use of nanoparticles. Zanganeh et al. were successful in determining the influence of employing silicone nano-coating on the single-slope solar distillation unit water systems productivity [37]. The findings suggest that the incorporation of silicon nanoparticles into a coated glass cover results in an approximately 20.3% improvement in productivity when compared to a regular glass cover. For a PV/T system, Al-Waeli performed experiments to look into using SiC nanofluid as the base fluid [38]. When compared to only using the PV system, adding 3% SiC nanofluid by weight was shown to boost electrical efficiency by 24.1%. Zanganeh et al. examined influence of titanium dioxide and silicon nanoparticles on the glass cover surface of a solar distillation unit [39]. The nanoparticles that are on the surface of the condensation have varying degrees of wetting characteristics. When compared to a solar desalination system that did not have a nano-coating, the results show that silicon nanocoating contributed to an increase in water production that was roughly 20% higher. In another work, the author employed a nano-coating approach to adjust the glass cover wettability in order to boost water production. This research was conducted in another study. To condense the surface, a nano-silicon solution was utilized, and a hot water bath tank with an immersed electrical heater combined with a heat exchanger was placed within the solar desalination system water. At a glass inclination angle of 50 degrees, they discovered that adding a nano-silicon solution to a solar desalination system produced a freshwater output

that was 23 percent higher than before. Experimental research by Sardarabadi et al. examined the impact of nanofluid on the thermal and electrical efficiency of a PV/T system [40]. Overall energy efficiency was found to be enhanced by 3.6% and 7.9%, respectively, for the instances with a silica/water nanofluid of 1 wt% and 3 wt%, compared to the case with pure water, in that study.

12.2.7 Silver Nanomaterial in Solar Desalination System

Parsa et al. accompanied an examination upon the efficiency of three distinct kinds of solar distillation unit [41]. In the first design of the solar distillation unit, the basin was linked to the thermoelectrically hot side of the system. In the second experiment, a silver-water nanofluid was employed in conjunction with the thermoelectric hot side. The thermoelectric cold side, glass cooling water, and an external condenser were used for increasing the rate of condensation. According to the findings, the thermal efficiency and solar water production of the solar desalination system coupled with the condenser/nanofluid were enhanced by 26.7%, and 100.5% respectively. This was accomplished by increasing the temperature of the nanofluid. According to the findings of other studies, the contribution of thermoelectric cooling and water cooling to the overall water production was around 26.3%. In a different piece of research, Parsa was observed utilizing a nanofluid consisting of silver and water at a concentration of 0.04% in a solar desalination system. When compared to a traditional solar desalination system, exergy and energy outputs of solar desalination systems utilizing silver nanofluid showed significant increases of 106 and 196%, respectively, when analyzed using.

12.2.8 TiO_2 Nanomaterial in Solar Desalination System

Researchers Shanmugan et al. evaluated the effectiveness of solar distillation units by applying a coating of TiO_2 nanoparticles to the basin liner that was combined with $Cr2O_3$ [42]. According to the findings, the production of a solar desalination system was 7.89 liters during the summer months and 5.39 liters during the winter months. Experimental research on improved solar desalination system water productivity was carried out by Sahota and colleagues utilizing a variety of solar photovoltaic and thermal techniques. The dimensions of the system were 2 square meters. In order to improve the performance of the solar desalination system, nanofluids including Al_2O_3-water, CuO-water, and TiO_2-water were heated using thermal and photovoltaic techniques. Both of these increases were seen in the solar desalination system. Kabeel et. al., carried out research that involved doing an exploratory evaluation of a pyramid solar distillation unit containing TiO2 nanoparticles combined with a variety of black paint in order to boost the rate of heat transmission [43]. The findings suggest that the incorporation of TiO_2 nanomaterial inside the black color coating of the pyramid solar distillation unit resulted in an increase of 6.1% in the amount of water produced.

12.3 Application of Nanofluids for Thermal Desalination

Desalinating seawater with heat is conceptually similar to how rain forms. Thermal distillation removes heavy metals and other contaminants from saltwater. The water that is generated is as pure as rainfall. Solar thermal technologies are one example of the many possible sources of thermal energy. Since nanofluids are capable of effective heat transmission, they have also been investigated for use in thermal desalination processes, in addition to studies aimed at improving the thermal characteristics of nanofluids for use in concentrated solar power production. In order to enhance the efficiency of solar desalination systems, Sharshir et al. conducted experiments with three distinct designs and used nanofluids [44]. Basin depths varied from 0.25 to 5 cm, while the micro flakes percentage in nanofluids varied from 2% to 0.125%. Micro-flakes of copper oxide and graphite had an average particle size of 1 micrometer, and 1.2-1.3 micrometers respectively. Productivity for solar desalination systems was increased by 44.91%, and 53.95% respectively, when copper oxide and graphite microparticles were used in conjunction with glass-cooling.

For desalination purposes, a greater thermal conductivity means more solar radiation may be absorbed and used as heat. Dispersing Fe3O4-modified MWCNTs nanoparticles in salt water, Chen et al. created

nanofluids of varying concentrations. Based on the research, we modified MWCNTs with a diameter of 8-15 nm and a purity of 95% to impart magnetic characteristics. Using a two-stage procedure, we could create nanofluids with 0 to 0.04 wt% concentrations. Furthermore, zeta-potential measurements were used to assess the stability of nanofluids, with results showing that the solutions exhibited outstanding stability in pure water but decreased when exposed to salt. The zeta potential value was deficient with a salt concentration of 5000 PPM in water. When placed in salt water, nanofluids are only somewhat stable thanks to the employment of certain surfactants. Furthermore, an investigation into the optical characteristics of magnetic MWCNTs was conducted, resulting in greater heat energy for the evaporation of salt water. When the fluid's thickness was more than 1 cm, the author found that it absorbed solar energy at a rate of 100%. With a nanofluid concentration of 0.04 wt%, we could see this absorption. In addition, it was discovered that a higher concentration of nanofluid resulted in greater evaporation efficiency. An experimental study of seawater-based silicon carbide nanofluids for solar distillation was also conducted by Chen et al. [36]. According to the results of the experiment, the thermal conductivity of the nanofluid based on seawater was increased by 5.2%. Since the concentration of salt in water has a detrimental impact on the thermal conductivity and stability of nanofluid, finding the optimal concentration is essential. The group found that concentrations above 5000 PPM reduced thermal conductivity. In addition, when concentration was increased, the samples were much less stable, as measured by their zeta potential values. At 10 degrees Celsius with a concentration of 50,000 parts per million, the thermal conductivity is 6% lower than it would be at zero parts per million. The study found that SiC nanofluids had superior stability and increased thermal conductivity at reduced salt concentrations of TDS of the seawater, proving the nanofluid's viability for solar desalination. The evaporation efficiency was found to be 24.91% at 0% wt% and 76.65% at 0.04 wt%. The model was put through its paces in a wide range of scenarios, from varying functional parameters to climate extremes, and the results were well documented. Modeling the system using copper nanoparticles revealed that it was extremely efficient but not economically viable due to the tiny scale of the unit employed in the study. Suggestions for lowering the overall price tag included things like increasing the collection area and utilizing the right volume fractions of nanoparticles. Using the created equations, it was concluded that a collecting area of a solar water heater is an important component in lowering water production costs. In addition, as the collecting area of a solar water heater expands, the cost per unit of generated water decreases. Increased freshwater generation at a lower cost is possible when nanoparticles make up a larger portion of the working fluid in solar collectors. The production of solar desalination systems initially rises with the particle concentration in the nanofluid, as shown in a study of their performance by Kumar et al. [45]. When there are more particles in the system, however, the viscosity rises and the pressure drop increases, worsening the system's performance. In this article, we looked at how nanofluidics may be employed in desalination processes. Enhanced thermal characteristics of nanofluids are explored, highlighting its potential as a foundation for creating effective desalination systems. Using eco-friendly technologies to power desalination systems is crucial because the process requires a lot of energy. Nanofluids have been dubbed "NegaWatt" because they can help reduce energy use right off the get. By definition, a NegaWatt is a fictitious measurement of power that is spared as a result of increased efficiency or reduced energy consumption. Table 2 provides a quick summary of the many uses of nanofluids in solar desalination systems.

12.4 Challenges in Nanofluids for Solar Energy

Human exposure to nanoparticles is associated with unknown adverse health consequences. This is because different nanoparticles can have wildly varying chemical compositions and, in certain cases, sizes. As a result of their larger surface areas, nanoparticles are more likely to do harm to both humans and the natural world than bulk materials. They also noted that particles were taken into cells in vitro via diffusion or adhesion contacts, allowing them direct access to the cell's DNA, proteins, and organelles.

The high superconductive qualities of copper oxide nanoparticles (CuO) make them appealing in a wide variety of applications, including batteries, electronics, solar panels, and many others. As of 2014, the United States produced more than 300 metric tonnes of CuO nanoparticles. Considering the toxicological

Table 2. Overview of various nanofluids in solar desalination system.

Nanofluid	Base Fluid	(%) Concentration	Thermal Conductivity (W/mk)	Outcome	Reference
Al_2O_3	Water	0.04, 0.08, 0.12	46	Productivity enhanced by 16.83% for 0.12% Concentration	[46]
Al_2O_3	Mix with black paint	-------	46	Productivity enhanced by 38.09%	[47]
CuO	Water	0.12	17.6	Productivity enhanced by 22.5%	[48]
CuO	Water	0.125–2	17.6	Productivity enhanced by 44.91%	[48]
CuO_2	Mix with black paint	10–40	76.5	Productivity enhanced by 25%	[22]
Fe_2O_3	Water	0.05–0.1	6	-------	[28]
Graphite Flakes	Water	0.125–2	129	Productivity enhanced by 53.95%	[28]
SnO_2	Water	0.05–0.1	1.34–1.38	Productivity enhanced by 18.63%	[28]
ZnO	Water	0.05–0.1	29	Productivity enhanced by 12.67%	[28]

impacts of Cu ions and CuO nanoparticles on aquatic species and earthworms, to a greater extent than usual, copper materials must be protected from the dangers of environmental contamination. Nanoparticles made of copper oxide frequently release copper ions into liquids, which may contribute to their toxicity.

The higher price of producing nanoparticles, the agglomerating and instability of nanoparticles, and the pressure loss and pumping power are all potential obstacles to the uses of nanofluids. As a result, nanotechnology relies on extremely clean environments with very few defects. The developed procedure must be trustworthy in order to exert precise control over nanoparticles' properties, which drives up the price of producing nanoparticles. Experimental research: Another issue with our solar systems is the instability and aggregation of nanoparticles. Experimental measurements of pumping power were made by Routbort et al. for nanofluids moving through a whole system of straight tubing, elbows, and expansions [49]. As expected, the addition of nanoparticles to a base fluid increased the pumping power. The high price of using nanoparticles in heat exchangers was discussed by Lee and Mudawar [50]. Adding nanoparticles to a fluid raises its viscosity, which in turn raises the pressure drop and, by extension, the pumping power required to move the fluid. At high temperatures, and especially when subjected to natural circulation, the agglomeration of nanoparticles is a major problem. Nanoparticle selection is becoming increasingly important in high-temperature applications.

12.5 Conclusions

In the decades, a new class of fluids called nanofluids has evolved. These fluids are advanced because they include particles on the nanoscale. Inexpensive heat transfer methods will be greatly aided by cutting-edge integrated systems based on nanofluids. Key findings from this review are discussed and recommendations for further research. Nanofluids in the energy industry face a number of significant issues, the most significant of which are the improvement of efficiency, reliability, and safety, as well as the decrease in the cost of nanoparticles. When the percentage of nanoparticles that are solid grows, so does daily productivity. Frictional and thermal irreversibilities are highest at the solar desalination system's bottom and top walls and lowest in the desalination system's center. Because of their low luminosity, low cost, and high thermal and mechanical durability, Silicon carbide nanoparticles are encouraged for use in solar desalination units. Solar desalination systems can increase their productivity by combining the nanoparticle process with additional passive and active methods. Using nanofluids improves the quantity of carbon dioxide reduction.

Since the creation of solar desalination systems has direct human applications, certain recommendations are provided for further research. The study of nanofluids requires the development of methodologies for the synthesis of nanoparticles at a cheap cost. As such, prior to its implementation, nanoparticles' potential

risks to people's well-being must be evaluated. The device's complexities need to be resolved. Stability in operations over the long term and life cycle evaluation are important considerations. Future studies in this area ought to take these things into account. In order to collect more complete information regarding this method, it is necessary to analyze the effects of nanoparticles on production in various climatic zones. Most studies in this area focus on single as well as double solar desalination systems because these are the most common kind of solar desalination systems used for research. Therefore, nanotechnology has tremendous promise for addressing the challenges faced by the desalination industry, as it will facilitate the creation of environmentally friendly desalination processes and the harnessing of solar thermal energy. More research is required into other sorts of solar desalination systems, such as the sun tracing, pyramid, semi-sphere, and cascade varieties.

Funding: There was no external funding received for conduction of this study.

Conflicts of Interest: The authors declare that they have no conflicts of interest.

Authors Contributions: All authors contributed equally to this work.

References

1. Karpat, F., Kalay, O. C., Dirik, A. E., & Karpat, E. (2022). Fault Classification of Wind Turbine Gearbox Bearings Based on Convolutional Neural Networks. *Transdisciplinary Journal of Engineering and Science,* 13, 71–83. https://doi.org/10.22545/2022/00190
2. Belkhode, P. N., Shelare, S. D., Sakhale, C. N., Kumar, R., Shanmugan, S., Soudagar, M. E. M., & Mujtaba, M. A. (2021). Performance analysis of roof collector used in the solar updraft tower. *Sustainable Energy Technologies and Assessments,* 48, 101619. https://doi.org/10.1016/j.seta.2021.101619
3. Bait, O., & Si–Ameur, M. (2018). Enhanced heat and mass transfer in solar stills using nanofluids: A review. *Solar Energy,* 170, 694–722. https://doi.org/10.1016/j.solener.2018.06.020
4. Dhande, H. K., Shelare, S. D., & Khope, P. B. (2020). Developing a mixed solar drier for improved postharvest handling of food grains. *Agricultural Engineering International: CIGR Journal,* 22(4), 166–173. https://cigrjournal.org/index.php/Ejounral/article/view/6049
5. Uysal, M. T., Turkan, B., & Etemoglu, A. B. (2022). Energy and Exergy Analyses for Flue Gas Assisted Organic Rankine Cycle. *Transdisciplinary Journal of Engineering and Science,* 13, 57–69. https://doi.org/10.22545/2022/00186
6. Model, C. E. (2022). Exploring Grassroots Renewable Energy Transitions: Developing a. *Transdisciplinary Journal of Engineering & Science,* 2, 137–163. https://doi.org/10.22545/2022/00215
7. Yavaş, Ö., Savran, E., Nalbur, B. E., & Karpat, F. (2022). Energy and Carbon Loss Management in an Electric Bus Factory for Energy Sustainability. *Transdisciplinary Journal of Engineering and Science,* 13, 97–110. https://doi.org/10.22545/2022/00207
8. Belkhode, P. N., Ganvir, V. N., Shelare, S. D., Shende, A., & Maheshwary, P. (2022). Experimental investigation on treated transformer oil (TTO) and its diesel blends in the diesel engine. *Energy Harvesting and Systems,* 9(1), 75–81. https://doi.org/10.1515/ehs-2021-0032

9. Aglawe, K. R., Yadav, R. K., & Thool, S. B. (2021). Preparation, applications and challenges of nanofluids in electronic cooling: A systematic review. *Materials Today: Proceedings,* 43, 366–372. https://doi.org/10.1016/j.matpr.2020.11.679
10. Aglawe, K. R., Yadav, R. K., & Thool, S. B. (2022). Current Technologies on Electronics Cooling and Scope for Further Improvement: A Typical Review. *Proceedings of the International Conference on Industrial and Manufacturing Systems* (CIMS-2020), 389–408.
11. Shelare, S. D., Aglawe, K. R., & Belkhode, P. N. (2022). A review on twisted tape inserts for enhancing the heat transfer. *Materials Today: Proceedings,* 54, 560–565. https://doi.org/10.1016/j.matpr.2021.09.012
12. Madiouli, J., Lashin, A., Shigidi, I., Badruddin, I. A., & Kessentini, A. (2020). Experimental study and evaluation of single slope solar still combined with flat plate collector, parabolic trough and packed bed.*Solar Energy,* 196, 358–366. https://doi.org/10.1016/j.solener.2019.12.027
13. Undirwade, S. K. (2022). Influence of Operational Variables in Bicycle Driven Bamboo Slicing Phenomena by Methodology of Response Surface Approach. *Transdisciplinary Journal of Engineering and Science,* 13, 23–41. https://doi.org/10.22545/2022/00174
14. Khalifa, A. J. N., & Hamood, A. M. (2009). Effect of insulation thickness on the productivity of basin type solar stills: An experimental verification under local climate.*Energy Conversion and Management,* 50(9), 2457–2461. https://doi.org/10.1016/j.enconman.2009.06.007
15. Shelare, S. D., Aglawe, K. R., Waghmare, S. N., & Belkhode, P. N. (2021). Advances in water sample collections with a drone – A review. *Materials Today: Proceedings,* 47, 4490–4494. https://doi.org/10.1016/j.matpr.2021.05.327
16. Singh, T., Atieh, M. A., Al-Ansari, T., Mohammad, A. W.,& McKay, G. (2020). The role of nanofluids and renewable energy in the development of sustainable desalination systems: A review. *Water* (Switzerland), 12(7). https://doi.org/10.3390/w12072002
17. Waghmare, S., Shelare, S., Aglawe, K., & Khope, P. (2022). A mini review on fibre reinforced polymer composites. *Materials Today: Proceedings,* 54, 682–689. https://doi.org/10.1016/j.matpr.2021.10.379
18. Elkelawy, M., Shenawy, E. A. El, Bastawissi, H. A., & Shams, M. M. (2022). Energy conservation management: X A comprehensive review on the effects of diesel/biofuell blends with nanofluid additives on compression ignition engine by response surface methodology,*Energy Convers. Manag. X,* vol. 14, no. July 2021, p. 100177, 2022, doi: 10.1016/j.ecmx.2021.100177.
19. Ghadimi, A., Saidur, R., & Metselaar, H. S. C. (2011). A review of nanofluid stability properties and characterization in stationary conditions. *International Journal of Heat and Mass Transfer,* 54(17–18), 4051–4068. https://doi.org/10.1016/j.ijheatmasstransfer.2011.04.014
20. Akkala, S. R., Kaviti, A. K., ArunKumar, T., & Sikarwar, V. S. (2021). Progress on suspended nanostructured engineering materials powered solar distillation- a review. *Renewable and Sustainable Energy Reviews,* 143(March), 110848. https://doi.org/10.1016/j.rser.2021.110848
21. (2021). Evaluation of the nanofluid-assisted desalination through solar stills in the last decade. Journal of Iqbal, A., Mahmoud, M. S., Sayed, E. T., Elsaid, K., Abdelkareem, M. A., Alawadhi, H., & Olabi, A. G. *Environmental Management,* 277, 111415. https://doi.org/10.1016/j.jenvman.2020.111415
22. Kabeel, A. E., Omara, Z. M., & Essa, F. A. (2014). Enhancement of modified solar still integrated with external condenser using nanofluids: An experimental approach. *Energy Conversion and Management,* 78, 493–498. https://doi.org/10.1016/j.enconman.2013.11.013
23. Muraleedharan, M., Singh, H., Udayakumar, M., & Suresh, S. (2019). Modified active solar distillation system employing directly absorbing Therminol 55–Al2O3 nano heat transfer fluid and Fresnel lens concentrator. *Desalination,* 457, 32–38. https://doi.org/10.1016/j.desal.2019.01.024
24. Karthikeyan, J., Selvaraj, P., & Nagaraj, G. (2020). Day and night yield performance analysis of solar still for saline water using energetic materials with thermocol insulation.*Materials Today: Proceedings,* 33, 4848–4851. https://doi.org/10.1016/j.matpr.2020.08.395

25. Thakur, A. K., Agarwal, D., Khandelwal, P., & Dev, S. (2018). Comparative Study and Yield Productivity of Nano-paint and Nano-fluid Used in a Passive-Type Single Basin Solar Still BT - *Advances in Smart Grid and Renewable Energy* (S. SenGupta, A. F. Zobaa, K. S. Sherpa, & A. K. Bhoi (eds.); pp. 709–716). Springer Singapore.
26. Arora, S., Singh, H. P., Sahota, L., Arora, M. K., Arya, R., Singh, S., Jain, A., & Singh, A. (2020). Performance and cost analysis of photovoltaic thermal (PVT)-compound parabolic concentrator (CPC) collector integrated solar still using CNT-water based nanofluids. *Desalination,* 495, 114595. https://doi.org/10.1016/j.desal.2020.114595
27. Sharshir, S. W., Eltawil, M. A., Algazzar, A. M., Sathyamurthy, R., & Kandeal, A. W. (2020). Performance enhancement of stepped double slope solar still by using nanoparticles and linen wicks: Energy, exergy and economic analysis. *Applied Thermal Engineering,* 174, 115278. https://doi.org/10.1016/j.applthermaleng.2020.115278
28. Nazari, S., Safarzadeh, H., & Bahiraei, M. (2019). Performance improvement of a single slope solar still by employing thermoelectric cooling channel and copper oxide nanofluid: An experimental study. *Journal of Cleaner Production,* 208, 1041–1052. https://doi.org/10.1016/j.jclepro.2018.10.194
29. Bahiraei, M., Nazari, S., Moayedi, H., & Safarzadeh, H. (2020). Using neural network optimized by imperialist competition method and genetic algorithm to predict water productivity of a nanofluid-based solar still equipped with thermoelectric modules. *Powder Technology,* 366, 571–586. https://doi.org/10.1016/j.powtec.2020.02.055
30. Abdullah, A. S., Essa, F. A., Bacha, H. Ben, & Omara, Z. M. (2020). Improving the trays solar still performance using reflectors and phase change material with nanoparticles. *Journal of Energy Storage,* 31, 101744. https://doi.org/10.1016/j.est.2020.101744
31. Behura, A., & Gupta, H. K. (2021). Use of nanoparticle-embedded phase change material in solar still for productivity enhancement. *Materials Today: Proceedings,* 45, 3904–3907. https://doi.org/10.1016/j.matpr.2020.06.285
32. Sharshir, S. W., Peng, G., Elsheikh, A. H., Edreis, E. M. A., Eltawil, M. A., Abdelhamid, T., Kabeel, A. E., Zang, J., & Yang, N. (2018). Energy and exergy analysis of solar stills with micro/nano particles: A comparative study. *Energy Conversion and Management,* 177, 363–375. https://doi.org/10.1016/j.enconman.2018.09.074
33. Kabeel, A. E., Sathyamurthy, R., Sharshir, S. W., Muthumanokar, A., Panchal, H., Prakash, N., Prasad, C., Nandakumar, S., & El Kady, M. S. (2019). Effect of water depth on a novel absorber plate of pyramid solar still coated with TiO2 nano black paint.*Journal of Cleaner Production,* 213, 185–191. https://doi.org/10.1016/j.jclepro.2018.12.185
34. Elango, T., Kannan, A., & Kalidasa Murugavel, K. (2015). Performance study on single basin single slope solar still with different water nanofluids. *Desalination,* 360, 45–51. https://doi.org/10.1016/j.desal.2015.01.004
35. Saleh, S. M., Soliman, A. M., Sharaf, M. A., Kale, V., & Gadgil, B. (2017). Influence of solvent in the synthesis of nano-structured ZnO by hydrothermal method and their application in solar-still. *Journal of Environmental Chemical Engineering,* 5(1), 1219–1226. https://doi.org/10.1016/j.jece.2017.02.004
36. Chen, W., Zou, C., Li, X., & Li, L. (2017). Experimental investigation of SiC nanofluids for solar distillation system: Stability, optical properties and thermal conductivity with saline water-based fluid. *International Journal of Heat and Mass Transfer,* 107, 264–270. https://doi.org/10.1016/j.ijheatmasstransfer.2016.11.048
37. Zanganeh, P., Goharrizi, A. S., Ayatollahi, S., & Feilizadeh, M. (2020). Nano-coated condensation surfaces enhanced the productivity of the single-slope solar still by changing the condensation mechanism. *Journal of Cleaner Production,* 265, 121758. https://doi.org/10.1016/j.jclepro.2020.121758
38. Al-Waeli, A. H. A., Sopian, K., Chaichan, M. T., Kazem, H. A., Hasan, H. A., & Al-Shamani, A. N. (2017). An experimental investigation of SiC nanofluid as a base-fluid for a photovoltaic thermal PV/T system. *Energy Conversion and Management,* 142, 547–558. https://doi.org/10.1016/j.enconman.2017.03.076

39. Zanganeh, P., Goharrizi, A. S., Ayatollahi, S., Feilizadeh, M., & Dashti, H. (2020). Efficiency improvement of solar stills through wettability alteration of the condensation surface: An experimental study. *Applied Energy,* 268, 114923. https://doi.org/10.1016/j.apenergy.2020.114923
40. Sardarabadi, M., Passandideh-Fard, M., & Zeinali Heris, S. (2014). Experimental investigation of the effects of silica/water nanofluid on PV/T (photovoltaic thermal units). *Energy,* 66, 264–272. https://doi.org/10.1016/j.energy.2014.01.102
41. Parsa, S. M., Rahbar, A., Koleini, M. H., Aberoumand, S., Afrand, M., & Amidpour, M. (2020). A renewable energy-driven thermoelectric-utilized solar still with external condenser loaded by silver/nanofluid for simultaneously water disinfection and desalination. *Desalination,* 480, 114354. https://doi.org/10.1016/j.desal.2020.114354
42. Shanmugan, S., Essa, F. A., Gorjian, S., Kabeel, A. E., Sathyamurthy, R., & Muthu Manokar, A. (2020). Experimental study on single slope single basin solar still using TiO2 nano layer for natural clean water invention. *Journal of Energy Storage,* 30, 101522. https://doi.org/10.1016/j.est.2020.101522
43. Kabeel, A. E., Sathyamurthy, R., Manokar, A. M., Sharshir, S. W., Essa, F. A., & Elshiekh, A. H. (2020). Experimental study on tubular solar still using Graphene Oxide Nano particles in Phase Change Material (NPCM's) for fresh water production.*Journal of Energy Storage,* 28, 101204. https://doi.org/10.1016/j.est.2020.101204
44. Sharshir, S. W., Peng, G., Wu, L., Yang, N., Essa, F. A., Elsheikh, A. H., Mohamed, S. I. T., & Kabeel, A. E. (2017). Enhancing the solar still performance using nanofluids and glass cover cooling: Experimental study. *Applied Thermal Engineering,* 113, 684–693. https://doi.org/10.1016/j.applthermaleng.2016.11.085
45. Arunkumar, T., Wang, J., Dsilva Winfred Rufuss, D., Denkenberger, D., & Kabeel, A. E. (2020). Sensible desalting: Investigation of sensible thermal storage materials in solar stills. *Journal of Energy Storage,* 32, 101824. https://doi.org/10.1016/j.est.2020.101824
46. Sahota, L., & Tiwari, G. N. (2016). Effect of Al2O3 nanoparticles on the performance of passive double slope solar still. *Solar Energy,* 130, 260–272. https://doi.org/10.1016/j.solener.2016.02.018
47. Ahmed, H. E., Ahmed, M. I., Seder, I. M. F., & Salman, B. H. (2016). Experimental investigation for sequential triangular double-layered microchannel heat sink with nanofluids. *International Communications in Heat and Mass Transfer,* 77, 104–115. https://doi.org/10.1016/j.icheatmasstransfer.2016.06.010
48. Gupta, B., Shankar, P., Sharma, R., & Baredar, P. (2016). Performance Enhancement Using Nano Particles in Modified Passive Solar Still. *Procedia Technology,* 25(Raerest), 1209–1216. https://doi.org/10.1016/j.protcy.2016.08.208
49. Routbort, J. L., Singh, D., Timofeeva, E. V, Yu, W., & France, D. M. (2011). Pumping power of nanofluids in a flowing system. *Journal of Nanoparticle Research,* 13(3), 931–937. https://doi.org/10.1007/s11051-010-0197-7
50. Lee, J., & Mudawar, I. (2007). Assessment of the effectiveness of nanofluids for single-phase and two-phase heat transfer in micro-channels. *International Journal of Heat and Mass Transfer,* 50(3–4), 452–463. https://doi.org/10.1016/j.ijheatmasstransfer.2006.08.001

About the Authors

Prof. (Mrs.) Trupti S. Gajbhiye (Shelare) is presently working as an Assistant Professor in the Department of Electrical Engineering at G H Raisoni Institute of Engineering and Technology, Polytechnic, Nagpur, Maharashtra, India. She has completed her M.Tech. in Industrial Drives & Control from the Department of Electrical Engineering, Priyadarshini College of Engineering, Rastrasant Tukdoji Maharaj Nagpur University Nagpur, Maharashtra, India. She has published more than 5 research articles throughout the several SCI / Scopus indexed journal, including International / National level conferences. During her academic career, she has authored a book of international publishers. Also, she has patents in her credentials.

Dr. Sagar D. Shelare is presently working as an Assistant Professor in the Department of Mechanical Engineering at Priyadarshini College of Engineering, Nagpur, Maharashtra, India. He has received a Doctor of Philosophy (Ph.D.) degree in the area of Mechanical Engineering, from the School of Mechanical Engineering, Lovely Professional University, Punjab, India. He has published more than 30 research articles throughout the several SCI / Scopus indexed journal, including International / National level conferences. He is also academically engaged as the reviewer with several SCI/ Scopus indexed Journals from the last 5 years. He has delivered several Expert Talks/Lectures at different levels of the platform throughout the country. He has received a Global Teacher award for his contribution to research and development. He is a lifetime member of more than eight reputed professional societies at the National and International levels. During his academic career, he has authored five books by international publishers. Also, he has five patents in his credentials in the field of Agricultural Mechanisation.

Prof. Kapil R. Aglawe is presently working as an Assistant Professor in the Department of Mechanical Engineering at Priyadarshini College of Engineering, Nagpur, Maharashtra, India. He is pursuing his the Doctor of Philosophy (PhD) degree in the area of Mechanical Engineering, from the Mechanical Engineering, National Institute of Technology, Raipur, India. He has published more than 15 research articles throughout the several SCI / Scopus indexed journal, including International / National level conferences. He is also academically engaged as the reviewer with several SCI/ Scopus indexed Journals from the last 2 years. He is a lifetime member of several reputed professional societies at National and International level. Also, he has a patent in his credentials in the field of Mechanical Engineering.

CHAPTER 13

Experimental Investigation of Al_2O_3 Nanofluid for Thermal Energy Management of Microchannel Heat Sink

Kapil R. Aglawe, Ravindra K. Yadav, and Sanjeev B. Thool

Article citation information: (2022), *TJES*, Vol. SP-2, pp. 203-216, doi:10.22545/2022/00218

Energy is one of the primary foundations supporting evolutionary changes. Because of small size and improved heat transfer properties, nanofluid-cooled microchannel heat sinks (MCHS) have become a popular choice for electronics and thermal applications. The influence of employing nanofluids for cooling a chip was investigated experimentally in this work to evaluate the heat transfer characteristics. The investigations were carried out to confirm the influence of nanofluid concentration and wall temperature upon the thermal-hydraulic properties of the microchannel heat sink. In the present study, Al2O3 water nanofluid was employed, with 0.1, 0.2, 0.3, 0.4, and 0.5% nanoparticle volume fractions, mass flow rate (MFL) 2, 5, and 8 m/s at various inlet tempreture. The resulting experimental findings were verified from other researchers' results, which showed an important correlation. The heat transfer efficacy of electronics cooling systems has been enhanced by the nanofluid technology and configuration of rectangular heat sink.

Keywords: Microchannel heat sink, alumina (Al_2O_3), nanofluids, thermal management, CFD, experimentation, heat transfer enhancement.

13.1 Introduction

Energy is one of the primary foundations supporting evolutionary changes [1]. The performance of mobile phones, tablets, computers, and other electronic devices improves dramatically every year as new technologies emerge and processing frequencies increase [2]. With the increasing emphasis on processing speed in the electronics sector, the problem of excessive heat production has been solved straightforwardly [3], [4]. If the heat produced by such parts isn't properly evacuated, their useful life will be cut short very quickly [5]. The existing technology for cooling has reached its limits; hence new solutions must be developed [6]. Nanofluids with improved thermal characteristics have been shown to be effective coolants in heat transfer applications [7], [8]. Many types of nanoparticles (NPs) can be employed in the production of nanofluids [9], [10]. Measurable increases in the coefficient of heat conductivity are the hallmark of such a process [11]. When it comes to cooling electronics, a higher integration level can generate a higher heat flux. Since the microelectronic device's reliability is highly dependent on its working temperature, consistency can decrease by as much as 5% for every additional degree above a temperature of 70 to 80°C [12].

Consequently, increasing the thermal conductivity is crucial to finding a solution to the heat transfer and flow difficulties that arise at the microscale [13]. However, due to the need for constructing more advanced

processors, these coolants have hit their limits due to their restricted thermal conductivity (for example, 0.65 W/mC) [14]. As a result, there is a requirement to implement a new coolant to accelerate the process of convective cooling that takes place inside the MCHS [15], [16].

While working at the Argonne National Laboratory in the United States on a programme supported by the Department of Energy, Choi and Eastman presented nanofluids ideas [17]. Colloidal dispersion systems, which nanofluids are, are made up of the base fluid (dispersion medium) and NPs (dispersed phase) [3]. The distributed NPs have a thermal conductivity that is greater than a basic liquid [18]. As a result, high thermal conductivity is found in produced nanofluids [19]. In addition, the contact and collision that occurs between NPs, as well as those that occur between NPs and the substrate solution, contribute to a rise in the effective thermal conductivity of nanofluids [20], [21]. The activity of NPs might cause wear difficulties that are caused by particles that are millimeters and micrometers in size [22]. Therefore, the use of nanofluids as novel refrigerants for the purpose of enhancing heat transfer has garnered a significant amount of interest from academics, which has resulted in numerous novel advancements in a field of heat transfer [20], [23].

Utilizing nanofluids to enhance thermal properties has gained traction as a research focus in recent years. Compared to pure fluids, the newly created family of ultrafine (1-100 nm) nanofluid coolants demonstrated encouraging behavior in laboratory trials [24]. Ellsworth et al. [25] examined the history and development of water cooling systems, which included hybrid cooling in early IBM units and later transitioned to passive water cooling. To supply the necessary cooling power while maintaining simple operation at the module level, water refrigeration has been implemented [4]. For calculating a heat transfer and pressure decreases for a parallel plate MCHS, the author Xu et al. [26] investigated analytical approaches. Flow conditions and fine-geometry optimization minimize the entropy production rate. Limitations of air conditioning estimation based on numerical model and heat sink effects. Raghuraman et al. [27] conducted a computational investigation of an improved liquid flow features and heat transfer characteristics of rectangular MCHS. The medium of operation was water. The author Ali et al. [28] investigated the MCHS's experimental pressure drop and heat transfer characteristics. A cooling effectiveness of a TiO_2 nanofluid diluted to 15% by weight in water was compared to that of distilled water at 150 W, 125 W, and 100 W. The findings demonstrated that heat flow was crucial to TiO2 nanofluid's thermal efficiency and that its usefulness could be maximized at a reduced thermal cost. Graphene (GNP) nanofluids in water were also used to examine the angular influence on a pine-fin heat sink channel (0.25–0.75 LPM). Azari et al. [12] studied the laminar convective coefficient of an Al2O3 / water nanofluid under the same surface conditions in an experimental and numerical circular tube setup.

Systemic effects on the geometry sink base temperature microprocessor with nanofluid were investigated by [29]. They used a cylinder-shaped block of copper to run a 325-W heat-generating microprocessor and compared its performance to that of generally accessible nanofluids and heat sinks. They looked at thermal sink geometry's potential, which is sufficient to bring down the higher temperatures produced by microprocessors to adequate and safe levels. Using numerical methods, Seyf et al. [30] examined usage of nanofluids in micro-pin-fin MCHS. The heat transfer behavior of Micro-Pin-Fin MCHS was considered by solving the Navier-Stokes equation and 3-dimensional steady energy equation using a finite volume approximation and the SIMPLE method. NPs impact on the performance of a microprocessor designed to cool a central processing unit was investigated by [31]. Experiments and numerical analysis were first performed on distilled water, and afterward on two concentrations of CuO-water (0.86 and 2.25 vol. %) used as nano-fluids.

A innovative battery module design using two-layer nanofluids superior phase change medium was investigated by [32]. In this plan, n stands for main containers, m represents the cells, and p stands for secondary containers. In two configurations (771 and 711), each Li-ion cell was allowed to discharge under three distinct settings [33]. The improvement in heat transport inside projecting heat sources was investigated by Sultan et al. [34]. In addition, he found a formula that relates the Nu to the Richardson number. Alumina nanofluids were analyzed for their thermal conductivity and viscosity by Shah et al. [35]. Their research demonstrated that a- Al_2O_3 nanofluid has greater thermal stability than common cooling fluids. From the heat source chilled by forced nanofluid flow, Esmaeil et al. [36] conducted tests for mixed convection heat transfer. Paraffin wax, an aluminum chip, and nano-silicon carbide (SiC) tubes were employed to enhance

the heater's performance by [37]. The experimental findings showed that the new air heater worked well in Bagdad's climate. For cooling, Siricharoenpanicha et al. [38] utilized a combination of Ag and Fe_3O_4 nanofluids. It was taken into account how the flow rate, shape, and MCHS design would affect thermal dissipation.

Elsayed et al. [39] investigated the influence that utilizing helical coils in conjunction with nanofluids had on the thermal performance and the pressure drops that occurred in a turbulent flow pattern. The behavior of a nanofluid combination of Al2O3 NPs and water has been investigated by [40]. This mixture is now being pumped into a closed system designed to cool chips and other electronic equipment. The findings of the turbulent flow indicated that the inclusion of NPs in the distilled fluid significantly enhanced the rate of heat transfer. Additionally, the Glycol Ethylene was utilized for a cooling procedure, with volumes ranging from 30 to 50 percent [41].

This research aims to investigate how microprocessors' cooling is affected by utilizing Al_2O_3 nanofluids, each of which has a different volume proportion of NPs. A heating chip with dimensions of 5 centimeters by 5 centimeters and a power output of 130 watts may be cooled using thermal management technology. The Al_2O_3 NPs were combined in water at varying concentrations of 0.1, 0.2, 0.3, 0.4, and 0.5% the total volume. The mass flow rate of the flowing fluid was varied as 2, 5, and 8 m/s at 25, 30 and 35°C inlet temperature. This work uses experimental data, verified using data from previous studies and the literature.

13.2 Experimental Setup

This section discusses details about the experimental setup, methodology adopted for conduction of experiments, and the information about the test section.

13.2.1 Experimental Setup

Figure 13.1 shows the block diagram of an experimental setup used in the current study. The various components used in the experimental setup are a Coolant tank, Syringe pump, Digital differential pressure transducer, Microchannel test section, Rectangular cartridge heaters, Thermostat, Data Acquisition system, Computer, Radiator, Digital temperature indicator, and Glass wool.

With the help of a thermostat, heat is sent to the bottom of the MCHS from a rectangular cartridge heater with a capacity of 300 W and a thickness of 1.5 mm. The heat flux from this heater can range from 40 kW/m2 to 84 kW/m2. This experiment uses Al_2O_3 nanofluid with a volume concentration of 0.1% to 0.5%. The leakiness of the MCHS was first examined, and the sensors' ability to detect changes in temperature and pressure were validated while water was circulating through them. To keep the MFL stable, a regulator controlled the speed of the stepper motor. The fluid's MFL has been timed with a stopwatch. By changing the flow metre, we can keep the nanofluid flow rate constant at 0.1 LPM. The data for temperature and pressure were obtained during conditions of relative calm. The following standard correlation was used to compute the output.

Fei Yu et al. provide the heat transfer correlation [42] as in Equation (13.1).

$$Q = mcT_{out} - T_{in} \tag{13.1}$$

Where, m – Mass flow rate; c - specific heat capacity.

Ganapathy et al. provided the following equation for determining the typical Nusselt number [43] as in Equation (13.2).

$$N_u = h_{exp}\frac{D_h}{k} \tag{13.2}$$

Where, k - thermal conductivity; D_h - hydraulic diameter of MCHS.

It is possible to get the heat transfer coefficient (HTC) by using Equation (13.3) [44]

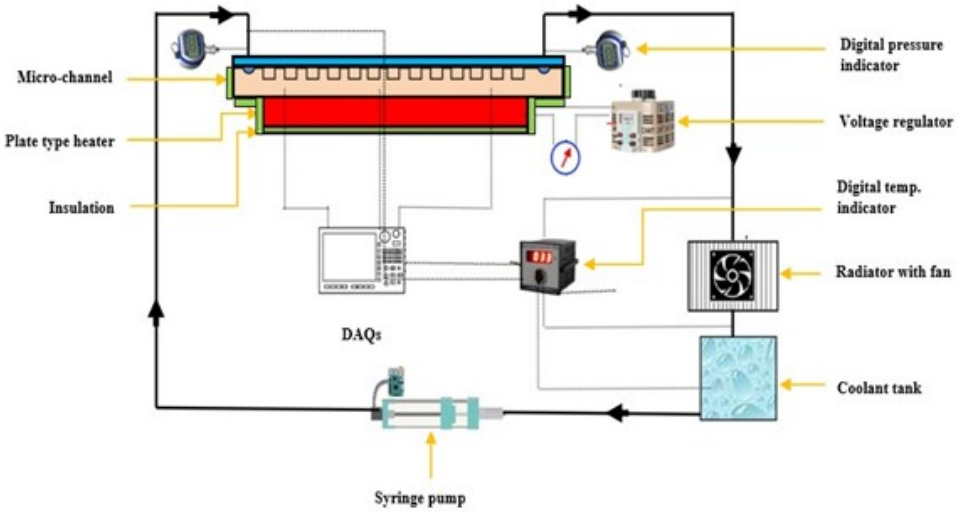

Figure 13.1: *Experimental setup block diagram.*

$$h = QT_w - T_m \times A_s \times 58 \tag{13.3}$$

Where, Q - heat carried by coolant, T_w, and T_m is the surface temperature of MCHS and mean temperature of the coolant, and as is the surface area of the channel. The equation (4) was used to figure out how much energy was needed for pumping.

$$P_P = \Delta_P \times V_c \times 58 \times 1000 \tag{13.4}$$

Where, V_c is the volume rate of flow. Yan Fan et al used to figure out the friction factor [45] by Equation (13.5).

$$F_{exp} = 2 \times \delta_P L \times \rho \times U_c^2 \tag{13.5}$$

Where, U_c is a fluid velocity and L is MCHS length.

Figure 13.2 shows the pictorial view of an experimental set-up used in the current study. The various components used in the experimental set-up are Coolant tank (1), Syringe pump (2), Digital differential pressure transducer (3), Microchannel test section (4), Rectangular cartridge heaters (5), Thermostat (6), Data Acquisition system (7), Computer (8), Radiator (9), Digital temperature indicator (10) and Glass wool.

Table 1 displays the descriptions of specific parts employed in the experimental setup. The nanofluid was moved from the acrylic Coolant tank to the MCHS test section with the help of a syringe pump. The regulator on the stepper motor that ran the syringe pump was utilized to control a flow rate of a nanofluid. Nanofluid has a MFL that ranges from 0.1 lpm to 0.5 lpm. After the radiator and coolant tank, the temperature of the nanofluid flowing through the MCHS was measured using an Ambetronics K-type thermocouple with a measuring range of 0°C to 3000°C. A digital differential pressure transducer made by Setra that can measures pressure values from 0 to 100Kpa was attached to the outlet and inlet sides of a MCHS for measuring the difference in pressure.

At the bottom of the MCHS, three more thermocouples were added to measure a temperature of the bottom surface of the MCHS. The first is a copper plate heat sink with parallel MCHS. The second part is a piece of acrylic glass that is put over the MCHS so that the flow can be seen. The last part is a 2 mm-diameter nozzle that is placed above the acrylic glass so that nanofluid can flow through. The nanofluid

Figure 13.2: *Typical experimental setup where Coolant tank (1), Syringe pump (2), Digital differential pressure transducer (3), Microchannel test section (4), Rectangular cartridge heaters (5), Thermostat (6), Data Acquisition system (7), Computer (8), Radiator (9), Digital temperature indicator (10) and Glass wool.*

Table 1: Specification of the experimental components

Components	Details
Microchannels	50 x 50 x 3 mm (L x W x H) d_h=0.2mm No of channel=58 Material: Copper
Syringe Pump	volume 22 ml (1 to 10 ml/sec)
Digital pressure indicator (Precision Engg. Pvt. Ltd.)	Pressure gauge range 0 to 100 Kpa
Rectangular cartridge heaters (Nichrome)	Max. Capacity 300 W 35*35mm
Dimmerstat	0 - 300 W
Thermocouple	k type 0°C - 300 °C ±0.1 °C
Digital temperature indicator	-25 °C – 250 °C
Heat exchanger/Radiator (For closed system) Cross flow	Dimensions:(80*80*26)mm Material: Aluminum No. of Tube:08 Tube Diameter:1mm
Fluid tank	Acrylic 0.5 litre capacity
Data acquisition system	VKV Engineering Solution Pvt. Ltd.
Insulation	Glass Wool max capacity 1200 °C

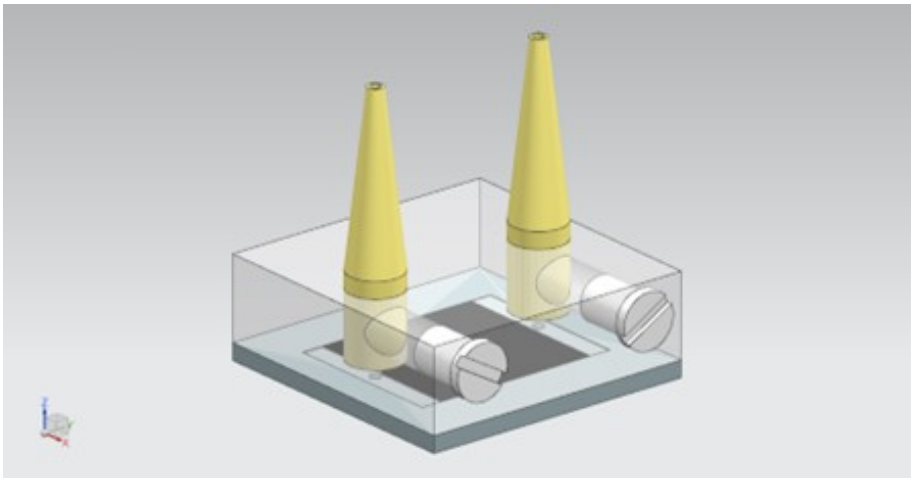

Figure 13.3: *CAD model microchannel assembly.*

can flow through the MCHS plate, which has channels for it to do so. The thermostat ensures that the rectangular cartridge heater at the bottom of the MCHS always gets the same heat. The nanofluid is cooled by a cross-flow type radiator that is attached to a MCHS test section and the reservoir. The data acquisition system sends the temperature of the MCHS to the computer.

13.2.2 Test Section Fabrication

CAD software was used to draw a model of a MCHS test section, and the vertical milling machine was used to do the machining. The MCHS was first cut to 50 mm x 50 mm and 3 mm thick for the straight parallel channels with a vertical milling machine. Then, a wire-cut EDM was used to cut channels in a copper plate to make the channels that were needed. MCHS was made in size of 35*35* mm with a hydraulic diameter of channel is 0.2 mm. The total number of channels is 58 and spacing between the channel is 0.5mm. Figure 13.3 shows CAD model of MCHS assembly.

At the top of the MCHS, a screw holds the acrylic glass that was cut with a CNC machine in place to stop leaks and let nanofluids flow through.

13.3 Results and Discussion

For cooling a MCHS, the current work experimentally examined the advantages of using an Al_2O_3-Water nanofluid over plain water. The heat transfer properties of Al_2O_3-Water nanofluid combinations are evaluated in a rectangular-shaped MCHS under varying circumstances.

13.3.1 Influence of Mass Flow Rate of Water at Heat Transfer Coefficient

Figure 13.4 shows the MFL effect of water at HTC with inlet temperature as 25°C, 30°C, and 35°C. By varying the MFL from 2 m/s to 8 m/s, the HTC are varied from 2847.38 to 8754.14, 2949.71 to 9550.42 and 3120.09 to 10066.73 W/m2K at 25°C, 30°C, and 35°C inlet temperature respectively. Highest HTC of 10066.73 W/m2k was observed at a MFL of 8 m/s at 35°C inlet temperature, whereas the lowest HTC of 2847.38 W/m^{2}K was observed at a MFL of 2 m/s at 25°C inlet temperature.

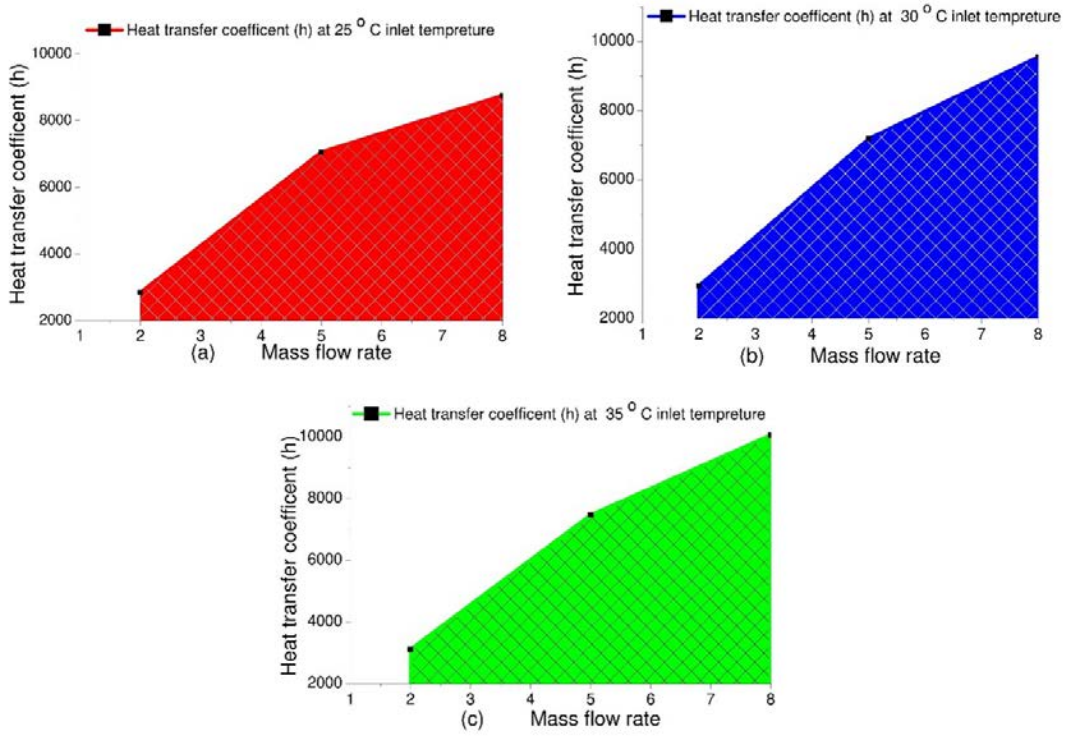

Figure 13.4: *Mass flow rate effect of water at heat transfer coefficient with varying inlet temperature.*

Compared to Al_2O_3 nanofluid, water is not very good at transferring heat. Because the water MFL has increased, the Reynolds number increased which made the HTC go up. The results of the experiment were very similar to those of the studies done by the [46].

13.3.2 Combined Influence of Mass Flow Rate, Nanofluid Concentration, and Inlet Temperature on Heat Transfer Coefficient

Influence of Mass Flow Rate and Nanofluid Concentration at 25° Inlet Temperature

Figure 13.5 shows the effect of MFL and % nanofluid concentration of Al2O3 nanofluid on HTC with inlet temperature as 25°C. By varying the nanofluid concentration from 0.1 to 0.5%, the HTC s are increased from 3156.14 to 4436.08, 8096.94 to 10514.16 and 11604.42 to 15044.68 W/m^{2}K for 2 m/s, 5 m/s, and 8 m/s respectively, at 25°C at inlet temperature. Highest HTC of 15044.68 W/m^{2}k was observed at a MFL of 8 m/s at 0.5% nanofluid concentration, whereas the lowest HTC of 3156.14 W/m^{2}K was observed at a MFL of 2 m/s at 0.1% nanofluid concentration.

The MFL and % nanofluid concentration of Al_2O_3 nanofluid have a considerable effect on the enhancement of the HTC such that with an increase in MFL and % nanofluid concentration, HTC increases considerably. Similar trend was found in the previous research carried out by various researchers. These findings are in a good agreement with the results reported in [46]. The average HTC was observed to increase with both the MFL and the % nanofluid concentration.

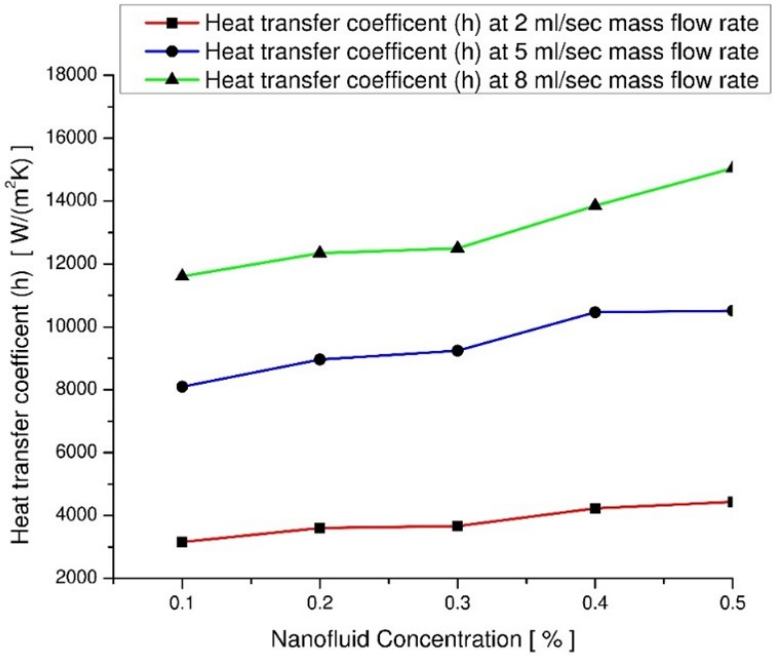

Figure 13.5: *Mass flow rate and nanofluid concentration at 25° inlet temperaturee.*

Influence of Mass Flow Rate and Nanofluid Concentration at 30° Inlet Temperature

Figure 13.6 shows the effect of MFL and % nanofluid concentration of Al_2O_3 nanofluid on HTC with inlet temperature as 30°C. By varying the nanofluid concentration from 0.1 to 0.5%, the HTC are increased from 3119.22 to 4493.23, 8195.53 to 11684.54 and 12476.89 to 16656.84 W/m^{2}K for 2 m/s, 5 m/s, and 8 m/s respectively, at 30°C at inlet temperature. Highest HTC of 16656.84 W/m^{2}k was observed at a MFL of 8 m/s at 0.5% nanofluid concentration, whereas the lowest HTC of 3119.22 W/m^{2}K was observed at a MFL of 2 m/s at 0.1% nanofluid concentration.

The MFL and %nanofluid concentration of Al_2O_3 nanofluid have a significant influence on HTC enhancement, such that as MFL and % nanofluid concentration rise, HTC increases significantly. A similar pattern was discovered in prior study conducted by several academics. These findings are consistent with the findings published in [46]. Overall, the average HTC was shown to be intensified by MFL and % nanofluid concentration.

Influence of Mass Flow Rate and Nanofluid Concentration at 35° Inlet Temperature

Figure 13.7 shows the effect of MFL and %nanofluid concentration of Al_2O_3 nanofluid on HTC with inlet temperature as 35°C. By varying the nanofluid concentration from 0.1 to 0.5%, the HTC are increased from 3419.13 to 4615.24, 8131.95 to 12803.49 and 12280.97 to 16524.01 W/m^{2}K for 2 m/s, 5 m/s, and 8 m/s respectively, at 35°C at inlet temperature. Highest HTC of 16524.01 W/m^{2}k was observed at a MFL of 8 m/s at 0.5% nanofluid concentration, whereas the lowest HTC of 3419.13 W/m^{2}K was observed at a MFL of 2 m/s at 0.1% nanofluid concentration.

Both the MFL and the % nanofluid concentration of Al_2O_3 nanofluid play a key role in the enhancement of HTC, with the latter increasing dramatically when both parameters are raised. Several scholars have found a similar pattern in their own research. The results here agree with those found in [46]. On the whole, it was

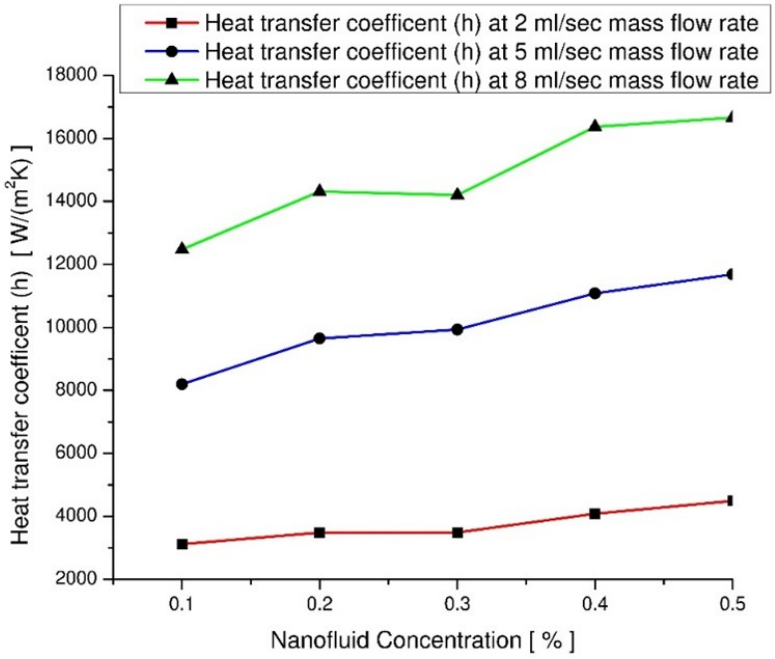

Figure 13.6: *Mass flow rate and nanofluid concentration at 30° inlet temperature.*

found that increasing the MFL and the concentration of nanofluids by a percentage both increased the HTC.

Experiments were conducted to determine an HTC of water and Al_2O_3-water nanofluids, and the findings are depicted in Figures 13.3 to 13.7. In this case, increasing the MFL results in a large rise in convective HTC of both Al_2O_3-water nanofluid and deionized water; nevertheless, the growth rate is very low. The increase in the NPs mass fraction results in a rise in the average convective HTC of Al_2O_3-water nanofluids. The average convective HTC is significantly greater than or remains very close to the average convective HTC of 0.4% when the mass fraction of NPs is 0.5%. Both of these outcomes are favorable. The primary reason for this is that the thermal conductivity of NPs is noticeably higher than that of deionized water, and that the effective thermal conductivity is improved by any increase in the concentration of NPs. In other words, increasing the concentration of NPs improves effective thermal conductivity. NPs have the capacity to simultaneously increase the amount of disturbance in the fluid, reduce the amount of laminar substrate thickness, and lower the barrier to convection heat transfer.

However, as the concentration of NPs is increased, a further increase in the viscosity coefficient causes a slowing of movement and particle dispersion, which eventually results in a slower rate of heat transfer. It was also found that there was a significant connection between the temperature of the fluid when it was introduced into the system and the phenomena of the HTC. The HTC had a significant increase as a direct result of the increase in the temperature of the input, which went from 25 degrees Celsius to 35 degrees Celsius. The average convection HTC of Al_2O_3-water nanofluids is much higher than that of water as a flowing medium. This difference is significant enough to be statistically significant. This is mostly owing to the fact that Al_2O_3 has a higher density than water, and that molecules with a high density, small size, and that are packed tightly together will always improve heat transmission.

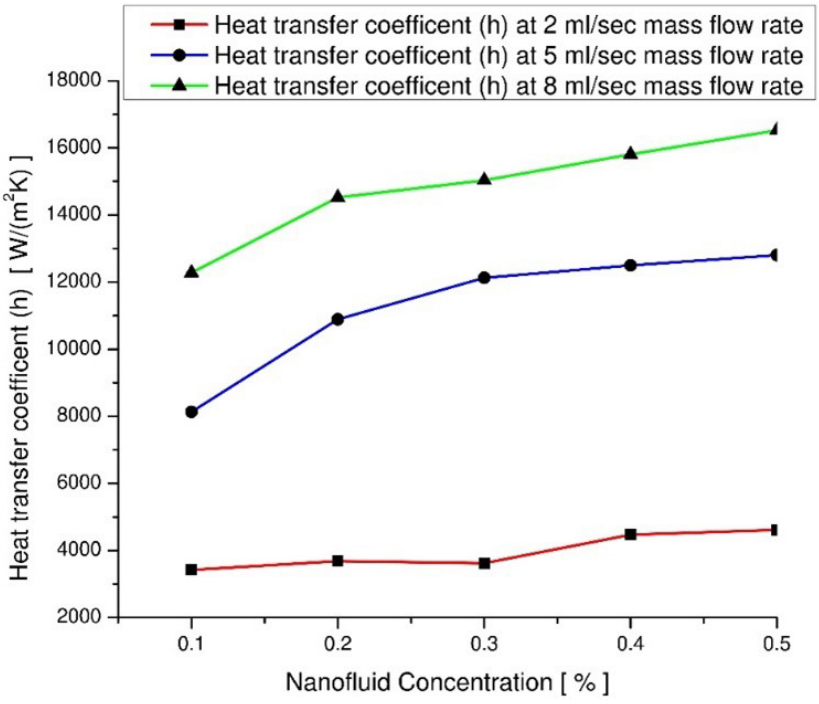

Figure 13.7: *Mass flow rate and nanofluid concentration at 35° inlet temperature.*

13.4 Conclusion

The thermal performance of an Al2O3-water nanofluid was tested inside a heat sink with a rectangular MCHS. From the results, following conclusions can draw:

1. The heat transfer characteristic was found to be enhanced at increasing concentrations of nanoparticles compared to lower percentages and pure water.
2. At a mass flow rate of 8 m/s and a concentration of 0.5% nanofluid, the maximum HTC is about 16524.01 W/m^{2}k.
3. Al_2O_3-water nanofluids demonstrated superior thermal performance compared to water as a flowing medium.
4. This study shows how the design of a rectangular MCHS geometry and the existence of a nanofluid mechanism can improve the thermal performance of electronic cooling.

Overall, the Al_2O_3-water nanofluids demonstrate plausible heat transfer capability, making them a suitable coolant for application in a MCHS. The friction factor and pressure drop need additional research before it can be used in a MCHS. Additional research is required to determine whether or not the presence of Al_2O_3-water nanofluids in the base fluid results in an increase in pressure drop.

Funding: This research received no external funding.

Conflicts of Interest: The authors declare no conflict of interest.

Authors Contributions: Co-authors contributed equally.

References

1. Karpat, F., Kalay, O. C., Dirik, A. E., & Karpat, E. (2022). Fault Classification of Wind Turbine Gearbox Bearings Based on Convolutional Neural Networks. *Transdisciplinary Journal of Engineering and Science,* 13, 71–83. https://doi.org/10.22545/2022/00190
2. Belkhode, P. N., Ganvir, V. N., Shelare, S. D., Shende, A., & Maheshwary, P. (2022). Experimental investigation on treated transformer oil (TTO) and its diesel blends in the diesel engine. *Energy Harvesting and Systems,* 9(1), 75–81. https://doi.org/10.1515/ehs-2021-0032
3. Yavaş, Ö., Savran, E., Nalbur, B. E., & Karpat, F. (2022). Energy and Carbon Loss Management in an Electric Bus Factory for Energy Sustainability. *Transdisciplinary Journal of Engineering and Science,* 13, 97– 110. https://doi.org/10.22545/2022/00207
4. Model, C. E. (2022). Exploring Grassroots Renewable Energy Transitions: Developing a. *Transdisciplinary Journal of Engineering & Science,*2, 137–163. https://doi.org/10.22545/2022/00215
5. Shelare, S. D., Aglawe, K. R., & Belkhode, P. N. (2022). A review on twisted tape inserts for enhancing the heat transfer. *Materials Today: Proceedings,* 54, 560–565. https://doi.org/10.1016/j.matpr.2021.09.012
6. Palande, D. D., Ghuge, N. C., & Dapase, C. R. (2022). Waste Heat Recovery From The Hot Water Boiling Plant Analysis using CFD. *Transdisciplinary Journal of Engineering and Science,* 13, 43–56. https://doi.org/10.22545/2022/00182
7. Aglawe, K. R., Yadav, R. K., & Thool, S. B. (2021). Preparation, applications and challenges of nanofluids in electronic cooling: A systematic review.*Materials Today: Proceedings,* 43, 366–372. https://doi.org/10.1016/j.matpr.2020.11.679
8. Gajbhiye, T., Shelare, S., & Aglawe, K. (2022). Current and Future Challenges of Nanomaterials in Solar Energy Desalination Systems in Last Decade. *Transdisciplinary Journal of Engineering & Science,* 13, 187–201. https://doi.org/10.22545/2022/00217
9. Aglawe, K. R., Yadav, R. K., & Thool, S. B. (2022). Current Technologies on Electronics Cooling and Scope for Further Improvement: A Typical Review. *Proceedings of the International Conference on Industrial and Manufacturing Systems* (CIMS-2020), 389–408. https://doi.org/10.1007/978-3-030-73495-4_27
10. Shelare, S. D., Aglawe, K. R., & Khope, P. B. (2021). Computer aided modeling and finite element analysis of 3-D printed drone. *Materials Today: Proceedings,* 47, 3375–3379. https://doi.org/10.1016/j.matpr.2021.07.162
11. Kurnia, J. C., Haryoko, L. A. F., Taufiqurrahman, I., Chen, L., Jiang, L., & Sasmito, A. P. (2022). Optimization of an innovative hybrid thermal energy storage with phase change material (PCM) wall insulator utilizing the Taguchi method. *Journal of Energy Storage,* 49, 104067. https://doi.org/10.1016/j.est.2022.104067
12. Azari, A., Kalbasi, M., & Rahimi, M. (2014). CFD and experimental investigation on the heat transfer characteristics of alumina nanofluids under the laminar flow regime. *Brazilian Journal of Chemical Engineering,* 31(2), 469–481. https://doi.org/10.1590/0104-6632.20140312s00001959
13. Palande, D. D., Ghuge, N. C., & Shrivastwa, R. (2022). Comprehensive Review of Karanja & Jatropha Biodiesel Fuelled Diesel Engines. *Transdisciplinary Journal of Engineering and Science,* 13, 85–96. https://doi.org/10.22545/2022/00201

14. Dhutekar, P., Mehta, G., Modak, J., Shelare, S., & Belkhode, P. (2021). Establishment of mathematical model for minimization of human energy in a plastic moulding operation.*Materials Today: Proceedings,* 47, 4502–4507. https://doi.org/10.1016/j.matpr.2021.05.330
15. Bayomy, A. M., Saghir, M. Z., & Yousefi, T. (2016). Electronic cooling using water flow in aluminum metal foam heat sink: Experimental and numerical approach. *International Journal of Thermal Sciences,* 109, 182–200. https://doi.org/10.1016/j.ijthermalsci.2016.06.007
16. Dhande, H. K., Shelare, S. D., & Khope, P. B. (2020). Developing a mixed solar drier for improved postharvest handling of food grains. *Agricultural Engineering International: CIGR Journal,* 22(4), 166–173.
17. Eastman, J.A., Choi, U.S. (1997). Enhancing thermal conductivity through the development of nanofluids.*In Materials Research Society Symposium – Proceedings* (Vol. 457, pp. 3–11). https://www.osti.gov/servlets/purl/459378
18. Waghmare, S., Shelare, S., Aglawe, K., & Khope, P. (2022). A mini review on fibre reinforced polymer composites. *Materials Today: Proceedings,* 54, 682–689. https://doi.org/10.1016/j.matpr.2021.10.379
19. Xuan, Y., & Li, Q. (2000). Heat transfer enhancement of nanofluids. *International Journal of Heat and Fluid Flow,* 21(1), 58–64. https://doi.org/10.1016/S0142-727X(99)00067-3
20. Belkhode, P. N., Shelare, S. D., Sakhale, C. N., Kumar, R., Shanmugan, S., Soudagar, M. E. M., & Mujtaba, M. A. (2021). Performance analysis of roof collector used in the solar updraft tower. *Sustainable Energy Technologies and Assessments,* 48, 101619. https://doi.org/10.1016/ j.seta.2021.101619
21. Belkhode, P. N., Ganvir, V. N., Shende, A. C., & Shelare, S. D. (2022). Utilization of waste transformer oil as a fuel in diesel engine. *Materials Today: Proceedings,* 49, 262–268. https://doi.org/10.1016/j.matpr.2021.02.008
22. Hu, Z. S., & Dong, J. X. (1998). Study on antiwear and reducing friction additive of nanometer titanium oxide. *Wear,* 216(1), 92–96. https://doi.org/10.1016/S0043-1648(97)00252-4
23. Sun, B., & Liu, H. (2017). Flow and heat transfer characteristics of nanofluids in a liquid-cooled CPU heat radiator. *Applied Thermal Engineering,* 115, 435–443. https://doi.org/10.1016/j.applthermaleng.2016.12.108
24. Kamyar, A., Saidur, R., & Hasanuzzaman, M. (2012). Application of Computational Fluid Dynamics (CFD) for nanofluids. *International Journal of Heat and Mass Transfer,* 55(15), 4104–4115. https://doi.org/10.1016/j.ijheatmasstransfer.2012.03.052
25. Ellsworth, M. J., Campbell, L. A., Simons, R. E., Iyengar, M. K., Schmidt, R. R., & Chu, R. C. (2008). The evolution of water cooling for IBM large server systems: Back to the future. *2008 11th IEEE Intersociety Conference on Thermal and Thermomechanical Phenomena in Electronic Systems,* I-THERM, 266–274. https://doi.org/10.1109/ITHERM.2008.4544279
26. Xu, G., Guenin, B., & Vogel, M. (2004). Extension of air cooling for high power processors. Thermomechanical Phenomena in Electronic Systems -*Proceedings of the Intersociety Conference,* 1(858), 186–193. https://doi.org/10.1109/itherm.2004.1319172
27. Raghuraman, D. R. S., Thundil Karuppa Raj, R., Nagarajan, P. K., & Rao, B. V. A. (2017). Influence of aspect ratio on the thermal performance of rectangular shaped micro channel heat sink using CFD code. *Alexandria Engineering Journal,* 56(1), 43–54. https://doi.org/10.1016/j.aej.2016.08.033
28. Ali, H. M., & Arshad, W. (2017). Effect of channel angle of pin-fin heat sink on heat transfer performance using water based graphene nanoplatelets nanofluids. *International Journal of Heat and Mass Transfer,* 106, 465–472. https://doi.org/10.1016/j.ijheatmasstransfer.2016.08.061
29. Jajja, S. A., Ali, W., Ali, H. M., & Ali, A. M. (2014). Water cooled minichannel heat sinks for microprocessor cooling: Effect of fin spacing. *Applied Thermal Engineering,* 64(1), 76–82. https://doi.org/10.1016/j.applthermaleng.2013.12.007
30. Seyf, H. R., & Feizbakhshi, M. (2012). Computational analysis of nanofluid effects on convective heat transfer enhancement of micro-pin-fin heat sinks.*International Journal of Thermal Sciences,* 58, 168–179. https://doi.org/10.1016/j.ijthermalsci.2012.02.018

31. Al-Rashed, M. H., Dzido, G., Korpyś, M., Smołka, J., & Wójcik, J. (2016). Investigation on the CPU nanofluid cooling. *Microelectronics Reliability,* 63, 159–165. https://doi.org/10.1016/j.microrel.2016.06.016
32. Jilte, R., Afzal, A., & Panchal, S. (2021). A novel battery thermal management system using nano-enhanced phase change materials. *Energy,* 219, 119564. https://doi.org/10.1016/j.energy.2020.119564
33. Sahu, P., Shelare, S., & Sakhale, C. (2020). Smart cities waste management and disposal system by smart system: A review. *International Journal of Scientific and Technology Research,* 9(3), 4467–4470.
34. Sultan, G. I. (2000). Enhancing forced convection heat transfer from multiple protruding heat sources simulating electronic components in a horizontal channel by passive cooling. *Microelectronics Journal,* 31(9), 773–779. https://doi.org/10.1016/S0026-2692(00)00058-6
35. Shah, J., Ranjan, M., Davariya, V., Gupta, S. K., & Sonvane, Y. (2017). Temperature-dependent thermal conductivity and viscosity of synthesized α-alumina nanofluids. *Applied Nanoscience,* 7(8), 803–813. https://doi.org/10.1007/s13204-017-0594-7
36. Esmaeil, K. K., Sultan, G. I., Al-Mufadi, F. A., & Almasri, R. A. (2019). Experimental Heat Transfer From Heating Source Subjected to Rigorous Natural Convection Inside Enclosure and Cooled by Forced Nanofluid Flow. *Journal of Heat Transfer,* 141(7). https://doi.org/10.1115/1.4043673
37. Jawad, Q. A., Mahdy, A. M. J., Khuder, A. H., & Chaichan, M. T. (2020). Improve the performance of a solar air heater by adding aluminum chip, paraffin wax, and nano-SiC. Case Studies in Thermal Engineering, 19, 100622. https://doi.org/10.1016/j.csite.2020.100622
38. Siricharoenpanich, A., Wiriyasart, S., Srichat, A., & Naphon, P. (2020). Thermal cooling system with Ag/Fe3O4 nanofluids mixture as coolant for electronic devices cooling. Case Studies in Thermal Engineering, 20, 100641. https://doi.org/10.1016/j.csite.2020.100641
39. Elsayed, A., Al-dadah, R. K., Mahmoud, S., & Rezk, A. (2015). Numerical investigation of turbulent flow heat transfer and pressure drop of Al_2O_3/water nanofluid in helically coiled tubes. *International Journal of Low-Carbon Technologies,* 10(3), 275–282. https://doi.org/10.1093/ijlct/ctu003
40. Nguyen, C. T., Desgranges, F., Roy, G., Galanis, N., Maré, T., Boucher, S., & Angue Mintsa, H. (2007). Temperature and particle-size dependent viscosity data for water-based nanofluids – Hysteresis phenomenon. *International Journal of Heat and Fluid Flow,* 28(6), 1492–1506. https://doi.org/10.1016/j.ijheatfluidflow.2007.02.004
41. Waghmare, S. N., Shelare, S. D., Tembhurkar, C. K., & Jawalekar, S. B. (2020). Pyrolysis system for environment-friendly conversion of plastic waste into fuel. In Lecture Notes in Mechanical Engineering (pp. 131–138). Springer. https://doi.org/10.1007/978-981-15-4748-5_13
42. Yu, X., Zhang, C., Teng, J., Huang, S., Jin, S., Lian, Y., Cheng, C., Xu, T., Chu, J.-C., Chang, Y.-J., Dang, T., & Greif, R. (2012). A study on the hydraulic and thermal characteristics in fractal tree-like microchannels by numerical and experimental methods. *International Journal of Heat and Mass Transfer,* 55(25), 7499–7507. https://doi.org/10.1016/j.ijheatmasstransfer.2012.07.050
43. Ganapathy, H., Shooshtari, A., Choo, K., Dessiatoun, S., Alshehhi, M., & Ohadi, M. (2013). Volume of fluid-based numerical modeling of condensation heat transfer and fluid flow characteristics in microchannels. *International Journal of Heat and Mass Transfer,* 65, 62–72. https://doi.org/10.1016/j.ijheatmasstransfer.2013.05.044
44. Shelare, S., Kumar, R., & Khope, P. (2021). Assessment of Physical, Frictional and Aerodynamic Properties of Charoli (buchanania Lanzan Spreng) Nut as Potentials for Development of Processing Machines. *Carpathian Journal of Food Science and Technology,* 13(2), 174–191. https://doi.org/10.34302/crpjfst/2021.13.2.16
45. Fan, Y., Lee, P. S., Jin, L.-W., & Chua, B. W. (2013). A simulation and experimental study of fluid flow and heat transfer on cylindrical oblique-finned heat sink. *International Journal of Heat and Mass Transfer,* 61, 62–72. https://doi.org/10.1016/j.ijheatmasstransfer.2013.01.075

46. Vinoth, R., & Sachuthananthan, B. (2021). Flow and heat transfer behavior of hybrid nanofluid through microchannel with two different channels. *International Communications in Heat and Mass Transfer,* 123, 105194. https://doi.org/10.1016/j.icheatmasstransfer.2021.105194

About the Authors

Kapil R. Aglawe is presently pursuing his Doctor of Philosophy (PhD) degree in the area of Mechanical Engineering, from the Mechanical Engineering, National Institute of Technology, Raipur, India. Also, he is working as an Assistant Professor in the Department of Mechanical Engineering at Priyadarshini College of Engineering, Nagpur, Maharashtra, India. He is pursuing his the Doctor of Philosophy (PhD) degree in the area of Mechanical Engineering, from the Mechanical Engineering, National Institute of Technology, Raipur, India. He has published more than 10 research articles throughout the several SCI / Scopus indexed journal, including International / National level conferences. He is also academically engaged with the reviewership with the several SCI/ Scopus indexed Journals from last 2 years. He is a life time member of several reputed professional societies at National and International level. Also he has a patent in his credentials in the field of Mechanical Engineering.

Dr. R. K. Yadav is presently working as an Associate Professor in the Department of Mechanical Engineering at National Institute of Technology, Raipur, India. He has received the Doctor of Philosophy (PhD) degree in the area of Mechanical Engineering, from Mechanical Engineering, National Institute of Technology, Raipur, India. He has published several number of research articles throughout SCI / Scopus indexed journal, including International / National level conferences. He is also academically engaged with the reviewership with the several SCI/ Scopus indexed Journals/ Conferences. He has delivered several Expert Talks/Lectures at different level of platform throughout the country. He is a life time member of several reputed professional societies at National and International level.

Dr. Sanjeev B. Thool is presently working as an Associate Professor in the Department of Mechanical Engineering at Dwarkadas Jivanlal Sanghvi College of Engineering, also known as D. J. Sanghvi, is an engineering college, Mumbai, Maharashtra, India. He has received the Doctor of Philosophy (PhD) degree in the area of Mechanical Engineering, from Mechanical Engineering, National Institute of Technology,

Raipur, India. He has published several number of research articles throughout SCI / Scopus indexed journal, including International / National level conferences. He is also academically engaged with the reviewership with the several SCI/ Scopus indexed Journals/ Conferences. He has delivered several Expert Talks/Lectures at different level of platform throughout the country. He is a life time member of several reputed professional societies at National and International level. During his academic career he has authored two books of international publishers.